Studies on the Effect of Noise in Boundary Quantum Phase Transitions

by

Gu Zhang

Department of Physics
Duke University

Date: _____

Approved:

_____
Harold U. Baranger, Supervisor

_____
Shailesh Chandrasekharan

_____
Gleb Finkelstein

_____
Ronen Plesser

_____
Stephen W. Teitsworth

Dissertation submitted in partial fulfillment of the requirements for the degree of
Doctor of Philosophy in the Department of Physics
in the Graduate School of Duke University
2018

Abstract

Studies on the Effect of Noise in Boundary Quantum Phase Transitions

by

Gu Zhang

Department of Physics
Duke University

Date: _____

Approved:

_____
Harold U. Baranger, Supervisor

_____
Shailesh Chandrasekharan

_____
Gleb Finkelstein

_____
Ronen Plesser

_____
Stephen W. Teitsworth

An abstract of a dissertation submitted in partial fulfillment of the requirements for the degree of Doctor of Philosophy in the Department of Physics in the Graduate School of Duke University
2018

Abstract

Boundary quantum phase transitions are abrupt ground state transitions triggered by the change of the boundary conditions at single or multiple (but finite) points. When boundary effects dominate, understanding boundary quantum phase transitions requires a deeper knowledge of strongly correlated electron systems that is beyond the widely applied mean field treatment. Meanwhile, with strong boundary effect, most systems with boundary quantum phase transition can generally be considered as effectively zero-dimensional, with reservoir details ignored. Consequently, the critical features of boundary quantum phase transitions only involve long-time correlations instead of long-range ones.

On the other hand, different from the geometrical confinement of boundaries, dissipation or quantum noise widely exists along the entire system. In bulk quantum phase transitions, dissipation decreases system coherence by reducing the long-range correlations. This fact makes it plausible that dissipation destroys the critical behavior of the quantum critical points. The effect of dissipation, however, remains unclear in boundary quantum phase transition systems due to their lack of long-range correlations.

In this thesis I thus focus on the effect of dissipation in boundary quantum phase transitions. These studies are motivated and encouraged by recent experimental triumphs where dissipation is realized and precisely measured in mesoscopic systems, which provide experimental evidences to check theoretical researches. This thesis

involves multiple dissipative mesoscopic systems, including the dissipative two impurity Kondo, two channel Kondo, resonant level, and Anderson models.

To begin with, the effect of dissipation in two impurity Kondo model has been explored and we find that the presence of dissipation restores the quantum phase transition by reducing the unwanted charge tunneling process. We further provide the phase diagram for the system that has an exotic double-quantum-critical-point feature.

After that, the non-equilibrium I-V feature of a dissipative resonant level model is studied. This model has been experimentally proven to host a boundary quantum phase transition. With different tuning parameters, we calculate the I-V feature at both the quantum critical point and in the crossover regime analytically. The theoretical calculation agrees remarkably with the experimental data.

As the spinful version of the resonant level model, the dissipative Anderson model has multiple unique features, including the experimentally observed peak position shifting and dissipation dependent saturated peak conductance. Through renormalization group studies and mapping the model to the quantum Brownian motion model, we understand these features qualitatively.

As an example of the application of above research achievements, we study the stabilization of a Majorana zero mode with the quantum frustration in a dissipative resonant level model. The Majorana zero mode is known to be unstable against the coupling to its partner at the other end of the Majorana hosted nanowire. We prove that the Majorana zero mode can be stabilized by coupling its partner to the quantum dot of a frustrated dissipative resonant level model, where an isolated impurity Majorana fermion is produced.

Finally, we study the relation between boundary quantum phase transitions and geometric phases. The calculation is carried out at the Toulouse point of a dissipative resonant level model. Although it satisfies the criteria of bulk quantum

phase transitions to host a non-trivial geometric phase, the dissipative resonant level model has zero geometric phase due to the identical zero geometric curvature. This phenomenon is generally explained by studying the geometric tensor of boundary quantum phase transition-hosted systems.

To my parents Li Zhang and Qiong Zhou

Contents

List of Figures

List of Abbreviations and Symbols

Abbreviations

QPT	Abbreviation for quantum phase transition
1d	Short for one-dimensional
RG	Short for renormalization group
QCP	Short for quantum critical point
2CK	Short for two channel Kondo
MZM	Short for Majorana zero mode
QBM	Short for quantum Brownian motion

Acknowledgements

It would have been impossible to finish my PhD study without the help from many persons. Here I have the chance to show my most sincere thanks to them.

To begin with, I would like to express my deep gratitude to my PhD advisor, Prof. Harold U. Baranger, with whom I have had a great PhD experience in last six years. As an experienced professor, Harold has a great insight and deep understanding of physics. With his broad eyesight in physics, Harold always has a clear physical picture about the our problems and provides me constructive suggestions. Those suggestions significantly helps me through my PhD years and with them I gradually develops a more physical and systematic way to think about physical problems. Apart from his great insight in physics, his enthusiasm and his rigorous attitude towards studies also greatly influence me, and teach me what it really means to be a physicist. Meanwhile, as a successful advisor, Harold never lacks the patience to listen to me and never interrupts me during our discussions. He always encourages me to develop my own ideas and tolerates my mistakes during the research. It is with his encouragement and patience that I have the space and freedom to learn new ideas and to develop my own way to handle physical problems. Meanwhile, I particularly appreciate that he really cares about his students beyond work. He is always willing to listen and provide daily-life suggestions when we have encountered any difficulty.

I would like to thank group members from Prof. Gleb Finkelstein's group, es-

pecially Prof. Gleb Finkelstein and Dr. Chung-Ting Ke for the collaboration and helpful discussion during my studies on multiple mesoscopic systems. Actually, three of my projects in this thesis are encouraged by their experiments. They have taught me a lot about graphene-related experimental details and are always willing to discuss with me about my projects. Through the collaboration with them, I have acquired a valuable experience in working with experimentalists, which will be of great help in my future researches. Meanwhile, I also would like to thank Gleb for his support during my PostDoc applications.

I would like to thank Prof. Eduardo Novais for the collaboration on multiple dissipative mesoscopic problems. With his broad knowledge, Eduardo provides multiple alternative directions when I have trouble in my researches. For instance, I have learned from him about the application of boundary conformal field theory and quantum Brownian motion model into mesoscopic systems. Those knowledge greatly enhance my physical vision and are significantly beneficial to my researches. I also would like to thank Eduardo for his support during my PostDoc applications.

I would like to thank Prof. Chung-Hou Chung for the collaboration on the dissipative resonant level model problem. Through the collaboration with him, I have noticed and better understood some of the non-equilibrium RG techniques. I also enjoy conversations with him and he always encourages me when facing problems. I also would like to thank Chung-Hou for his support during my PostDoc applications.

I would like to thank Prof. Shailesh Chandrasekharan for his suggestion and support during my study and application of quantum Monte Carlo. I am also grateful to thank Prof. Serge Florens for the discussion of multiple problems with him and his hospitality when I visited France.

I would like to thank my fellow graduate students. Leo (Dr. Yao-Lung Fang) is always happy to discuss physics with me even we are working on different projects. He is also willing to help me about computer tricks. Dr. Chung-Ting Ke and Dr. Ming-

Tso Wei are my experimental collaborators. More specifically, Ting and Ming share with me their data and experimental details that are greatly helpful in multiple projects.

Finally and most importantly, I would like to thank my parents Li Zhang and Qiong Zhou for their support and understanding through all these years.

1

Introduction

1.1 Introduction

Typically physical systems contain at least one bulk part and one boundary part, which may comprise the surface of a three dimensional material, the edge of a two dimensional plane, or a point of a one dimensional line. Although it has negligible "size" compared with the bulk part, the system boundary sometimes decides the features of the entire material. The strong boundary effect, for instance, is key when we think about the thermal radiation of a black body and the electron tunneling feature of a surface-oxidized metal.

The strength of the boundary effect is even stronger in quantum physics. One example consists of the famous quantum Hall (QH) states [185]. In QH states, electrons propagate only along the edge of a two dimensional material. The system's electrical and thermal features thus mainly depend on the edge characteristics, irrelevant of the bulk details. Another example is the one dimensional tunneling models. In these models it is assumed that the systems are uniform everywhere except at one or a finite number of points, known as impurities. Although the bulk part is infinitely

larger than the boundary points, the tunneling feature of these models mostly relies on the details of the impurities, or boundary conditions next to the impurities.

The importance of boundaries in systems further enables scientists to define a special type of quantum phase transitions —- the boundary quantum phase transitions or impurity quantum phase transitions [177]. As hinted by the name, boundary quantum phase transitions are defined with respect to abrupt changes of boundary parameters or boundary conditions, while keeping bulk parameters invariant. The Kondo model is one of the most famous examples. In a Kondo model, the Kondo exchange coupling strength determines the system ground state, where a KT quantum phase transition is realized between the ferromagnetic and anti-ferromagnetic Kondo fixed points [83]. Compared with their bulk counterparts, boundary quantum phase transitions are often more easily accessible since the critical point only relies on the local parameter at the boundaries. However, it is normally difficult to define order parameters in boundary quantum phase transitions [177] so that the observation of a boundary quantum phase transition relies on some indirect measurements, which may require a better understanding of the transition.

Quantum noise is another important ingredient in quantum dynamics. It normally originates from quantum fluctuations of the system. Because quantum noise generally dissipates system energy into the environment, it is also called quantum dissipation. Intuitively, the presence of quantum noise will suppress the quantum effect since it decreases quantum coherence of the system, and this has been proved in multiple systems, both in [119; 180; 105; 116; 33; 37; 86; 152; 23] and out of equilibrium [45; 64; 39; 100; 173]. One of the famous examples is a quantum noise-Ising chain [86]. In that model, the dissipative modes that couples to the Ising chain smear out the transition between the ordered and disordered states.

However, the suppression of the quantum phase transition mentioned above does not always occur. Generally speaking, quantum states will not be destroyed if dis-

sipation couples to some irrelevant operators. We can understand this by thinking about the quantum Hall states. In these states, material impurities won't increase system noise due to the topological protection of the quantum Hall filling factors. Based on this fact, we can simply ignore quantum noise once it decouples with physically interesting operators.

As a brief summary, we have noticed that quantum noise is usually coherence destructive but sometimes irrelevant. With this knowledge in mind, one natural question to ask is: can we further make use of quantum noise to decrease the unwanted physical processes, while keeping the operators that are relevant to the quantum phase transitions invariant? The answer is yes. More specifically, in some systems [103; 191], the quantum phase transition is replaced by a crossover due to the competition between two equally important operators. If we can utilize the quantum noise to kill one of them while leaving the other one invariant, the quantum phase transition will be restored. This noise induced quantum phase transition has been experimentally observed in a dissipative spinless resonant level model. In this model, with the competing level broadening suppressed by quantum noise, an asymmetry induced boundary quantum phase transition has been observed. Consequently, quantum noise will not trivially destroy quantum phase transitions. The conditions for this phenomenon deserve further investigation.

1.2 Outline of the thesis

In this thesis, I will mostly focus on the theoretical understanding of the effect of quantum noise in mesoscopic systems where boundary effects are critical. I will study the following problems in particular:

1. Two impurity Kondo model with the presence of dissipation: How is the quantum phase transition destroyed by the initially weak charge transport? How can we restore the quantum phase transition with dissipation? And how can we

experimentally prove our theoretical predictions?

2. The conductance feature of a dissipative resonant level model: How does the weak coupling model flow to the strong coupling regime? What is system's non-equilibrium differential conductance both at the critical point and that when system flows towards the crossover regime? Moreover, what will the system look like if the system becomes spinfull instead of spinless?

3. The Majorana fermion in a dissipative resonant level model: How does this Majorana fermion form in a dissipative resonant level model? What is its difference from that in a two channel Kondo model? Is it just a mathematically effective "concept" or a real operator that can decide system features? Finally, what will happen when it couples to the quantum dot of a resonant level model?

4. Geometric phase in boundary quantum phase transitions. In boundary quantum phase transitions, the connection between the singularity at the quantum critical point and a possibly non-trivial geometric phase is still unknown. Here we analytically calculate the geometric phase of a dissipative resonant level model and use the result to study the geometric phase in a system that hosts boundary quantum phase transition.

The thesis is organized as follows. Background reviews of relevant material will be provided in Chapters 2, 3 and 4. In Chapter 2, I review the one-dimensional problems that host most of the known boundary quantum phase transitions. I review bosonization, which is among the most powerful techniques in dealing with one dimensional interacting systems. In Chapter 3, I review quantum phase transitions, including their categories and scaling behaviors. I also introduce the renormalization group method to physically understand the quantum phase transitions. After that I introduce boundary quantum phase transitions in Chapter 4, where the dissipative spinless resonant level model, Kondo model and two channel Kondo models are used as three examples.

I begin to introduce my own work beginning with Chapter 5. In this chapter I introduce the rescue of the quantum phase transition in the two impurity Kondo model by quantum noise. After that I introduce the non-equilibrium I-V feature at the quantum critical point of the dissipative spinless resonant level model in Chapter 6, and continue with the calculation of non-equilibrium conductance in the crossover regime in Chapter 7. Both Chapters 6 and 7 provide analytical results in excellent agreement with the experimental data. In Chapter 9 I move beyond the spinless case by introducing our study of the Anderson model, where our theoretical work qualitatively agrees with the experimental data. However, due to the complexity of this problem, we have not got quantitative results. In Chapter 8 I introduce my work where quantum frustration is used to stabilize a Majorana zero mode. My most recently work is introduced in Chapter 10 about the geometric phase in a boundary quantum phase transition. Finally I will summarize my thesis in Chapter 11.

2

Background: One-dimensional Systems, Bosonization and Quantum Noise

This chapter provides a review of multiple one dimensional structures, mainly focusing on their electronic tunneling features. For later convenience, This chapter also briefly introduces Bosonization in one dimensional systems, which is especially useful in one-dimensional problems. This chapter contains only review material and not my original work.

I begin with the introduction to multiple simplest one dimensional systems and the experimental way to realise them in Section 2.1. I also review their tunneling behavior and the physical picture behind the experimental data. After that, I introduce the bosonization method, which is powerful in solving one dimensional problems in Section 2.2. Finally, since quantum noise is one of the most important ingredients of this thesis, I briefly introduce the method to model quantum noise in 1d systems in Section 2.3.2.

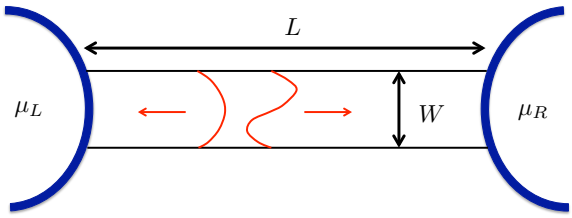

FIGURE 2.1: Illustration of a perfect one dimensional nanowire with length L and diameter W with scale $W \ll L$. When the diameter is small enough, discrete energy levels form in the wire as represented by the two red modes that propagate towards either direction. The wire is connected to two reservoirs with chemical potential μ_L and μ_R, respectively.

2.1 Tunneling Feature of non-interacting One-dimensional Nanostructures

As will be introduced in more detail in Section 2.2, due to the special geometry of 1d materials, excitation modes in interacting 1d systems are distinct compared with those in higher-dimensional ones. Actually, even non-interacting 1d materials have some special features. In this section I will briefly introduce two non-interacting 1d systems (free 1d quantum wire and resonant level model) with interesting transport phenomenon.

2.1.1 Tunneling Feature of an Ideal Quantum Wire

We begin with an ideal quantum wire as shown in Fig. 2.1. The system consists of two reservoirs with different chemical potential μ_L and μ_R, respectively. Between two reservoirs is a perfect nanowire with length L and diameter W. Here we assume that $L \gg W$ such that the system is approximately one-dimensional.

For later convenience, we model the wire length along the x direction and its width in the y and z directions. With this modelling, system wave function is spacially separable, with free propagating modes along the translationally invariant

x axis, and a standing wave solution along the y and z axes [91]

$$\psi_{nk}(\vec{r}) = \chi_n(y,z)\frac{1}{\sqrt{L}}e^{ikx}, \tag{2.1}$$

with the energy

$$E_n(k) = \epsilon_n + \frac{\hbar^2 k^2}{2m}, \tag{2.2}$$

where ϵ_n is the energy of the nth transverse mode $\chi_n(y,z)$ along the x direction and m is the electron mass. In Eq. (2.1), the transmission mode is normalized with the factor $1/\sqrt{L}$, and k is the momentum along the x direction.

In an ideal nanowire, electrons with wave function in Eq. (2.1) travel in the wire without inter-mode backscattering or forward scattering. In this sense, the current through the wire consists of contributions from different modes that transmit independently, each contributing to the current density

$$\begin{aligned} j_{n,k}(\vec{r}) &= -\frac{e\hbar}{2im}[\psi^*_{nk}(\vec{r}) \bigtriangledown \psi_{nk}(\vec{r}) - \psi_{nk}(\vec{r}) \bigtriangledown \psi^*_{nk}(\vec{r})] \\ &= -\frac{e}{L}|\chi_n(y,z)|^2\frac{\hbar k}{m^*}\vec{e}_x, \end{aligned} \tag{2.3}$$

where e_x is the unit vector that labels the transmission direction of the current. Total current density involves the summation over all modes n and k in Eq. (2.3). Finally, the current involves the spacial integral of the current density, which can be simply done if the transverse wave function $\chi_n(y,z)$ has been correctly normalized. The calculations are then straightforward, with the final expression

$$I = \sum I_n = -g_s\frac{e}{h}\sum_n \int_{\epsilon_n}^{\infty} dE[f_L(E) - f_R(E)], \tag{2.4}$$

where g_s is the spin degeneracy and

$$f_i(E) = \frac{1}{\exp(\frac{E-\mu_i}{k_B T}) + 1} \tag{2.5}$$

is the Fermi distribution function in the reservoir i with chemical potential μ_i. At zero temperature, $f_i(E)$ simply becomes a step function $\Theta(\mu_i - E)$. With this simplification, the integral in Eq. (2.4) is only nonzero when the energy E is between two chemical potentials so that $\int_{\epsilon_n}^{\infty} dE[f_L(E) - f_R(E)] = -f_L(\epsilon_n)V_{\text{bias}}$, where V_{bias} is the applied bias between left and right reservoirs. We have thus arrived at the conductance expression

$$G = g_s \frac{e^2}{h} \sum_n f_L(\epsilon_n). \tag{2.6}$$

Eq. (2.6) involves the contribution from all possible transverse modes. In the ideal quantum wire model, the excitation of these modes requires external sources (temperature or applied bias, for instance). Based on the strength of the source, two regimes develop. To better illustrate this, we define $\Delta\epsilon \equiv \epsilon_2 - \epsilon_1$ as the energy spacing between two neighboring standing wave modes. If the temperature is significantly larger than the energy spacing $k_B T \gg \Delta\epsilon$, the wire spectrum can be approximately considered as continuous so that the G-V_g curve is linear. However, with small temperature $k_B T \ll \Delta\epsilon$, the conductance becomes stepwise, where the appearance of each plateau indicates the opening of one transverse mode (represented by the red curves in Fig. 2.1) by the applied bias. Finally, since $\Delta E \propto 1/W^2$, the narrower the nanowire is, it will be easier to observe the quantized conductance plateau shown in Fig. 2.2 [91].

2.1.2 Quantum Dot and Coulomb Diamond

In Section 2.1.1, the general physical picture behind the calculated conductance is the existence of multiple transverse modes and two independently counter propagating channels, which highly requires the uniformity of the nanowire. Consequently, the physical picture changes with the presence of impurities such as quantum dots.

Generally speaking, a quantum dot can be considered as a middle-sized region or

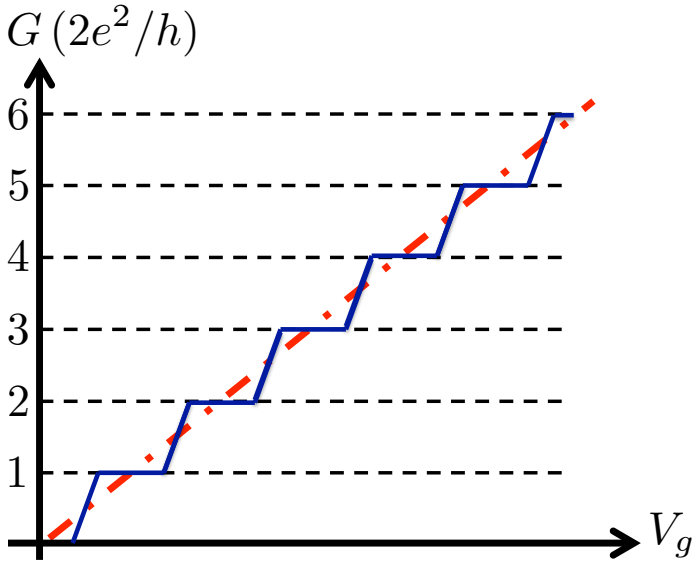

FIGURE 2.2: The conductance of the perfect 1d quantum wire in Fig. 2.1 as a function of the applied bias V_g. The conductance is plotted as a function of $2e^2/h$, where "2" is the spin degeneracy. With different temperature, the conductance shows two distinct patterns. With high temperature $k_BT \gg \Delta\epsilon$, G-V_g has the linear feature as shown by the dashed red line. On the contrary, when $k_BT \ll \Delta\epsilon$, the G-V_g plot has plateaus (indicated by the solid dark line) that correspond to the excitation of transverse modes.

artificial atom [159; 76; 91] that contains multiple electrons with different energies. We called a quantum dot "middle-sized" in the sense that it should be small enough such that the its level spacing must be large enough to observe; Meanwhile, it should be large enough to contain enough electron levels. Finally, to guarantee the confinement of electrons in a quantum dot, the quantum dot-reservoir coupling is required to be small enough.

These requirements lead to peculiar phenomena of quantum dot coupled systems. Intuitively, due to the strong interaction within the quantum dot, the transport feature of a quantum dot system relies heavily on the status of the quantum dot although the size of a quantum dot is normally negligible compared with the entire system. The locally strong interacting feature of the quantum dot is thus essential in the realization of a variety of boundary quantum phase transitions. Here I briefly

review the tunneling feature of a spinless quantum dot model.

The system we are considering consists of a quantum dot that sits between two semi-infinite wires. In this model, both leads are considered as infinitesimal such that they contain free fermionic modes with the Hamiltonian

$$H_{\text{leads}} = \sum_k (\epsilon_k - \mu_S) c^\dagger_{S,k} c_{S,k} + \sum_k (\epsilon_k - \mu_D) c^\dagger_{D,k} c_{D,k}, \tag{2.7}$$

where S (D) labels the source (drain) lead with chemical potential μ_S (μ_D). Experimentally, the quantum dot can be realized by a short length carbon nanotube [134] or by a confined area in a two dimensional electron gas (2DEG) [97]. The energy of the quantum dot can be experimentally adjusted through a plunger gate with backgate voltage V_g.

To model the Hamiltonian of the quantum dots we first need to understand two most relevant energy scales in the dot, the charging energy and the confinement energy. The charging energy origins from the Coulomb interaction so that is related to the Coulomb energy. It is normally evaluated by considering the quantum dot as a capacitor with self-capacitance $C \propto 1/L$, where L is the dot diameter. If we assume N electrons in the dot already, the energy required to add the $N+1$th electron becomes [91]

$$\begin{aligned} \Delta E(N+1) &= E_{\text{Coulomb}}(N+1) - E_{\text{Coulomb}}(N) = \frac{e^2(N+1)^2}{2C} - \frac{e^2 N^2}{2C} \\ &= \frac{e^2}{C}(N + \frac{1}{2}). \end{aligned} \tag{2.8}$$

The charging energy is then defined as the difference between the energy required to add the Nth and the $N+1$th dot electrons

$$E_c = \Delta E(N+1) - \Delta E(N) = \frac{e^2}{C}, \tag{2.9}$$

which is a constant. The definition convention in Eq. (2.9) is related to the experimental tuning of the quantum dot, where the backgate voltage V_g changes the dot electron energies simultaneously. Alternatively, since the charging energy is constant in Eq. (2.9), experimentally the adding of another dot electron requires the tuning of backgate voltage by a constant value.

Another important energy scale is the confinement energy. A simple model is to treat the confined area as a confined 2DEG. In this case, the energy required to add N free electrons into a quantum dot with diameter L becomes

$$E_{\text{conf}} = \frac{\hbar^2}{2mL^2} N^2. \tag{2.10}$$

So that the energy difference between neighboring states is

$$\Delta = \frac{\hbar^2}{mL^2}, \tag{2.11}$$

which is also a constant. The comparison between Eqs. (2.9) and (2.11) shows that when L decreases, the charging energy diverges more slowly compared with the confinement energy. The different divergence pattern thus indicates a transition between the region where charging energy dominates to the region where confinement energy dominates. In this thesis, we always take the region where $E_c \gg \Delta$ so that we can compare our result with the experimental data [134; 135].

Based on the discussion above, a spinless quantum dot can be modeled with the Hamiltonian

$$H_{\text{dots}} = \sum_n \epsilon_n d_n^\dagger d_n + E_c(\hat{N} - N_0)^2, \tag{2.12}$$

where n labels the energy level of the dot electrons and E_c is the charging energy. $\hat{N} = \sum_n d_n^\dagger d_n$ is the number operator for the total number of electrons in the dot and $N_0 \propto V_g$ is the number of dot electrons that minimizes the charging energy.

Finally, we model the connection between the quantum dot and two leads with the tunneling Hamiltonian

$$H_{\mathrm{T}} = \sum_{n,k} [t_{n,S,k} c^{\dagger}_{S,k} d_n + t_{n,D,k} c^{\dagger}_{D,k} d_n + h.c.], \tag{2.13}$$

where $t_{n,\alpha,k}$ is the lead-dot tunneling strength that can be tuned by side gates. Normally, with small temperature $T \ll E_c$, only one dot level n_0 is relevant and we set $t_{n,\alpha,k} = 0$ if $n \neq n_0$. Meanwhile, the tunneling strength is normally assumed to be momentum independent $t_{n,\alpha,k} \to t_\alpha$ and only contains the lead labeling.

The conductance feature of the quantum dot system, known as the Coulomb diamond is shown in Fig. 2.3 as a function of the source drain applied bias V_{bias} and the backgate voltage V_g. The high conductance region is highlighted by the shaded area. Here we emphasize multiple features in Fig. 2.3 [91]. To begin with, with zero bias ($V_{\mathrm{bias}} = 0$) high conductance feature is observed at discrete points. Those points correspond to the V_g values where $\epsilon_N + E_c[N - N_0(V_g)]^2 = E_c[N - 1 - N_0(V_g)]^2$. These points are called the on-resonance points where the adding or removal of electrons at the Nth level costs zero energy. Between two high-conductance point we see the regime with weak conductance. In these regimes, the tunneling of one electron through the quantum dot leads to a temporary electric field that counters the tunneling of the next electron, thus leading to the weak-conductance phenomenon called the Coulomb blockade.

Now we look at the non-equilibrium regime where $V_{\mathrm{bias}} \neq 0$. There we see a strong conductance region between the lines $|\Delta V_g|\alpha_{bg} = |V_{\mathrm{bias}}|$, where α_{pg} is the lever arm of the backgate. A cartoon to illustrate the tunneling in this regime is given in Fig. 2.4, where the finite applied bias opens a window through which electrons are capable to tunnel between two leads.

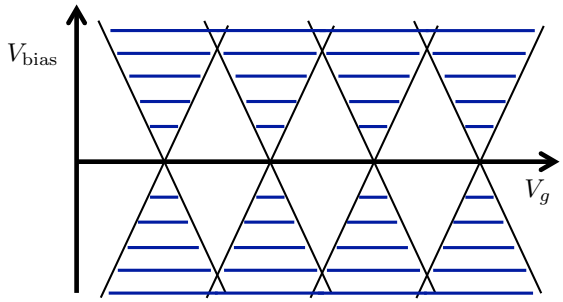

FIGURE 2.3: The conductance of a resonant level model as a function of the applied bias V_{bias} and the gate voltage V_g. The shaded area represents the high-conductance areas. These areas are bounded by the black lines where the dot level is aligned with one of the lead chemical potentials.

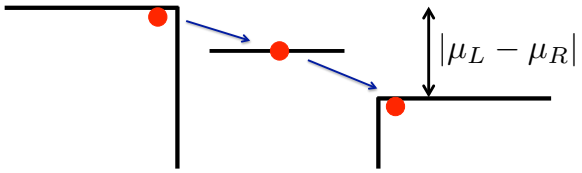

FIGURE 2.4: Non-equilibrium tunneling in a resonant level model that corresponds to the high conductance area in Fig. 2.3. The finite bias opens a window $|\mu_L - \mu_R|$ that enables tunneling through the detuned quantum dot.

2.2 Bosonization

In Section 2.1 I have briefly reviewed two non-interacting one-dimensional systems where the quasiparticles in the leads are free fermions. In this section I will briefly introduce a powerful technique for handing interactions in 1d systems.

In higher dimensional systems, interactions will not greatly modify the physics of the system: according to the Fermi liquid theory, interaction can be easily incorporated by replacing the electron mass with an effective one. The situation is, however, much more complicated in 1d systems. More specifically, due to the geometric restriction, electrons in one dimensional materials can not move across each other without pushing all other electrons. This formalism leads to the failure of the Fermi liquid theory (will be discussed in detail in Section 2.2.1) in interacting 1d

models.

To sufficiently describe the one-dimensional excitations, bosonization has thus been introduced. In contrast to the Fermi liquid theory where quasiparticles are approximately dressed free electrons, bosonization method models system excitations with bosonic modes that represent the collective motions of interacting electrons [71]. With bosonization formalism, an interacting 1d system has a similar Hamiltonian as that of a non-interacting one: the only difference is a dressed Fermi velocity and a Luttinger liquid interaction parameter.

2.2.1 Failure of Fermi Liquid Theory in One-dimensional Models

Most condensed matter systems contain quasiparticles with well defined energy and momentum. In non-interacting systems, those quasiparticles are exact electron states with infinitely long life time since they are eigenstates of the Hamiltonian. Near the Fermi surface, the dispersion relation of those electron states is approximately

$$E(k) = \mu + \frac{k_F}{m}(k - k_F). \tag{2.14}$$

At zero temperature, electrons will occupy lower energy states until the Fermi sea is filled, thus leading to a discontinuity at the Fermi level, where the occupation number abruptly drops from one to zero.

The non-interacting theory depicted above is normally considered as trivial since most realistic physical materials contain disorders or interactions. As a remarkable theory, Fermi liquid theory states that the adding of interaction in higher-dimensional systems will not greatly modify the quasiparticles [22]: they are still approximately considered as free fermions with different dispersion relation

$$E(k) = \mu + \frac{k_F}{m^*}(k - k_F), \tag{2.15}$$

where $m^* \neq m$ is the effective electron mass after the incorporation of interac-

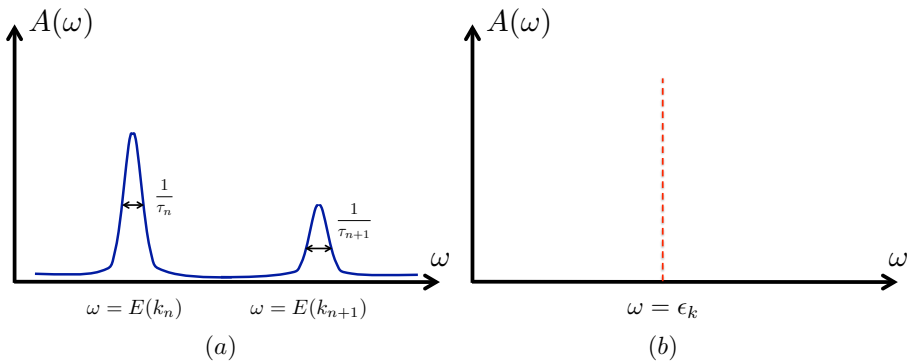

FIGURE 2.5: The spectral function of free electrons (b) and quasiparticles in Fermi liquid (a). In contrast to the delta spectral function of free electrons, Fermi liquid quasiparticles have Lorentzian spectral functions with finite half-width $1/\tau_n$. Here τ_n is the life time of the nth quasiparticle state.

tions. Meanwhile, the occupation discontinuity at the Fermi surface change from one to $Z < 1$ and the magnitude of Z represents the fraction of electrons in the quasiparicle states. Meanwhile, in contrast to eigenstates in free electron systems, quasiparticles in Fermi liquid theory have finite life time τ [22; 71]. This finite life time grants the peak of the spectral function a Lorentzian shape with half width τ, instead of the delta function in free systems. The comparison between the spectral function of free electrons and that of quasiparticles is provided in Fig. 2.5. Meanwhile, it has been proved that this half width diverges near the Fermi surface $\lim_{k\to k_F} |\tau(k)/[E(k) - E_F(k)]| \to \infty$ [71]. The divergence of half width guarantees that quasiparticles are well defined near the Fermi surface. One remarkable success of the Fermi liquid theory is that it avoids the necessity of perturbative expansions in treating interactions since those quasiparticles are extremely robust and even remain valid in systems with strong interactions.

Despite its great success in higher dimensional systems, Fermi liquid theory fails in the description of one dimensional interacting systems, or the Luttinger liquid systems [71]. The difficulty of Fermi liquid theory in Luttinger liquid can be seen by checking the susceptibility that describes the response of the density correlation

function to the applied potential

$$H_{\text{ext}} = \int d^d x V(x,t)\rho(x), \tag{2.16}$$

where d is the system dimension and $\rho(x)$ is the position dependent density. This susceptibility has been calculated [71]

$$\chi(q,\omega) = \frac{1}{\Omega}\sum_k \frac{f_F(\epsilon_k) - f_F(\epsilon_{k+q})}{\omega + \epsilon_k - \epsilon_{k+q} + i\delta}, \tag{2.17}$$

where $f_F(\epsilon)$ is the Fermi-Dirac distribution function, Ω is the system volume and $\delta \to 0^+$ is an infinitesimal positive number.

The susceptibility of Eq. (2.17) is known to diverge when the nesting property

$$\epsilon_{Q+k} = -\epsilon_k \tag{2.18}$$

is satisfied for a given Q and a range of momentum k. To better illustrate this point, we assume that in a wide range of k the nesting property Eq. (2.18) is satisfied with a certain Q. We thus substitute the nesting property into Eq. (2.17) and calculate the static susceptibility at $\omega = 0$

$$\begin{aligned} \text{Re}\chi(Q,\omega=0) &= -\frac{1}{\Omega}\sum_k \frac{\tanh(\beta\epsilon_k/2)}{2\epsilon_k} \\ &= -\int d\epsilon N(\epsilon)\frac{\tanh(\beta\epsilon/2)}{2\epsilon} \\ &\sim -N(0)\log(D/T), \end{aligned} \tag{2.19}$$

where the summation is over the momentum that satisfies the nesting property and $N(\epsilon)$ is the energy density of states per unit volume, T is the temperature and D is the high energy cutoff. It is also assumed that $N(\epsilon)$ is almost a constant in the energy regime with nesting property.

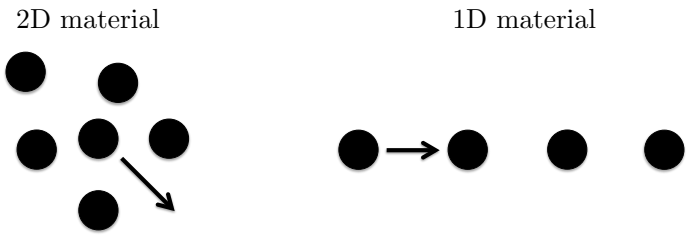

FIGURE 2.6: The illustration of the difference between higher dimensional materials (a) and one dimensional materials (b). In higher dimensional materials, particles can be considered as effectively free during the life time τ. However, electrons can not pass through each other in one dimensional models. System excitations are thus bosonic modes instead.

Eq. (2.19) shows a diverging susceptibility at zero temperature. Physically, the singularity in Eq. (2.19) indicates that the adding of any interaction of Eq. (2.16) greatly modifies the system ground state.

In higher dimensional systems, the nesting property only happens at several points so that the singularity can be smoothed by the average in momentum space. This is why in Fermi liquid theory the interacting electrons are effectively the same as free ones. However, in one dimensional systems, if we consider the linearised dispersion near the Fermi surface, the nesting property is satisfied at $Q = 2k_F$ for a wide range of k. Consequently, in one dimensional materials, the systems always have a strong response to any interaction, which indicates a distinct ground state from the Fermi liquid theory.

The difference between Fermi liquid and Luttinger liquid can also be more intuitively understood from Fig. 2.6. In higher dimensional systems, an electron detours when encountering other electrons. Consequently, during two collision events, interacting electrons can be considered as effectively free particles with life time τ. However, electrons encountered in one-dimensional materials always got backscattered or forwardscattered. Consequently, no free electron quasiparicle exists in Luttinger liquid: it only allows collective motion of bosonic quasiparticles excitations.

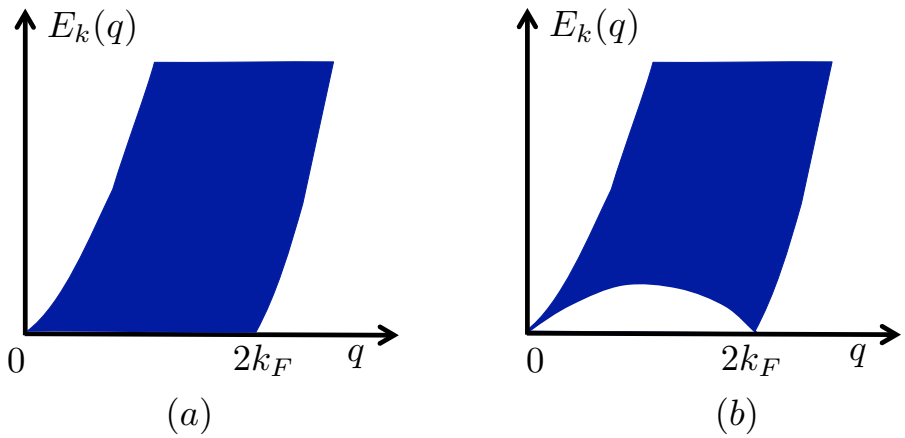

FIGURE 2.7: The spectrum of particle-hole excitations in higher dimensional materials (a) and one dimensional materials (b). In one dimensional materials, the low-energy excitation is gapped at zero energy except at $k = 0$ and $k = 2k_F$. This gap leads to well defined particle-hole quasiparticle states that can be effectively described by bosonization.

Before the end of this section, we further illustrate why the bosonic modes can efficiently model the Luttinger liquid excitations by checking a particle-hole excitation operator $c^\dagger_{k+q}c_k$ where $|k+q| > k_F > k$. This operator promotes an electron below the Fermi surface to a state above it, with energy cost $E_k(q) \equiv \epsilon_{k+q} - \epsilon_k > 0$. In higher-dimensional systems, the particle-hole excitation energy has no low energy gap, as shown in Fig. 2.7(a). As a contrary, Fig. 2.7(b) shows a low energy dome in Luttinger liquid – only when $q = 0$ or $2k_F$ the particle-hole excitation energy can vanish. This dome structure grants the bosonic excitation modes in Luttinger liquid the feature of quasiparticles. More specifically, considering the momentum $k \in C = [k_F - q, k_F]$ so that $c^\dagger_{k+q}c_k$ corresponds to a particle-hole excitation. We define $E(q)$ as the average energy of $k \in C$ and $\delta E(q)$ as the energy difference between the highest and the lowest energy excitations. It is straightforward to get that

$$E(q) = v_F q, \qquad \delta E(q) = \frac{E(q)^2}{m v_F^2}. \tag{2.20}$$

Two major features can be seen from Eq. (2.20). To begin with, if we define the

excitations with momentum shift q in a Luttinger liquid, it corresponds to a realistic particle with energy $v_F q$ —- the particle-hole excitation thus behaves as a relativistic particle. Meanwhile, since $\delta E(q)$ vanishes as $E(q)^2$, the fluctuation of this quasiparticle near the Fermi level vanishes. The vanishing of energy fluctuation, which also happens in higher-dimensional Fermi liquid theory, guarantees that the electron-hole excitation modes are well defined near the Fermi surface.

2.2.2 Bosonization Method

As explained in previous section, in Luttinger liquid systems excitations are bosonic collective modes. Bosonization, which transforms fermionic operators into bosonic ones, thus becomes efficient in the description of Luttinger liquid systems. In this subsection I will briefly introduce the technique of bosonization.

We start with a one dimensional Hamiltonian

$$H = -t \sum_i c_i^\dagger c_{i+1} + h.c. + \frac{V}{2} \sum_i c_i^\dagger c_i c_{i+1}^\dagger c_{i+1}, \tag{2.21}$$

where t is the hopping strength and V is the interaction. If $V = 0$, system can be exactly solved where the eigenstates correspond to freely traveling fermions in the momentum space with energy $-t\cos(k)$. When $V \neq 0$, as introduced above, free fermion picture breaks and we need to consider bosonic modes instead. Bosonization can be introduced in multiple ways [58; 178; 71]. Here I follow the review paper by M. A. Fisher and L. Glazman [58]. The first step is to transform fermion operators into bosonic ones through Jordan-Wigner transformation

$$b_j = e^{-i\pi \sum_{j<i} n_i} c_j, \tag{2.22}$$

where $n_i = c_j^\dagger c_j$ is the occupation number operator at site j. After this transformation, it is straightforward to check that b_j operators now have the bosonic commutation relation, where the change of the commutation relation originates from the

Jordan-Wigner string.

Next step is to define bosonic field

$$b_j = \sqrt{n_j} e^{i\phi_j}, \tag{2.23}$$

where ϕ_j is the bosonic phase at site j. Notice that both $\exp\left(-i\pi \sum_{j<i} n_i\right)$ and $\sqrt{n_j}$ commute with n_j. The task to change the occupation number n_j (by c_j) must be accomplished by the bosonic field $\exp(i\phi_j)$. Consequently, the occupation number operator n_j and the bosinc field ϕ_j must be canonical conjugate operators. Following this, if we extend both operators to be continuous $\phi_j \to \phi(x)$ and $n_j \to \rho(x)$, they have the commutation relation

$$[\phi(x), \rho(x')] = i\delta(x - x'). \tag{2.24}$$

For later convenience, we decompose density into two parts $\rho(x) = \rho_0 + \tilde{\rho}(x)$, where $\rho_0 = k_F/\pi$ is the mean value of the density. We further define another phonon-like operator $\theta(x)$

$$\partial_x \theta(x) = \pi \tilde{\rho}(x). \tag{2.25}$$

Together with Eq. (2.24), we have the commutation relation between those two bosonic fields

$$[\phi(x), \theta(x')] = \frac{i\pi}{2} \mathrm{sgn}(x - x'), \tag{2.26}$$

where $\mathrm{sgn}(x - x')$ is the sign function. At this moment, we are ready to write the bosonization equation for a fermionic operator. To distinguish it from the discrete form c_j, we write the continuous fermionic operator as $\psi(x)$, with the bosonization equation [58]

$$\psi(x) = e^{\pm i[k_F x + \theta(x)]} e^{i\phi(x)}, \tag{2.27}$$

where $\pm$ indicates the propagating direction of electrons. More generally, the bosoniza-

tion can be written as [1]

$$\psi(x) = \sum_{m_{\text{odd}}} e^{im[k_F x + \theta(x)]} e^{i\phi(x)}, \tag{2.28}$$

where m takes odd values to satisfy the anti-commutators between fermions. Normally, we take $m = \pm 1$ only since other options normally correspond to less relevant processes. Eqs. (2.27) and (2.28) are called the canonical form of bosonization since they contain a pair of canonically conjugate fields $\phi(x)$ and $\theta(x)$. Finally, since $\partial_x \theta$ is proportional to the density as defined in Eq. (2.25), it is easy to check that the other field $\partial_x \phi$ is proportional to the current density such that

$$\begin{aligned} \partial_x \theta(x) &= \pi \tilde{\rho}(x) = \pi[\rho_L(x) + \rho_R(x)] \\ \partial_x \phi(x) &= \pi j(x) = \pi[-\rho_L(x) + \rho_R(x)], \end{aligned} \tag{2.29}$$

where $j(x)$ is the current density, while ρ_L and ρ_R represent the density of electrons that propagate leftward and rightward, respectively.

With the conical fields, a non-interacting one-dimensional Hamiltonian becomes

$$H = \frac{v}{2\pi}[(\partial_x \phi)^2 + (\partial_x \theta)^2], \tag{2.30}$$

where v is the Fermi velocity. Now we are ready to consider the density-density interaction in Eq. (2.21). Intuitively, since fermionic density can be rewritten as the derivative of bosonic fields, the finally Hamiltonian should still be quadratic. The detailed derivation is also straightforward. For simplicity, here I only address the final result for the Hamiltonian of the Luttinger liquid

$$H = \frac{v}{2\pi}[g(\partial_x \phi)^2 + \frac{1}{g}(\partial_x \theta)^2], \tag{2.31}$$

[1] Notice that here we do not have the Klein factor used in Chapter 6. In that chapter the Klein factor is used to create the correct anticommutation relation between fermions. Here the anticommutation relation $\{\psi^\dagger(x), \psi(x')\} = \delta(x - x')$ is guaranteed by the commutator between two fields $\theta(x)$ and $\phi(x)$.

where g is the Luttinger liquid interaction parameter

$$g = (\frac{1 + V_1/2\pi v_F - V_2/2\pi v_F}{1 + V_1/2\pi v_F + V_2/2\pi v_F})^{1/2}, \tag{2.32}$$

and V_1 and V_2 correspond to the density-density interaction between electrons with the same and different propagating directions, respectively. The comparison between Eqs. (2.30) and (2.31) presents the strong power of bosonization in treating Luttinger liquid problems —- electron interactions can be naturally absorbed into the interaction parameter g, while keeping the general form unchanged. In this sense, lots of Luttinger liquid problems can be dealt with by resorting to techniques developed in non-interacting models.

Before the end of this section, I introduce another bosonization form and the effective electron fractionalization in Luttinger liquid. In Eq. (2.27), fermions in the Luttinger liquid are divided into two counter-propagating channels with propagating direction labeled by the sign in front of the θ field. Another way is to consider the left and right propagating modes as two chiral channels. The chiral bosonic operators are defined through the rotation [58]

$$\phi_R = g\phi + \theta, \quad \text{and} \quad \phi_L = g\phi - \theta, \tag{2.33}$$

with the commutators $[\phi_\alpha(x), \phi_{\alpha'}(x')] = i\pi g \delta_{\alpha\alpha'} \text{sgn}(x - x')$. Compared with the canonical fields, chiral fields are two independent fields that are self conjugate to themselves. With the chiral fields defined in Eq. (2.33), we can define the effective density operators [2]

$$n_R = \frac{1}{2\pi}\partial_x \phi_R, \quad \text{and} \quad n_L = -\frac{1}{2\pi}\partial_x \phi_L, \tag{2.34}$$

[2] In the canonical bosonization Eq. (2.27), fermionic anticommutators are guaranteed by the commutators between canonical fields θ and ϕ. In the chiral bosonization, since $[\phi_L(x), \phi_R(x')] = 0$, it is conventional to add a Klein factor $F_{L,R}$ to the bosonization formula.

with the commutation relation

$$[\phi_\alpha(x), n_{\alpha'}(x')] = ig\delta_{\alpha\alpha'}\delta(x-x'). \tag{2.35}$$

With those effective number operators defined above, Luttinger liquid Hamiltonian now becomes

$$H = \frac{v}{4\pi g}[(\partial_x\phi_R)^2 + (\partial_x\phi_L)^2]. \tag{2.36}$$

Now consider an infinite Luttinger liquid wire that is uniform everywhere except at $x = 0$, where an impurity triggers the backscattering between two chiral modes

$$H_{\text{imp}} = u\psi_R^\dagger(0)\psi_L(0) + h.c.. \tag{2.37}$$

We further assume that the effect of this impurity is weak such that the backscattering u is infinitesimal. In this case, we can take the bosonization as Eq. (2.27) such that the backscattering becomes

$$H_{\text{imp}} \propto 2\cos[2\theta(0)] = e^{i\phi_R(0)}e^{-i\phi_L(0)} + h.c.. \tag{2.38}$$

Based on the commutator Eq. (2.35) between the chiral fields and the density, we know that the exponential factor in Eq. (2.38) transfers an fractionalized effective charge ge between two effectively independent channels. This is to some extend similar to the quasiparticles in fractional quantum Hall effect.

2.3 Dissipative EM Quantum Noise in One Dimensional Systems

As introduced in Chapter 1, this thesis mainly focuses on the effect of dissipation, or quantum noise in mesoscopic systems. For later convenience, here we thus briefly review the method to model dissipative modes in 1d systems.

2.3.1 Dissipation in a One Dimensional Single Barrier Model

We begin with the simplest dissipation relevant mesoscopic system as shown in Fig. 2.8 (dissipative single barrier 1d wire model). The system consists of two leads

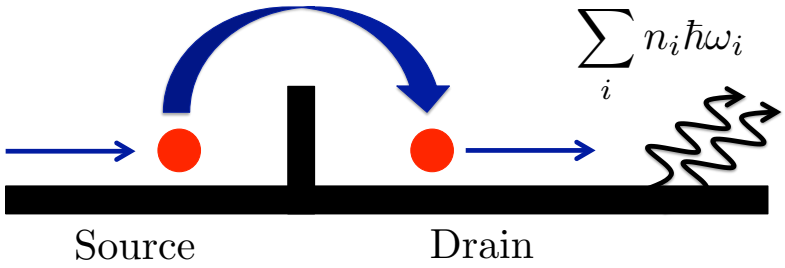

FIGURE 2.8: The dissipative single barrier problem. Relaxation of tunneling electron excites bosonic modes in the leads, leading to the dynamical Coulomb blockade effect.

(source and drain) and the inter-lead tunnelings. Dissipation is labeled by the curling arrows in Fig. 2.8. Effectively, the structure in Fig. 2.8 can be considered as a perfect nanowire with a capacitor C at the junction that is followed by an impedance $Z(\omega)$ [92]. If the environment is Ohmic, then $Z = R$ with R the resistance in the leads. Experimentally, Ohmic dissipation has been realized through a disordered metallic lead [134; 135], a thin chromium wire and an extra quantum point contact [98].

Physically, dissipation influences the tunneling events by coupling to the fluctuation in the system induced by the shot noise [122]. To better illustrate this, consider an event where an electron tunnels from the source to the drain. Since the tunneling junction can be physically viewed as a capacitor, the tunneled electron will produce a counter-propagating barrier that prevents the next tunneling event. Consequently, before the second tunneling event, the first electron must relax through the entire circuit. This relaxation process encounters inelastic backscattering events and dissipates energy. At low temperature and low bias, the system lacks the source to pay this energy, thus leading to a weak conductance, similar as the weak tunneling Coulomb blockade regime in Fig. 2.3. However, unlike the Coulomb blockade effect, tunneling events are now prevented by the dynamical bosonic modes so that the dissipation induced weak conductance phenomenon is also called the dynamical Coulomb blockade effect.

2.3.2 Mathematically Model the Dissipation

In this section I review the way to mathematically model dissipation in a one dimensional single barrier model. Without loss of generality, this method also applies to other one dimensional models including the Anderson and Kondo models where inter-lead electron tunneling happens.

To begin with, we introduce the phase related to the bias across the junction

$$\varphi(t) = \frac{e}{\hbar}\int_{-\infty}^{t} dt' U(t'), \tag{2.39}$$

where $U(t) = Q(t)/C$ is the dynamical voltage across the junction, as a function of the charge $Q(t)$ on the capacitor. Notice that the voltage bias $U(t)$ contains two parts $U(t) = V(t) + \delta V(t)$, where $V(t)$ is the externally applied voltage and $\delta V(t)$ is the voltage fluctuation induced by the quantized electrons tunnelings. Meanwhile, $\delta V(t)$ is also the part that couples to the dissipation. To focus on the discussion of the effect of the dissipative modes, it is thus convenient to define the fluctuation-related phase [92]

$$\tilde{\varphi}(t) = \varphi(t) - \frac{e}{\hbar}Vt. \tag{2.40}$$

and the fluctuation-related charge

$$\tilde{Q}(t) = Q(t) - CV. \tag{2.41}$$

With those two operators defined, if the system is free from dissipation, the single barrier can be viewed as an $LC-$circuit with the Hamiltonian

$$H = \frac{\tilde{Q}^2}{2C} + \frac{1}{2L}(\frac{\hbar}{e}\tilde{\varphi})^2. \tag{2.42}$$

From Heisenberg equation, it is easy to check that two operators $\tilde{Q}$ and $\tilde{\varphi}$ in Eq, (2.42) are canonical operators with the commutator

$$[\tilde{\varphi}, \tilde{Q}] = ie. \tag{2.43}$$

As illustrated in the previous section, tunneling process couples to dissipation by exciting dissipative modes in the leads. Those dissipative modes are normally considered as the modes of simple harmonic oscillators [26; 92]. The coupling between the phase φ_n of those bosonic modes and $\tilde{\varphi}$ of the barrier voltage fluctuation thus enables the description of the tunneling-dissipation interactions. More specifically, this interaction can be modelled by the Hamiltonian [92]

$$H_{\rm env} = \frac{\tilde{Q}^2}{2C} + \sum_n [\frac{q_n^2}{2C_n} + (\frac{\hbar}{e})^2 \frac{1}{2L_n}(\tilde{\varphi} - \varphi_n)^2], \tag{2.44}$$

where L_n and C_n are the "inductance" and "capacitance" of the nth bosonic mode with frequency $\omega_n = 1/\sqrt{L_n C_n}$. The summation over n in Eq. (2.44) is limited by the upper bound with the energy cutoff ω_R. We understand Eq. (2.44) by checking its effect after one tunneling process. Before the tunneling process, we assume that the system is at the ground state such that the wave function of each bosonic modes is $\Psi_0(\varphi_n - \tilde{\varphi})$, which is the ground state of a harmonic oscillator centered at the "position" $\tilde{\varphi}$. When tunneling happens, $\tilde{\varphi}$ fluctuates so that $\Psi_0(\varphi_n - \tilde{\varphi})$ is no longer the ground state of the nth oscillator, but a linear combination of all excitation states. Consequently, through the junction-environment coupling in Eq. (2.44), electron tunneling processes excite bosonic modes of the environment and dissipate system energy. This is how dissipation works.

2.3.3 Dissipation and the Tunneling Amplitude

In Section 2.3.2 we have introduce the way to model dissipation in mesoscopic systems by coupling the dissipative phases φ_n to the junction voltage fluctuation phase $\tilde{\varphi}$. However, in real calculations, it will be too complicated to work with an infinite number of bosonic modes. In this section, we thus further simplify the Hamiltonian by studying the dynamics of the field $\tilde{\varphi}$ after incorporating the effect of these dissipative modes.

Without loss of generality, in this section we continue to use the single barrier model as an example. We further take the strongly spin-polarized limit such that the system is effectively spinless. Without the presence of dissipation, the tunneling Hamiltonian can be writtern as

$$H_{\mathrm{T}} = \sum_{k,q} t_{k,q} c^{\dagger}_{k,S} c_{q,D} + h.c., \tag{2.45}$$

where S and D refer to the source and drain, respectively. When the leads are dissipative, as illustrated in the previous section, tunneling process couples to dissipation by exciting bosonic modes through the relaxation of a tunneling electron. This process can be modeled by adding a dynamical phase operator $\exp(-i\varphi)$ [3] to the tunneling Hamiltonian

$$H_{\mathrm{T}} = t_{k,q} \sum_{k,q} c^{\dagger}_{k,S} c_{q,D} e^{-i\varphi} + h.c., \tag{2.46}$$

In Eq. (2.46), φ is the canonical phase introduced in Section 2.3.2 [4]. Since φ and Q are canonical variables, physically $\exp(i\varphi)$ refers to the a single charge tunneling between the source and drain.

Here we use the fluctuation-dissipation theorem to derive the dynamics of the phase φ. To begin with, electron tunneling produces a current pulse through the junction. The phase φ responds to the current as

$$\varphi(\omega) = \chi(\omega) I(\omega), \tag{2.47}$$

where $I(\omega)$ is the quantum current fluctuation and $\chi(\omega)$ is the susceptibility. The fluctuation-dissipation theorem states that in such a system, the expectation value

[3] The physical significance of this factor can be understood once we notice that φ is canonical to the lead charge operator.

[4] In Eq. (2.46), the effect of dissipation has been incorporated into the dynamics of phase φ, represented by the correlator $\langle \varphi(t)\varphi(0) \rangle$. Details will be discussed later.

of φ satisfies the expression [180]

$$\int_{-\infty}^{\infty} dt e^{i\omega t}[\langle\varphi(t)\varphi(0)\rangle - \langle\varphi(0)^2\rangle] = \frac{2\hbar}{e^{-\beta\hbar\omega}-1}\mathrm{Im}[\chi(\omega)], \tag{2.48}$$

where $\beta = 1/k_B T$ is the temperature inverse.

The susceptibility can be calculated by considering the barrier as a capacitor C, with the result

$$\chi(\omega) = (\frac{e}{\hbar})^2 \frac{Z_t(\omega)}{i\omega}, \tag{2.49}$$

where

$$Z_t(\omega) = \frac{1}{i\omega C + 1/Z(\omega)} \tag{2.50}$$

is the effective impedance of the circuit. Combining Eqs. (2.47) and (2.48), the dynamics of the phase φ becomes [92]

$$\langle\varphi(t)\varphi(0)\rangle - \langle\varphi(0)^2\rangle = 2\int_{-\infty}^{\infty} \frac{d\omega}{\omega} \frac{\mathrm{Re}Z_t(\omega)}{R_Q} \frac{e^{-i\omega t}}{1-e^{\beta\hbar\omega}}, \tag{2.51}$$

where $R_Q = h/e^2$ is the dissipation quanta. Eq. (2.51) shows that the correlation function of the dissipative phase relies on the details of the dissipation. As a simple example, when the dissipation is Ohmic, $Z(\omega) = R$ is frequency independent. In this case, the long-time phase-phase correlation function becomes

$$\langle\varphi(t)\varphi(0)\rangle - \langle\varphi(0)^2\rangle \sim -2r\ln(\omega_R t), \tag{2.52}$$

where ω_R is the energy cutoff of the bosonic modes and $r = R/R_Q$ is the dimensionless dissipation strength. Eq. (2.52) shows that $\exp(i\varphi)$ has the correlator of a primary field in the conformal field theory. Consequently, as will be discussed later (Section 3.2), it is easy to incorporate the effect of an Ohmic dissipation into the RG equations.

2.3.4 Dynamical Coulomb Blockade Method

With the knowledge of the dynamics of the dissipation, the conductance through the dissipative single barrier model can be effectively calculated through the dynamical Coulomb blockade method. The essence of this method is the Fermi's golden rule so that it is a second order perturbation theory with respect to the tunneling strength $t_{k,q}$. Consequently, it produces reasonable results only when the tunneling strength is weak enough. Meanwhile, although seems generalizable to other perturbative systems, dynamical Coulomb blockade method is only valid when the operator with small coefficient is RG irrelevant (to be specified in Section 3.2).

The Fermi's golden rule states that the transmission rate between the initial state $|i\rangle$ and final state $|f\rangle$ can be approximately calculated as

$$\Gamma_{i\to f} = \frac{2\pi}{\hbar}|\langle f|H_T|\rangle|^2\delta(E_i - E_f), \tag{2.53}$$

where the delta function in Eq. (2.53) guarantees the conservation of energy, while E_i and E_f are the energies of the initial and final states, respectively. Experimentally, the observed tunneling rate involves all possible initial and final states

$$\Gamma = \sum_{i,f}\frac{2\pi}{\hbar}|\langle f|H_T|i\rangle|^2 p(E_i)[1-p(E_f)]\delta(E_i - E_f), \tag{2.54}$$

where $p(E)$ is the possibility that the state with energy E is filled.

In contrast to the dissipation free situation where the initial and final states are purely fermionic states, dissipative systems contain an extra bosonic part with respect to the dissipative modes. The dissipative modes are independent from the fermionic reservoir and are thus simply added to fermionic tunneling processes. Consequently, the initial and final states can be described as direct products of two components $|i\rangle = |E_i\rangle|R_i\rangle$ and $|f\rangle = |E_f\rangle|R_f\rangle$, where $|E\rangle$ and $|R\rangle$ represent the fermionic and bosonic reservoirs, respectively. With both parts taken into consideration, the

energy conservation requirement now becomes $E_i^e + E_i^r + eV_{\rm bias} = E_f^e + E_f^r$, with E^e and E^r representing the energy of fermionic and bosonic states, respectively. Here $V_{\rm bias}$ is the applied source-drain bias. With those ingredients, the total source-drain tunneling rate becomes

$$\Gamma^{S\to D}(V) = \frac{2\pi|V_T|^2}{\hbar}\int_{-\infty}^{\infty} dEdE' f(E)[1-f(E'+eV_{\rm bias})]P(E-E') \tag{2.55}$$

where we have assumed that $V_T = t_{kq}$ as a constant tunneling strength in the tunneling Hamiltonian. In Eq. (2.55) the occupation of fermionic states is described by the Fermi-Dirac distribution $f(E)$ and the bosonic distribution has been represented by the function $P(E)$

$$P(E) = \frac{1}{2\pi\hbar}\int_{-\infty}^{\infty} dt \exp(\frac{i}{\hbar}Et)[\langle\varphi(t)\varphi(0)\rangle - \langle\varphi(0)^2\rangle], \tag{2.56}$$

where the conservation of energy has already be included. From Eq. (2.54) the current through the weak single tunneling junction can thus be calculated as

$$I = e[\Gamma^{S\to D}(V_{\rm bias}/2) - \Gamma^{D\to S}(-V_{\rm bias}/2)]. \tag{2.57}$$

With an Ohmic dissipation, we can then combine the correlator Eq. (2.50) and Eqs. (2.55), (2.56) and (2.57) to calculate the observed current.

One thing to emphasize is that the bias $V_{\rm bias}$ in Eq. (2.57) does not need to be small: in general, the dynamical Coulomb blockade method also applies to non-equilibrium conditions. One natural question to ask is the connection between dynamical Coulomb blockade and the famous Keldysh formalism. Physically, Coulomb blockade method origins from the time-dependent perturbation theory to the second order of the weak tunneling strength. Keldysh formalism, on the other hand, involves all possible diagrams and is thus strictly correct. A practical way to apply the Keldysh formalism to the single barrier junction model is through the full counting

statistics method [121; 73]. This method calculates the generating function

$$\chi(\lambda) = \sum_q e^{iq\lambda} P_q, \tag{2.58}$$

where P_q is the possibility that charge q transfers through the junction during the measuring time τ and λ is the measuring field. Since current is defined as the charge transferred per unit time, it can be easily calculated once we know the expression of the generating function

$$I = \frac{e\langle q\rangle}{\tau} = -i\frac{e}{\tau}\frac{\partial}{\partial_\lambda}\ln\chi(\lambda)\Big|_{\lambda=0}. \tag{2.59}$$

In a single barrier model, the generating function has the general form following the Levitov-Lesovik formula [121; 73]

$$\ln\chi_0(\lambda; V; \{T(\omega)\}) = \tau\int\frac{d\omega}{2\pi}\ln\left\{1 + T(\omega)[n_S(1-n_D)(e^{i\lambda}-1) + n_D(1-n_S)(e^{-i\lambda}-1)]\right\}, \tag{2.60}$$

where $T(\omega)$ is the dressed tunneling amplitude that has included all possible interactions. For the non-interacting and dissipation free case, the tunneling amplitude can be easily calculated as

$$T(\omega) = \frac{4\Gamma}{(1+\Gamma)^2}, \tag{2.61}$$

where $\Gamma = (\pi\rho_0 t)^2$ is the level broadening and ρ_0 is the constant density of states near the Fermi surface. From Eqs. (2.59) and (2.60) we get the general expression of the current

$$I = e\int\frac{d\omega}{2\pi}T(\omega)\left\{n_S(\omega, V/2)[1-n_D(\omega,-V/2)] - n_D(\omega,-V/2)[1-n_S(\omega,V/2)]\right\}. \tag{2.62}$$

In general $T(\omega)$ is frequency dependent and has no analytical solution. However, if the tunneling strength is weak, we can approximate $T(\omega)$ to the second order of the

tunneling strength, which becomes proportional to the expression $P(\omega)$ in Eq. (2.56). In this sense, the result of the dynamical Coulomb blockade method Eqs. (2.55) and (2.57) is equivalent to the Keldysh formalism result Eq. (2.62) to the second order of the tunneling strength. Meanwhile, while approximately treating tunneling strength to the second order, the dynamical Coulomb blockade method strictly incorporates the applied bias and dissipation. Consequently, dynamical Coulomb blockade is highly efficient (and much easier compared with the Keldysh formalism) in dealing with non-equilibirum and dissipative tunneling problems once the tunneling strength is weak and RG irrelevant (to be specified later).

3

Background: Quantum Phase Transitions and Renormalization Group method

This chapter provides an overview of quantum phase transitions and the renormalization group (RG) method. This chapter only contains review material and not my original work.

I begin with the introduction of quantum phase transitions, including the definition, physical significance as well as their scaling features. After that, I introduce the general steps and physical significance of the RG method. Finally, I take the single barrier Luttinger liquid model as an example to illustrate the application of the RG method into the study of QPTs. I also provide an alternative understanding of dissipation with the RG method.

3.1 Quantum Phase Transitions

Phase transition is defined as the phenomenon where the state of the system abruptly changes between two ground states. To distinguish between different phases, order parameters are introduced: order parameters are distinct on two sides of the transition point, indicating the change of system's ground state.

To better study their physical significance, phase transitions are categorized into two classes – thermal phase transitions and quantum phase transitions (QPT) [161; 176]. Those transitions are categorized based on the source of fluctuation that triggers the transition. Been discovered before the establishment of quantum mechanics, thermal phase transitions are transitions that are triggered by thermal fluctuations such as the transition between vapor and liquid. In contrast to thermal phase transitions, QPTs are triggered by the quantum fluctuation. In quantum mechanical systems, this quantum fluctuation Δ is the typical energy scale of long-range order parameter fluctuations at zero temperature [161; 176]. When both thermal and quantum fluctuations exist, a phase transition is categorized based on the leading source of fluctuations. More specifically, to realize quantum phase transition, quantum fluctuation must dominate against the thermal fluctuation such that $\Delta \gg T$. However, in quantum mechanical systems, since typically $\Delta = 0$ at the transition point, strictly QPT only occurs at zero temperature.

Theoretically, QPT can be understood from the change of system spectrum [161]. As a simple example we consider an infinite system with Hamiltonian $H = H_0 + gH_1$, where $[H_0, H_1] = 0$ so that they (H_0 and H_1) share the same group of eigenstates. The energy of those eigenstates thus changes as a function of the parameter g. By tuning g, we may be able to find a point $g = g_c$ where the system ground state has a level crossing or an avoided level crossing. If it is the case, the ground state singularity at this point then indicates a QPT between the state with $g > g_c$ to the

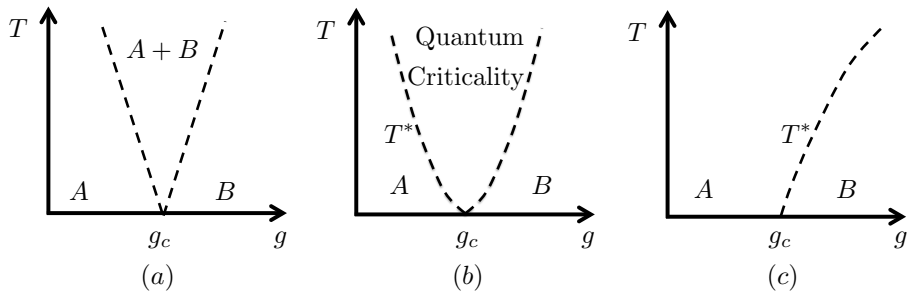

FIGURE 3.1: Finite temperature phase diagrams of three different QPTs with the critical points at $g = g_c$. First order QPT (a) consists of an area where different ground states A and B coexist. The coexistence is guaranteed by the first-order derivative discontinuity of the free energy. On the contrary, second order QPT (b) has an unstable fixed point that is physically different from both A and B. Meanwhile, it has a quantum critical regime bounded by the critical temperature $T^* \propto |g - g_c|^{\nu z}$, where ν is the correlation length critical exponent and z is the dynamical critical exponent. KT transition (c), on the other hand, does not host an unstable fixed point. Instead, the system state transforms from A to B below the critical temperature T^*.

state with $g < g_c$. QPT can thus be defined as the phenomenon where the ground state non-analyticity happens at the transition point $g = g_c$.

In condensed matter physics, QPTs are of fundamental importance in a wide variety of condensed matter many-body systems ranging from quantum materials to quantum magnets and nanostructures. To better study QPTs, they are divided into three main categories: first order, second order and KT transitions. These QPTs are differently categorized based on the continuity feature of their free energies at the transition point, similar like that of thermal phase transitions. Meanwhile, they can also be distinguished based on the finite temperature behavior near the transition point as shown in Fig. 3.1.

A first order QPT is defined as the transition where the first derivative of its free energy is discontinuous. Alternatively, this kind of QPT is characterized by a level crossing at the transition point. Similar like that of a thermal first order transition, the free energy of a first order QPT has two local minimums at its transition point. The phase diagram of the first order QPTs is shown in Fig. 3.1(a), where two ground

states coexist over a wide range in the parameter space at finite temperatures.

In contrast to that of the first order QPT, the first-order derivative of the free energy of a second order QPT is continuous and this transition is thus also called a continuous QPT. Another important feature of a second order QPT is the existence of a quantum critical regime. As shown in Fig. 3.1(b), two competing ground states can not coexist at finite temperatures. Instead, a quantum critical regime forms where the system's ground state is different from both competing phases. This quantum critical regime is bounded by the critical temperature $T^* \propto |g - g_c|^{\nu z}$, where $g = g_c$ determines the transition point, ν is the correlation length critical exponent and z is the dynamical critical exponent. Due to the existence of the finite temperature critical regime, the transition point of a second order QPT is also called a quantum critical point. I will explain the second order QPT later in better detail in Section 3.1.1.

The last class of quantum phase transitions is the KT transition. The KT transition is known after the name Kosterlitz and Thouless and is first realized in a classical two-dimensional XY model. In this model, a thermal KT transition occurs between the state with free vortices and that with only vortex-antivortex bound [1]. It is later realized that the KT transition also describes the QPT between the ferromagnetic and anti-ferromagnetic Kondo models as well as that of the spin boson model. The connection between the classical two dimensional XY model and those two one-dimensional quantum models can be understood through the quantum-classical mapping [176]. The phase diagram of a KT transition is present in Fig. 3.1(c). Different from that of a second order QPT, RG equations (will be introduced in Section 3.2) of a KT transition indicate the missing of an unstable intermediate fixed point: for instance, in the Kondo model, the magnetic impurity becomes either ferromagnetic

[1] The introduction of vortex topology also leads to the foundation of topological materials in condensed matter physics. This is, however, irrelevant to the topic of this thesis.

or anti-ferromagnetic. The missing of the quantum critical regime also leads to the missing of the scaling invariance of systems around the critical point. Instead, in KT transitions, quantum fluctuation drops exponentially $\Delta \sim \exp(-\alpha/|g - g_c|)$. Due to this feature, the free energy of a KT transition does not possess singularity under any order of differentiation and KT transitions are thus called infinite order transitions. As a further illustration, an RG study of the KT-transition-hosted Kondo model will be provided in Section 4.3.1.

3.1.1 Continuous Quantum Phase Transition and Scaling Behaviors

As introduced above, a continuous QPT has a quantum critical regime that is different from either competing ground states. When approaching zero temperature, this quantum critical regime shrinks to the transition point so that the transition point of a continuous QPT is also called the quantum critical point (QCP). One of the features of the QCP is the scaling invariance that leads to the divergence of multiple quantities. For instance, the correlation length diverges in the way

$$\xi \sim |t|^{-\nu}, \tag{3.1}$$

where $|t| = |g - g_c|$ is the distance to the critical point and $\nu > 0$ is the correlation length critical exponent. Equivalently, the scaling invariance can be understood by the divergence of the correlation time

$$\tau_c \sim \xi^z \sim |t|^{-\nu z}, \tag{3.2}$$

where z is the dynamic critical exponent. With a finite temperature T, the quantum criticality extends from just the critical point to a range $|\Delta| \sim 1/\tau_c \sim T$, such that the critical temperature becomes

$$T^* \sim |t|^{\nu z}. \tag{3.3}$$

Due to the divergences of both the correlation length and the correlation time, near the critical point, only the correlation length ξ and the correlation time τ_c are relevant spatial and time scales. Alternatively, the divergence of those quantities indicates the system scaling invariance right at the critical point.

Another interesting feature of the continuous phase transition is the universality class. Universality guarantees that most of the local features of the system Hamiltonian is unimportant in getting the critical exponents in Eqs. (3.1) and (3.2). The universality class is also beneficial in the study of different systems that share the same set of dynamical exponents.

3.2 The Renormalization Group Method

In theoretical physics, interaction plays two contradictory roles. On one hand, the presence of interaction leads to a huge amount of interesting physical phenomena. Superconductivity is among the most known examples. In a superconductor, the pair interaction couples electrons into Cooper pairs, opening a superconducting gap, and thus leading to the exotic low temperature ground state where backscattering are prevented by the lack of free quasiparticle excitations [174]. Another famous example is the Mott insulator, where interaction leads to a second order quantum phase transition [141].

However, interaction may also greatly increase the difficulty in solving those problems. For instance, in quantum field theories, a non-interacting system with only linear or quadratic terms in the Lagrangian density can be easily solved. The problem becomes greatly more complicated with an extra ϕ^4 term introduced in the Hamiltonian. Normally this term comes from density-density interactions or two-particle scatterings that are closely related to the interacting phenomenon [13]. One way to treat this ϕ^4 term is through perturbative expansion. However, the perturbative expansion does not apply to strong interacting systems. Meanwhile, the perturbation

theory also fails in understanding the quantum fluctuation near the critical point, no matter how small $|g - g_c|$ is [2].

Renormalization group (RG) method provides a way to treat interaction problems. Ideally, RG method simplifies problems by integrating out less relevant degrees of freedom —- either the energy levels above the high energy cutoff or the spatial details below the spatial cutoff. Since the integrating out of less relevant degrees of freedom is normally accompanied by the decreasing of temperature, the RG method is powerful in the study of low temperature behaviors, including QPTs. Meanwhile, as introduced in Section 3.1.1, QCPs of continuous QPTs have the feature of scaling invariance. In RG language, scaling invariance is equivalent to the invariance of the critical point under RG equations. Finally, the scaling law given by RG equations also reflects the critical exponents in Eqs. (3.1) and (3.2). Based on those reasons, theoretically the RG method is powerful in the study of interacting QPT-hosted systems, the searching of their critical points, as well as the study of universality around the critical points.

3.2.1 General Steps of the RG Method

As described above, the general idea of the RG method is to simplify the system through the integration out of unimportant degrees of freedoms. However, those high-energy levels will not just disappear. Instead, their effect will be incorporated into the redefinition of the system parameters, leading to the so called RG flow equations. Meanwhile, since the energy cutoff physically represents the upper bound of the relevant system energy, the RG method can also be understood as the method to get the effective system Hamiltonian with decreasing system temperature (if the system is in equilibrium). In this sense, RG equations describe the trend of the

[2] From the RG point of view, the operator with coefficient $g - g_c$ is always RG relevant. Consequently, $|g - g_c|$ effectively increases under lower temperature, thus invalidate any low temperature perturbation theory with respect to $|g - g_c|$.

system towards different regimes with a decreasing temperature.

There are multiple ways to get the RG equations [182; 18; 13; 15], ranging from the so called Wilsonian RG, functional RG, Coulomb gas RG, numerical RG, etc. However, all those RG methods are developed based on the central idea that the sytem before and after a RG step should be effectively the same. This central idea is satisfied by requiring the invariance of Lagrangian, action, partition function, or even correlators. Without loss of generality, in this section we introduce the RG method by considering a system with the action

$$S[\phi] = \sum_{a=1}^{N} g_a \hat{O}_a[\phi], \tag{3.4}$$

where ϕ is a field operator, a labels N different kinds of operators that correspond to different physical processes and g_a is the coefficient of the ath operator.

In an RG method, the system starts with an initial cutoff Λ above which the states are considered as unimportant. To simplify the system, we decrease the cutoff $\Lambda \to \Lambda/b$, where $b = 1 + l$ (with $0 < l \ll 1$) is a real number that is infinitesimally larger than one. By doing so, we divide the phase ϕ into two parts: slow modes ϕ_s and fast modes ϕ_f, where the fast modes ϕ_f have energies $\Lambda/b \leqslant E_f < \Lambda$ between the original and new cutoffs and the slow modes ϕ_s have energies $E_s \leqslant \Lambda/b$ smaller than the new cutoff. Based on this division, system action can be divided into three parts

$$S[\phi] = S[\phi_s] + S[\phi_f] + S_I[\phi_s, \phi_f], \tag{3.5}$$

where $S_I[\phi_s, \phi_f]$ represents the interaction between the slow and the fast modes, while $S[\phi_s]$ and $S[\phi_f]$ are the actions that only contain the slow and fast modes, respectively.

Next step is the central part of the RG method, that is to integrate out the fast modes in both the fast and interacting actions of Eq. (3.5). This can be done,

for instance, in field theory. To make the system physically invariant, after the integration, the form of the action or partition function should be unchanged. The effect of the energy levels above the new cutoff Λ/b has been incorporated into the new action

$$S'[\phi_s] = \sum_a g'_a \hat{O}'_a[\phi_s], \tag{3.6}$$

with new coupling constants g'_a.

Several things need to be pointed out concerning the effective action Eq. (3.6). One thing is that in contrast to the original action Eq. (3.4), the effective action may contain extra operators that are produced during the RG process. If a newly produced operator $\hat{O}'_a$ is RG relevant (to be specified later), this operator is important at low temperature so that it should be included into the RG flow at the beginning with the initial strength $g'_a = 0$.

Meanwhile, we notice that in contrast to the initial action, Eq. (3.6) only contains the slow modes, which is also the reason we relabel the operators by $\hat{O}'_a$. Consequently, to compare Eq. (3.6) with Eq. (3.4), we need to take the transformation $E_s \to bE_s$ that restores the energy space. This is called rescaling in the RG theories. After this step, we get the effective action after integrating out the fast modes between Λ/b and Λ

$$S[\phi] = \sum_a g'_a \hat{O}_a[\phi]. \tag{3.7}$$

Now, the comparison between Eq. (3.4) and Eq. (3.7) shows that through the integration out the fast modes, the action restores its starting form, except for the changing of the coupling constants

$$\vec{g}' = \tilde{R}(\vec{g}), \tag{3.8}$$

where the vectors $\vec{g}$ and $\vec{g}'$ are the operator coefficient vectors before and after the RG process, respectively and $\tilde{R}(\vec{g})$ is the function that determines the RG equations.

Notice that although the form of the action keeps invariant, the high energy levels do not simply disappear: instead, their effect has been incorporated into the redefinition of the coupling constants.

3.2.2 Physical Significance of the RG Equations

If the system size is large enough, we can effectively consider the system spectrum to be continuous so that the cutoff variation $l = b - 1 > 0$ becomes infinitesimal in each step. With this simplification, the change of the coupling constants after each step is infinitesimal so that we can write $g'_a = g_a + dg_a$ with $dg_a \ll g_a$. Consequently, the change of effective coefficients in Eq. (3.8) can be rewritten into the differential equations known as the RG flow equations

$$\frac{d\vec{g}}{dl} = R(\vec{g}), \tag{3.9}$$

where $R(\vec{g}) = \lim_{l\to 0}[\tilde{R}(\vec{g}) - \vec{g}]/l$. To predict system behavior at low temperature, it is thus essential to calculate the function $R(\vec{g})$.

Now we try to understand the physical significance of the RG equations by considering different situations. To begin with, if $R_a(\vec{g}) > 0$, $|g_a|$ increases when we integrate out the high energy states and is called relevant. Physically, when g_a is relevant, it becomes more and more important under RG flows, until it approaches its critical value or the infinity. On the contrary, if $R_a(\vec{g}) < 0$, $|g_a|$ is irrelevant and will decrease along RG flows until it reaches the critical value or becomes infinitesimal. Finally, if $R_a(\vec{g}) = 0$, $|g_a|$ stays invariant during RG flows and is called marginal.

Based on the RG equations, sometimes we can make multiple approximations onto the original Hamiltonian to simplify the system. One common choice is to take the value of irrelevant operators to be zero in the original Hamiltonian. Notice that this approximation is not always reasonable. For instance, if we take the coupling strength of an irrelevant operator to be identically zero, we will lose the details

about how the system arrives at the critical point. However, this approximation is reasonable if we are interested in studying a system that is weakly detuned from the critical point and when the combination of this irrelevant operator and other operators will not produce any relevant operator.

Another simplification is to fix the coupling strength of an operator to the value at the stable fixed point. Once again, this approximation is reasonable if we are only interested in the detuning of the system out of this point. However, it may wash out some important information when the system flows towards this fixed point. Notice that this is different from fixing the value of a marginal operator to its initial point. The former is an approximation while the latter is exact.

Finally, if an operator is relevant and will keep growing to infinity, it means that this operator will enter the strong coupling regime so that before it arrives infinity the RG method may have already failed. Due to its growing importance at lower temperatures, any perturbation theory, including the Coulomb dynamical method introduced in Section 2.3.4 fails when dealing with relevant operators at zero temperature. One way to deal with this situation is to consider the dual point of the system. This idea is briefly talked about in Section 3.2.3.

Before the end of this subsection, we provide a RG flow diagram to illustrate some of the ideas of the RG method. Fig. (3.2) is an example of the RG flows in a virtual system, with five fixed points represented by the red dots. For simplicity, we define the operator between two fixed points as $\hat{O}_{ij}$, where $i, j = \{A, B, C, D, E\}$ labeling the starting and the final fixed points, respectively.

To begin with, point A is stable along the $\hat{O}_{AE}$ direction and unstable along the $\hat{O}_{AC}$ direction. Fixed points like point A are thus conventionally called saddle points. Point B, instead, is called an unstable fixed point since all operators near it are relevant. This feature is also shared by point E. The most interesting points are points C and D. Those two points are stable along the $\tilde{\gamma}_1$ direction and marginal

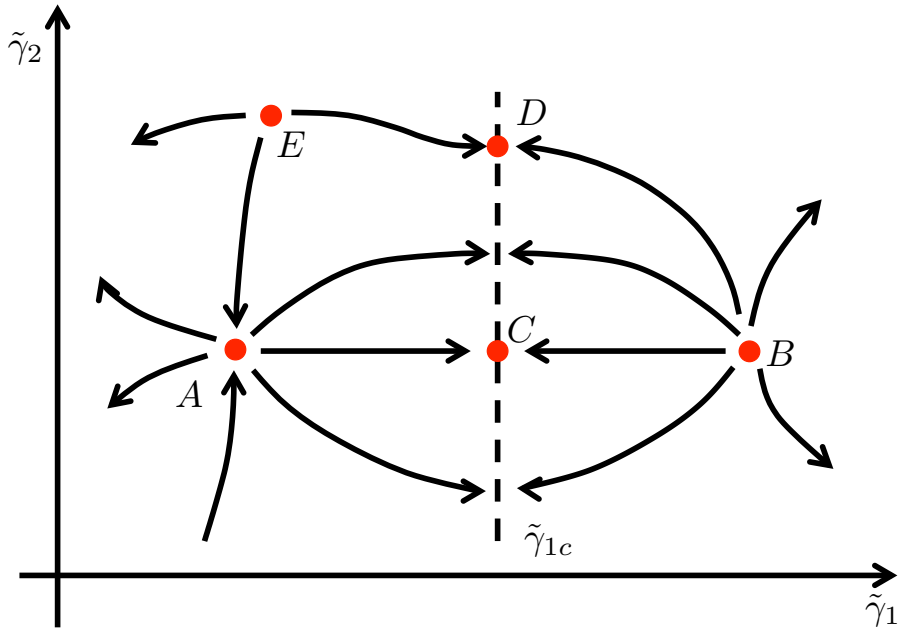

FIGURE 3.2: RG flow of a certain system in the parameter space $(\tilde{\gamma}_1, \tilde{\gamma}_2)$. Red dots represent five fixed points and arrows shows the RG flow between them. Dashed lines connecting points C and D represent marginal operators.

along the other one. Being marginal means that if we consider the leading relevant operator $\hat{O}_{CD}$ along CD line, it has the RG equation

$$\frac{d\hat{O}_{CD}}{dl} = 0, \tag{3.10}$$

and thus becomes RG invariant. Finally, if we consider the $A - E - D$ line, we can interpret the point E as an unstable intermediate fixed point between the point A and D. This is the feature of the QCP of a QPT.

3.2.3 Renormalization Group Method in the Study of Luttinger Liquid Models

In Section 2.1 we have introduced some tunneling features of several non-interacting one-dimensional models. In those cases, the absence of interaction greatly simplifies the picture where quasiparticles are simply free fermions.

In Luttinger liquid, however, things are more complicated as explained in Section

2.2. Here I briefly review the application of the RG method in the solution of the single barrier Luttinger liquid problem.

We begin with the simplest model where there is a single defect in the bulk of a Luttinger liquid. Without loss of generality, in this subsection we always assume that the impurity sits at the position $x = 0$. To model this problem, we begin with the bosonization of the Luttinger liquid. Here we take the canonical bosonization formula Eq. (2.28)

$$\psi(x) = \sum_{m_{\rm odd}} e^{im[k_F x+\theta(x)]} e^{i\phi(x)}, \tag{3.11}$$

to write the Hamiltonian of the uniform Luttinger liquid as

$$H = v[\frac{g}{2}(\bigtriangledown\phi)^2 + \frac{1}{2g}(\bigtriangledown\theta)^2], \tag{3.12}$$

where v is the Fermi velocity and g is the Luttinger liquid interaction. During RG calculations, we keep the action invariant. The Luttinger liquid actions can be written as

$$S = \int dxd\tau \frac{v}{2g}[(\bigtriangledown\theta)^2 + \frac{1}{v^2}(\partial_\tau\theta)^2], \quad \text{or} \quad S = \int dxd\tau \frac{vg}{2}[(\bigtriangledown\phi)^2 + \frac{1}{v^2}(\partial_\tau\phi)^2], \tag{3.13}$$

which is expressed with either θ or ϕ. Notice that two expressions in Eq. (3.13) are equivalent and one should choose the form that better suits certain problems or regimes.

We begin with the weak barrier regime. In this regime, we assume that the barrier produces a potential kink at $x = 0$. We further assume that the kink is so small such that the uniform Luttinger liquid model is a good approximation in this regime. With this assumption, the function of the single barrier is to produce backscatterings at $x = 0$ that transform electrons between the left and right moving channels that

contribute to an extra term

$$\delta S = \sum_{n=-\infty}^{n=\infty} \frac{1}{2} v_n \int d\tau e^{i2n\sqrt{\pi}\theta(x=0,\tau)} \tag{3.14}$$

in the action after the bosonization. Here v_n is the Fourier transformation of the potential kink at momentum $2nk_F$. Since Eq. (3.14) only contains the field θ, it is then natural to choose the free action as the first form in Eq. (3.13). Meanwhile, since backscattering only occurs at the impurity $x = 0$, it is convenient to integrate out all $x \neq 0$ fields and substitute them with their values along the classical path $\theta(x, \omega_n) = \theta(\omega_n) \exp[-|\omega_n x|/v]$, where ω_n is the bosonic Matsubara frequency. After integrating out the $x \neq 0$ freedoms, the action Eq. (3.13) becomes effectively zero-dimensional

$$S_{\text{eff}} = \frac{1}{\beta g} \sum_n |\omega_n||\theta(\omega_n)|^2. \tag{3.15}$$

To take an RG study of the system, we rewrite the summation in Eq. (3.15) over ω_n into an integral and add a cutoff Λ. The effective action then becomes

$$\begin{aligned} S[\theta] &= \frac{1}{\beta g} \sum_n |\omega_n||\theta(\omega_n)|^2 + \sum_{n \geqslant 1} \int d\tau v_n \cos[2n\sqrt{\pi}\theta(0)] \\ &= \frac{1}{g} \int_{|\omega|<\Lambda} \frac{d\omega}{2\pi} |\omega||\theta(\omega)|^2 + \sum_{n \geqslant 1} \int d\tau v_n \cos[2n\sqrt{\pi}\theta(0)]. \end{aligned} \tag{3.16}$$

Following the steps in Section 3.2.1, now we set a new cutoff $\Lambda - d\Lambda$ where $d\Lambda/\Lambda \ll 1$ is an infinitesimal positive number. Next, we divide $\theta(\omega)$ into the fast modes $\theta_f(\omega)$ (with $\Lambda - d\Lambda < \omega < \Lambda$) and the slow modes $\theta_s(\omega)$ (with $\omega < \Lambda - d\Lambda$) and integrate out the fast modes in the partition function

$$\begin{aligned} Z &= \iint D\theta_s D\theta_f e^{-S_f - S_s - S_I} \\ &= \int D\theta_s e^{-S_s} \langle e^{-S_I} \rangle_{S_f}, \end{aligned} \tag{3.17}$$

where S_f and S_s correspond to the fast and slow mode actions, respectively, and S_I is the action of the backscattering processes. The expectation value $\langle S_I \rangle_{S_f}$ is defined with respect to all fast modes, which can be calculated with the formula [92]

$$\langle e^{i\alpha\varphi(t)} e^{-i\alpha\varphi(0)} \rangle = \exp\left\{\alpha^2 \langle [\varphi(t) - \varphi(0)]\right\} \varphi(0)\rangle, \tag{3.18}$$

and that $\langle [\theta(t) - \theta(0)]\theta(0)\rangle = -2g \ln|t|$ with the action Eq. (3.15)

$$\langle S_I \rangle_{S_f} = \sum_{n \geqslant 1} v_n e^{-n^2 g \frac{d\Lambda}{\Lambda}} \int d\tau \cos[2n\sqrt{\pi}\theta(\tau)]. \tag{3.19}$$

The final step is the rescaling $\omega = \omega'\Lambda/(\Lambda + d\Lambda)$ such that the cutoff of ω returns to Λ. After all those steps, we see that now the backscattering strength changes from v_n to v_n^{eff}

$$v_n^{\text{eff}} = v_n + dv_n = v_n e^{\frac{d\Lambda}{\Lambda} - n^2 g \frac{d\Lambda}{\Lambda}} \approx v_n[1 + (1 - n^2 g)\frac{d\Lambda}{\Lambda}], \tag{3.20}$$

thus leading to the final RG equation for the single barrier Luttinger liquid model with a weak barrier

$$\frac{dv_n}{dl} = (1 - n^2 g) v_n, \tag{3.21}$$

where $dl = d\Lambda/\Lambda$ as introduced in Section 3.2.2. The RG equation Eq. (3.21) shows that the leading terms ($n = \pm 1$) has scaling dimension g. Based on the content in Section 3.2.2, we know that when $g > 1$, all backscattering processes are irrelevant so that the impurity at $x = 0$ will be "healed" at zero temperature where the system becomes an effectively uniform Luttinger liquid. On the contrary, when $g < 1$, the leading $2k_F$ backscattering becomes relevant so that the impurity grows under lowering temperatures.

However, Eq. (3.21) is only valid at the weak barrier regime so that it is unable to predict the system's zero temperature behavior when the backscattering grows ($g < 1$) to a value that is beyond approximate expansion. Consequently, to predict

the system status at $g < 1$, we need to study the dual system of the weak barrier regime, where two Luttinger liquid leads are separated by a huge barrier.

With a huge barrier at $x = 0$, the Luttinger liquid can be viewed as two semi-infinite Luttinger liquid leads that are connected at $x = 0$ with a weak tunneling strength t

$$\delta H = -t[\psi_S^\dagger(0^-)\psi_D(0^+) + h.c.], \tag{3.22}$$

where $\psi_S(0)$ and $\psi_D(0)$ refer to fermionic operators in different leads. Once again, we bosonize Eqs. (3.13) and (3.22) and integrate out $x = 0$ parts to arrive at the effective 0d action

$$\begin{aligned} S_{\text{eff}} &= \frac{g}{\beta}\sum_n |\omega_n||\phi(\omega_n)|^2 \\ \delta S &= -t\int d\tau \cos[2\sqrt{\pi}\phi(\tau)], \end{aligned} \tag{3.23}$$

where $\phi \equiv [\phi_R(0^+) - \phi_L(0^-)]/2$ is the phase difference. Notice that Eq. (3.23) is expressed with the ϕ field instead of the θ field. To understand the change of variables, we first notice that the Luttinger liquid is viewed as approximately disconnected at $x = 0$, thus leading to the vanishing of electron density at the barrier. This means $\theta(0) = 0$ with the density expression Eq. (2.29). Consequently, at the strong barrier regime, $\theta(0)$ is fixed to be zero and loses its dynamics so that only ϕ appears in the tunneling action. We can also understand the change of the action as resulted from the change of boundary conditions (between the Dirichlet and the Neumann boundary conditions).

Before calculating the RG equations for the action Eq. (3.23), we also want to emphasize the connection between the weak and strong barrier regimes. The comparison between actions in different regimes shows that Eqs. (3.16) becomes (3.23) under the transformation $\phi \to \theta$ and $g \to 1/g$. This means that the single barrier Luttinger liquid model is self-dual.

Now, we are ready to calculate the RG equations of the strong barrier regime. Just following the calculation in the weak barrier regime, it is straightforward to get the RG equation for the weak tunneling t

$$\frac{dt_n}{dl} = (1 - n^2/g)t_n, \tag{3.24}$$

which indicates that the strong barrier regime is stable with $g < 1$, where all tunneling operators are irrelevant. On the contrary, the $n = 1$ leading tunneling parameter grows with $g > 1$. The strong barrier regime thus has the transition point at $g = 1$, which is the same as that of the weak barrier regime! Now, we can get the full picture of the single barrier Luttinger liquid model with the RG equations (3.21) and (3.24). When $g > 1$, the system is unstable at the strong barrier regime and flows to the stable weak barrier regime. At zero temperature, the Luttinger liquid with a single barrier will thus be completely healed into a uniform wire with perfect conductance. On the contrary, when $g < 1$, the unstable weak barrier regime flows to the stable strong barrier regime with a decreasing temperature. In this regime, the system conductance drops to zero at zero temperature when the system is in equilibrium. The phase diagram is shown in Fig. 3.3 [103; 58].

3.2.4 Understanding the effect of dissipation with renormalization group (RG) theory

In Section 2.3 I have introduced the effect and the physical understanding of dissipation in 1d systems: basically, tunneling processes are prevented when the system fails to pay for the dissipated energy. In this section I will present another way to view the effect of dissipation using the RG method.

As has been introduced, the derivation of RG equations involves the integration out of all high energy states or freedoms. Since physically dissipation consists of various bosonic modes, it also contains high-energy freedoms that will modify the

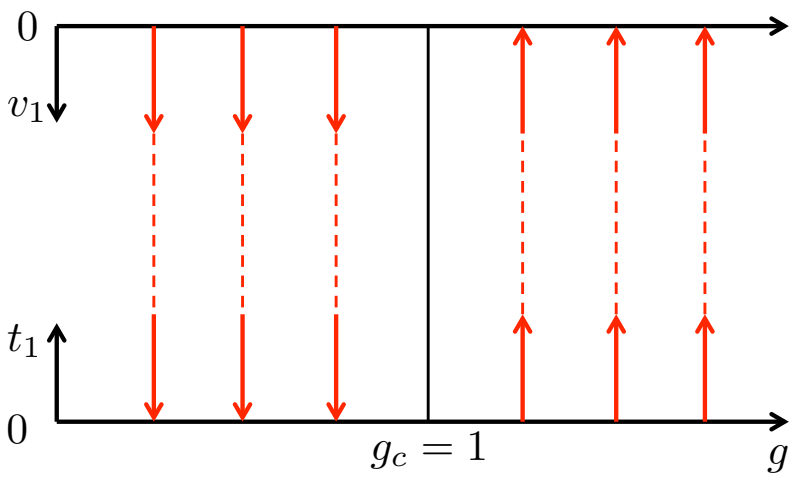

FIGURE 3.3: The phase diagram of the single barrier luttinger liquid model. Red arrows represent the RG flows of the system at both the weak barrier (with small v_1) and strong barrier (with small t_1) regimes. Notice that the dashed lines that connect RG flows in those two regimes come from speculations.

dissipation-free RG equations. To be consistent with the picture where dissipation prevents tunneling events, it is expected that the dissipation-involved RG equations for tunneling processes will have higher scaling dimension.

Once again we use the single barrier model as an example. The weak tunneling Hamiltonian of a single barrier model is given by Eq. (2.46) with $c^\dagger_{k,S}c_{q,D} \to c^\dagger_{k,S}c_{q,D}e^{-i\varphi}$ [92]. In RG equations, the tree level scaling dimension α_O of an operator $\hat{O}$ is related with its long time correlation function

$$\langle \hat{O}(t)\hat{O}(0)\rangle \propto \frac{1}{|t|^{2\alpha_O}}. \tag{3.25}$$

When the system is dissipation free, tunneling Hamiltonian contains two independent free fermionic operators with the long time correlator $\propto |t|^{-2}$. Consequently, in the dissipation free systems, the tunneling Hamiltonian has scaling dimension one and is invariant during the RG flow.

However, with dissipation involved, Eq. (2.46) contains an extra phase factor that associates with the fermionic tunneling process. As shown by Eq. (2.52), this

dissipative phase introduces an extra long time power $|t|^{-2r}$ in the correlator so that the scaling dimension of the tunneling Hamiltonian changes from 1 to $1 + r$.

Several comments can be made about the dissipation dependent scaling dimension. To begin with, dissipation involved tunneling operators now have higher scaling dimensions and become less relevant. As has been mentioned above, this agrees with the physical expectation since at lower temperatures, the presence of dissipation makes the system harder to afford the energy that dissipates during the tunneling processes. Meanwhile, since $1 + r > 1$, the tunneling Hamiltonian now becomes irrelevant. Physically, this predicts a decaying conductance at lower temperatures. At zero temperature, the system becomes two effectively independent semi-infinite wires with zero conductance. This is totally different from the dissipation free tunneling, whose zero temperature conductance is known to be finite. Finally, since the dissipative tunneling is RG irrelevant, the dynamical Coulomb blockade, which is only valid to the second order of the tunneling strength, becomes applicable to the dissipative single barrier model.

4

Background: Boundary Quantum Phase Transitions

This chapter provides an overview of the boundary quantum phase transition. To better illustrate the ideas, several boundary QPT-hosted systems are also introduced. This chapter only contains review material and not my original work.

I begin with the general definition of boundary QPTs. It is then followed by the introduction to three boundary QPT hosted systems, including the dissipative spinless resonant level, Kondo, and two channel Kondo models.

4.1 Boundary Quantum Phase Transitions

Boundary quantum phase transitions (or impurity quantum phase transitions) are special kinds of QPTs. Typically, a boundary QPT Hamiltonian contains the impurity, the bath and the interaction between them [177]. They have multiple features that are distinct from bulk QPTs.

To begin with, normally a boundary QPT reaches its critical point simply though the tuning of boundary parameters, such as the bath-impurity coupling strength and the boundary condition next to the impurity. This feature can be seen, for instance, in the Kondo and spin-boson models. This feature of boundary QPTs is surprising and highly non-trivial since it requires that the tuning of $N-1$ dimensional parameters greatly changes the expectation value of an operator in an N dimensional system, which is intuitively impossible. This is the reason that boundary QPTs are most commonly seen in one dimensional structures where excitations rely mostly on collectively motions of the entire system.

Another feature of boundary QPTs is the missing of order parameter [177]. As introduced in Section 3.1.1, order parameter is a strong signature of a continuous QPT: generally, bulk continuous QPT happens at the critical point where the expectation value of the order parameter abruptly changes between a non-zero value (ordered state) and a zero value (disordered state). However, the definition of both the ordered and disordered states requires the changing of the entire bulk. In a boundary QPT, normally the transition is between two states with different boundary conditions near impurities or boundaries. Consequently, in boundary QPTs it is hard to define any order parameter.

Below I provide the dissipative resonant level model and the Kondo models as examples to introduce the boundary quantum phase transition.

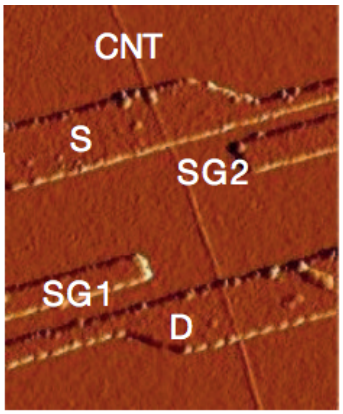

FIGURE 4.1: The experimental realization of the dissipative resonant level model. This picture comes from Professor Gleb Finkelstein's group. In the experimental setup, a carbon nanotube that is confined by two metallic leads hosts discrete levels and can be considered as an effective quantum dot. Two resistive leads (labeled source and drain) contain dissipative bosonic modes that couple to the electron tunneling processes. The dot lead tunnelings can be tuned by two side gates SG1 and SG2.

4.2 Dissipative Resonant Level Model

In this section I will provide an overview of the boundary quantum phase transition in a dissipative spinless resonant level model. The material introduced here is closely related to Chapters 6 and 7, which study the nonequilibrium I-V curve at and away from the quantum critical point, respectively. We begin with the introduction to the dissipative spinless resonant level model. The experimental realization of this model has been shown in Fig. 4.1. The model consists of a nanowire attached to two metallic leads. Those metallic leads creates two large potential barrier between nanowire segments, thus preventing the electron in the central nanowire from transporting outside. Due to the confinement effect, if the nanowire is short enough, it can be effectively considered as a quantum dot with discrete energy levels. This nanowire, together with the backgate on top of it, can thus be considered as the impurity part of the system.

As mentioned above, a boundary QPT also requires a bath part. In our model,

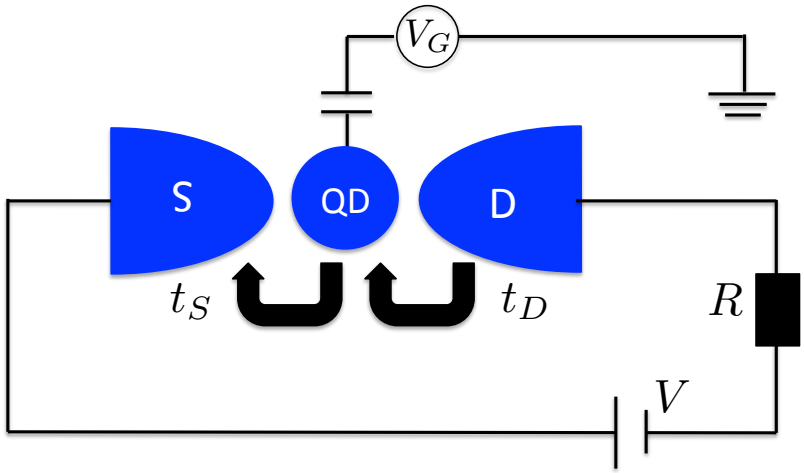

FIGURE 4.2: The theoretical sketch of the dissipative resonant level model with applied bias V. Here t_S and t_D are the dot-lead tunneling strengths that can be tuned by two side gates in Fig. 4.1. V_g is the backgate voltage that tunes the quantum dot energy ϵ_d. The dissipative environment is represented by the Ohmic impedance R.

this bath is provided by two metallic leads. Dissipation has been put into the system through diffusive metallic leads and will be modeled as bosonic modes as introduced in Section 2.3. The impurity-bath interaction is modeled by the tunneling between the nanowire and the metallic leads, which can be tuned through two side gates in Fig, 4.1. Meanwhile, the theoretical sketch of this model has been provided in Fig. 4.2.

System Hamiltonian can thus be written as [124]

$$H = H_{\text{dot}} + H_{\text{lead}} + H_{\text{T}} + H_{\text{env}}, \tag{4.1}$$

where $H_{\text{dot}} = \epsilon_d d^\dagger d$ describes the quantum dot with a single relevant energy level. Here ϵ_d is the energy with respect to the chemical potential of the leads and it can be tuned though the backgate.

The bath part of the system is

$$H_{\text{leads}} = \sum_{\alpha=S,D} \epsilon_k c^\dagger_{\alpha,k} c_{\alpha,k}, \tag{4.2}$$

where S and D label the source and drain leads, respectively.

The impurity and bath parts are connected through the tunnling Hamiltonian

$$H_{\mathrm{T}} = t_S \sum_k (c^\dagger_{S,k} e^{-i\varphi_S} d + h.c.) + t_D \sum_k (c^\dagger_{D,k} e^{i\varphi_D} d + h.c.), \tag{4.3}$$

with the dissipative phases $\varphi_{S,D}$ included. In the dissipative resonant level model, the common phase $\phi_S + \phi_D$ couples to the backgate so that decouples with the lead dissipation. It is thus conventional [124] to replace ϕ_S (ϕ_D) by $\varphi/2$ ($-\varphi/2$), with the dynamics of φ modeled by the correlator [following Eq. (2.52)]

$$\langle e^{i\varphi(\tau)} e^{-i\varphi(0)} \rangle \propto \frac{1}{|\tau|^{2r}}, \tag{4.4}$$

where $r = R/R_Q$ is the dissipation strength as define in Section 2.3. Without dissipation, the system is non-interacting and can thus be exactly solved through, e.g, equation of motion method [22]. The zero temperature zero bias differential conductance is a Lorentzian function

$$G = \frac{e^2}{h} \frac{4\Gamma_S \Gamma_D}{(\Gamma_S + \Gamma_D)^2 + \epsilon_d^2}, \tag{4.5}$$

where $\Gamma_{S,D} = 2\pi t^2_{S,D} \rho_0$ is the level broadening of the impurity levels due to their coupling to the leads. The system is on resonant with both particle-hole symmetry ($\epsilon_d = 0$) and left-right symmetry ($\Gamma_S = \Gamma_D$), with perfect conductance e^2/h. Due to the finite level broadening, both the left-right asymmetry $t_S - t_D$ and the particle-hole asymmetry ϵ_d are marginal. The phase diagram is shown in Fig, 4.3(a), where the points on the dashed lines represent Fermi liquid fixed points that are connected by marginal operators.

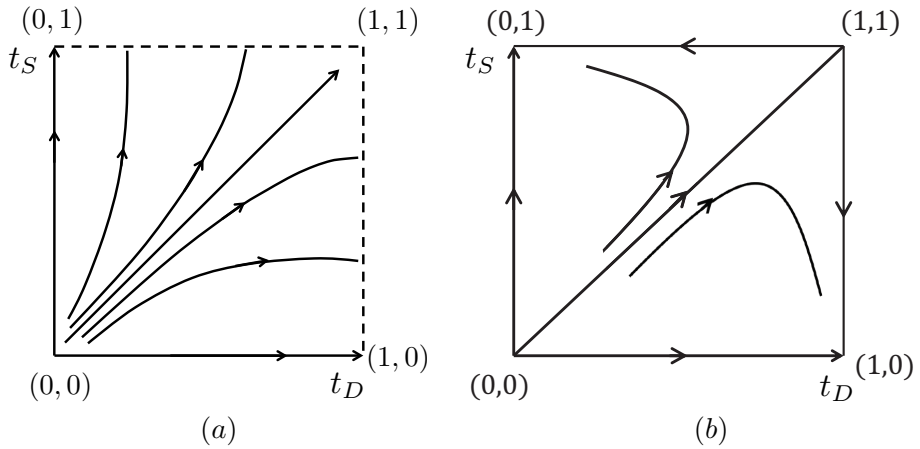

FIGURE 4.3: The RG flow diagram of the dissipative resonant level model with different initial coupling strength t_S and t_D. (a) The RG flow of the dissipation free case. In this case the source-drain asymmetry is marginal, leading to the dashed line that consists of Fermi liquid fixed points. (b) The RG flow of the dissipative case. Here the source-drain asymmetry is relevant, and system will flow to one of the stable fixed points where the dot is totally hybridized by the stronger lead.

However, the zero temperature conductance feature is greatly modified under the presence of dissipation. When the system is on resonant, the zero temperature system is uniform where dissipation will not be excited. In this sense, the conductance at the resonant point will remain the prefect value e^2/h [1]. However, the system uniformity is destroyed by the presence of any asymmetry (either source-drain asymmetry $t_S \neq t_D$ or particle-hole asymmetry $\epsilon_d \neq 0$), thus leading to the dissipation of energy during the tunneling processes. The dissipated energy cost can not be afforded by the system at zero temperature, thus leading to the vanish of conductance, in strong contrast to the dissipation free conductance Eq. (4.5). Boundary QPT is thus induced by system asymmetry, with the quantum critical point sitting at the perfect symmetric point. As a comparison to the dissipation free case, the RG flow diagram as a function of left-right asymmetry (with particle-hole symmetry $\epsilon_d = 0$) is shown in Fig. 4.3(b)

[1] With perfect symmetry, it can be studied that the Luttinger liquid resonant level model is perfect healed (into a perfect 1d wire) at zero temperature [103]. This argument also applies to the dissipative resonant level model [124]. Since the system is now uniform, it will be free from dissipative modes.

[124]. There we can see the stable fixed point $(1,0)$ $[(0,1)]$, corresponding to the state where the impurity is totally hybridized by the source (drain), and decouples with the drain (source). Between them is the unstable fixed point $(1,1)$ with perfect symmetry where the impurity is hybridized by both leads, leading the the healing of the impurity. The presence of this unstable fixed point signifies the boundary QPT in the dissipative spinless resonant level model. Finally, the QPT also predicts the zero width of the resonant level peak at zero temperature.

The QPT in Fig. 4.3(b) can be understood by considering the non-uniformity in the impurity system. To begin with, system asymmetry can not be healed, thus generating non-uniformity at the impurity. This non-uniformity, which produces bosonic modes excitations, dissipates energy into the environment and thus totally prevents any dot-lead tunneling events at zero temperature. On the contrary, at the QCP, system symmetry protects the system against dissipations and thus leading to the healing of the system at zero temperature with a perfect conductance e^2/h. The asymmetry sensitive conductance thus provides a strong signature for the experimental observation of this boundary QPT, which has been reported six years ago [134; 135].

The dissipative spinless resonant level model has several advantages in studying the boundary QPT. To begin with, it is a simple model that can be fully understood through multiple methods [175; 54; 85], including the RG method, boundary Sine-Gordon model, as well as the boundary conformal field theory. For instance, its near-equilibrium off-resonant current-bias curve has been predicted to be $I \propto V^{2r}$ based on some simple RG argument [104; 92]. These known results provide clear physics picture of this model that can be borrowed for our study. Meanwhile, although a simple model, the dissipative resonant level model is closely related to multiple physically interesting models, such as the two channel Kondo, Luttinger liquid and the quantum Brownian motion models. Finally, the dissipative spinless resonant

level model has been experimentally realized by Professor Gleb Finkelstein's group at Duke University [134; 135] so that any theoretically predictions may be checked or supported by the experimental data. Consequently, it is among the simplistic models that contain a boundary QPT and rich physics that worth further investigations.

4.3 Kondo Models and boundary QPTs

The Kondo model is named after the Kondo effect that was first explained by Jun Kondo [110]. In his famous paper, Jun Kondo provides a second order perturbation calculation to understand the anomalous low temperature resistance of a magnetic-atom-contained metal. Although his calculation leads to a diverging resistance at zero temperature, his pioneering work encourages other talented studies of the Kondo model, including the the fermi-liquid description of the Kondo model by P. Nozieres [147] and the poor man's scaling by P. Anderson [17]. In the latter work, Anderson shows that the integration out of the higher energy levels will lead to an increasing value of the Kondo interactions. With the RG equations derived by Anderson, one can calculate an characteristic Kondo temperature T_K, below which the Kondo model obeys P. Nozieres' Fermi liquid explanation, where the impurity can be considered as totally screened by the lead. After that, the Kondo model continues to attract wide interests from the academia community since it is among the simplest and most experimentally friendly strong correlated models that contain rich physical significance. To begin with, the RG equations of the Kondo model have the same structure of that of the XY model, which is known to possess a thermal KT transition. Consequently, the Kondo model provides a great platform in the study of the quantum KT transitions. Meanwhile, since the Kondo model Hamiltonian is relatively simple, lots of extensions have been done on it. Those extensions lead to famous structures including the multichannel Kondo models and multi-impurity Kondo models, where second order quantum phase transitions are predicted [67; 43]

(and even observed [154; 89]). In this section, I will provide a brief overview of these Kondo models and their boundary quantum phase transitions.

4.3.1 Anderson Model

Strictly speaking, the Kondo model is an effective low temperature Anderson model when the impurity is tuned into the Kondo valley (where the dot is singly occupied). To better understand the Kondo model, we will begin this section with the introduction to the Anderson model [155]. The Anderson model simply consists of a lead and a dot that couples to it. Electrons in the lead are assumed to be interaction free with linearized dispersion relation. We also assume perfect $SU(2)$ spin symmetry such that the lead Hamiltonian becomes

$$H_{\text{lead}} = \sum_{k,\sigma} \epsilon_k c^\dagger_{k\sigma} c_{k\sigma}, \tag{4.6}$$

where $c_{k\sigma}$ is the annihilation operator of the lead electron with momentum k and spin σ, and ϵ_k is its energy.

In contrast to those in the lead, dot electrons are confined in a mesoscopic scale so that they will feel both the Coulomb and confinement energies as introduced in Section 2.1.2. The general dot Hamiltonian is given by Eq. (2.12). However, here we assume that the energy difference between neighboring levels is large enough so that only one level is relevant. The dot Hamiltonian then becomes

$$H_{\text{dot}} = \sum_{\sigma} \epsilon_d d^\dagger_\sigma d_\sigma + U n_\uparrow n_\downarrow, \tag{4.7}$$

where ϵ_d is the dot level that is tunable by the backgate and $n_\sigma = d^\dagger_\sigma d_\sigma$ is the number operator with spin σ. Charging energy is represented by the onsite interaction U, that is only nonzero when the dot is doubly occupied. To match the experiment, here we assume that $U \gg k_B T$ is the positive leading energy scale.

The final part is the dot-lead connection, which is modeled by the tunneling Hamiltonian

$$H_{\mathrm{T}} = t \sum_{k,\sigma} (c^{\dagger}_{k\sigma} d_{\sigma} + h.c.), \tag{4.8}$$

where t is the momentum and spin-independent tunneling strength.

As other boundary models, features of the Anderson model heavily rely on the boundary parameters: the dot energy level and the dot-lead tunneling decide the observed features of the system. More specifically, when $\epsilon_d = 0$, impurity-lead electron tunnelings are greatly enhanced by the energy degeneracy between the empty and the singly-occupied dot configuration. In this section we are more interested in the particle hole symmetric point $\epsilon_d = -U/2 < 0$. This point is at the center of the Kondo valley, where system only allows singly occupied quantum dot as the real state. In the resonant level model, this point has the minimum conductance due to the energy punishment. However, in the Anderson model, the $SU(2)$ spin symmetry grants the quantum dot an extra degeneracy, which leads to a perfect conductance at the Kondo valley. This conductance is completely distinct compared with that of the resonant level model. To better understand this, it is more convenient to introduce the Kondo model Hamiltonian, which is the low energy effective Hamiltonian of the Anderson model in the Kondo valley.

4.3.2 Effective Hamiltonian of Kondo Model

As introduced in the previous section, when $\epsilon_d = -U/2$, the system is deep in the Kondo valley and it is more convenient to use the effective Hamiltonian where the quantum dot can only be singly occupied. This can be realized through the Schrieffer-Wolff transformation [83], where high-energy dot states are treated as virtual ones. In this section I will introduce how to arrive at the effective low temperature Kondo Hamiltonian through the Schrieffer-Wolff transformation.

We start by dividing the Hilbert space of the Anderson model into three parts $G = G_0 \otimes G_1 \otimes G_2$, where G_i is the subspace where the quantum dot contains i electrons. Those subspaces are connected by the tunneling Hamiltonian Eq. (4.8). For later convenience, we define operators H_{ij} that transform the states in Hilbert space j to the states in space i if $i \neq j$.

$$\begin{aligned} H_{10} &= t \sum_{k,\sigma} d_\sigma^\dagger (1 - n_{\bar{\sigma}}) c_{k\sigma} \\ H_{21} &= t \sum_{k,\sigma} d_\sigma^\dagger n_{\bar{\sigma}} c_{k\sigma}, \end{aligned} \tag{4.9}$$

where $\bar{\sigma}$ refers to the opposite spin of σ. Meanwhile, the Hamiltonian that models the states in subspace i is defined as H_{ii}. With those operators defined, the Schrodinger equation of the Anderson model can be written in the matrix form

$$\begin{bmatrix} H_{00}, H_{01}, H_{02} \\ H_{10}, H_{11}, H_{12} \\ H_{20}, H_{21}, H_{22} \end{bmatrix} \begin{bmatrix} \psi_0 \\ \psi_1 \\ \psi_2 \end{bmatrix} = E \begin{bmatrix} \psi_0 \\ \psi_1 \\ \psi_2 \end{bmatrix}, \tag{4.10}$$

where $H_{20} = H_{02} = 0$ and ψ_j is the wavefunction in the subspace with j electrons in the quantum dot. The goal of the Schrieffer-Wolff transformation is to express the Schrodinger equation with wave functions only in the singly occupied subspace [83]

$$[H_{11} + H_{12}(E - H_{22})^{-1} H_{21} + H_{10}(E - H_{00})^{-1} H_{01}]\psi_1 = E\psi_1, \tag{4.11}$$

with the energy E. Left side of Eq. (4.11) contains three contributions. The first part is the subspace Hamiltonian where the dot is strictly singly occupied. The second and the third parts, on the other hand, come from the second-order perturbation theory that effectively include the effect of the higher-energy subspace states (zero and doubly occupied dot). For instance, $H_{12}(E - H_{22})^{-1} H_{21}$ describes a process where an quantum becomes doubly occupied (H_{21}), pays for the energy penalty ($E - H_{22}$)

and returns to the ground state subspace (H_{12})

$$H_{12}(E-H_{22})^{-1}H_{21}=\sum_{k,k',\sigma,\sigma'}\frac{t^2}{(E-U-2\epsilon_d-H_{\rm lead}+\epsilon'_k)}c^\dagger_{k\sigma}c_{k'\sigma'}d_\sigma d^\dagger_{\sigma'}n_{\bar{\sigma}'}, \quad (4.12)$$

where ϵ'_k is the energy of the electron that enters the quantum dot and $H_{\rm lead}$ is the pure lead Hamiltonian Eq. (4.6). The energy $E\rightarrow\epsilon_d+H_{\rm lead}$ is the ground state energy of ψ_1. Similarly, contribution from the third term of Eq. (4.11) can be calculated with the same technique. Physically, due to the forbidden of single electron tunnelings by the energy requirement, Eq. (4.12) contains the lowest order lead-dot tunneling processes of the Kondo model in the Kondo valley. We thus keep only the lowest order tunnelings and write the effective Hamiltonian of the Anderson model in the Kondo valley as

$$H_{\rm Kondo}=J\vec{S}\cdot\vec{s}+H_{\rm lead}, \quad (4.13)$$

where $\vec{S}$ is the dot spin operator and $\vec{s}=\sum_{k,k'}c^\dagger_{k\sigma}\vec{\tau}_{\sigma\sigma'}c_{k'\sigma'}$ is the lead spin density operator. A simple comparison between Eqs. (4.12) and (4.13) gives us the expression of the Kondo exchange coupling strength in terms of the Anderson model parameters

$$J_{k,k'}=t^2[\frac{1}{U+\epsilon_d-\epsilon_{k'}}+\frac{1}{\epsilon_k-\epsilon_d}]. \quad (4.14)$$

Notice that in deriving Eq, (4.13), particle-hole symmetry $\epsilon_d=-U/2$ is required: only then the potential scattering vanishes [83]. We can further simplify the Kondo exchange expression by noticing $\epsilon_k\ll U$ so that Kondo interaction becomes $J=4t^2/U\ll t$. We thus have arrived at the effective Kondo Hamiltonian that is valid at the particle-hole symmetric point of the Kondo valley when the temperature is low enough.

4.3.3 Poor Man's Scaling

Intuitively, J is so small such that the Kondo exchange coupling seems to be negligible. However, with the famous "poor man's scaling" paper, P. Anderson [17] shows that the Kondo exchange is marginally relevant in RG point of view. This is why Kondo model has a full conductance at zero temperature. In this section, I provide a review of the poor man's scaling and derive the Kondo temperature based on the one loop RG equations. The connection between Kondo model and KT transition will also be touched.

To begin with, in this section we rewrite the isotropic Kondo model Eq. (4.13) into the more general form

$$H_{\text{Kondo}} = H_{\text{lead}} + \sum_{k,k'}[J^+ S^+ c^\dagger_{k\downarrow} c_{k'\uparrow} + J^- S^- c^\dagger_{k\uparrow} c_{k'\downarrow} + J^z S^z (c^\dagger_{k\uparrow} c_{k'\uparrow} - c^\dagger_{k\downarrow} c_{k'\downarrow})]. \quad (4.15)$$

As introduced in Section 2.2, RG method simplifies the system by integrating out higher energy freedoms. This is also the central idea of the poor man's scaling. Here we start the Kondo model with an initial bandwidth D in the lead, which gradually decreases during the scaling processes. More specifically, in each RG step we take an infinitesimal bandwidth change $0 < \delta D \ll D$. The change of the bandwidth decouples lead electron states within the range $D - \delta D < \epsilon < D$ and hole states within $-D < \epsilon < \delta D - D$. The effect of those decoupled states are then incorporated into the effective Kondo strength $J(D)$ through the poor man's scaling.

Without loss of generality, in this section we provide detailed derivation of the poor man's scaling RG equations only for the coefficients of the S^+ processes. The renormalization of the S^+ terms includes higher order terms that changes the quantum dot spin from down to up, while leaving the spin of the middle state to be either up or down. To incorporate the effect of high energy levels integrated out during the bandwidth change, lead electrons are lifted into the levels $D - \delta D < |\epsilon_k| < D$ as

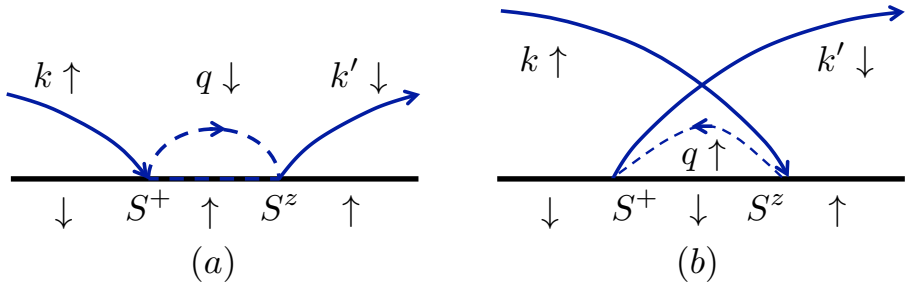

FIGURE 4.4: The diagrams of the two poor man scaling processes that correspond to Eqs. (4.16) and (4.17). Here arrows below the dark solid line represent dot spin state and the blue arrows represent the change of the lead electron state during the scaling. The virtual lead electrons in the reduced band $D-\delta D<|\epsilon_q|<D$ is represented by the dashed arrows.

virtual processes, and moves back into the decreased band $|\epsilon_k|<D-\delta D$ after each RG step. To begin with, we consider the processes shown in Fig. 4.4.

If the virtual state has a lead electron in the band $D-\delta D<\epsilon_k<D$ and an impurity with spin up [Fig. 4.4(a)], we get a higher-order operator

$$\begin{aligned}&(-J^z)S^z\sum_{q'}c^\dagger_{k'\downarrow}c_{q'\downarrow}\frac{1}{\epsilon_k-\epsilon_q}J^+S^+\sum_q c^\dagger_{q\downarrow}c_{k\uparrow}\\ &\approx -J^zJ^+\frac{\rho_0|\delta D|}{2(\epsilon_k-D)}S^+c^\dagger_{k'\downarrow}c_{k\uparrow},\end{aligned}\tag{4.16}$$

where we have used the fact that $\sum_{q,q'}c_{q'\uparrow}c^\dagger_{q\uparrow}=\delta D$, $S^zS^+=S^+/2$ and have taken the approximation that $\epsilon_q\approx D$. Similarly, if the virtual state contains a hole with its energy $-D<\epsilon_k<-D+\delta D$ and an impurity spin down [Fig. 4.4(b)], we get another contribution

$$\begin{aligned}&J^+S^+\sum_{q'}c^\dagger_{q'\downarrow}c_{k\uparrow}\frac{1}{\epsilon_k-\epsilon_q}J^zS^z\sum_q c^\dagger_{k\uparrow}c_{q\uparrow}\\ &\approx -J^zJ^+\frac{\rho_0|\delta D|}{2(\epsilon_k-D)}S^+c^\dagger_{k'\downarrow}c_{k\uparrow},\end{aligned}\tag{4.17}$$

which is the same as Eq. (4.16).

Due to the electron-hole and spin symmetry, we know that there are two more terms that contribute to the RG scaling of the S^+ operator. They can be similarly calculated, leading to the same result

$$J^+ J^z \frac{\rho_0 |\delta D|}{2(-D-\epsilon_k)} S^+ c_{k'\uparrow} c^\dagger_{k\downarrow}. \tag{4.18}$$

Combining those four processes we have the poor man's scaling RG equations

$$\delta J^+ = -J^+ J^z \rho_0 |\delta D| [\frac{1}{-D+\epsilon_k} + \frac{1}{-D-\epsilon_k}]. \tag{4.19}$$

Due to the spin symmetry, the RG equation for the S^- terms is the same as Eq. (4.19), simply with the substitution $J^+ \to J^-$.

Now we consider the RG equations of the S^z terms. The calculation is basically the same as those above. More specifically, since $S^+ S^- = 1/2 + S^z$, the renormalization of S^z involves double spin flip processes.

$$\delta J^z = -J^+ J^- \rho_0 |\delta D| [\frac{1}{-D+\epsilon_k} + \frac{1}{-D-\epsilon_k}]. \tag{4.20}$$

Finally, we further simplify Eqs. (4.19) and (4.20) with $\epsilon_k \ll D$ and the spin degenerate assumption $J^+ = J^- = J^\perp$. We have thus arrived at the poor man's scaling RG equations

$$\begin{aligned} \frac{dJ^\pm}{d\ln D} &= -2\rho_0 J^z J^\pm \\ \frac{dJ^z}{d\ln D} &= -2\rho_0 (J^\pm)^2. \end{aligned} \tag{4.21}$$

Notice that D is decreasing during the RG processes. Consequently, Eq. (4.21) indicates that the Kondo interactions increase with a decreasing bandwidth, and the quantum dot will thus be completely screened by the lead at zero temperature. Meanwhile, physically $\vec{J} \to \infty$ means that the dot spin combines into spin singlet

with the electron next to it. This result indicates that the strong coupling regime of the Kondo model is similar as that of the weak coupling regime. The difference is the "missing" of the electron on the site next to the quantum dot and the change of the phase shift [114] based on the Friedel sum rule [2].

Now we are ready to solve Eq. (4.21) for the Kondo temperature. The solution is simple once we have realized that $d[(J^z)^2 - (J^\perp)^2] = 0$ such that

$$(J^z)^2 - (J^\perp)^2 = \text{constant}. \tag{4.22}$$

We begin with the isotropic Kondo model where the constant is zero. At this point we set $J^z = J^\perp = J$, with the RG equation

$$\frac{dJ}{d\ln D} = -2\rho_0 J^2. \tag{4.23}$$

When the width D decreases to the value of the Kondo temperature T_K, Kondo coupling diverges and we get the Kondo temperature

$$T_K = De^{-\frac{1}{2\rho_0 J}}. \tag{4.24}$$

A more precise calculation of T_K involves higher-order loops. However, higher-order terms only changes the prefactor of Eq. (4.7) to be $D\sqrt{|2J\rho_0|}$, while leaving the exponential behavior unchanged [83].

It is more interesting to consider the more general case where J^z does not necessarily equal to $J^\perp$. The RG flow diagram of the general case is shown in Fig. 4.5. This RG diagram signifies the close connection between the Kondo model and the classical 2d XY model, which is known to host a KT transition. More specifically, when $J^z < -|J^\perp|$, the Kondo model flows to a line of fixed points that represent for the ferromagnetic fixed points, where the impurity spin is aligned with the electron

[2] Strictly speaking, the poor man's scaling only applies to high temperature Kondo models. It will be more precise to understand the Kondo model below the Kondo temperature T_k with the Fermi liquid explanation [147].

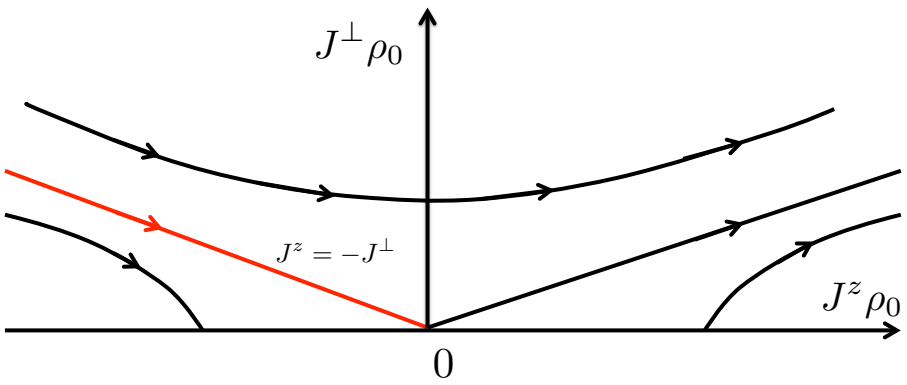

FIGURE 4.5: The RG flow diagram of the anisotropic Kondo model. When $J^z < -J^\perp$, the system flows to the ferromagnetic Kondo fixed points where the impurity spin aligns up with the spin next to the impurity. On the contrary, when $J^z \geqslant -J^\perp$, the system flows to the anti-ferromagnetic fixed point that is asymptotically isotropic. The transition line is colored red in the figure.

spin next to the dot. On the contrary, when $J^z \geqslant -|J^\perp|$, the Kondo model flows to the anti-ferromagnetic point, where the dot spin forms a singlet with the spin next to it. This point is also asymptotically isotropic where $J^z/J^\perp \to 1$ when approaching the strong coupling regime. Finally, as illustrated in Section. 3.1, the KT transition of the Kondo model has no unstable intermediate fixed point, which is in strong contrast to the continuous quantum phase transitions.

4.4 Two Channel Kondo Model

In the previous section, we have seen that at the strong Kondo fixed point, dot spin combines with the spin next to it into a singlet, thus forming into a Fermi liquid ground state at zero temperature. This Fermi liquid feature guarantees the stability of the strong coupling fixed point of the Kondo model. However, this fixed point is replaced by a non-Fermi liquid fixed point with non-zero impurity entropy in the multi-channel Kondo models. In this section, I will review the simplest multi-channel Kondo model: the spin 1/2 two channel Kondo model. I will represent multiple ways to understand the quantum-frustration induced non-Fermi liquid fixed point in the

two channel Kondo model. The symmetry-breaking induced continuous quantum phase transition in the two channel Kondo model will also be discussed.

4.4.1 Two Channel Kondo Model and System Hamiltonian

As its name signifies, the two channel Kondo (2CK) model consists of two independent channels that are equally screening a single dot simultaneously. In this model, the equal Kondo exchange coupling strength leads to the competition between two channels, resulting to the so called quantum frustration. Physically, the quantum frustration is the source of these interesting quantum phenomena in the 2CK model. However, to better understand the physics and the contained QPT of the 2CK model, here we start with the most general Hamiltonian [166]

$$\begin{aligned} H_{\rm 2CK} =& H_{\rm leads} + H_{\rm Kondo} \\ =& iv_F \sum_{\alpha=L,R} \sum_{\sigma=\uparrow,\downarrow} \int_{-\infty}^{\infty} \psi^{\dagger}_{\alpha\sigma}(x) \frac{\partial}{\partial x} \psi_{\alpha\sigma}(x) dx \\ &+ J^{\alpha\alpha'}_{\lambda} \psi^{\dagger}_{\alpha\sigma}(0) (\tau^{\lambda})^{\sigma\sigma'} \psi_{\alpha'\sigma'} S^{\lambda}, \end{aligned} \tag{4.25}$$

where v_F is the Fermi velocity, S is the impurity spin operator, τ^{λ} is the Pauli matrix of the λth direction and $\alpha = L, R$ labels the two channels of the two channel Kondo model, with the Kondo coupling strength $J^{\alpha\alpha'}_{\lambda}$ that transfers electrons between lead α and α'. Einstein summation is assumed in Eq. (4.25). Also notice that the lead Hamiltonian in Eq. (4.25) contains two chiral channels. This can always been done through the extension of a semi-infinite lead (with electrons propagating along both directions) into a full-infinite chiral channel [124].

Notice that Eq. (4.25) is the most general 2CK Hamiltonian. Without the loss of physical significance, we take the simplification that $J^{LR}_{x,y} = J^{RL}_{x,y} = J^{LR}_{\perp}$, $(J^{LL}_{x,y} + J^{RR}_{x,y})/2 = J_1$, $(J^{LL}_{x,y} - J^{RR}_{x,y})/2 = J_2$, and $J^{\alpha\alpha'}_{z} = J_z$. Notice that the simplifications are experimentally reasonable and accessible with the presence of the $SU(2)$ spin

symmetry.

4.4.2 Bosonization of Two Channel Kondo Model and Further Simplifications

Since the lead Hamiltonian contains two chiral channels, we use the chiral bosonization formalism as introduced in Section 2.2 [3]

$$\psi_{\alpha\sigma}(x) = \frac{F_{\alpha\sigma}}{\sqrt{2\pi a}} e^{-i\phi_{\alpha\sigma}(x)}, \tag{4.26}$$

where $F_{\alpha\sigma}$ is known as the Klein factor with the anti-commutators $\{F_{\alpha\sigma}, F_{\alpha'\sigma'}\} = 2\delta_{\alpha\alpha'}\delta_{\sigma\sigma'}$, and a is the lattice constant. The dynamics of the fermion $\psi_{\alpha\sigma}(x)$ is now granted by the bosonic field $\phi_{\alpha\sigma}(x)$ with the commutator $[\phi_{\alpha\sigma}(x), \phi_{\alpha'\sigma'}(x')] = i\pi\delta_{\alpha\alpha'}\delta_{\sigma\sigma'}\mathrm{Sign}(x-x')/2$. For later convenience, we rotate the original fields into four new ones

$$\begin{aligned} \phi_c &= (\phi_{L\uparrow} + \phi_{L\downarrow} + \phi_{R\uparrow} + \phi_{R\downarrow})/2, & \phi_s &= (\phi_{L\uparrow} - \phi_{L\downarrow} + \phi_{R\uparrow} - \phi_{R\downarrow})/2, \\ \phi_{cf} &= (\phi_{L\uparrow} + \phi_{L\downarrow} - \phi_{R\uparrow} - \phi_{R\downarrow})/2, & \phi_{sf} &= (\phi_{L,\uparrow} - \phi_{L\downarrow} - \phi_{R\uparrow} + \phi_{R\downarrow})/2, \end{aligned} \tag{4.27}$$

where ϕ_c (ϕ_s) represents the charge (spin) that transfers into or out of the quantum dot, and ϕ_{cf} (ϕ_{sf}) represents the charge (spin) that transfers between two channels. We further simplify the expression through the rotation $H'_{2\mathrm{CK}} = UH_{2\mathrm{CK}}U^\dagger$, where $U = \exp[i\phi_s S^z]$. We then have arrived at the effective Hamiltonian

$$\begin{aligned} H'_{2\mathrm{CK}} = \frac{v_F}{4\pi} \sum_{\nu=c,s,cf,sf} \int_{-\infty}^{\infty} dx (\partial_x \phi_\nu)^2 + \frac{J_1}{\pi a} S^y \cos[\phi_{sf}(0)] \\ - \frac{J_2}{\pi a} S^x \sin[\phi_{sf}(0)] - \frac{J_\perp^{LR}}{\pi a} S^x \sin[\phi_{cf}(0)] + (\frac{J_z}{2\pi} - v_F)\partial_x \phi_s(0) S^z, \end{aligned} \tag{4.28}$$

which contains the free bosonic part, the tunneling part, and the last part (extra anisotropy) that comes from the unitary transformation introduced above. Notice

[3] As introduced in Section 2.2, we should add a Klein factor in the chiral bosonization formalism to guarantee the correct anticommutation relations.

that the charge degrees of freedom ϕ_c has decoupled from the impurity (due to the invariance of the impurity charge state) so that can be ignored from further considerations.

4.4.3 Refermionization and Analysis

From simple scaling analysis, the tunneling terms all have scaling dimension 1/2 so that can be refermionized

$$\Psi_\nu = \frac{e^{i\pi d^\dagger d}}{\sqrt{2\pi a}} e^{-i\phi_\nu}, \tag{4.29}$$

where $\nu = s, cf, sf$ and $d = iS^+$ is the fermionic representation of the impurity. In doing so, we have treated the spin state of the quantum dot as a two level system. To guarantee the anticommutation relation between d and Ψ_ν, a Jordan-Wignar-like string operator $\exp(i\pi d^\dagger d)$ has been added in the refermionization formula. With the definition of the two level system and the refermionization, we finally have arrived at the effective Hamiltonian of the two channel Kondo model [166]

$$\begin{aligned} H'_{\rm 2CK} = iv_F \sum_{\nu=c,cf,sf} \int_{-\infty}^{\infty} \Psi_\nu^\dagger(x) \frac{\partial}{\partial_x} \Psi_\nu(x) dx + \frac{J_1}{2\sqrt{2\pi a}} [\Psi_{sf}^\dagger(0) + \Psi_{sf}(0)](d^\dagger - d) \\ + \frac{J_\perp^{LR}}{2\sqrt{2\pi a}} [\Psi_f^\dagger(0) - \Psi_f(0)](d^\dagger + d) + \frac{J_2}{2\sqrt{2\pi a}} [\Psi_{sf}^\dagger(0) - \Psi_{sf}(0)](d^\dagger + d) \\ - (J_z - 2\pi v_F) : \Psi_s^\dagger(0)\Psi_s(0) : (d^\dagger d - \frac{1}{2}), \end{aligned} \tag{4.30}$$

where the charge sector Ψ_c has been ignored since it decouples from the dot freedoms. Meanwhile, the spin fermions Ψ_s only appears at the effective density-density interaction term. We begin to analyse Eq. (4.30) at the critical point where two channels are symmetric ($J_2 = 0$) and independent ($J_\perp^{LR} = 0$). At this point, the J_1 term has scaling dimension 1/2 and is thus much more relevant compared with the density-density interaction, which has the marginal scaling dimension. Conse-

quently, J_1 increase with RG flow and finally arrives at the strong coupling fixed point, where the impurity operator $(d^\dagger - d)$ has been absorbed by the lead Majorana channel $\Psi^\dagger(x)_{sf} + \Psi_{sf}(x)$. The absorption of $(d^\dagger - d)$ simultaneously alters the scaling dimension of the density-density interaction to be $3/2 > 1$ [52]. Consequently, during the RG flow, the density-density interaction must be irrelevant and will decay to zero at the two channel Kondo fixed point [4]. Physically, the vanishing of the density-density interaction indicates the decoupling of $d + d^\dagger$ at the two channel Kondo fixed point, leading to the non-Fermi liquid behavior with impurity entropy $\ln\sqrt{2}$.

Now we add back symmetry breaking $J_2 \neq 0$ but still keep $J_\perp^{LR} = 0$. Since $\left\{\Psi^\dagger(x)_{sf} + \Psi_{sf}(x), \Psi^\dagger(x)_{sf} - \Psi_{sf}(x)\right\} = 0$ and $\left\{d + d^\dagger, d - d^\dagger\right\} = 0$, the screening of the channel asymmetry is independent from the symmetric Kondo screening part (J_1) and thus has scaling dimension $1/2$ at the two channel Kondo fixed point. This RG relevant asymmetry operator will thus screen the decoupled dot Majorana fermion, leading to a Fermi-liquid ground state as that of a single channel Kondo model. Depending on the sign of J_2, at this Fermi-liquid ground state, the quantum dot is either totally screened by the left channel $(J_2 > 0)$ or the right channel $(J_2 < 0)$ [6; 166].

Finally we consider the case where $J_\perp^{LR} \neq 0$ and $J_2 = 0$. Similar as the L-R asymmetric situation, the decoupled dot Majorana fermion is screened by the left-right Kondo operator $(\propto J_{LR})$ that is independent from the symmetric Kondo screening and has scaling dimension $1/2$. This relevant operator also destroys the two channel Kondo fixed point, leading the system to another Fermi-liquid ground state where the quantum dot is totally screened by the even channel [166]. However,

[4] Strictly speaking, this density-density interaction is important, for instance, when we are interested in the finite temperature conductance of the two channel Kondo model. However, since it is RG irrelevant compared with both J_1 and J_2, it will not participate in the screening of the impurity and is thus not important when we discuss about the impurity entropy at the 2CK QCP.

there is no quantum phase transition in this situation.

Based on the analysis above, we see that the 2CK model hosts a continuous boundary quantum phase transition between two distinct one channel Kondo models, with the two channel Kondo point as the critical point.

Before the end of this section, I want to introduce the g-theorem [5] in the understanding of the quantum phase transition in the 2CK model. g-theorem is the counterpart of the famous c-theorem [189] in boundary systems. It states that when two fixed points in a boundary system are connected by an boundary operator that does not involve the change of bulk parameters, the system will flow towards the fixed point with smaller impurity entropy. The decoupling of an impurity Majorana fermion (leading to the impurity entropy $\ln\sqrt{2}$) at the two channel Kondo fixed point has thus become the signature and necessity of the existence of the unstable intermediate fixed point, which indicates the existence of a boundary QPT in the 2CK model.

5

Rescue Quantum Phase Transition with Quantum Noise

We show that placing a quantum system in contact with an environment can enhance non-Fermi-liquid correlations, rather than destroy quantum effects as is typical. The system consists of two quantum dots in series with two leads; the highly resistive leads couple charge flow through the dots to the electromagnetic environment, the source of quantum noise. While the charge transport inhibits a quantum phase transition, the quantum noise reduces charge transport and restores the transition. We find a non-Fermi-liquid intermediate fixed point for all strengths of the noise. For strong noise, it is similar to the intermediate fixed point of the two-impurity Kondo model [1].

[1] Part of the text of this chapter has been adapted from the following previously published article: Gu Zhang, Eduardo Novais and Harold U. Baranger, "Rescuing a Quantum Phase Transition with Quantum Noise", *Physical Review Letters*, **118**, 050402 (2017)

5.1 Introduction

Quantum fluctuations and coherence are key distinguishing ingredients in quantum matter. Two phenomena to which they give rise, for instance, are QPTs and *quantum noise* [119; 180; 92], the effect on the system of quantum fluctuations in its environment, for no system is truly isolated. Understanding the intersection of these two topics—the effects of quantum noise on QPTs—is important for understanding quantum matter. It is natural to suppose that decoherence produced by the noise will suppress quantum effects, and in particular inhibit or destroy a quantum critical state. Indeed, a variety of calculations demonstrate this in both equilibrium [119; 180; 105; 116; 33; 37; 86; 152; 23; 24] and non-equilibrium [46; 45; 64; 39; 100; 173] contexts. There are also a few known cases that do not follow this rule [181; 143; 130]. Here, we present a striking counter-example to the notion that environmental noise necessarily harms quantum many-body effects: in the system we study, the addition of (equilibrium) quantum noise stabilizes a non-Fermi liquid quantum critical state.

We discuss the phase diagram of two quantum dots connected to two leads in the presence of environmental quantum noise. The noiseless model has a quantum phase transition that is transformed into a crossover by charge transport across the double dot. We show that quantum fluctuations of the field associated with the source and drain voltage counteract this charge transport. The competition between these two processes restores the delicate balance of the quantum critical state. The result is that the quantum phase transition is rescued from the undesired crossover for *any* strength of the noise.

This chapter is organized as follows. Two better convey the idea contained in this chapter, I will start with the background introduction of the two impurity Kondo model in Section 5.2. This is followed by the introduction to the system of this

chapter: the dissipative two impurity Kondo model in Section 5.3. After the introduction of the system, in Sections 5.4 and 5.5 I will first talk about the result concerning the low temperature behavior of a two impurity Kondo model with or without the noise, respectively. I also provide the final RG diagram of the dissipative two impurity Kondo model in Section 5.5. To understand the results presented in these two sections, we study the effective Hamiltonian in Section 5.6. With the effective Hamiltonian, the low temperature feature around two intermediate fixed points is discussed in Section 5.7, which provide a potential connection to possible experiments. Finally, we draw the conclusion in Section 5.8.

5.2 Two Impurity Kondo Model

For later convenience, in this section I briefly introduce the boundary QPT and its disappearance in the two impurity Kondo model.

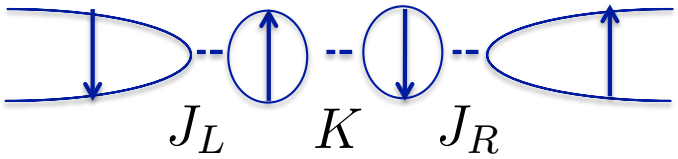

FIGURE 5.1: Schematic of the two impurity Kondo model: two quantum dots coupled to left and right leads. $J_{L,R}$ and K refer to the Kondo and inter-impurity exchange coupling strengths, receptively.

The set-up of the two impurity Kondo model consists of two spinful quantum dots and two spinful leads, as shown in Fig. 5.1. For simplicity, it is assumed that both dots have particle hole symmetry $\epsilon_d = -U/2$, thus forbidding first order lead-impurity communications. Higher order hopping, however, is possible through virtual states, thus enabling the dot-lead Kondo coupling and the inter-dot exchange coupling. The second-order processes are shown in Fig. 5.1 with strength from the Schrieffer-Wolff transformation (details of the Schrieffer-Wolff transformation have been provided in

Section 4.3.2)

$$J_{L,R} = 2\frac{t_{L,R}^2}{U}, \qquad K = 2\frac{V^2}{U}, \tag{5.1}$$

where $t_{L,R}$ is the first order impurity-lead hybridization, while V is the direct inter-dot hopping strength. With those assumptions, the system Hamiltonian becomes $H = H_0 + H_{\text{dots}}$, where H_0 is the non-interacting Hamiltonian of two leads and

$$H_{\text{dots}} = J_L \vec{s}_L(0) \cdot \vec{S}_L + J_R \vec{s}_R(0) \cdot \vec{S}_R + K \vec{S}_L \cdot \vec{S}_R \tag{5.2}$$

contains the Kondo screening from the leads and the inter-dot exchange coupling. Here $\vec{s}_{L,R}$ and $\vec{S}_{L,R}$ correspond to the lead spin density and impurity spin, respectively. For simplicity, it is also assumed that $J_L = J_R = J$. [2]

In this model, a quantum phase transition is expected to occur when the exchange coupling K is tuned while keeping J unchanged (or the other way around). Intuitively, when $K \gg J$, two impurities bound together into a singlet. This is called the local singlet fixed point (denoted LSPF) where the singlet formed by two impurities decouples from two leads. On the contrary, if $K \ll J$, both quantum dots are screened by the corresponding leads, thus destroying the exchange coupling between two quantum dots. This point has a ground state equivalent to two independent Kondo models, and is thus called the Kondo fixed point (KFP). The quantum phase transition is shown in Fig. 5.2. Since the ground states at both fixed points are fermi liquid [3], intuitively, this quantum phase transition can be understood by looking at the phase shift of those two fixed points. At the KFP, each lead screens its corresponding impurity independently, leading the phase shift $\pi/2$, which equals that of an antiferromagnetic Kondo model. On the contrary, at the LSFP, both dots decou-

[2] Unlike that of the 2CK model, L-R asymmetry in the two impurity Kondo model is not important: it only shifts the position of the critical point and thus can be ignored.

[3] The KFP contains two independent Kondo models, which are known to host fermi liquid ground states [147]. At the LSFP, since quantum dots form into a singlet and decouple from the leads, the ground state is also a fermi liquid.

ple from the leads, so that the phase shift of the leads vanishes. Due to the missing of any other fixed point, a point must exist where the phase shift abruptly changes between $\pi/2$ and zero, indicating a boundary QPT in the two impurity Kondo model.

FIGURE 5.2: Two phases of the two impurity Kondo model. The blue box represents a strong coupling between two parts of the system. Left panel: the Kondo fixed point where two impurities are totally screened by the corresponding leads. The system at this point can thus be considered as two independent single channel Kondo models. Right panel: the local singlet fixed point where two impurities are bound into a singlet. At this point, two leads totally decouple from the quantum dots.

However, the two impurity Kondo Hamiltonian Eq. (5.2) is incomplete or experimentally inaccessible. More specifically, Eq. (5.2) only contains operators from the second order Schrieffer-Wolff transformation. This treatment is valid in single impurity Kondo models where higher order terms are irrelevant. However, the two impurity Kondo model consists of a relevant higher order term that leads to the direct charge tunneling between the source and drain. As will be discussed later in Section 5.6, although with a comparatively small initial coefficient, this term has scaling dimension 1/2 near the two impurity Kondo QCP, and will thus destroy the QPT.

5.3 Model for Dots and Leads

The dissipative two impurity Kondo model has three parts: leads, dots, and electromagnetic environment. Following standard procedures, we linearize the spectrum of each lead, notice that a one-dimensional subset of electrons couples to each dot, and represent it using chiral fermions by analytic continuation with open boundary conditions [74]. The resulting lead Hamiltonian is the sum of four free Dirac

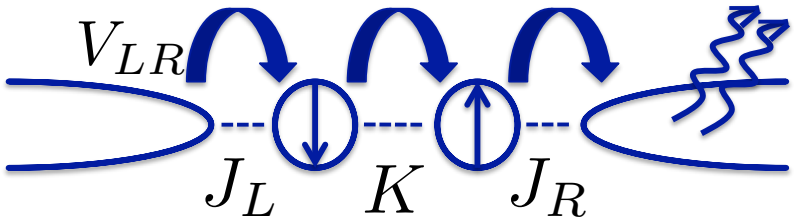

FIGURE 5.3: Schematic of the system: two quantum dots coupled to left and right leads. $J_{L,R}$ and K refer to the Kondo and exchange coupling strengths, respectively. V_{LR} is the strength of direct charge transport between the leads. Dissipative modes in the leads are represented by wiggly arrows.

fermions,

$$H^0_{\text{leads}} = \sum_{\alpha,\sigma} \int_{-\infty}^{\infty} dx\, \psi^\dagger_{\alpha,\sigma}(x) i\partial_x \psi_{\alpha,\sigma}(x), \tag{5.3}$$

where α and σ are the lead and spin labels and both the Fermi velocity and $\hbar$ are set to unity.

For the dots, we consider the Coulomb blockade regime in which charge fluctuations are suppressed and the electron number is odd [187]. The single-level Anderson model is suitable for each dot, as the spacing between levels in the carbon nanotube dots is large [134; 135]. Each dot, then, has a low energy spin-$\frac{1}{2}$ degree of freedom, $\vec{S}_\alpha$. Projecting onto this low-energy subspace via a second-order Schrieffer-Wolff transformation produces two Kondo-like terms with couplings $J_{L,R}$ and a spin-spin anti-ferromagnetic interaction. The Hamiltonian is already given in Eq. (5.2). With the lead definition Eq. (5.3), here we write the lead spin density operator next to the impurity as $\vec{s}_\alpha = \psi^\dagger_\alpha(0)\vec{\sigma}\,\psi_\alpha(0)$. Though none of our results depend on left-right symmetry, we take $J_L = J_R$ for simplicity.

Charge transfer between the two leads is key to the physics of this system [99; 70; 191; 170; 128; 96]. The effective hopping between the leads that arises from the third-order Schrieffer-Wolff transformation of the original Anderson model must be

added [96]:

$$\begin{aligned} H_{LR} &= V_{LR}\Big[\big(\psi^\dagger_{L\uparrow}\psi_{R\uparrow}+\psi^\dagger_{R\downarrow}\psi_{L\downarrow}\big)S^-_L S^+_R \\ &+ \big(\psi^\dagger_{L\uparrow}\psi_{R\uparrow}+\psi^\dagger_{L\downarrow}\psi_{R\downarrow}\big)S^z_L S^z_R \\ &+ \big(\psi^\dagger_{L\uparrow}\psi_{R\downarrow}-\psi^\dagger_{R\uparrow}\psi_{L\downarrow}\big)\left(S^z_L S^-_R - S^-_L S^z_R\right)\Big] + \text{h.c.}, \end{aligned} \tag{5.4}$$

where $x=0$ for the lead operators. This form is obtained because moving an electron across the dots necessarily involves the dot spins. Much of the physics added by (5.4) is obtained from a simpler direct hopping, $\hat{H}_{LR}=\hat{V}_{LR}\psi^\dagger_{L\sigma}(0)\psi_{R\sigma}(0)+\text{h.c.}$ [96; 129]. We therefore simplify the discussion by using $\hat{H}_{LR}$ rather than H_{LR} when possible.

The final ingredient in our system is the "quantum noise." Quantum fluctuations of the source and drain voltage require a quantum description of the tunneling junction [92; 187]. The standard procedure is to introduce junction charge and phase fluctuation operators that are conjugate to each other and (bilinearly) coupled to modes of the ohmic environment with resistance R. Treating the latter as a collection of harmonic oscillators with the desired impedance, we write the environment as a free bosonic field, $H^0_\varphi=\int\frac{dx}{4\pi}(\partial_x\varphi)^2$, which is excited in a tunneling event through the charge-shift operator $e^{i\sqrt{2r}\varphi(0)}$ [92]. As introduced in Section 2.3.3, such a shift operator is added to every term in H_{LR} according to

$$\psi^\dagger_{L\sigma}\psi_{R\sigma}\rightarrow e^{i\sqrt{2r}\varphi(0)}\psi^\dagger_{L\sigma}\psi_{R\sigma}, \tag{5.5}$$

where $r=Re^2/h$ is the dimensionless resistance. The environment does not modify the second-order exchange couplings Eq. (5.2) because those virtual processes occur on the very short time scale of the inverse charging energy [63], typically smaller than the time scale of the environment. The decoupling of the Kondo exchange from the environment, for instance, has been detailed introduced for a quantum dot in the Kondo regime [63]. In summary, the starting point of our discussion is the

Hamiltonian

$$H = H^0_{\text{leads}} + H^0_{\varphi} + H_{\text{dots}} + H_{LR}(r)\,. \tag{5.6}$$

5.4 Quantum Phase Transition or Crossover?

In this chapter, we introduce system features when the two impurity Kondo model is free from dissipation. Further physical illustration will be provided in Section 5.6.

First, following the bosonization formula with chiral fields in Section 2.2.2 we bosonize the chiral fermions describing the leads, Eq. (5.3), thereby introducing chiral bosonic fields $\phi_{\alpha,\sigma}$. One can then see that the ultraviolet fixed point, described by $H^0_{\text{leads}} + H^0_{\varphi}$, is unstable. There are two important energy scales connected to this instability: the Kondo temperature, T_K, associated with the screening of each dot by its own lead, and the "crossover temperature," $T^* < T_K$ [128; 129].

The Kondo temperature T_K is defined by ignoring the inter-lead tunneling V_{LR}. As introduced in Section 5.1, with $V_{LR} = 0$, the system flows to either the LSPF or the KFP. T_K is then defined as the characteristic temperature below which the system can be described by either of those two fermi liquid ground states. Those two ground states have distinct phase shifts, indicating the exist of an intermediate (unstable) fixed point [127; 7], which we call IFP_1 (see Fig. 5.4).

Inter-lead tunneling, $V_{LR} \neq 0$, changes the behavior dramatically. In the absence of dissipation, $r = 0$, it is known that H_{LR} destabilizes IFP_1 [169; 191; 170; 128; 96], becoming effective below a scale T^*. The low-energy physics is described by Fermi-liquid Hamiltonians with scattering phase shift varying from $\delta = 0$ to $\pi/2$ depending on the initial values of the couplings [70; 170; 128; 129]. The finite temperature conductance is $G = G_0 \sin(2\delta)[1 - \kappa(T/T^*)^2]$, where $G_0 = 2e^2/h$ and κ is non-universal. Therefore, for $T < T^*$, the quantum phase transition of the two-impurity Kondo model is transformed into a crossover between the Kondo and local-singlet regimes.

5.5 Quantum Noise Effects

Close to the KFP and LSFP, the tunneling Hamiltonian in the absence of noise, H_{LR}, is a marginal operator [170; 128; 129]: without noise, any bilinear operator that transfers charge between the leads is marginal at these two fixed points. A key effect of the noise, as has been introduced in Section 3.2.4, is that the scaling dimension of such an operator increases, making it irrelevant. In the tunneling operator H_{LR}, the increase is caused by the exponential charge-shift operator introduced in Eq. (5.5). The line of Fermi-liquid fixed points existing at $r = 0$ is then destroyed. The conductance around the KFP and LSFP follows from perturbation theory in the tunneling, leading to $G(T) \sim T^{2r}$ [92; 104; 103].

The new found stability of the Kondo and local-singlet fixed points with respect to tunneling demands once again the existence of an intermediate fixed point. We denote this "dissipative intermediate fixed point" by IFP_2, as shown in Fig. 5.4.

IFP_2 occurs for the same value of K as IFP_1, namely $K = K_c$, as we now show. It is known that the effect of a resistive environment on a bilinear tunneling operator is connected to the partition noise produced by the tunneling [122; 163]: when there is no partition noise, the environment is not excited by the current and so has no effect. This is the case at $K = K_c$: the phase shift is $\delta = \pi/4$, so the zero temperature conductance is $G = 2e^2/h$ and the transmission is unity. Thus, there is no partition noise: from the line of $r = 0$ Fermi-liquid fixed points, this fixed point survives at non-zero r and is, in fact, IFP_2. We now turn to characterizing both IFP's in detail.

5.6 Effective Hamiltonian at the Intermediate Fixed Points

Previous two sections present main features of the two impurity Kondo model without and with dissipation, respectively. The understanding of those features involves the calculation of the effective Hamiltonian near the critical point. We begin with the

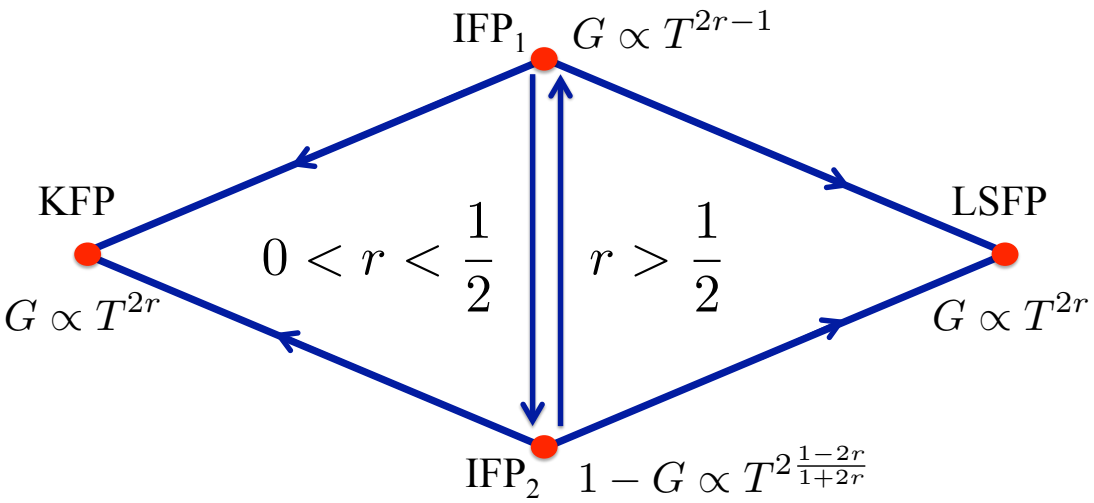

FIGURE 5.4: Stability diagram for different noise strengths r, and the temperature dependence of the conductance at each fixed point. The KFP and LSFP are stable for any non-zero r, while the nature of the IFP changes as a function of r. For $r < 1/2$, the intermediate state is controlled by IFP$_2$—the fixed point that evolves from one of the $r = 0$ Fermi-liquid fixed points. In contrast, for $r > 1/2$, IFP$_1$—which evolves from the two-impurity-Kondo IFP—is relevant. For $r = 1/2$ a line of fixed points connects IFP$_1$ to IFP$_2$.

bosonization

$$\psi_{\beta\sigma} = \frac{F_{\beta\sigma}}{\sqrt{2\pi\alpha}} e^{i\phi_{\beta\sigma}}, \tag{5.7}$$

where β and σ are lead and spin indices, respectively, and $F_{\beta,\sigma}$ are Klein factors that preserve the fermionic anti-commutation relation for different fermionic flavors. The constant α is of order the inverse of the bare cut-off of the fermionic theory.

It will be convenient to make spin-charge separation explicit by rotating the bosonic fields [this is the same as Eq. (4.27) in Section 4.4.2],

$$\begin{aligned} \phi_c &= (\phi_{L\uparrow} + \phi_{L\downarrow} + \phi_{R\uparrow} + \phi_{R\downarrow})/2, & \phi_s &= (\phi_{L\uparrow} - \phi_{L\downarrow} + \phi_{R\uparrow} - \phi_{R\downarrow})/2, \\ \phi_{cf} &= (\phi_{L\uparrow} + \phi_{L\downarrow} - \phi_{R\uparrow} - \phi_{R\downarrow})/2, & \phi_{sf} &= (\phi_{L,\uparrow} - \phi_{L\downarrow} - \phi_{R\uparrow} + \phi_{R\downarrow})/2. \end{aligned} \tag{5.8}$$

The charge field ϕ_c would couple to the fluctuation of the total charge on the two dots; since we consider the singly occupied regime of the quantum dots in which there can be no charge fluctuations, this field decouples from the problem. The

charge flavor field, ϕ_{cf}, encodes charge transfer between the two leads, and thus is the bosonic field that couples to the environmental noise in our model. Similarly, ϕ_s and ϕ_{sf} correspond, respectively, to total spin and spin transfer between the leads. With those bosonized fields, the effective Hamiltonian becomes

$$\begin{aligned} H_1 = & \sum_{\beta=c,s,sf,cf} H^0_\beta + \frac{J}{2\pi}\left\{\partial_x\phi_s(0)S^z_+ + \partial_x\phi_{sf}(0)S^z_-\right\} + K\,\vec{S}_L\cdot\vec{S}_R \\ & + \frac{J}{\pi\alpha}\left\{\cos\phi_{sf}(0)[\cos\phi_s(0)S^x_+ - \sin\phi_s(0)S^y_+] - \sin\phi_{sf}(0)[\sin\phi_s(0)S^x_- + \cos\phi_s(0)S^y_-]\right\} \end{aligned} \tag{5.9}$$

where $\sum_\beta H^0_\beta$ refers to the free bosonic lead Hamiltonian.

To further simplify the system, it is convenient to rotate the system with the unitary $\hat{U} = e^{-iS^z_+\phi_s(0)}$, a transformation that is well known in the Kondo literatures. This transformation has several effects. First, its action on $S^x_\pm$ and $S^y_\pm$ leads to a decoupling of these operators from ϕ_s. Second, its action on $\partial_x\phi_s(0)$ leads to two additional terms, $-\partial_x\phi_s(0)S^z_+$ and $-\frac{J-\pi}{\pi\alpha}(S^z_+)^2$, that change the coupling with $S^z_{L,R}$. The resulting form of the Hamiltonian,

$$\begin{aligned} H_1 = & \sum_\beta H^0_\beta + \frac{J}{\pi\alpha}\left\{\cos\phi_{sf}(0)S^x_+ - \sin\phi_{sf}(0)S^y_-\right\} + \frac{J-2\pi}{2\pi}\partial_x\phi_s(0)S^z_+ \\ & + \frac{J}{2\pi}\partial_x\phi_{sf}(0)S^z_- + K\sum_{\lambda=x,y} S^\lambda_L S^\lambda_R + \left[K - \frac{2}{\pi\alpha}(J-\pi)\right]S^z_L S^z_R, \end{aligned} \tag{5.10}$$

is clearly highly anisotropic in the dot's spin degrees of freedom.

We now switch back to fermionic representations through the refermionization equations

$$\begin{aligned} \psi_{sf}(x) &= \frac{1}{\sqrt{2\pi\alpha}}e^{i\phi_{sf}(x)}, \qquad \psi^\dagger_s(x)\psi_s(x) = \frac{1}{2\pi}\partial_x\phi_s(x), \\ \psi_{cf}(x) &= \frac{1}{\sqrt{2\pi\alpha}}e^{i\phi_{cf}(x)}e^{-i\pi\int_{-\infty}^{\infty}dx\psi^\dagger_{sf}(x)\psi_{sf}(x)}, \end{aligned} \tag{5.11}$$

which are not, of course, the original fermions because of the several rotations during the bosonic description. In terms of these new fermions, H_1 becomes

$$\begin{aligned} H_1 = &\sum_{\lambda} K^{\lambda} S_L^{\lambda} S_R^{\lambda} + (J - 2\pi)\psi_s^{\dagger}(0)\psi_s(0)S_+^z + J\psi_{sf}^{\dagger}(0)\psi_{sf}(0)S_-^z \\ &+ \frac{J}{2\sqrt{2\pi\alpha}} \left\{ [\psi_{sf}(0) + \psi_{sf}^{\dagger}(0)]S_+^x + iJ[\psi_{sf}(0) - \psi_{sf}^{\dagger}(0)]S_-^y \right\}, \end{aligned} \tag{5.12}$$

where $K^x = K^y = K$ and $K^z = K - \frac{2}{\pi\alpha}(J - \pi)$. Ref. [69] points out that the second term in Eq. (5.12) only renormalizes the K^z part of the original Hamiltonian, thus perhaps shifting the value of K_c but not affecting the physics at $K = K_c$. We therefore drop this term from the Hamiltonian in later paragraphs.

The main consequence of $\hat{U}$ is now evident [69]. In this representation, the symmetry in the exchange couplings is explicitly broken. These new local degrees of freedom (dressed by $\hat{U}$) have a different energy level structure than the original ones. There are four local states (see Fig. 5.6) to consider: (i) The state $(|\uparrow\uparrow\rangle - |\downarrow\downarrow\rangle)/\sqrt{2}$ decouples from the fermionic leads and therefore its energy is not changed by the transformation. (ii) The triplet state $(|\downarrow\uparrow\rangle + |\uparrow\downarrow\rangle)/\sqrt{2}$ has its energy raised by exchange anisotropy. (iii) Finally, the states $(|\uparrow\uparrow\rangle + |\downarrow\downarrow\rangle)/\sqrt{2}$ and $(|\uparrow\downarrow\rangle - |\downarrow\uparrow\rangle)/\sqrt{2}$ have their energy reduced. They are exactly degenerate at the critical coupling $K = K_c$; the value of K_c for which this occurs depends, of course, on the value of J.

At the critical $K = K_c(J)$ Eq. (5.12) can be projected onto the Hilbert space of these two lowest energy states through a Schrieffer-Wolff transformation. First, a new set of local fermionic operators is defined,

$$\begin{aligned} d^{\dagger}d|\Omega\rangle = 0 \;\rightarrow\; |\Omega\rangle = (|\uparrow\uparrow\rangle + |\downarrow\downarrow\rangle)/\sqrt{2}, \\ d^{\dagger}d|\Omega'\rangle = |\Omega'\rangle \;\rightarrow\; |\Omega'\rangle = (|\uparrow\downarrow\rangle - |\downarrow\uparrow\rangle)/\sqrt{2}. \end{aligned} \tag{5.13}$$

A key aspect of the physics at the IFP's is the degeneracy in the dots between the two dressed spin states $|0\rangle \equiv (|\uparrow\uparrow\rangle + |\downarrow\downarrow\rangle)/\sqrt{2}$ and $|1\rangle \equiv (|\uparrow\downarrow\rangle - |\downarrow\uparrow\rangle)/\sqrt{2}$ that leads

to an effective Kondo problem with Kondo temperature $\tilde{T}_K$ [69]. We also rotate the refermionize operator $\tilde{\psi}_\beta(x) = \psi_\beta(x) e^{-i\pi d^\dagger d}$ to ensure the anti-commutation relations. Projecting onto this low-energy two-dimensional subspace yields

$$H_1 = \sum_{\beta=\{c,s,sf,cf,\varphi\}} H^0_\beta + \tilde{J}[\tilde{\psi}_{sf}(0) - \tilde{\psi}^\dagger_{sf}(0)](d + d^\dagger) - (K - K_c) d^\dagger d, \tag{5.14}$$

where

$$\tilde{J} = \frac{J}{\sqrt{2\pi\alpha}} \left[1 + \frac{J}{4\pi\alpha(K_c + \tilde{T}_K)} \right]. \tag{5.15}$$

To validate the Schrieffer-Wolff transformation above, $K - K_c \ll \tilde{J}$ must be satisfied such that those two ground states are approximately degenerate. $\tilde{T}_K$ here is the Kondo temperature that results from the leads screening the doublet described by

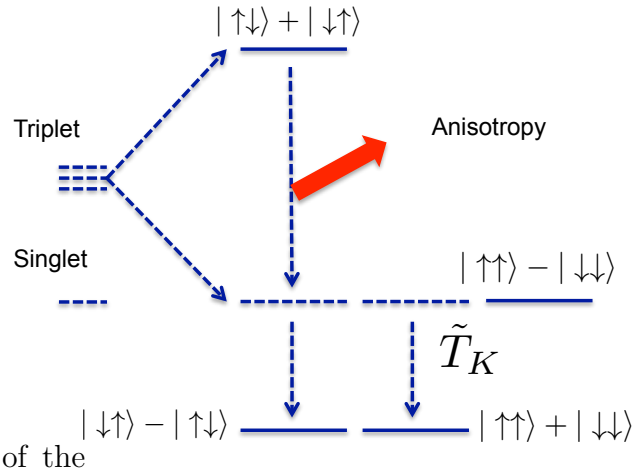

FIGURE 5.5: Low energy states of the system. One of the four states, $|\uparrow\downarrow\rangle + |\uparrow\downarrow\rangle$, is lifted due to the anisotropy of K^z and another state, $|\uparrow\uparrow\rangle - |\downarrow\downarrow\rangle$, has higher energy due to its decoupling in Eq. (5.12). The remaining doublet forms a two-dimensional low-energy space onto which we project via a Schrieffer-Wolff transformation.

d and $d^\dagger$. The $d^\dagger d$ term of Eq. (5.14) is a relevant perturbation (since it breaks the degeneracy between the two states of Fig. 5.6). Hence, for $K \neq K_c$ the system is driven away from the two-impurity Kondo fixed point.

Here we assume that $J \gg K - K_c$ such that the system flows to a fixed point with strong Kondo coupling J first. At that point, the Majorana branch $i[\tilde{\psi}_{sf}(0) - \tilde{\psi}^\dagger_{sf}(0)]$ absorbs the impurity Majorana fermion $d + d^\dagger$ and changes its boundary condition. If $K = K_c$, the other impurity Majorana fermion $i(d - d^\dagger)$ becomes totally decoupled so that the impurity entropy of the intermediate fixed point is $\ln\sqrt{2}$, larger than that of either the Kondo or local singlet fixed point (with zero entropy since they are Fermi liquid). From g-theorem, the intermediate fixed point is thus an unstable critical point.

On the other hand, if $K - K_c \neq 0$, after the absorption of the impurity Majorana fermion, the detuning part becomes $(K - K_c)[\tilde{\psi}_{sf}(0) - \tilde{\psi}^\dagger_{sf}(0)](d - d^\dagger)$, which is a relevant operator with scaling dimension 1/2. Consequently, the detuning will increase near the critical point and result into a quantum phase transition.

However, in an experimentally accessible two impurity Kondo model, the Hamiltonian contains another part that transports electrons between left and right leads. Here we begin with the dissipation free situation with the charge transport Hamiltonian

$$
\begin{aligned}
H_{LR} &= V_{LR}\Big\{[\psi^\dagger_{cf}(0) + \psi_{cf}(0)](-S^-_L S^z_R + S^z_L S^-_R - S^+_L S^z_R + S^z_L S^+_R) && \text{(5.16a)}\\
&\quad + [\psi^\dagger_{cf}(0)\psi^\dagger_{sf}(0) - \psi^\dagger_{sf}(0)\psi_{cf}(0)]S^-_L S^+_R + \text{h.c.} && \text{(5.16b)}\\
&\quad + [\psi_{sf}(0) - \psi^\dagger_{sf}(0)][\psi_{cf}(0) + \psi^\dagger_{cf}(0)]S^z_L S^z_R\Big\}, && \text{(5.16c)}
\end{aligned}
$$

where $V_{LR} \sim t_L t_R V/U^2$ is the tunneling strength that is much smaller compared with the Kondo and exchange couplings. Following the same steps we take onto the

other part of the Hamiltonian, near the critical point the charge transport becomes

$$H_{LR} = 2\tilde{V}_{LR}\frac{F_{cf}}{\sqrt{2\pi\alpha}}\cos[\phi_{cf}(0)](d - d^{\dagger}), \tag{5.17}$$

where

$$\tilde{V}_{LR} = V_{LR}\left[1 + \frac{J^2}{8(K_c + \tilde{T}_k)^2(2\pi\alpha)^{5/2}}\right] \tag{5.18}$$

is the dressed tunneling strength. Compared with Eq. (5.14), we see that effectively charge transport couples to the decoupled impurity Majorana fermion at the critical point and has scaling dimension 1/2. Consequently it grows with RG flow and finally hybridizes the critical impurity Majorana fermion so that the final intermediate fixed point has zero impurity entropy, the same as that of the Kondo and the local singlet fixed points. The quantum phase transition then transforms into a crossover instead.

Finally, we are ready to study the dissipation involved effective Hamiltonian. The dissipative bosonic fields can be further untangled by performing a rotation that combines the field representing charge transfer between the leads, ϕ_{cf}, with the environmental noise, φ: $\tilde{\phi}_{cf} \equiv (\phi_{cf} + \sqrt{2r}\,\varphi)/\sqrt{1+2r}$ and $\tilde{\varphi} \equiv (\sqrt{2r}\,\phi_{cf} - \varphi)/\sqrt{1+2r}$. At high temperature, Kondo couplings are weak where system symmetries are explicitly shown by defining six Majorana fermionic fields [170; 128; 127] with Ramond boundary conditions, $\chi_{\beta}^{1,2}(0^+) = \chi_{\beta}^{1,2}(0^-)$: $\chi^{(1)}_{\beta=\{c,s,sf\}}(x) = \frac{F_\beta}{\sqrt{\pi\alpha}}\sin[\phi_\beta(x)]$ and $\chi^{(2)}_{\beta=\{c,s,sf\}}(x) = \frac{F_\beta}{\sqrt{\pi\alpha}}\cos[\phi_\beta(x)]$. Because the boundary interaction $2i\tilde{J}\chi^{(1)}_{sf}(0)a$ has scaling dimension 1/2 (a is an impurity operator), $\tilde{J}$ flows to strong coupling [170; 128]. $\chi^{(1)}_{sf}$ then incorporates a and can be expressed as a simple change of boundary condition from Ramond to Neveu-Schwarz: $\chi^{(1)}_{sf}(0^+) = -\chi^{(1)}_{sf}(0^-)$ [127].

The effective IFP Hamiltonian can, thus, be written in terms of six free Majorana fields—five with Ramond and one with Neveu-Schwarz boundary condition—one free

bosonic field ($\tilde{\varphi}$), and a boundary sine-Gordon model for $\tilde{\phi}_{cf}$:

$$\begin{aligned} H_{\rm IFP} &= \sum_{j=1}^{5}\int\frac{dx}{2}\chi_j(x)i\partial_x\chi_j(x) + \int\frac{dx}{2}\chi_{sf}^{(1)}(x)i\partial_x\chi_{sf}^{(1)}(x) \\ &+ \int\frac{dx}{4\pi}[\partial_x\tilde{\varphi}(x)]^2 + \int\frac{dx}{4\pi}[\partial_x\tilde{\phi}_{cf}(x)]^2 \\ &+ 2i\,\tilde{V}_{LR}\frac{F_{cf}}{\sqrt{\pi\alpha}}\cos\Big[\sqrt{1+2r}\,\tilde{\phi}_{cf}(0)\Big]\,b. \end{aligned} \tag{5.19}$$

This Hamiltonian has an inherent $SO(5)\times U(1)$ symmetry from the five Majorana fields and the dressed dissipation field $\tilde{\varphi}$. With regard to the dot degrees of freedom, while Majorana mode a is effectively incorporated into the leads, mode b is coupled to the charge transport. For the two-impurity Kondo model, $\tilde{V}_{LR}=0$ and b is a decoupled Majorana zero mode.

5.7 Dependence of IFP on Dissipation

The boundary sine-Gordon model, which is the last element in Eq. (5.19), is well known to have a quantum phase transition [77; 3; 74] as the parameter in the boundary term varies, in our case r. The simplest description of this transition is via the scaling equation, $\frac{d\tilde{V}_{LR}}{d\ell} = \Big(\frac{1}{2}-r\Big)\tilde{V}_{LR}$, which results from noticing that the scaling dimension of the operator $\cos[\sqrt{1+2r}\,\tilde{\phi}_{cf}(0)]$ is $(1+2r)/2$ [74]. There are three distinct scaling behaviors depending on the value of r.

For *weak* dissipation, $r<1/2$, $\tilde{V}_{LR}$ grows. As in the $r=0$ case [170; 128], the cosine gets pinned at a particular value. The fixed point Hamiltonian is obtained by changing the boundary condition on $\tilde{\phi}_{cf}$ at $x=0$ from Dirichlet [for open boundary conditions on the fermionic fields in Eq. (5.3)] to Neumann [3]. IFP_2 is the corresponding fixed point; it develops from the $\delta=\pi/4$ Fermi-liquid fixed point [170] of the dissipationless case.

The leading irrelevant operator at IFP_2 is, because of the change in boundary condition, simply the dual of the relevant operator at IFP_1 that causes $\tilde{V}_{LR}$ to grow [74; 180]. Its scaling dimension is $2/(1+2r)$—the inverse of that of the cosine operator above. The temperature dependence of the conductance is therefore expected to be

$$G \sim G_0\big[1 - \gamma T^{2(1-2r)/(1+2r)}\big] \qquad (\text{at } \mathrm{IFP}_2) \tag{5.20}$$

with γ a non-universal constant. We see that modification of the boundary interaction by dissipation introduces a Luttinger-liquid-like character. In addition to the conductance, the non-Fermi liquid nature of this fixed point is also manifest in its residual boundary entropy, which can be shown to be $\ln g_{\mathrm{IFP}_2} = \frac{1}{4}\ln(1+2r)$ [183; 149].

The break down of scaling (i.e. when $\tilde{V}_{LR}$ becomes of order one) defines the crossover temperature, $T^{LR}_{\mathrm{noise}} \approx T_K \left(\tilde{V}^0_{LR}\right)^{2/(1-2r)}$, in terms of the initial value of tunneling from left to right, $\tilde{V}^0_{LR}$. For higher temperatures, $T^{LR}_{\mathrm{noise}} < T < T_K$, the physics is controlled by the $\tilde{V}_{LR} = 0$ fixed point, IFP_1, as $\tilde{V}_{LR}$ is initially small. For lower temperatures, $T < T^{LR}_{\mathrm{noise}}$, the physics is controlled by IFP_2.

To study the effect of deviations of the antiferromagnetic coupling K from K_c, we follow the discussion in Refs. [128; 129] and define the crossover temperature $T_{\delta K} = a(K - K_c)^2/T_K$, where a is a dimensionless constant. If $T^{LR}_{\mathrm{noise}} < T_{\delta K}$, the low energy physics will be governed by the KFP or LSFP. However, for $T_{\delta K} < T^{LR}_{\mathrm{noise}}$ an experiment would initially observe a rise in the conductance due to proximity to IFP_2 before the crossover to the Kondo or local-singlet physics took over (for which $G \to 0$). Using the remarkable tunability of quantum dots, access to the regime $T_{\delta K} \ll T^{LR}_{\mathrm{noise}}$ is possible, in which case the power law approach of the conductance to the quantum limit G_0, given above, should be observable. As has been introduced a lot in previous sections, this parameter sensitive conductance becomes a signature in the detecting of boundary QPTs, which has recently been realized in a single dissipative quantum

dot [134; 135].

In sharp contrast, for *strong* dissipation, $r > 1/2$, $\tilde{V}_{LR}$ shrinks, and the properties of the system are controlled by IFP_1. The boundary condition on the field $\tilde{\phi}_{cf}$ remains the Dirichlet condition. The scaling dimension of the boundary sine-Gordon term implies that the conductance decreases at low temperature according to [103; 149]

$$G \sim T^{2r-1} \qquad (\text{at } \mathrm{IFP}_1). \tag{5.21}$$

The non-Fermi liquid nature of this fixed point is further shown by the residual boundary entropy, $\ln g_{\mathrm{IFP}_1} = \frac{1}{4}\ln[4/(1+2r)]$ [183; 149], and by the decoupling of the b Majorana in the dots as the last term in Eq. (5.19) flows to zero.

IFP_1 evolves from the intermediate fixed point of the two-impurity Kondo model ($r = 0$). Formally, however, IFP_1 is a distinct fixed point—the residual boundary entropy, for instance, depends on r. Nevertheless, for reasonable values of $r \sim 1/2$, this system can emulate the physics of the two-impurity Kondo model: the $SO(7)$ symmetry manifest in the Majorana fields [127; 128], for instance, is restored asymptotically. Any observable not directly related to charge transfer between the leads, such as the magnetic susceptibility, will have the same behavior in the two models.

The crossover temperature to the KFP or LSFP, $T_{\delta K}$, is given by the same expression as in the weak noise case. Thus, for $T_{\delta K} < T < T_K$ the physics of IFP_1, bearing strong resemblance to that of the two-impurity Kondo model, will be experimentally accessible.

Finally, the *borderline* $r = 1/2$ case is particularly interesting. The cosine in Eq. (5.19) is exactly marginal [27], corresponding to an $SU(2)$ chiral symmetry. Hence, we can replace the cosine by the Abelian chiral current $\partial_x \tilde{\phi}_{cf}$ [3]. The model becomes quadratic and the conductance can be calculated exactly [104; 74]—G depends on the initial value $\tilde{V}^0_{LR}$ and so is not universal. The exactly marginal operator creates a line of fixed points connecting IFP_1 to IFP_2, all with residual boundary

entropy $\frac{1}{4}\ln 2$. The line is unstable to deviations from the critical coupling K_c; as in the previous cases, $T < T_{\delta K}$ leads to flow toward the KFP or LSFP. Even at K_c, corrections to the effective Hamiltonian (5.19) will presumably cause flow away from this line at the lowest temperatures (which we have not analyzed); however, because their initial strength is very small, the cross-over temperature T^* to see these effects will be very low. Thus, in a wide range of temperatures, $T^* < T < T_K$, the properties of the line of fixed points could be seen experimentally, varying V_{LR}^0 to move among them.

5.8 Conclusion

We have presented an example in which the introduction of a quantum environment reveals a quantum phase transition previously hidden under a crossover: *the quantum noise has rescued the quantum phase transition.* There are two quantum critical points (Fig. 5.4): one dominant for weak dissipation (IFP_2, $r < 1/2$) and the other at strong dissipation (IFP_1, $r > 1/2$)—this latter fixed point is similar to that of the two-impurity Kondo model.

A broader view is obtained by connecting to the idea of "quantum frustration of decoherence" of a qubit [32; 146]: a quantum system acted upon by *two* processes that are at cross purposes may retain more coherence than if acted upon by just one. The quantum system to be protected here is the non-Fermi-liquid quantum critical state delicately balanced between the KFP and LSFP, a striking signature of which is the decoupled, and so completely coherent, Majorana mode. Charge transfer between the electron reservoirs associated with the leads is the first process acting on the system, one that completely destroys the delicate quantum state and the coherence of the Majorana mode. Adding the quantum noise produced by the resistive EM environment impedes the deleterious effect of the first process, rendering the coherent Majorana zero mode again manifest at IFP_1.

This quantum critical state is highly non-trivial and clearly unstable toward the KFP and LSFP, but it has experimental consequences in a wide temperature range. We emphasize that measurements of the conductance near IFP_1 and IFP_2 are experimentally feasible at this time—similar amounts of tuning have been used successfully, for instance, in recent experiments [134; 135]. An experimental study along these lines would directly contradict the general notion that more noise leads inevitably to less quantum many-body behavior.

6

Universal Nonequilibirum I-V Curve at an Interacting Impurity Quantum Critical Point

Nonequilibrium properties of correlated quantum matter are being intensively investigated because of the rich interplay between the nonequilibrium drive and the many-body correlations. Of particular interest is the behavior at a quantum critical point (QCP) when a system is delicately balanced between different possible ground states; accessing such a point, however, is typically out of reach theoretically. Here, we provide an analytical calculation of the I-V curve at a QCP under nonequilibrium conditions and, furthermore, present experimental results to which the theory is compared. The system is a quantum dot coupled to resistive leads: a spinless resonant level interacting with an ohmic electromagnetic environment. A two channel Kondo QCP occurs when the level is on resonance and symmetrically coupled to the leads. Using a bosonized representation, we calculate the nonlinear I-V curve at this QCP. We then show that it has a physically intuitive interpretation in terms of weak backscattering of non-interacting fermions coupled to a modified environment, thus arriving at the same I-V through dynamical Coulomb blockade theory. The quan-

titative agreement between our theoretical and experimental results, with no fitting parameter, is remarkable. As our system is fully accessible to both theory and experiment, it provides an ideal setting for addressing non-equilibrium phenomena in correlated quantum matter[1].

[1] Part of the text of this chapter has been adapted from the following arXiv article: Gu Zhang, Chung-Hou Chung, Chung-Ting Ke, Chao-Yun Lin, Henok Mebrahtu, Alex I. Smirnov, Gleb Finkelstein and Harold U. Baranger, "Universal Nonequilibrium I-V Curve at an Interacting Impurity Quantum Critical Point", arXiv: 1609.04765v2

6.1 Introduction

As introduced in Section 4.2, a boundary QPT exists in a dissipative spinless resonant level model. This QPT is second order in the sense that it hosts a quantum critical regime as in Fig. 6.1. The presence of the quantum critical regime distinguishes two physically distinct paths when the system approaches zero temperature: by tuning to the QCP, the system stays in the critical region down to zero temperature (path 1 in Fig. 6.1). In contrast, detuning results in a crossover from quantum critical behavior to one of the trivial phases (path 2). Along path 1 (i.e., at the QCP), it is well established that thermodynamic observables at finite temperature show universal scaling.

Although interplay between nonequilibrium and many-body effects has been studied in a variety of nanosystems through nonlinear I-V characteristics, both experimentally [34; 76; 35; 138; 131; 157; 111; 133; 98; 56] and theoretically [137; 55; 166; 125; 160; 81; 38; 39; 162; 108; 151; 41; 79; 51; 11; 169; 168; 139], to our knowledge, the nonequilibrium I-V curve of a system tuned to its QCP (path 1) has not been theoretically calculated beyond the powerlaw scalings. The lack of the theoretical result is partially related to the difficulty in the experimental realization of the current measurement along path 1 —- to date, except for the spectroscopy measurements, we are only aware of the work done in Professor Gleb Finkelstein's group that fully measures the nonequilibrium I-V curve in at the QCP of the spinless resonant level model [134; 135]. As discussed in Section 4.2, the spinless resonant level model thus provides us a great chance to study the QCP of a boundary QPT whose critical features are experimentally accessible.

In this chapter, we thus present an analytical calculation of the nonequilibrium I-V curve in the quantum critical region of a QCP (path 1 in Fig. 6.1) and compare our results with the experimental data in detail. The system is a spin-polarized

carbon nanotube quantum dot connected to resistive leads via tunable tunnel barriers (Fig. 6.1). The resistive leads create an ohmic electromagnetic (EM) environment [21; 134; 135], and the quantum dot serves as the quantum impurity. The theoretical study of the crossover regime (path 2 in Fig. 6.1) will be presented in Chapter 7.

As introduced in Section 4.2, in spinless resonant level model, QCP occurs at the perfect symmetric point where (i) a level in the dot is resonant with the leads and (ii) the dot is symmetrically coupled to them. At the QCP, the conductance through the dot at zero temperature becomes perfect (e^2/h when $T \to 0$), while otherwise it tends to zero. The QCP is experimentally shown to be *two-channel Kondo* type [134], which will also be theoretically further investigated in Chapter 7.

The plan and main results of the paper are as follows. We start by defining our model for the dissipative resonant-level problem (Sec. 6.2) and then immediately bosonize it (Sec. 6.3). In Sec. 6.4 we carry out the key step of obtaining the effective

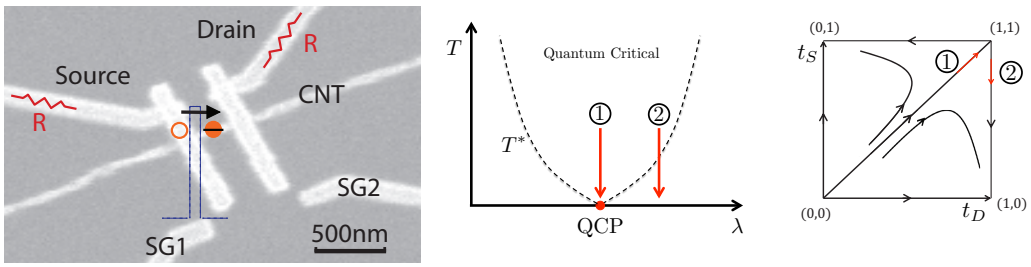

(a) (b) (c)

FIGURE 6.1: (a) Schematic of the system overlaid on a SEM image of the sample measured. A quantum dot is formed in the carbon nanotube (CNT) segment between the source and drain leads. These resistive leads create a dissipative EM environment for electrons tunneling through the dot. The tunneling barriers can be tuned with the side gates SG1 and SG2. Applying a bias between the source and drain produces a nonequilibrium steady state. (b) Diagram of the quantum critical region. When tuned to the QCP, the quantum critical region extends down to zero temperature (path 1), otherwise a crossover to one of the trivial ground states occurs (path 2). In this work, we study path 1. (c) The RG flow of source and drain coupling (t_S, t_D) when the system is on resonance. For symmetric coupling, the flow is into the strong coupling fixed point (1,1) (path 1) corresponding to the QCP. A slight detuning leads to a crossover to a trivial fixed point (path 2).

Hamiltonian at strong tunneling, Eq. (6.21). This then is the model of the QCP.

Resonant tunneling in a Luttinger liquid (LL) provides considerable theoretical guidance in Secs. 6.3 and 6.4 because tunneling in an EM environment is an emulation of that system [132; 60; 164; 163; 117; 134; 135; 98]. In equilibrium, resonant peaks of perfect conductance in a LL have been studied extensively [103; 102; 52; 68; 66; 188; 153; 109; 136; 75], and this system has a similar two-channel Kondo QCP, separating single-barrier (left or right) dominated weak-tunneling regimes [52; 109]. However, there are significant differences in the strong-coupling model, and nonequilibrium properties at the LL resonant tunneling QCP have been studied only in the scaling regime (see e.g. [103; 52]).

In Sec. 6.5, we find the I-V characteristics in the quantum critical regime beyond simple scaling. We start from a Keldysh approach which immediately reduces to finding backscattering rates from the golden rule. As introduced in Section 2.3.4, this simplification is possible because we work to second order in the backscattering amplitude (but to all orders in the coupling to the environment). The main theoretical result of the paper is the analytical expression for the nonlinear I-V curve at finite temperature, Eq. (6.27).

Experimental results are presented in Sec. 6.6 and compared with the theory. In particular, Fig. 6.2 shows excellent agreement between theory and experiment.

Before concluding, we then show in Sec. 6.7 that this result has a simple physical interpretation, one that is not available in the corresponding LL problem. Here, modes that initially do not couple to the environment map to *non-interacting* left-moving and right-moving fermions. Indeed, at the QCP the natural degrees of freedom are right-moving and left-moving fermionic channels between which there is weak tunneling in a modified environment. In this form, dynamical Coulomb blockade theory [92; 187; 50] yields the same expression for the I-V curve.

Finally, we end this chapter with the conclusion in Section 6.8.

6.2 Model and Hamiltonian

Our system is shown in Fig. 6.1: a spinless resonant level between two resistive leads. As introduced in Section 4.2, Hamiltonian in the weak-tunneling regime consists of several parts,

$$H = H_{\rm Dot} + H_{\rm Leads} + H_{\mu} + H_{\rm T} + H_{\rm Env}. \tag{6.1}$$

$H_{\rm Dot} = \epsilon_{\rm d} d^{\dagger} d$ models the dot with single energy level $\epsilon_{\rm d}$, which may be tuned by the backgate voltage $V_{\rm gate}$.

$$H_{\rm Leads} = \sum_{\alpha={\rm S,D}} \sum_{k} \epsilon_k c^{\dagger}_{k\alpha} c_{k\alpha} \tag{6.2}$$

represents the electrons in the source (S) and drain (D) leads, and

$$H_{\mu} = \sum_{\alpha={\rm S,D}} \sum_{k} \mu_{\alpha} c^{\dagger}_{k\alpha} c_{k\alpha} \tag{6.3}$$

is the chemical potential term driving the system out of equilibrium through the applied bias V, $\mu_{S/D} = \pm V/2$.

As introduced by Eq. (4.3), the dissipation-involved tunneling Hamiltonian contains extra dynamical phases $\varphi_{S,D}$ to model the dissipative modes

$$H_{\rm T} = \sum_{k} \left(t_S c^{\dagger}_{kS} e^{-i\sqrt{\frac{\pi}{2}}\varphi} d + t_D c^{\dagger}_{kD} e^{i\sqrt{\frac{\pi}{2}}\varphi} d + {\rm h.c.} \right), \tag{6.4}$$

where $\varphi = \varphi_S - \varphi_D$. Because of the sum over momentum, only the fields at $x = 0$ couple to the dot and environment.

As introduced in Section 4.2, dissipative phase dynamics is modeled by the long time correlator Eq. (4.4). In this chapter, for later convenience, we further extend the 0d dissipative phase into a 1d effective Luttinger liquid model, with bosonic fields $\varphi(x)$ and its conjugate $\vartheta(x)$. More specifically, the dissipative phase is now depicted

by the Hamiltonian

$$H_{\rm Env} = \frac{1}{2}\int_0^\infty dx\, \left[\frac{1}{2r}(\partial_x\varphi)^2 + 2r(\partial_x\vartheta)^2\right], \tag{6.5}$$

which is coupled to the junction by identifying $\varphi(x=0)$ as the phase φ in Eq. (6.4). The interaction parameter r should yield the correct correlation functions for φ, thus $r \equiv Re^2/h$.

6.3 Bosonization at weak coupling

Our strategy is to develop a bosonized form of the weak-coupling Hamiltonian. Bosonization is possible because an impurity couples to only an effectively one-dimensional (1D) subset of lead states. We label these semi-infinite 1D leads $x \in (-\infty, 0)$ for S and $(0, +\infty)$ for D (and set their Fermi velocities equal to one).

We bosonize in the standard way [71; 103], choosing the conventions of Ref. [103] [2]:

$$c^\dagger_{\alpha,L/R}(x,t) = e^{\pm ik_F x}\frac{F_\alpha}{\sqrt{2\pi a_0}}e^{i\sqrt{\pi}[\phi_\alpha(x,t)\pm\theta_\alpha(x,t)]} \tag{6.6}$$

where $\alpha = S/D$ and L/R indicates left- or right-moving particles. ϕ_α and θ_α are conjugate bosonic fields that describe electronic states in the semi-infinite leads, a_0 is a short time cutoff, and F_α are Klein factors. In bosonic form $\rho_{L/R}(x) = [\pm\partial_x\phi(x) + \partial_x\theta(x) + k_F/\sqrt{\pi}]/(2\sqrt{\pi})$ is the electron density. It is convenient to form the the charge and flavor fields [55],

$$\begin{aligned}\phi_{f/c}(x) &\equiv \tfrac{1}{2}\left[\phi_S(-x) \mp \phi_D(x) \pm \theta_S(-x) - \theta_D(x)\right]\\ \theta_{c/f}(x) &\equiv \tfrac{1}{2}\left[\pm\phi_S(-x) + \phi_D(x) + \theta_S(-x) \pm \theta_D(x)\right].\end{aligned} \tag{6.7}$$

[2] Notice that here we are using the canonical bosonization formula instead of the chiral ones in Eq. 4.26 (and will be used in Chapter 7). The reason is that in this chapter we want to derive the leading irrelevant operator at the strong coupling fixed point by checking the leading relevant operator at the weak coupling fixed point. Those two fixed points are connected through the dual transformation $\phi \to \theta$ between two canonical fields. Using the canonical bosonization thus grants us an alternative option in the understanding of the physics.

Note that $\phi_f(x)$ is conjugate to $\theta_c(x)$ and likewise $\phi_c(x)$ to $\theta_f(x)$.

The voltage bias in H_μ is handled using a time-dependent gauge transformation [92; 103] that moves the bias to the tunneling term—physically, when an electron hops from a lead to the dot it acquires a phase factor corresponding to the drop in bias (change in energy) across that barrier. Since the QCP occurs at symmetric coupling, we take identical coupling to the source and drain leads, $t_S = t_D \equiv t$. With symmetric tunneling and capacitance, the bias voltage drops symmetrically as well. The tunneling term is, then,

$$\begin{aligned} H_{\mathrm{T}+\mu} = \frac{t}{\sqrt{2\pi a_0}} \Big[& F_S d e^{i\sqrt{\pi}\phi_c} e^{i\left(\sqrt{\pi}\phi_f - \sqrt{\frac{\pi}{2}}\varphi + eVt/2\right)} \\ & + F_D d e^{i\sqrt{\pi}\phi_c} e^{-i\left(\sqrt{\pi}\phi_f - \sqrt{\frac{\pi}{2}}\varphi + eVt/2\right)} + \mathrm{h.c.} \Big]. \end{aligned} \tag{6.8}$$

All fields in Eq. (6.8) are taken at $x=0$, and we have used $\theta_{S/D}(0)=0$ [103; 85] due to the Dirichlet boundary condition.

Notice that the fields $\phi_f(x=0)$ and φ enter in the same way in Eq. (6.8), so it is natural to combine them via

$$\begin{aligned} \phi_f'(x) &= \phi_f(x) - \frac{1}{\sqrt{2}}\varphi(x) \\ \varphi'(x) &= \sqrt{r}\phi_f(x) + \frac{1}{\sqrt{2r}}\varphi(x). \end{aligned} \tag{6.9}$$

Since the field φ' completely decouples from the problem, we drop it from further consideration. The final expression for the Hamiltonian at weak coupling is

$$\begin{aligned} H^{\mathrm{eff}}_{\mathrm{Leads+Env}} + H_{\mathrm{Dot}} &= \frac{1}{2}\int_0^\infty dx \Big[(\partial_x\theta_f)^2 + (\partial_x\phi_c)^2 + (1+r)(\partial_x\theta_c')^2 + \frac{1}{1+r}(\partial_x\phi_f')^2 \Big] + \epsilon_{\mathrm{d}} d^\dagger d \\ H_{\mathrm{T}+\mu} &= \frac{t}{\sqrt{2\pi a_0}} \Big\{ F_S d e^{i\sqrt{\pi}\phi_c} e^{i(\sqrt{\pi}\phi_f' + eVt/2)} + F_D d e^{i\sqrt{\pi}\phi_c} e^{-i(\sqrt{\pi}\phi_f' + eVt/2)} + \mathrm{h.c.} \Big\}. \end{aligned} \tag{6.10}$$

Thus we see that the coupling of each tunneling electron to the environment generates an effective interaction between them. Here, *one* of the sets of lead fields, (ϕ'_f, θ'_c), becomes interacting; in contrast, in a Luttinger liquid, *both* sets of lead fields would be interacting, an important distinction when we come to interpreting our results (see Sec. 6.7).

As introduced in Section 4.2, the dissipative resonant level model is symmetry-sensitive: the zero conductance is e^2/h when the system is perfect symmetric and vanishes to zero with any asymmetry present. In this chapter we only consider the perfect symmetric case so that the system flows towards the strong coupling fixed.

6.4 The strong tunneling limit: Link to a weak double barrier

As the system scales to strong coupling, it approaches a fixed point at which the system is translationally invariant and so fully transparent. The properties of this fixed point are heavily constrained by its being one of the two possible boundary fixed points in the corresponding conformal field theory (the "periodic" fixed point) [183]. Because of this constraint, the strong coupling fixed point in our dissipative resonant level model is the same as in the Luttinger liquid case [103; 102; 52; 68]; indeed, the effect of the total charge field (ϕ_c, θ_f) (which are interacting in a Luttinger liquid but non-interacting here) scales to zero at the fixed point. Furthermore, any model that scales to the strong coupling point can be used to deduce the properties near that point. In particular, a wire with two weak potential barriers is a good model for the residual effect of the quantum dot [103; 102; 153].

For an explicit description of the strong tunneling limit that allows calculation of the I-V curve, we therefore start with two symmetric δ-function barriers spaced by ℓ in a 1D wire of fermions denoted $\psi_R(x)$ and $\psi_L(x)$ for left and right movers. The fermions are then described via bosonization by the canonical bosonic fields θ and ϕ [103]. For the moment the fields are non-interacting; we add the effect of the

environment and the bias in a second stage. The Hamiltonian is $H_0 + H_T$ where

$$H_0 = \int_{-\infty}^{\infty} dx[(\partial_x\theta)^2 + (\partial_x\phi)^2], \tag{6.11a}$$

$$H_{\rm T} = A\sum_{\pm}\cos[2\sqrt{\pi}\theta(\pm\ell/2) \pm k_F\ell]. \tag{6.11b}$$

The form $\cos[2\sqrt{\pi}\theta]$ appears because it corresponds to $2k_F$ backscattering of the underlying fermions [103], $\psi_R^\dagger\psi_L + \text{h.c.}$, as can be checked by using the bosonization relation Eq. (6.6) for $\psi_{L,R}$ to refermionize this term. This is, of course, the expected effect of scattering from a potential barrier.

As in the weak barrier case, it is convenient to form the sum and difference fields

$$\theta_c \equiv [\theta(\ell/2) + \theta(-\ell/2)]/2 \text{ and } \theta_f \equiv [\theta(\ell/2) - \theta(-\ell/2)]/2. \tag{6.12}$$

(In contrast to the weak-tunneling case, the ϕ fields now have Dirichlet boundary conditions, becoming discretized constants at strong coupling [103; 85], and so do not appear in the expressions for θ_c and θ_f here.) When on resonance for a single level, one has $k_F\ell = \pi/2$ at strong coupling [71], so that the barrier terms become

$$H_{\rm T} = A\cos(2\sqrt{\pi}\theta_c)\sin(2\sqrt{\pi}\theta_f). \tag{6.13}$$

We now incorporate the external bias potential V and the fluctuating potential caused by the environmental field φ. The environmental potential fluctuations are given by $\sqrt{2\pi}\dot{\varphi}$ which in a Hamiltonian formulation corresponds to $ir2\sqrt{2\pi}\partial_x\vartheta(0)$, where $\partial_x\vartheta(0)$ appears naturally as the charge fluctuation operator conjugate to φ [see Eq. (6.5)]. Though at weak coupling this potential difference is applied between the source and drain contacts, Eq. (6.3), at strong coupling, in contrast, the potential is applied between the right-moving fermions (those coming from the source) and left-moving fermions (from the drain). Applying the potential in this way is commonly done, for instance, in discussing the quantum Hall effect [91]. Thus, in terms of the

strong coupling fermions $\psi_R(x)$ and $\psi_L(x)$ the bias and environmental coupling are

$$\begin{aligned} H_{\mu+\mathrm{Env}} &= \frac{eV + ir2\sqrt{2\pi}\partial_x\vartheta(0)}{2}\Big[\int_{-\infty}^{-\ell/2} dx\, \psi_R^\dagger(x)\psi_R(x) - \int_{\ell/2}^{\infty} dx\, \psi_L^\dagger(x)\psi_L(x)\Big] \\ &= \frac{eV + ir2\sqrt{2\pi}\partial_x\vartheta(0)}{4}\frac{1}{\sqrt{\pi}}\Big[\int_{-\infty}^{-\ell/2} dx[\partial_x\theta(x) - \partial_x\phi(x)] \\ &\quad - \int_{\ell/2}^{\infty} dx[\partial_x\theta(x) + \partial_x\phi(x)]\Big] \\ &= -\left[\frac{eV}{4\sqrt{\pi}} + i2\sqrt{2}r\partial_x\vartheta(0)\right]\int_0^{\infty} dx\ \partial_x\theta_c(x). \end{aligned} \tag{6.14}$$

The dependence on bias, the first term in (6.14), is handled by performing a time-dependent gauge transformation that moves the bias into the barrier term H_T, as at weak coupling. Thus, in Eq. (6.13) $\cos(2\sqrt{\pi}\theta_c) \to \cos(2\sqrt{\pi}\theta_c + eVt)$. Since the right-moving particles (from the source) have chemical potential eV higher than that of the left-moving particles (from the drain), it is natural that the bias appears as a phase eVt in the backscattering operator.

We now integrate out the environmental degrees of freedom $\vartheta(x)$ and $\varphi(x)$. The bilinear coupling to the lead fermions, the second term in the last line of (6.14), then generates an effective coupling that causes $\theta_c(x)$ and $\phi_f(x)$ to be interacting fields. This integration process can be more easily done in the action form so we begin by rewriting the free lead and environment Hamiltonian in the form of an action,

$$\begin{aligned} S_0 &= S_{\mathrm{Leads}} + S_{\mathrm{Env}} \\ &= \frac{1}{2}\iint d\tau dx[(\partial_x\theta_c)^2 + (\partial_\tau\theta_c)^2 + (\partial_x\theta_f)^2 + (\partial_\tau\theta_f)^2] \\ &\quad + \frac{1}{2}\iint d\tau dx\ 2r\,[(\partial_x\vartheta)^2 + (\partial_\tau\vartheta)^2]. \end{aligned} \tag{6.15}$$

(We write the action in terms of the θ fields rather than the ϕ because of the boundary conditions connected to the very weak barrier.) Since the action is quadratic except

for the backscattering occurring at the origin, the $x \neq 0$ degrees of freedom can be integrated out. If the backscattering is not too strong, the free action is minimized when $\theta(x, \omega_n) = \theta(x = 0, \omega_n) \exp(-|\omega_n x|)$ and $\vartheta(x, \omega_n) = \vartheta(x = 0, \omega_n) \exp(-|\omega_n x|)$, where ω_n is the Matsubara frequency [103]. We can thus integrate out the $x \neq 0$ part of the system so that the free action becomes zero-dimensional,

$$S_0 = \frac{1}{\beta} \sum_{\omega_n} |\omega_n| [\theta_f(\omega_n)^2 + \theta_c(\omega_n)^2 + 2r\vartheta(\omega_n)^2], \tag{6.16}$$

where all the fields are evaluated at $x = 0$.

The coupling between the leads and the environment is given by the second term in Eq. (6.14), which in action form is

$$\begin{aligned} S_{\text{coup.}} &= -i2\sqrt{2} \int d\tau \, r \, [\partial_x \vartheta(0)] \, \theta_c(0) \\ &= i \frac{2\sqrt{2}\, r}{\beta} \sum_{\omega_n} |\omega_n| \vartheta(\omega_n) \theta_c(-\omega_n), \end{aligned} \tag{6.17}$$

rewritten in Matsubara summation form. Since this term is a quadratic product of ϑ and θ_c, we can easily integrate out the environment ϑ with a Gaussian path integral. The integral is done with the partition function,

$$Z = \iiint D[\theta_c] D[\theta_f] D[\vartheta] e^{-S_0[\theta_c, \theta_f, \vartheta] - S_{\text{coup.}}[\theta_c, \vartheta] - S_{\text{T}}[\theta_c, \theta_f]}, \tag{6.18}$$

after which the effective partition function becomes

$$Z^{\text{eff}} = \iint D[\theta_c] D[\theta_f] e^{-S'_{\text{Leads}} - S_{\text{T}}}, \tag{6.19}$$

where

$$\begin{aligned} S'_{\text{Leads}} = \frac{1}{2} \iint d\tau dx \, \big[&(\partial_x \theta_f)^2 + (\partial_\tau \theta_f)^2 \\ &+ (1 + r)(\partial_x \theta_c)^2 + (1 + r)(\partial_\tau \theta_c)^2 \big] . \end{aligned} \tag{6.20}$$

Here we have extended the fields back to their original semi-infinite domains. Notice that the interaction between dissipative environment and the θ_c field has been effectively incorporated into the free action of θ_c so that it becomes effectively interacting with strength $1/(1+r)$. Finally, we convert to the Hamiltonian form and, to be consistent with the notation of the main text, relabel (θ_c, ϕ_f) as (θ_c', ϕ_f'). The relabeling should also be carried out, of course, in the backscattering term, $H_{\rm T} \to A\cos(2\sqrt{\pi}\theta_c' + eVt)\sin(2\sqrt{\pi}\theta_f)$.

We thus arrive at our strong coupling effective Hamiltonian

$$
\begin{aligned}
H^{\rm eff} &= \frac{1}{2}\int_0^\infty dx\Big[(\partial_x\theta_f)^2 + (\partial_x\phi_c)^2 && \text{(6.21a)}\\
&+ (1+r)(\partial_x\theta_c')^2 + \frac{1}{1+r}(\partial_x\phi_f')^2\Big] && \text{(6.21b)}\\
&+ A\cos\left[2\sqrt{\pi}\theta_c'(0) + eVt\right]\sin\left[2\sqrt{\pi}\theta_f(0)\right]. && \text{(6.21c)}
\end{aligned}
$$

We emphasize that the modes represented by fields θ_f and ϕ_c are free while those represented by θ_c' and ϕ_f' are interacting [3]. The coupling between these two sets of modes is given by the barrier term, (6.21c), that describes the deviation from the uniform state characterizing the QCP. Recalling that a bosonic operator of the form $\cos(2\sqrt{\pi}\theta)$ corresponds to backscattering of the underlying fermions, we see that this coupling involves the *simultaneous* backscattering of both sets of modes. Note that the bias enters the backscattering of the interacting modes.

The strength of the barrier term, A, is not known microscopically as it is the result of the flow from weak to strong coupling. It is helpful to recall at this point the equilibrium flow to the strong coupling point. The equilibrium RG scaling equation

[3] The effect of the region $|x| < \ell/2$ of the original wire on the charge transport (backscattering and leads) is included here; typically, there are boundary degrees of freedom that become decoupled at the fixed point [52; 183].

for A coming from Eq. (6.21c) is

$$\frac{dA}{d\ln D} = \frac{1}{1+r}A, \tag{6.22}$$

where the energy cutoff D runs from $D_0 = 1$ down to 0. The scaling dimension of the backscattering operator is then $\Omega \equiv 1 + 1/(1+r)$, showing that the operator is irrelevant and $A \to 0$ at the QCP.

The linear response conductance at zero temperature is thus that of the system defined by Eqs. (6.21a)-(6.21b). By combining the charge and flavor fields, one clearly obtains a translationally invariant system [4], in which one therefore has perfect transmission and thus $G = e^2/h$ [134]. This is the same result as for resonant tunneling in a Luttinger liquid [103; 52]. To better illustrate their connection, consider the backscattering operator in resonant tunneling through a LL at zero bias [52], namely $\cos[2\sqrt{\pi}\theta'(0)]\partial_x\theta'(0)$, where $\theta'(x)$ is the interacting field describing the LL. Note in this regard that both the c and f modes are interacting in a LL and related to $\theta'(x)$. To arrive at this form from Eq. (6.21c), expand about the midpoint of the two barriers and call this point $x = 0$. Then from Eq. (6.12), $\theta'_c \approx \theta'(0)$ and $\theta'_f \approx \partial_x\theta'(0)\ell/2$. Since $\partial_x\theta'(0)\ell/2$ is small and fluctuating, the $\sin[2\sqrt{\pi}\theta_f(0)]$ factor is simply expanded to yield $\pi^{3/2}\partial_x\theta'(0)/2k_F$, where we have used $k_F\ell = \pi/2$ on resonance. Combining this with $\cos\theta'_c \approx \cos\theta'(0)$, we arrive at the expression above for backscattering from two barriers in a LL. We have thus proved the connection between the dissipative spinless resonant level model and the Luttinger liquid model at the strong coupling fixed point. From general considerations (see, e.g., [52]) one thus expects the low temperature or bias deviation from perfect transmission to be

[4] To explicitly obtain a translationally invariant system, first rescale θ'_c and ϕ'_f in Eq. (6.21b) so as to absorb the factors of $(1+r)^{\pm 1}$. Since there is no interaction, this can be done without any compensating change in other terms. Then combine the flavor and charge fields into fields defined for all x, e.g. $\theta'(x>0) = \theta'_c(x) + \theta_f(x)$, $\theta'(x<0) = \theta'_c(-x) - \theta_f(-x)$, and similarly for $\phi(x)$. The Hamiltonian now becomes $\int_{-\infty}^{\infty} dx[(\partial_x\theta')^2 + (\partial_x\phi')^2]$, which is manifestly translationally invariant.

a power law related to this scaling dimension, namely $|dI/dV - e^2/h| \propto T^{2/(1+r)}$ or $\propto V^{2/(1+r)}$.

6.5 The I-V curve

We now turn to an explicit calculation of the I-V curve: we find the correction to perfect transmission caused by the joint backscattering term Eq. (6.21c). We work to leading order in this term but keep all orders in the bosonic fields, and use a Keldysh approach to find the nonequilibrium current [80]. The fact that we work to only second order in A leads to a considerable simplification [121; 73]: a Keldysh calculation for scattering by a local operator to second order shows that the current is related to the backscattering rate $\Gamma(V,T)$, which in turn is given simply by a golden rule expression [121; 73]. The current is given by the difference between the forward and backward rates; consequently, the backscattering-related current is $\Delta I(V,T) = e[\Gamma(V,T) - \Gamma(-V,T)]$.

The backscattering matrix element needed is [164]

$$\langle f|H_{\mathrm{T}}|i\rangle = A\langle R_1^f|\cos[2\sqrt{\pi}\theta_c'(0)]|R_1^i\rangle \times \langle R_2^f|\sin[2\sqrt{\pi}\theta_f(0)]|R_2^i\rangle, \tag{6.23}$$

where $|R_1\rangle$ and $|R_2\rangle$ represent the states of θ_c' and θ_f, respectively, and i and f label the initial and final states. Recall that in time-dependent perturbation theory, an explicit oscillatory time dependence such as eVt in Eq. (6.21c) factors out and enters the energy conservation constraint. The rate is, then, given by

$$\begin{aligned}\Gamma(V,T) = A^2\frac{2\pi}{\hbar}\sum_{R_1^iR_1^f}\sum_{R_2^iR_2^f} &\times|\langle R_1^f|\cos\left[2\sqrt{\pi}\theta_c'(0)\right]|R_1^i\rangle|^2 P_\beta(R_1^i)\\ \times|\langle R_2^f|\sin\left[2\sqrt{\pi}\theta_f(0)\right]|R_2^i\rangle|^2 &P_\beta(R_2^i)\times\delta(E_{R_1^i}+E_{R_2^i}+eV-E_{R_1^f}-E_{R_2^f}),\end{aligned} \tag{6.24}$$

where $P_\beta(R_{1,2}^i) = \langle R_{1,2}^i|\rho_\beta|R_{1,2}^i\rangle$ refers to the density matrices of the fields and the subscript β is a reminder of the effect of temperature.

To evaluate the rate, first rewrite the δ-function as an integral over time of an exponential. Then, notice that the factors $\exp(iE_{i,f}t/\hbar)$ can be produced by acting on the initial or final state with $\exp(iHt/\hbar)$. Thus, changing to the Heisenberg picture for the fields and dropping the argument $x = 0$ for clarity, we find

$$\begin{aligned}\Gamma(V,T) = \frac{A^2}{\hbar^2}\int_{-\infty}^{\infty} dt \sum_{R_1^i R_1^f} &\langle R_1^i|\cos\left[2\sqrt{\pi}\theta_c'(t)\right]|R_1^f\rangle\langle R_1^f|\cos\left[2\sqrt{\pi}\theta_c'(t=0)\right]|R_1^i\rangle P_\beta(R_1^i) \\ \times \sum_{R_2^i R_2^f} &\langle R_2^i|\sin\left[2\sqrt{\pi}\theta_f(t)\right]|R_2^f\rangle\langle R_2^f|\sin\left[2\sqrt{\pi}\theta_f(t=0)\right]|R_2^i\rangle P_\beta(R_2^i) e^{ieVt/\hbar} \\ = \frac{A^2}{\hbar^2}\int_{-\infty}^{\infty} dt e^{ieVt/\hbar} &\left\langle\cos\left[2\sqrt{\pi}\theta_c'(t)\right]\cos\left[2\sqrt{\pi}\theta_c'(0)\right]\right\rangle\left\langle\sin\left[2\sqrt{\pi}\theta_f(t)\right]\sin\left[2\sqrt{\pi}\theta_f(0)\right]\right\rangle.\end{aligned} \tag{6.25}$$

Evaluation of the bosonic correlation function is standard, see for example Refs. [71; 92]. In terms of the scaling dimension $\Omega = 1+1/(1+r)$ of the backscattering operator, the result for the rate is

$$\begin{aligned}&\Gamma(V,T) \\ &= \frac{A^2}{4\hbar^2}\int_{-\infty}^{\infty} dt e^{ieVt/\hbar}\exp\left[-2\Omega\ln\sinh\left(\frac{\pi k_B T|t|}{\hbar}\right) + 2\Omega\ln\frac{\pi k_B T}{\hbar\omega_R} - \Omega i\pi\,\mathrm{Sign}(t) - 2\Omega\gamma\right] \\ &= \frac{A^2}{4\hbar^2}\frac{\pi}{\Gamma(2\Omega)}\left(\frac{2\pi k_B T}{\hbar\omega_R}\right)^{2\Omega-1}\frac{1}{\omega_R}\exp\left(\frac{eV}{2k_B T}\right)\left|\Gamma\left(\Omega + i\frac{eV}{2\pi k_B T}\right)\right|^2,\end{aligned} \tag{6.26}$$

where ω_R is the energy cutoff of the bosonic bath and γ is Euler's constant. Physically, as this rate involves gain of energy, it corresponds to backscattering from the right-moving to left-moving channel [using the convention of Eqs. (6.3) and (6.14)]. The net current is related to the difference of this rate and that in the opposite sense, namely $\Gamma(-V,T)$. Since the energy associated with the bias in each backscattering event is eV, we conclude that the charge carried by each quasi-particle is e. Consequently, the backscattering-related current is $\Delta I(V,T) = e[\Gamma(V,T) - \Gamma(-V,T)]$.

Adding this to the perfect transmission when $A = 0$, we arrive at our final result for the I-V curve

$$I(V,T) = \frac{e^2}{h} V \left\{ 1 - \frac{A^2\pi^2}{\hbar^2\omega_R^2} \frac{1}{\Gamma(\frac{2}{1+r}+2)} \left(\frac{2\pi k_B T}{\hbar\omega_R}\right)^{\frac{2}{1+r}} \left| \frac{\Gamma\left(\frac{1}{1+r} + 1 + i\frac{eV}{2\pi k_B T}\right)}{\Gamma\left(1 + i\frac{eV}{2\pi k_B T}\right)} \right|^2 \right\}. \tag{6.27}$$

This is the main theoretical result of this paper: the nonlinear I-V curve to leading order in the backscattering amplitude A as the system flows into the strong-coupling QCP (path 1 in Fig. 6.1). Flow to this QCP occurs by tuning the system (described by the original microscopic Hamiltonian in Sec. 6.2) to be on resonance and to have symmetric source and drain barriers. At large bias, a power-law dependence is found, $|dI/dV - e^2/h| \propto V^{2/(1+r)}$, as expected from the equilibrium RG analysis at the end of Sec. 6.4. A plot of the full result is shown in Fig. 6.2.

6.6 Comparison to experiment

Experiments were performed on quantum dots fabricated from carbon nanotubes contacted by Cr/Au electrodes in the group of Prof. Gleb Finkelstein. The electrodes were further connected to the bonding pads by Cr resistors that provided dissipation. For further information on the fabrication and characteristics of the samples, see Refs. [134; 135]. In Fig. 6.2 we show data from a sample with $r = 0.5$ and 0.75. The conductance G is measured in units of e^2/h and rescaled such that at a given temperature $1-G(V)$ is divided by $1-G(V=0)$.

Fig. 6.2 shows that the full non-linear result (6.27) captures the experimental behavior remarkably well. Note that there are no free parameters in the theory—this is not a fit. The value of r is determined in an independent equilibrium measurement of $G(T)$ off resonance [134], and the value of A is eliminated by plotting the ratio.

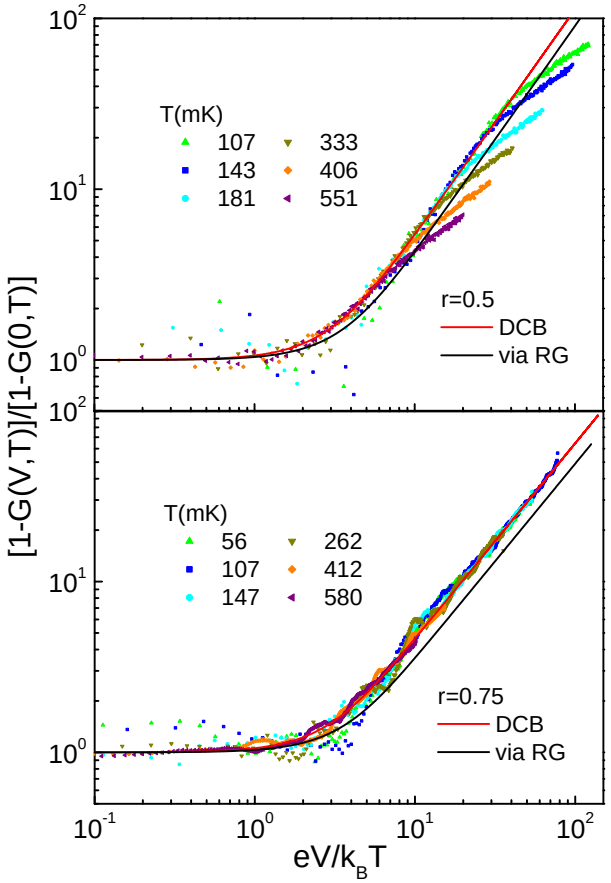

FIGURE 6.2: Deviation from perfect conductance $1-G(V,T)$, scaled by $1-G(V=0,T)$, as a function of eV/k_BT for $r=0.5$ and $r=0.75$. Here $G(V,T)$ is the differential conductance $G=(h/e^2)\,dI/dV$. The symbols are the experimental results at the color-coded temperatures. The red line is the result of the full non-linear theory [Eq. (6.27)], in which there are no free parameters. Note the excellent agreement between the theory and data in both the crossover and power-law regimes. At larger V/T, non-universal effects begin to set in due to $1-G(V,T)$ becoming non-negligible compared to 1.

For this value of r, $1-G$ on resonance is shown to scale as $T^{2/(1+r)}$ as expected in equilibrium [135].

Comparing closely the experimental and theoretical results, we see two striking features of the theory: first, it captures the *crossover regime* $eV\sim kT$ very accurately, and, second, it yields the correct *prefactor* of the universal $\propto V^{2/(1+r)}$ dependence at high bias. *The excellent agreement between the theory and experiment in a wide*

range of eV/k_BT is a striking confirmation of our far-from-equilibrium calculation.

It is important to realize that, unlike measurements that use a weakly coupled contact to probe the equilibrium density of states at finite bias (for example [120; 126; 154; 106]), here the two biased contacts remain equally coupled to the quantum dot, creating genuinely nonequilibrium conditions [137; 156].

At high enough eV/k_BT, the experimental curves deviate from the theoretical prediction (Fig. 6.2). There are several possible contributions to this deviation. Because $1 - G$ is no longer small, irrelevant operators not included in our effective strong-coupling model [Eq. (6.21)] may become significant. An additional possible contribution is that the second order analysis of the present model is inadequate at high bias. The range of applicability of our analytical results is pushed to higher and higher eV/k_BT as the temperature is lowered.

6.7 Interpretation as Dynamical Coulomb Blockade

To enhance the physical understanding of our main results, Eq. (6.27) and Fig. 6.2, we rewrite our strong coupling effective system as a fermionic problem and thereby make a direct connection to dynamical Coulomb blockade (DCB) theory. In order to use non-interacting fermions, we choose to refermionize the non-interacting bosonic fields (θ_f, ϕ_c) in Eq. (6.21), using the bosonization relation Eq. (6.6) where α now denotes this pair. It is also convenient to move the bias out of the barrier term by undoing the time-dependent gauge transformation. The coupling term Eq. (6.21c) is, then, replaced by the two terms

$$\begin{aligned} H_{\mathrm{T}} &= \pi a_0 A \cos\left[2\sqrt{\pi}\theta_c'(0)\right]\left[\psi_L^\dagger(0)\psi_R(0) + \mathrm{h.c.}\right] \\ H_\mu &= -eV\theta_c'(0)/\sqrt{4\pi}. \end{aligned} \tag{6.28}$$

The fact that the bias couples to the interacting field θ_c' is a serious complication. However, note that we will calculate the I-V curve only to leading order

in A, as in Sec. 6.5. In the expression for the rate, the bias appears only in the energy-conservation δ-function as the particle gains (or loses) energy eV when it backscatters. Note that the excitations of θ_c' and θ_f are tightly linked in the single term in Eq. (6.21c), leading to a single connection between a given $|i\rangle$ and its $|f\rangle$. Thus, whether the energy eV comes from coupling to the interacting or non-interacting field cannot be distinguished at this order. We can, then, calculate the I-V curve using the bias term

$$H'_\mu = -eV\theta_f(0)/\sqrt{4\pi}. \tag{6.29}$$

Refermionizing this term using relations analogous to those in Eq. (6.6), we arrive at the auxiliary model

$$\begin{aligned} H' = &\frac{1}{2}\int_{-\infty}^{\infty} dx \left[\psi_R^\dagger(x)\partial_x\psi_R(x) - \psi_L^\dagger(x)\partial_x\psi_L(x)\right] \\ &+ \frac{1}{2}\int_0^\infty dx\Big[(1+r)(\partial_x\theta_c')^2 + \frac{1}{1+r}(\partial_x\phi_f')^2\Big] \\ &+ \pi a_0 A\cos\left[2\sqrt{\pi}\theta_c'(0)\right]\left\{\psi_L^\dagger(0)\psi_R(0) + \text{h.c.}\right\} \\ &+ \frac{eV}{2}\left[\int_{-\infty}^0 dx\psi_R^\dagger(x)\psi_R(x) - \int_0^\infty dx\psi_L^\dagger(x)\psi_L(x)\right]. \end{aligned} \tag{6.30}$$

Each line of (6.30) can be interpreted physically: the first line is right- and left-moving non-interacting fermions, second line is an interacting bosonic environment, third line shows that backscattering of the fermions excites the environment, and fourth line accounts for the voltage bias between the right- and left- moving fermions.

We thus recognize the form for tunneling of non-interacting particles through a barrier in the presence of an environment [92; 187; 50], albeit with a strange barrier and strange environment. Tunneling through the barrier consists of backscattering between two chiral fermion modes, and the environment θ_c' involves a nonlinear combination of the original electrons and environment [the rotation Eq. (6.9) applies to

quantities in the exponent]. Nevertheless, the standard techniques of DCB theory [92; 187; 50] can be applied to obtain the nonlinear I-V curve to second order in A. The result [164; 196] is the same as in the last section, Eq. (6.27), with the coefficient of the correction $(A\pi/\hbar\omega_R)^2$ replaced by $(h/e^2)/R_T$, where R_T is the tunneling resistance of the effective barrier in the absence of dissipation.

The equivalence of these two coefficients is shown by considering the standard single-barrier tunneling Hamiltonian. Denote the backscattering amplitude of the fermions by $t_{k,q}$, where k and q label the initial and final fermionic particle states, $H_T = \sum_{k,q} t_{k,q} c^\dagger_{L,k} c_{R,q} + \text{h.c.}$. The standard result for the conductance of a tunneling barrier when the amplitude is momentum independent is $1/R_T = (e^2/h)|\bar{t}|^2[\Xi N(0)]^2$, where $\Xi N(0)$ is the number of states per unit energy and $\bar{t}$ is the average matrix element. In our case, the number of states is the size of the system L divided by the bosonization cutoff a_0, and the maximum energy for a particle excitation is $\hbar\omega_R$, the cutoff for the bosonic modes ($-\hbar\omega_R$ for a hole excitation). The amplitude $\bar{t}$ follows from Eq. (6.30) noting that a factor of $1/L$ is introduced in the conversion from continuous x to discrete k. Putting these elements together one finds

$$\frac{1}{R_T} = \frac{e^2}{h}\left(\frac{\pi a_0 A}{L}\right)^2 \left(\frac{L/a_0}{\hbar\omega_R}\right)^2 = \frac{e^2}{h}\left(\frac{\pi A}{\hbar\omega_R}\right)^2 . \tag{6.31}$$

Thus the I-V curve that results from a DCB theory treatment of the auxiliary strong-coupling model (6.30) and that found from the true effective bosonic description (6.21) are identical.

This allows then the physically intuitive interpretation of the I-V curve Eq. (6.27) as tunneling of non-interacting fermions (between left-movers and right-movers) in the presence of an environment.

6.8 Conclusions

We have carried out an analytic calculation of a far-from-equilibrium I-V curve at a strong-coupling QCP, and then presented experimental results enabling a detailed theory-experiment comparison. The calculation is made possible through an effective bosonic description at strong-coupling. The agreement with the experimental results throughout the crossover and asymptotic regimes, as shown in Fig. 6.2, is excellent.

A simple physical interpretation is possible because only one of the charge modes in the system couples to the EM environment, leaving the mode corresponding to fluctuations of the total charge in the dot free. This feature is not present, for instance, in the related problem of resonant tunneling in a Luttinger liquid. It allows us to find the I-V curve, alternatively, from the problem of tunneling between left- and right-moving non-interacting fermions in the presence of a modified environment. The solution to that problem from dynamical Coulomb blockade theory yields an explicit expression for the nonlinear I-V curve. Comparing the results of the bosonic and fermionic calculations, one finds that they are identical.

To our knowledge, this is the first calculation or measurement of the nonequilibrium nonlinear I-V curve at a QCP (path 1 in Fig. 6.1). As mentioned in the introduction, unlike measurements that use a weakly coupled contact to probe the equilibrium density of states at finite bias (for example [120; 126; 154; 106]), here the two biased contacts remain equally coupled to the quantum dot, creating genuinely nonequilibrium conditions [137; 156].

A remarkable aspect of this system is that it is fully accessible to both theory and experiment, allowing for a detailed comparison between the two. This accessibility is characteristic of other nanoscale systems exhibiting boundary QPT as well, see e.g. [106; 89; 90], one of the reasons for increasing interest in this topic. As nonequilibrium results at a QCP are exceedingly rare, our results provide a valuable bench mark and

test case for future studies of nonequilibrium steady states.

7

Equilibrium Crossover near a Non-Fermi-Liquid Quantum Critical Point: Conductance of a Dissipative Quantum Dot

We study the non-equilibrium conductance of a dissipative resonant level model system as it crosses over from the strong coupling critical point to the weak cotunneling ground state. The system consists of a spin-polarized quantum dot connected to two dissipative leads whose resistance is R. At the Toulouse point with $R = R_Q$ (the quantized dissipation), the strong tunneling critical point of this system is the same as that of the two-channel Kondo model; it is unstable under hybridization asymmetry or detuning of the level in the dot, both of which cause flow to a Fermi liquid ground state. Meanwhile, through Keldysh formalism, system's conductance can be analytically calculated at this Toulouse point. For other cases with general dissipation strength, we find that the crossover regime of our system is equivalent to that of a single barrier Luttinger liquid (LL), whose conductance has been calculated through Boltzmann equation. Comparison between numerical calculation and experimental data shows great agreement.

7.1 Introduction

The Kondo model has inspired a myriad of different physical problems and fundamental advances in theoretical physics. Among these related problems a very contemporary one is the dissipative spinless resonant level model, where a quantum dot is embedded between two dissipative leads [134; 135; 124] or a Luttinger liquid (LL) resonant model [103; 68; 67]. As has been introduced in Chapter 4, the dissipative resonant level model shares similarities with the 2CK model in the sense that they both host QCPs that are unstable against system asymmetry. More specifically, in the dissipative resonant level model, universal conductance has been predicted as a function of $\Delta V_{\rm gate}/\max(V,T)^{r/(1+r)}$, where $\Delta V_{\rm gate}$, V and T represents the detuning, bias and temperature, respectively, and $r = R/R_Q$ is the dimensionless dissipation strength. As introduced in Chapter 4, the dissipative resonant level model has been experimentally realized [134; 135]. One important features of the observed conductance curve is that the temperature and bias, which are both regarded as energy cutoffs in the renormalization group (RG) near the fixed points, become distinguishable at the crossover regime [135]. Thus, in order to understand the crossover it is necessary to investigate beyond the usual scaling analyses.

A simpler problem is the charge transport of a dissipative single barrier model. In this case, an interesting approach to go beyond the usual scaling was been put forward by Fendley et al. They discussed the non-equilibrium I-V curve using a particular quasi-particle basis and the Boltzmann equation for those quasi-particles [54; 55]. However, as far as we know, the application of such method directly to the resonant model is still absent. In this chapter we establish a connection between these models, thus proving that the resonant tunneling model I-V curve can be found using the Boltzmann equation method [190; 55].

In this chapter, we analytically calculate both the equilibrium and non-equilibrium

I-V curve of the dissipative resonant level model. For the particular case of $r = 1$, we evaluate the non-equilibrium conductance [166; 168] that successfully captures the feature of the crossover regime. We also prove that the $r = 1$ situation can be mapped to the two channel Kondo (2CK) model [53; 139]. For the general case of $r \neq 1$, we argue that the system can effectively be described as a point contact tunneling barrier model, that can be numerically evaluated using the Boltzmann equation method developed by Fendley et al [54; 55]. The comparison between our $r = 0.75$ theoretical result and the experimental data shows great agreement.

The manuscript is organized as follows. In section 7.2, we briefly introduce the model and the bosonization of the system. We derive the connection between the dissipative model and the point contact tunneling in section 7.3 and compare our theoretical result with the known experimental data. In section 7.4 we discuss the mapping of the resonant level model onto the 2CK model and use this to derive the conductance. Finally we discussed the physical understanding of the difference between temperature and bias in the crossover regime in section 7.5.

7.2 The Model and Bosonization with Chiral Fields

The system we consider in this chapter has the general form of the dissipative resonant level model. More specifically, system Hamiltonian can be depicted by the equations from Eq. (4.1) to Eq. (4.4). However, in contrast to the model in Chapter 6 where the system is perfectly symmetric, in this chapter we consider the effect of both the particle-hole (ϵ_d) and source-drain ($t_S - t_D$) asymmetries.

Same as Chapter 2, the standard approach to study the dissipative resonant level model is to use the Abelian bosonization and to combine the bosonic fields with the dissipative phase. In this chapter, it is more convenient to unfold the semi-infinite

source and drain leads into two full infinite chiral channels

$$c_{S,D}(x) = \frac{1}{\sqrt{2\pi a_0}} F_{S,D} \exp[i\phi_{S,D}(x)], \tag{7.1}$$

where a_0 is the lattice constant and $F_{S,D}$ is the Klein factor that guarantees the fermionic anti-commutator. The chiral bosonic fields obey the standard commutation relation,

$$[\partial_x \phi_\alpha(x), \phi_{\alpha'}(x')] = i\delta_{\alpha,\alpha'} \pi \delta(x - x'). \tag{7.2}$$

The relation between the chiral bosonic fields and the canonical ones has been provided in Chapter 2. Here we choose the chiral bosonization form since then it is easier to map the model onto the single barrier Luttinger liquid model, which has been exactly solved through the Boltzmann equation method.

To combine the dissipative phase with the lead bosons, we rotate the source and drain fields

$$\phi_{c,f}(x) = \frac{\phi_S(x) \pm \phi_D(x)}{\sqrt{2}}, \tag{7.3}$$

where $\phi_c(x)$ and $\phi_f(x)$ can be understood as the total charge in the leads and the charge difference between two leads, respectively. The Ohmic environmental field can be analytically extended to be effectively one-dimensional $\varphi(t) \to \varphi(t, x)$ such that the extended field satisfies the commutation relation

$$[\partial_x \varphi(x), \varphi(x')] = i2r\pi\delta(x - x'). \tag{7.4}$$

Finally, we define two new fields through the rotation

$$\begin{aligned} \phi'_f(x) &\equiv \sqrt{\frac{1}{1+r}}[\phi_f(x) + \frac{1}{\sqrt{2}}\varphi(x)], \\ \varphi'(x) &\equiv \sqrt{\frac{1}{1+r}}[\sqrt{r}\phi_f(x) - \frac{1}{\sqrt{2r}}\varphi(x)], \end{aligned} \tag{7.5}$$

that allows us to re-write the Hamiltonian as

$$\begin{aligned} H'_{\rm dot} &= H_{\rm dot} \\ H'_{\rm leads} &= \frac{v_F}{4\pi}\int_{\infty}^{\infty} dx \left\{[\partial_x\phi_c(x)]^2 + [\partial_x\phi'_f(x)]^2\right\} \\ H'_{\rm T} &= t_S \frac{F_S}{\sqrt{2\pi a_0}} e^{-i\sqrt{\frac{1+r}{2}}\phi'_f(0) - i\frac{1}{\sqrt{2}}\phi_c(0)} d \\ &\quad + t_D \frac{F_D}{\sqrt{2\pi a_0}} e^{i\sqrt{\frac{1+r}{2}}\phi'_f(0) - i\frac{1}{\sqrt{2}}\phi_c(0)} d + h.c., \end{aligned} \tag{7.6}$$

where we have already ignored the decoupled phase φ'.

7.3 I-V curve for general dissipation strength

7.3.1 Non-equilibrium I-V Curve of the System with a Detuned Quantum Dot

In this section, we study the system where the quantum dot is detuned $\epsilon_d \neq 0$. For simplicity, we take a symmetric lead-dot coupling $t_D = t_S$ with the tunneling Hamiltonian

$$H'_{\rm T} = \frac{t_S}{\sqrt{2\pi a_0}} \cos\left[\sqrt{\frac{1+r}{2}}\phi'_f(0)\right] e^{-i\sqrt{\frac{K}{2}}\phi_c(0)}\sigma^- + h.c., \tag{7.7}$$

where K is proportional to the RG-variant scaling dimension of the ϕ_c operator with initial value one. σ^- is the effective Pauli matrix constructed by the combination of impurity operator d and the Klein factor. This Hamiltonian shows a strong resemblance to the Abelian bosonization of the two channel anisotropic Kondo model (see section 7.4 for details) and the double barrier tunneling in a LL that is studied by Kane and Fisher [103]. The weak coupling renormalization group equations can be derived by writing the system partition function into the Coulomb gas form. This method has been applied, for instance, to the quantum Brownian motion [59] and Luttinger liquid models [103]. As introduced in Chapter 6, the dissipative resonant

level model can be considered as an effective Luttinger liquid model with ϕ_f interacting. We can thus follow the Coulomb gas RG method to get the RG equations

$$\begin{aligned}\frac{dt_S}{d\ln\tau_c} &= t_S\Big(1-\frac{1+r}{4}-\frac{K}{4}\Big)\\ \frac{dK}{d\ln\tau_c} &= -8\tau_c^2 t_S^2 K,\end{aligned} \tag{7.8}$$

where τ_c is the RG cutoff.

The first equation of Eq. (7.8) shows that the hybridization increases with $r<2$, while the second one shows that the scaling dimension of the ϕ_c field decreases as the renormalization group flow develops. This fact physically means that the resonant level is screened by the lead fermions so that the particle number between two barriers are fixed to be a half integer. As a consequence we can consider a two step RG and after this initial RG flow, the remaining dynamics of the tunneling Hamiltonian can be expressed as the effective model[1]

$$\tilde{H}'_{\rm T} = \frac{\tilde{t}_S}{\sqrt{2\pi a_0}}\cos[\sqrt{\frac{1+r}{2}}\phi'_f(0)]\sigma^x, \tag{7.9}$$

with $\tilde{t}_S$ as the renormalized hybridization strength. If we consider $\epsilon_d \ll \tilde{t}_S$ initially, the tunneling strength $\tilde{t}_S$ increases and the system approaches the strong coupling regime with $r<3$. The tunneling Hamiltonian Eq. (7.9) mimics that in a Luttinger liquid resonant level model: near the strong coupling fixed point of a Luttinger liquid resonant level model, the quantum dot detuning prevents the healing of the system, leaving a weak backscattering barrier at the quantum dot site [103]. Since the effectively Hamiltonian Eq. (7.9) with ϕ_c decoupled is the same as that of a Luttinger liquid with effective Luttinger interaction $\sqrt{(1+r)/2}$, this argument applies to our

[1] Here we are simplifying the system with known RG equations Eq. (7.8). This technique has been introduced in Section 3.2.2. Notice that with this simplification, details of the system when flowing into the critical point (this is the content of Chapter 6) are lost.

case, with the effective Hamiltonian near the strong coupling regime

$$\Delta\tilde{V}_{\text{gate}}\sin[\sqrt{\frac{2}{1+r}}\phi'_f(0)]\sigma^y, \tag{7.10}$$

where $\Delta\tilde{V}_{\text{gate}}\propto\Delta V_{\text{gate}}$ is the renormalized detuning strength. Another way to understand the connection between Eqs. (7.9) and (7.10) is through the boundary condition variation of the ϕ'_f field after the fusion with the dot operator σ^x. This method can also be applied to understand the effect of a weak source-drain asymmetry, which will be provided in detail in Section 7.3.2. Notice that operator in Eq. (7.10) has scaling dimension $1/(1+r)$ and is relevant with $r > 0$, thus becoming the leading operator in the second RG process.

The Sine-Gordon form of Eq. (7.10) allows us to note that the near-resonant transport in the noise environment can be effectively described as a point contact tunneling between two LL leads (which can also be described by an effective boundary Sine-Gordon operator). It is therefore expected that the system will flow towards a co-tunneling regime through a crossover with a $2k_F$-backscattering-like operator (generated by the detuning operator). The transport properties of this model have been studied before using the Boltzmann equation method, where kink and anti-kink are quasi-particles.

In order to verify our mapping, we calculate the conductance of the equilibrium case and the zero temperature case with $r = 0.75$ based on the Boltzmann equation method and compare the result with the experimental data (that comes from Professor Gleb Finkelstein's group). The result is given in Fig. 7.1, where the blue and red curves are the theoretical results for equilibrium and zero temperature case, respectively. The experimental data is represented by the black dots. Here we can see that the equilibrium result perfect agrees with the experimental data. Compared with the exact and perfect equilibrium result, the zero temperature (non-equilibrium) curve

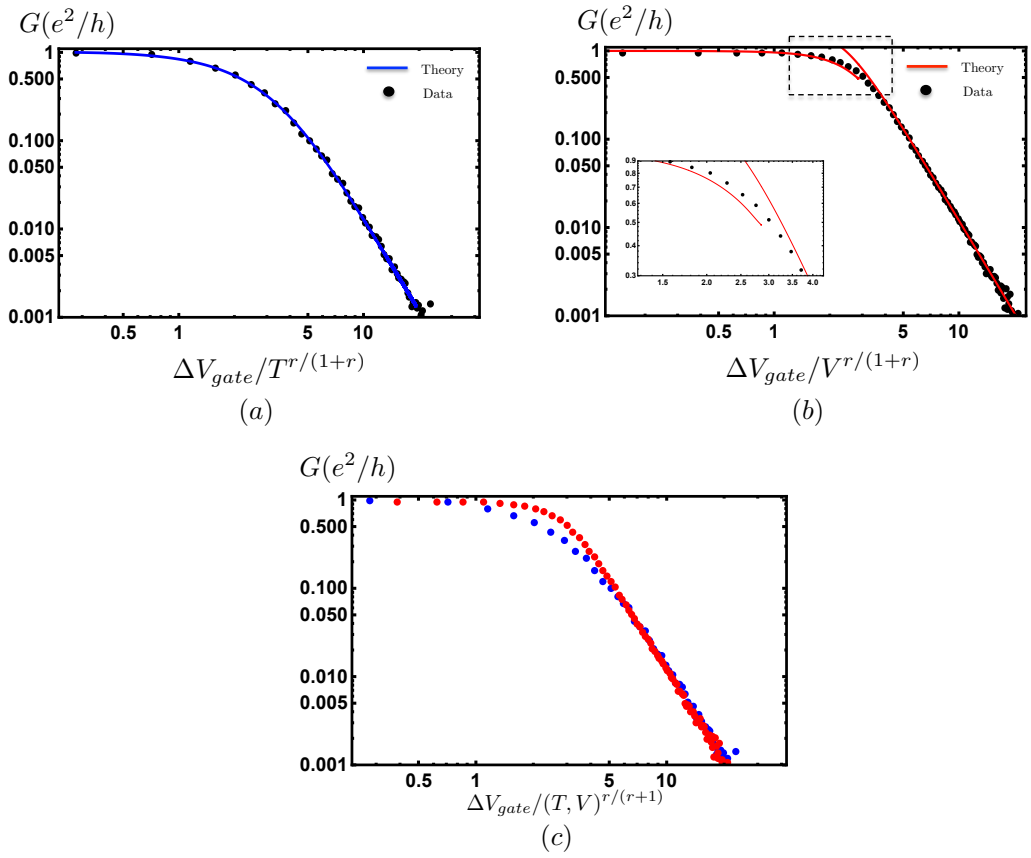

FIGURE 7.1: The comparison between experimental data and theoretical results. The dissipation strength is $r = 0.75$ for both cases. The solid lines are the theoretical result and the black dots are experimental data provided by Professor Gleb Finkelstein's group. Fig. 7.1(a) is the equilibrium result under finite temperature and Fig. 7.1(b) is the zero temperature result calculated by the summation of polynomial series. In the crossover regime, both the weak cotunneling and weak backscattering treatment fails and we can see the transition between those two regimes. Fig, 7.1(c) shows two experimental data in a single plot.

is perturbative and is constructed through the summation of polynomials in two different regimes. More specifically, near the strong coupling regime, the G-V curve is calculated by summing over all $\Delta V_{\text{gate}}/V^{r/(1+r)}$ polynomials. On the contrary, near the fermi liquid ground state, $V^{r/(1+r)}/\Delta V_{\text{gate}}$ becomes small so that the conductance is calculated by summing over all orders of $V^{r/(1+r)}/\Delta V_{\text{gate}}$. That is why the deviation between experimental data and the theoretical calculation develops when $\Delta V \sim V_{\text{gate}}$. Except for that regime, the theoretical result agrees quite well with the

experimental data.

7.3.2 Effect of Source-Drain Asymmetry

In Section 7.3.1, we have shown that the dissipative resonant level model with a detuned quantum dot maps to a single barrier Luttinger liquid model that can be solved through the Boltzmann equation method. It also shows a great agreement between our theoretical calculation and the experimental data. In this section, we instead consider the other case where the quantum dot is fine tuned ($\epsilon_d = 0$), while the source-drain symmetry is broken $t_S \neq t_D$ with a simple argument based on the conformal field theory (CFT). As proved by J. Cardy [30], in CFT, the fusion between primary fields corresponds to the change of boundary conditions. Below we show that through the fusion process, the source-drain asymmetry effectively shares the form of Eq. (7.10), with $\Delta\tilde{V}_{\rm gate}$ replaced by $\tilde{t}_S - \tilde{t}_D$ (the renormalized source-drain asymmetry) and sin replaced by cos.

We begin with the free action and the Hamiltonian after the absorption of dissipation

$$\begin{aligned} S_0 &= \frac{1}{\beta}\sum_{\omega_n} |\omega_n|(|\phi_c|^2 + |\phi_f'|^2) \\ H_T &= t_S F_S e^{-i[\frac{1}{\sqrt{2}}\phi_c(0) + \sqrt{\frac{1+r}{2}}\phi_f'(0)]} d \\ &\quad + t_D F_D e^{-i[\frac{1}{\sqrt{2}}\phi_c(0) - \sqrt{\frac{1+r}{2}}\phi_f'(0)]} d + h.c., \end{aligned} \tag{7.11}$$

where the decoupled effective dissipation φ' has been neglected.

Next is the transformation $U = \exp[i\gamma(d^\dagger d - 1/2)\phi_c(0)]$. Here we take $\gamma = 1/\sqrt{2} - 1$ so that the tunneling Hamiltonian becomes

$$\begin{aligned} H_T &= t_S F_S e^{-i[\phi_c(0) + \sqrt{\frac{1+r}{2}}\phi_f'(0)]} d \\ &\quad + t_D F_D e^{-i[\phi_c(0) - \sqrt{\frac{1+r}{2}}\phi_f'(0)]} d + h.c. \end{aligned} \tag{7.12}$$

Now if we rename the fields $c \to s$, $cf \to sf$ and define spin operators as the combination of impurity operators and Klein factors, we get an effective 2CK Hamiltonian where the spin flavor field ϕ_{sf} is interacting [2]. In this sense, the effect of the source-drain asymmetry in a dissipative resonant level model mimics that of the channel asymmetry in a two channel Kondo model.

Having noticed this fact, we detour a little bit and discuss about the source-drain (S-D) asymmetry operator in a spin 2CK model. In a spin 2CK model, the S-D asymmetry can be written as [65]

$$\frac{1}{2}(J_L - J_R)[\vec{J}_L - \vec{J}_R] \cdot \vec{S} \sim [\vec{\phi} \times \epsilon] \cdot S, \tag{7.13}$$

where $\vec{\phi}$ represents the $j = 1$ field in the SU(2) level two Kac-Moody algebra and ϵ is the "energy operator" in the Ising sector. In the SU(2) 2CK model, the flowing towards the 2CK critical point corresponds to the absorption of a spin 1/2 in the SU(2) level two sector, which is realized through the double fusion with g_α (the $j = 1/2$ spin field) fields. Since $g_\alpha \times \vec{\phi} \to g_\alpha$ and $g_\alpha \times g_\alpha \to 1 + \vec{\phi}$ [72], the S-D asymmetry operator around the critical point $\sim \epsilon$, which has scaling dimension 1/2 ($\vec{\phi} \times \epsilon$ has a higher scaling dimension and is thus ignored).

Now we go back to our case. From Eq. (7.12) we see that the c field is not interacting. Because of that, if with $c \to s$ and $d \to S^-$ we see that in our effective interacting 2CK model the spin sector is not interacting so that the total spin can once again be described by the SU(2) level two KM algebra. Consequently, we can write the asymmetry as

$$\vec{\phi} \times \sin[\sqrt{\frac{1+r}{2}}\phi'_{sf}], \tag{7.14}$$

where the impurity operator has been ignored since it is irrelevant in the Boltzmann

[2] A more strict mapping between the two channel Kondo model and the $R = R_Q$ dissipative resonant level model is provided in Section 7.4.1.

equation calculations. Similar as the spin 2CK case, the S-D asymmetry Hamiltonian corresponds to the double fusion of Eq. (7.14) with field g_α, which takes $\vec{\phi} \to 1$.

In contrast to the spin 2CK model, in this case we also need to take into consideration the change of boundary condition in the spin flavor sector by taking $\sin[\sqrt{\frac{1+r}{2}}\phi'_{sf}] \to \cos[\sqrt{\frac{2}{1+r}}\phi'_{sf}]$ [183]. Now rename ϕ'_{sf} as ϕ'_f, we get the same form as Eq. (7.10) with sin replaced by cos. Since this relevant operator originates from the source-drain asymmetry, it will be proportional to $\tilde{t}_S - \tilde{t}_D$. Consequently, we have proved that the source-drain asymmetry generates an effective operator that has the same dynamics of that of the dot detuning: thus the crossover I-V curve of the S-D asymmetric case should also be the same as that of the dot detuned case.

7.4 Toulouse Point with Critical Dissipation Strength

In Chapter 4 we have introduced the 2CK model and its hosted second order boundary QPT. We have also mentioned the similarity between the dissipative resonant level model and the 2CK model. Actually, connection between the dissipative resonant level model and the 2CK has already been pointed out [134; 135; 124]. Physically, in a resonant level model, one can define the isospin [7] with respect to the charge number in each lead, which mimics the $SU(2)$ symmetric real spin in the 2CK model. Meanwhile, the competition between two leads' hybridization to the dot mimics the Kondo screening between two channels in the 2CK model [166]. In this section we analytically prove that when $r = 1$, the resonant level model can be exactly mapped to the 2CK model. We also calculate the I-V curve at this Toulouse point in the crossover regime.

7.4.1 Mapping towards the 2CK Model

We start with the effective Hamiltonian Eq. (7.6) and prove its equivalency to that of the 2CK model. For simplicity, bias voltage will only be considered in next subsection

when we are ready to calculate the conductance.

To proceed, we introduce the unitary transformation

$$U = \exp[i\gamma(d^\dagger d - \frac{1}{2})\phi_c(0)], \tag{7.15}$$

where γ is some undetermined constant. It is easy to check its effect on impurity operators

$$\begin{aligned} U^\dagger dU &= \exp[i\gamma\phi_c(0)]d \\ U^\dagger d^\dagger U &= \exp[-i\gamma\phi_c(0)]d^\dagger, \end{aligned} \tag{7.16}$$

such that this transformation will change the exponential coefficient of the field ϕ_c. The side effect is that it also introduces a potential interaction from the lead Hamiltonian

$$U^\dagger H'_{\text{leads}} U = H'_{\text{leads}} - v_F\gamma(d^\dagger d - 1/2)\partial_x\phi_c(0). \tag{7.17}$$

When $r = 1$ we take $\gamma = 1/\sqrt{2} - 1$ and the tunneling Hamiltonian becomes

$$\begin{aligned} H'_{\text{T}} = t_S\frac{F_S}{\sqrt{2\pi a_0}}e^{-i\sqrt{2}\tilde{\phi}_S}d + t_D\frac{F_D}{\sqrt{2\pi a_0}}e^{-i\sqrt{2}\tilde{\phi}_D}d + h.c. \\ + v_F\frac{\sqrt{2}-1}{2}(d^\dagger d - \frac{1}{2})\partial_x[\tilde{\phi}_S + \tilde{\phi}_D](0), \end{aligned} \tag{7.18}$$

where $\tilde{\phi}_{S,D}(x) \equiv [\phi_c(x) \pm \phi_f(x)]/\sqrt{2}$ is the effective lead field after the incorporation of dissipation. We have put the generated potential interaction into H_{T} so that H_{leads} is still free. Physically, the unitary transformation effectively changes the interaction between the field ϕ_c and the impurity. And the quartic potential interaction is thus introduced to compensate for this change.

One important feature of the transformed Hamiltonian Eq. (7.18) is that the hybridization terms have scaling dimension one such that they share the RG feature of operators in a Kondo problem. This feature signifies the connection between the $r = 1$ resonant level model and the 2CK model, and enables the mapping between

them. However, since the spin 2CK model has four independent fields (instead of two in the resonant level model), we need to introduce another two auxiliary fields $\bar{\phi}_{L,R}$ in our model to complete this mapping. Luckily, we are also free to choose $\bar{\phi}_{L,R}$ as non-interacting since they are actually fictitious. Then we can rotate over those fields

$$\begin{aligned}\Phi_{L/R,\uparrow}(x) &= \frac{1}{\sqrt{2}}[\tilde{\phi}_{L.R}(x) + \bar{\phi}_{L/R}(x)] \\ \Phi_{L/R,\downarrow}(x) &= \frac{1}{\sqrt{2}}[-\tilde{\phi}_{L.R}(x) + \bar{\phi}_{L/R}(x)],\end{aligned} \tag{7.19}$$

to produce the virtual spin. Next, we substitute the spinless impurity operators into the SU(2) spinful ones $F_S d \to F_{S,\uparrow}F_{S,\downarrow}S^-$, $F_D d \to F_{D,\uparrow}F_{D,\downarrow}S^-$ and $d^\dagger d - 1/2 \to S^z$ so that the resonant level now behaves as a localized spin where the detuning $\Delta V_{\text{gate}} = \epsilon_d - \mu$ mimics the magnetic field that lifts the spin SU(2) symmetry in the 2CK model. Now, we refermionize the new fields defined in Eq. (7.19)

$$F_{\alpha,\sigma}e^{-i\Phi_{\alpha,\sigma}(x)} = \psi^\dagger_{\alpha,\sigma}(x), \tag{7.20}$$

and arrive at the effective 2CK Hamiltonian

$$\begin{aligned}H_{\text{leads}} &= iv_F\int_{-\infty}^{\infty}dx\sum_{\alpha,\sigma}\psi^\dagger_{\alpha,\sigma}(x)\frac{d}{dx}\psi_{\alpha,\sigma}(x) \\ H_{\text{Kondo}} &= J_z S^z[\psi^\dagger_{S,\uparrow}\psi_{S,\uparrow} - \psi^\dagger_{S,\downarrow}\psi_{S,\downarrow} + \psi^\dagger_{D,\uparrow}\psi_{D,\uparrow} - \psi^\dagger_{D,\downarrow}\psi_{D,\downarrow}] \\ &\quad + J_S\psi^\dagger_{S,\uparrow}\psi_{S,\downarrow}S^- + J_D\psi^\dagger_{D,\uparrow}\psi_{D,\downarrow}S^- + h.c.,\end{aligned} \tag{7.21}$$

where $\sigma = \uparrow, \downarrow$ labels the pseudo-spin and $x = 0$ is assumed for the lead operators in H_{Kondo}. The anisotropic Kondo parameters are defined as

$$\begin{aligned}J_z &= \sqrt{2}\pi v_F(\sqrt{2} - 1) \\ J_S &= \sqrt{2\pi a_0}t_S \\ J_D &= \sqrt{2\pi a_0}t_D.\end{aligned} \tag{7.22}$$

Some comments can be made about the effective 2CK Hamiltonian in Eq. (7.21). We begin with the explanation of the physical meaning of those two auxiliary fields. From Eq. (7.21), we see that the inter-lead Kondo coupling is missing, which freezes the charge flavor field in the 2CK model. Meanwhile, the Kondo feature freezes the total charge number in the leads. Consequently, the effective Kondo Hamiltonian in Eq. (7.21) only contains two independent fields, the same as that of the resonant level model. Actually, the frozen of these two freedoms also originates from the fact that the fields $\bar{\phi}_{L/R}$ are only virtual. This explains why a resonant level model can effectively describe the 2CK model.

Due to the missing of the inter-lead Kondo tunneling, the 2CK fixed point of the effective model Eq. (7.21) becomes easier accessed compared with the spin 2CK model. Such behavior is also present in the charge 2CK model, where the inter-lead tunneling is missing due to the decoherence at two sides of the "large dot". Consequently, the I-V curve of our resonant level model is similar to that predicted in a charge 2CK model [139], where the source-drain asymmetry and impurity level detuning are relevant operators near the charge 2CK fixed point (with perfect conductance). Finally, due to the equivalence to the 2CK model, the $R = R_Q$ dissipative resonant level model also hosts a decoupled Majorana fermion at the quantum dot. This Majorana fermion, which consists of real impurity electron creation and annihilation operators, is different from the effective Majorana fermion in a spin 2CK model (that is created by spin operators). An application of this feature will be introduced in Section 8.

7.4.2 I-V Curve of the Toulouse point

In Section 7.4.1, we have showed that the resonant level model with $r = 1$ maps to a 2CK model and we have predicted a similar crossover $I - V$ feature as that of the charge 2CK model. Here we provide a detailed calculation of the nonequilibrium

conductance.

In this section we also take the $r = 1$ dissipation. This time we take the coefficient of the unitary transformation to be $\gamma = 1/\sqrt{2}$ and refermionize the ϕ'_f and ϕ_c fields. The tunneling Hamiltonian becomes

$$\begin{aligned}\tilde{H}_{\mathrm{T}} = (t_S - t_D)\frac{\psi_f^\dagger(0) - \psi_f(0)}{\sqrt{2}}a \\ + i(t_S + t_D)\frac{\psi_f^\dagger(0) + \psi_f(0)}{\sqrt{2}}b \\ + i[\epsilon_d - \pi v_F/\sqrt{2} : \psi_c^\dagger\psi_c(0) :]ab,\end{aligned} \tag{7.23}$$

where $a = (d + d^\dagger)/\sqrt{2}$ and $b = (d - d^\dagger)/\sqrt{2}i$ are the two impurity majorana fermion operators. These two lead fermions ψ_f and ψ_c are refermionized from ϕ'_f and ϕ_c, respectively.

One can quickly see that the Hamiltonian (7.23) can be exactly solved if we can drop the quartic ψ_c-impurity interaction. Normally this interaction is important since it is marginal and has a large initial value. However, when we are only interested in the crossover regime, we can take several arguments to rule out the effect of this quartic term. In the arguments below we assume that the detuning is small such that the system flows to the strong coupling regime first and then got driven away by the (initially) small detuning into the crossover regime.

The first one is about the screening out of the ϕ_c field from the RG point of view. The RG equations of the dissipative resonant level model are given in Eq. (7.8). Based on these equations, when the system flows towards the strong coupling fixed point, the scaling dimension of the factor $e^{i\phi_c}$ decreases from 1/2 to zero [103; 167]. Physically, this can be understood as the screening of the ϕ_c field by the dot-lead hybridization. Practically, due to its zero scaling dimension near the strong coupling regime, ϕ_c lost its dynamics in the ensued crossover regime so that the quartic term

is not important here.

The second argument comes from the known effect of this quartic interaction: it is important when the system flows towards the strong coupling fixed point but trivial in the crossover regime [195]. Consequently, when we are only interested in the crossover regime we are free to drop this quartic term.

Now, we assume that the system is at the crossover regime with small detuning and asymmetry such that $\Delta V_{\text{gate}}, |V_S - V_D| \ll T_c$, where T_c is the critical temperature at which the system reaches the strong coupling regime.

For later convenience, we define two lead Majorana fermions $\chi_1^f = (\psi_f^\dagger + \psi_f)/\sqrt{2}$ and $\chi_2^f = (\psi_f^\dagger - \psi_f)/\sqrt{2}i$ such that the tunneling Hamiltonian becomes

$$H_{\text{T}} = it_e \chi_1^f b + it_o \chi_2^f a + i\Delta V_{\text{gate}} ab, \tag{7.24}$$

where $t_{e,o} = t_S \pm t_D$ is the even (odd) combination of the hybridization strengths. Based on our assumption we have $t_e \gg t_o, \Delta V_{\text{gate}}$. Notice that the leading relevant operators in Eq. (7.24) have scaling dimension 1/2 in the crossover regime, further supporting the leading relevant operator Eq. (7.10) in section 7.3: with $r = 1$, the operator of Eq. (7.10) also has scaling dimension $1/(1 + r) = 1/2$. We also notice that the Hamiltonian above has a similar form of the two impurity Kondo model [7].

Before further calculation, we derive the current operator and bias Hamiltonian written with those new fields. Our strategy is to calculate these operators in the original model first and transform them with the same transformations on the equilibrium Hamiltonian. It is easy to see that the bias voltage Hamiltonian and the current operator can be written as

$$\begin{aligned} H_{\text{bias}} &= -i\frac{V}{2}\int_{-\infty}^{\infty} dx \chi_1^f(x)\chi_2^f(x) \\ \hat{I} &= -\frac{i}{2}t_o \chi_1^f a + \frac{i}{2}t_e \chi_2^f b, \end{aligned} \tag{7.25}$$

where V is the applied bias as defined in earlier sections. Now we are ready to calculate the current with the standard Keldysh formalism. The result is

$$I = V - \frac{\lambda^2}{2} \operatorname{Im} \psi(\frac{1}{2} + \frac{\lambda^2/2 + iV/2}{2\pi T}) \tag{7.26}$$

in unit of e^2/h, where $\lambda^2 \equiv t_o^2/v_F + 4\Delta V_{\text{gate}}^2 v_F/t_e^2$ signifies the total system asymmetry. The function $\psi(x)$ is the digamma function [168; 166]. Eq. (7.26) is one of the essential results of this paper.

As analyzed in section 7.4.1, the I-V curve Eq. (7.26) is similar to that of the charge 2CK model: they both have a perfect conductance that is destroyed by detuning operators. The only difference is that in the charge 2CK model, the strong coupling conductance is $e^2/2h$ due to the decoherence between two barriers. To more intuitively understand Eq. (7.26), system conductance and current based on it have been provided in Fig. (7.2).

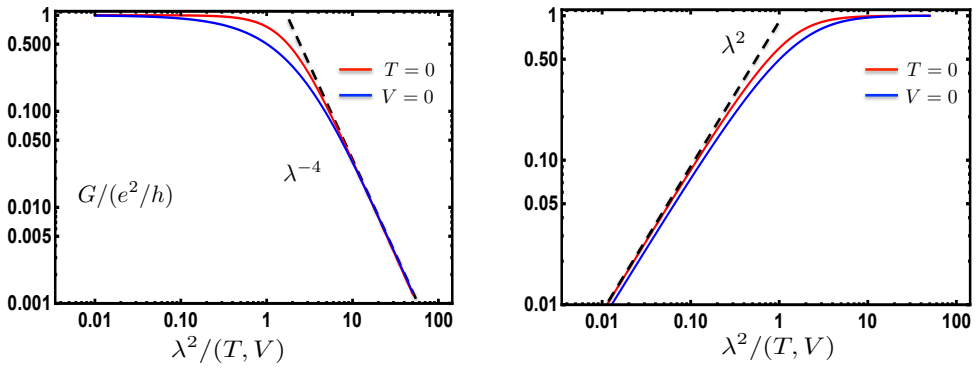

FIGURE 7.2: The differential conductance of the $r = 1$ case as a function of $\lambda^2/\max(T, V)$. λ^2 is the strength of detuning and asymmetry. The red curve is the result with low bias and zero temperature and the blue curve is the result of the low temperature equilibrium case.

We verify the result of Eq. (7.26) by checking the conductance scaling at the weak and strong coupling regimes. In the strong coupling regime, the leading relevant operator is the backscattering triggered by λ, which has scaling dimension $1/(1+r) =$

1/2 so that the current follows the behavior $1 - Ih/e^2V \propto 1/\max(T, V)$. On the other hand, around the weak coupling regime, the leading irrelevant operator is the cotunneling process with scaling dimension $1 + r = 2$ so that the powerlaw should be $G \propto \max(T^2, V^2)$. Our result in Fig. (7.2) agrees well with those RG expectations.

We also see that at the crossover regime, bias and temperature behave quite different. More precisely, the low bias curve has a much sharper transition between the weak and strong coupling regimes compared with that of the low temperature case, which agrees with the experimental data observed with $r = 0.75$ (Fig. 7.1). We will illustrate the physical significance behind this phenomenon in Section 7.5.

7.5 Physical Understanding of the Crossover regime

In previous sections we have provided analytical calculations of the I-V curvature of the Toulouse point (with $r = 1$) and numerical results of that with general dissipation. We further make the $r = 0.75$ G-V plots to compare with the experimental data. One important features of both the analytic and numerical results [from Figs. 7.1 and 7.2] is that temperature and bias lead to different conductance behaviors in the crossover regime, which does not agrees with the intuitive RG expectation. In this section we provide a physical understanding of this result.

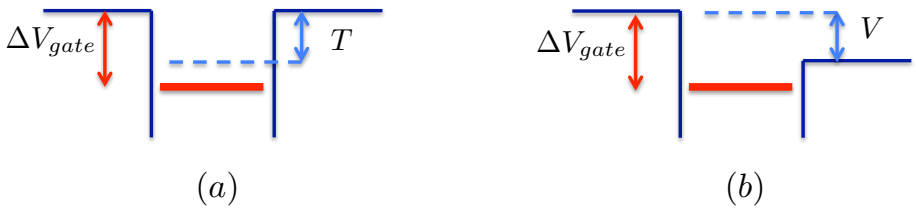

FIGURE 7.3: Illustration of the different behaviors of temperature and bias dependent conductance in the crossover regime. The red bold line represents the energy level of the dot and ΔV_{gate} is the quantum dot detuning. Here we consider either the equilibrium (a) case with temperature T or the zero temperature (b) case with bias V.

The illustration of the resonant level model in the crossover regime is depicted

in Fig. 7.3. Here the red bold line represents the impurity energy level and ΔV_{gate} refers to the quantum dot detuning. Fig. 7.3(a) represents the equilibrium case with temperature T slightly smaller than the detuning such that $0 < \Delta V_{\text{gate}} - T \ll T$, while Fig. 7.3(b) represents the zero temperature case with $0 < \Delta V_{\text{gate}} - V \ll V$. Without loss of generality, these two cases can describe the physics at the crossover regime.

In the equilibrium case [Fig. 7.3(a)], the lead-dot hybridization is exponentially suppressed by an increasing detuning. However, the lead-dot hopping is always possible (although with an exponentially decaying amplitude) even with $T < \Delta V_{\text{gate}}$.

The analysis above, however, does not apply to the zero temperature case [Fig. 7.3(b)]. In this case, a weak impurity detuning $\Delta V_{\text{gate}} < V$ will not significantly change the lead-dot hybridization. This hybridization, however, suddenly vanishes once the detuning ΔV_{gate} exceeds the bias V (since dissipation suppresses the impurity level broadening).

With the above analysis, we have the physical picture of the system. When detuning is weak, it behaves as a $2k_F$ backscattering where both the temperature and bias serve as the RG cutoff such that they have the same behavior. When the system enters the crossover regime [with $\Delta V_{\text{gate}} < \max(V, T)$], the lead-dot hybridization of the equilibrium case is exponentially suppressed by the detuning while that of the zero temperature case is not significantly affected. This explains why the zero temperature curve has a higher conductance in this regime. Then, when ΔV_{gate} becomes slightly larger than V in the zero temperature case, the hybridization is suddenly turned off compared with the exponential suppression of the equilibrium case, which explains the sharper transition between the weak cotunneling and the weak backscattering regimes in the zero temperature case. Finally, when the system enters the weak cotunneling regime, once again both the temperature and bias work as the RG cutoff so that they have the same behavior.

7.6 Summary

In this chapter we investigate the crossover regime nonequilibrium conductance as a function of either temperature or bias voltage in a dissipative resonant level model. We consider a situation where the weak detuning and source-drain asymmetry destabilize the reachable strong coupling regime and drive the system towards the weak cotunneling regime through the crossover regime. To begin with, we combine the bosonic environmental modes with the bosonized lead fields to redefine their dynamics. For the $r = 1$ special case, we map the system to the 2CK model, where the system can be exactly solved through the Keldysh formalism. For the cases with general r, we map our system to a single barrier LL model, where the system can be numerically solved through the Boltzmann equation method with kinks as quasiparticles. To verify our mapping, we compare the $r = 0.75$ numerical curves with the experimental data, which shows great agreement. We also provide a physical picture to illustrate the difference between temperature and bias in the crossover regime beyond the perturbative RG understanding.

8

Stabilizing a Majorana Zero Mode with Quantum Frustration

We show that a Majorana zero mode can be stabilized by hybridizing its partner with an effective two channel Kondo (2CK) state. Frustration inherent in the effective 2CK state leads to a decoupled Majorana degree of freedom which can naturally hybridize with one of a pair of Majorana modes in a topological superconducting wire, thereby leaving an unpaired Majorana zero mode at the other end of the wire. Concretely, the system that we study consists of two (left and right) on-resonance quantum dots that couple to two interacting Majorana fermions on the same grounded topological superconducting wire. The right dot is connected to two dissipative leads with $R = R_Q$, thus creating an effective 2CK state with an isolated Majorana zero mode on the dot. The left dot is connected to two regular leads and the transmission through it is monitored. We find that the coupling between the isolated dot Majorana and the Majorana in the superconducting wire stabilizes the non-trivial Majorana transmission signature of the left system. This also provides a clear signature of the presence of the 2CK Majorana.

8.1 Introduction

Majorana zero modes (MZMs) are exotic self-conjugate edge states that are predicted to exist in non-trivial condensed matter structures [9]. They have attracted wide range of interests due to their non-Abelian statistical feature [158; 93; 10] that is widely believed to be an option in the realization of the quantum computation [144]. To construct and observe the MZMs, researchers have proposed multiple structures [9] to effectively realize the celebrated theoretical model invented by Kitaev [107]. Besides multiple pioneering Majorana fermion evidence [142; 47; 48; 57; 40; 49; 84; 8; 193], most recently experimentalists finally observed the $2e^2/h$ conductance [194] through a superconductor-proximatized nanowire system under the influence of a magnetic field and the spin-orbit coupling. This conductance has been considered as one of the signatures of the MZM [172; 115; 61].

Once the existence of the MZMs is established, it will be interesting to investigate the effect of the MZMs in classical problems. For instance, the community has studied multiple MZM-coupled quantum impurity systems [62; 123; 118; 4; 36; 179; 94]. Generally, a MZM will greatly modify the property of a quantum dot that couples to it due to its exotic irrational degeneracy. The simplest MZM-induced modification happens in a MZM coupled resonant level model, whose on-resonance conductance changes from e^2/h to $e^2/2h$, referring to the decoupling of a "half chain" of this resonant level model [123]. This modification of the impurity property can thus be used to detect the presence of the MZMs. A more interesting example happens when a MZM couples to a Kondo model [118; 36] —- in this case, the Kondo interaction is interrupted by the MZM-dot coupling, thus generating an interesting Andreev $\otimes$ Normal boundary condition [36; 4].

In contrast to the free elementary particle predicted by Majorana, in condensed matter community the effective MZMs always appear in pairs in finite size systems

[9]. Unfortunately, the hybridization between a MZM and its partner will destabilize its coupling to a quantum dot [123; 36; 112], both in the spinless and the more complicated Kondo models. In the resonant level model, the non-trivial Majorana featured conductance $e^2/2h$ will be buried by the relevant hybridization between the MZM and its partner [123]. In the Kondo model, the MZM hybridization will destabilize the coupling between the MZM and the quantum dot, thus leading to a regime where the Kondo system decouples from the MZM [36]. In reality, the inter-MZMs coupling decays as $\propto \exp(-L/\xi)$ [123], with L the distance and ξ the superconducting correlation length in the nanowire. Experimentally, $L \sim 1\ \mu$m [194], $\xi \sim 300$ nm so that the hybridization can not be generally ignored. Consequently, we need to stabilize the MZM against the inter-MZM coupling before coupling it to the quantum impurity models.

In this Chapter, we try to stabilize a MZM against the hybridization with its partner by coupling its partner to an unpaired Majorana fermion of a frustrated resonant level model. Actually, long before the recent experimental triumph of the paired MZM, unpaired Majorana fermion has been predicted to exist in several models, including the 2CK [148; 192; 53; 154; 89], two impurity Kondo [95; 7] as well as the dissipative (with dissipation $R = R_Q = h/e^2$) resonant level model [135; 195]. In these models, the frustration between two channels induces a degeneracy $\sqrt{2}$ at the impurity, which indicates the existence of an unpaired impurity Majorana fermion. Compared with the paired MZMs experiments, the unpaired Majorana fermion hosted systems are easier to realize experimentally [154; 135; 89] since generically they only require perfect symmetry between different channels. However, this Majorana fermion has been considered as barely effective and is not yet known how to manipulate in nonlocal quantum operations and is thus widely ignored by the community. In this chapter, however, we show that the frustration induced Majorana fermion of the $R = R_Q$ dissipative resonant level model can be experimentally

detected and is helpful in the stabilization of a MZM.

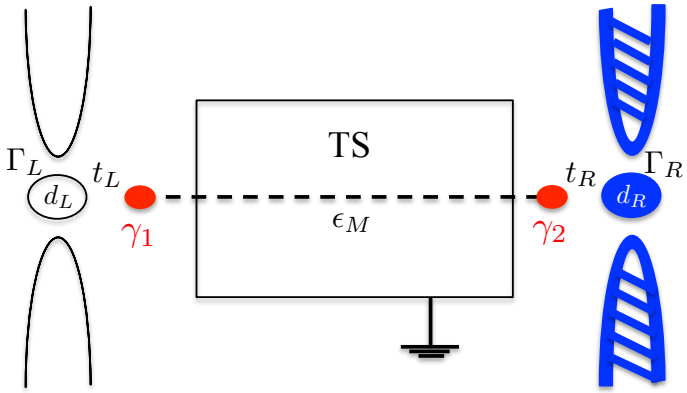

FIGURE 8.1: The structure of the system. Two MZMs γ_1 and γ_2 are realized at two ends of a nanowire on top of a grounded topological superconductor. We calculate the conductance through the left resonant level model to detect the existence of the MZM γ_1. The right resonant level model couples to γ_2 to stabilize γ_1.

The system we consider is shown in Fig. 8.1. Here we place a nanowire on top of a topological superconductor such that two MZMs γ_1 and γ_2 form at two ends of the nanowire. The left resonant level model couples to γ_1 to detect its existence. To stabilize γ_1, we couple a right resonant level model to its partner (γ_2). We calculate the conductance through the left resonant level model to indicate the stability of γ_1 and use the renormalization group (RG) method to physically interpret the result. Based on our calculation, when the right resonant level model is dissipation-free, the MZM γ_1 is partially stabilized, where the inter-MZM coupling is RG marginal. This stabilization of γ_1 is complete if the right resonant level model has dissipation $R = R_Q$, where the zero temperature on-resonance conductance through the left resonant level model always has the Majorana nontrivial value $e^2/2h$.

This chapter is organized as follows. In section 8.2 we provide a review about the realization of Majorana fermions in condensed matter structures. After that, in 8.3 we couple the partner MZM to a resonant level model and show that the coupling between two MZMs becomes marginal. We also use renormalization group and g-

theorem to physically interpret the result. In section 8.4 we show that when a MZM is coupled to the isolated Majorana fermion provided by the dissipative resonant level model, its partner is stabilized in the sense that the probing resonant level model always has the $e^2/2h$ non-trivial zero temperature conductance. In section 8.5 we further verify our result with the full counting statistical technique and show that in the near equilibrium regime quasiparticles tunnel with the effective charge $e^* = e/2$ if the MZM is stabilized. Finally, we summarize this chapter in section 8.6.

8.2 Review of Majorana Fermion in Condensed Matter Physics

For later convenience, here I briefly review the way to realize Majorana fermions in condensed matter structures. This section contains only review material and not my original work.

Majorana fermions have been predicted by E. Majorana as a category of exotic fermions. Unlike ordinary Dirac fermions, Majorana fermions are fermions that coincide with their own anti-particles. Despite the possibility that some particles may be Majorana fermions (for instance, neutrinos), to date there is no indisputable experimental evidence about the existence of Majorana fermions as fundamental particles.

However, without the restriction of being fundamental particles, Majorana fermions naturally exist in condensed matter theories. More specifically, we can always define two operators γ_1 and γ_2 with the Dirac fermionic operators $d^\dagger$ and d

$$\gamma_1 = \frac{d + d^\dagger}{\sqrt{2}}, \quad \gamma_2 = \frac{d - d^\dagger}{i\sqrt{2}}. \tag{8.1}$$

It is straightforward to show that γ_1 and γ_2 obey the anticommutators of Majorana fermions $\{\gamma_i, \gamma_j\} = \delta_{i,j}/2$. Consequently, any Dirac fermionic operator can produce two independent Majorana operators. However, despite of the wide existence of effec-

tive Majorana fermions in condensed matter systems, Majorana fermion signatures are hard to detect.

To begin with, free Majorana fermi "liquid" are extremely difficult to realize due to the instability of Majorana fermions against the inter-Majorana interactions —- interaction between two Majorana fermions leads to the condensation of them into a fermionic singlet [9]. It is thus more practical to realise the delocalized Majorana fermions rather than the Majorana liquids: the interaction between two delocalized Majorana fermions decays exponentially with the increasing distance.

Meanwhile, since Majorana fermions consist of both creation and annihilation operators just as those superconducting quasiparticles, it is natural to expect delocalized Majorana fermions in materials with superconducting pairing interactions. This construction, however, can easily be sabotaged by the fermionic doubling problem: in spin 1/2 systems, spin degeneracy guarantees that the existence of two Majorana fermions at the same place! Once again, these two Majorana fermions are unstable against the hybridization and tend to combine into a Dirac fermion.

Consequently, the detection of Majorana signature requires superconducting effect in spinless fermions, or the p-wave superconductors. Based on those considerations, Kiteav proposed his famous model as presented in Fig. 8.2. This model consists of a finite-size (with $2N$ sites) one-dimensional nanowire placed on top of a p-wave superconductor, with the Hamiltonian

$$H = -\mu \sum_{j=-N}^{N} c_j^\dagger c_j - \frac{1}{2}\sum_j (t c_j^\dagger c_{j+1} + \Delta e^{i\phi} c_j c_{j+1} + h.c.), \tag{8.2}$$

where μ is the chemical potential, t is the neighboring-site tunneling strength, and $\Delta e^{i\phi}$ is the superconducting pairing parameter. We can understand the physics of terms in Eq. (8.2) by considering the Dirac fermionic operator at each site as two independent Majorana operators as in Eq. (8.1): $\gamma_{1,j} = (c_j^\dagger + c_j)/\sqrt{2}$ and $\gamma_{2,j} =$

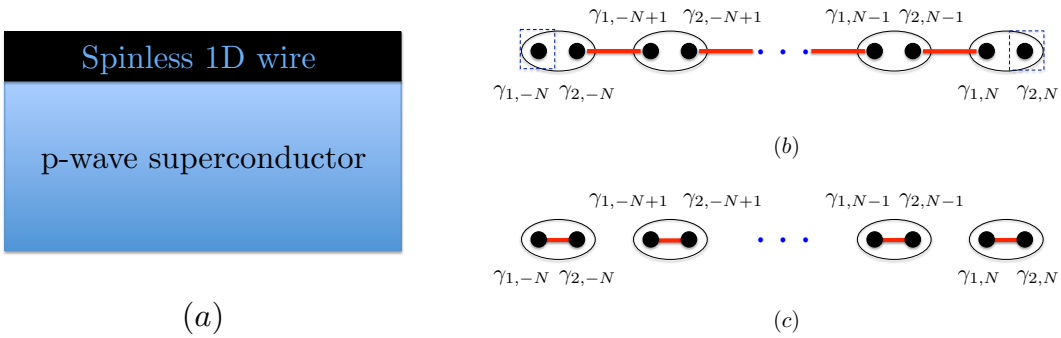

FIGURE 8.2: The famous Kitaev model. (a) The structure of the Kitaev model that consists of a one dimensional spinless wire on top of a p-wave superconductor. (b) (c) Two topologically distinct configurations of the Kitaev model. Here black circles indicate Dirac fermions that contain two Majorana fermions (represented by the black dots). Red lines represent the interaction between Majorana fermions. Majorana fermions from different fermionic sites combine into singlets in (b), leaving two decoupled Majorana zero modes sitting at two ends of the wire (indicated by the dot in the black dashed boxes). Topological doublet degeneracy hence forms due to the decoupled Majorana fermions. On the contrary, in (b) Majorana fermions from the same Dirac fermion recombines into singlets. The ground state is trivially non-degenerate.

$(c_j^\dagger - c_j)/i\sqrt{2}$. With those Majorana fermions, it is easy to see that the chemical potential μ in Eq. (8.2) couples Majorana fermions at the same site, while t and Δ combine Majorana fermions at neighboring sites. More specifically, Eq. (8.2) can be rewritten with these Majorana fermions

$$H = -\frac{\mu}{2}\sum_{j=-N}^{N}(1 + i\gamma_{1,j}\gamma_{2,j}) - \frac{i}{4}\sum_{j=-N}^{N-1}[(\Delta + t)\gamma_{2,j}\gamma_{1,j+1} + (\Delta - t)\gamma_{1,j}\gamma_{2,j+1}]. \quad (8.3)$$

Consequently, if the system is fine tuned $\mu = 0$ and $\Delta = t$, two Majorana fermions $\gamma_{1,-N}$ and $\gamma_{2,N}$ at two ends of the wire decouple from the system, thus forming two isolated Majorana fermions.

Multiple structures are proposed to realize the Kiteav model [9]. One of the simplest structures consists of a one-dimensional nanowire on top of an s-wave superconductor, as shown in Fig. 8.3(a).

In this structure, the fermion doubling problem is solved through the combination

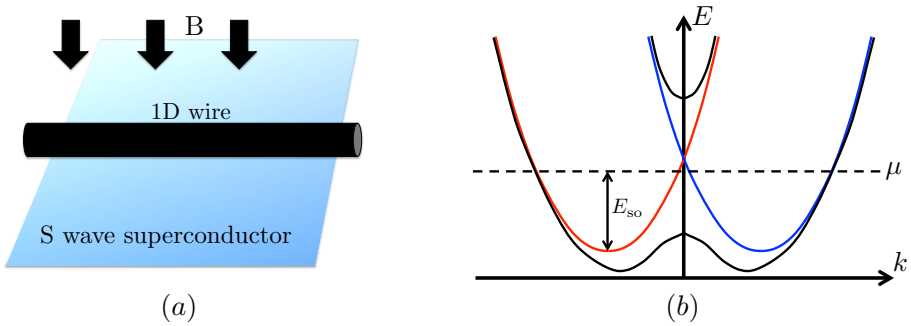

FIGURE 8.3: One of the proposals to experimentally realize the Majorana zero modes. (a) The proposed structure that possibly hosts Majorana zero modes. It consists of a one dimensional nanowire that is proximitized by an s-wave superconductor. The nanowire contains spin-orbit couplings and is under the influence of a magnetic field B applied perpendicular to the wire direction. (b) The energy band of the nanowire when exposed to multiple interactions. The spin orbit coupling breaks the spin degeneracy in the nanowire, leading to two effectively "spinless" channels (represented by red and blue curves). These two independent channels, while influenced by the applied magnetic field, form into two bands separated by a gap. When the chemical potential is tuned within this gap, the lower band corresponds to an effective spinless channel. Thus the proximitized s-wave superconducting pairing becomes effective p-wave pairing in the wire.

of the spin orbit interaction and an applied magnetic field. Those two ingredients opens a gap in the energy spectrum as shown in Fig. 8.3(b). When the chemical potential of the system is tuned to be within the gap, electrons can be effectively considered as spinless. The Cooper pair coupling in the nanowire, on the other hand, is provided by the contact with the superconductor. Superconductor exchanges electrons with the nanowire, leading to the proximitized effective Cooper pairing in the nanowire. The structure in Fig. 8.3 is thus considered as effectively equivalent to the Kitaev model that possibly hosts Majorana at two ends of the nanowire.

To detect the Majorana fermion, two metallic leads are attached at two ends of the nanowire, forming the so called topological Kondo model. In this model, two isolated Majorana fermions form into a topologically protected doublet that corresponds to the spin degeneracy in a real Kondo model [20]. Meanwhile, similar as the Kondo model, with low enough temperature, the topological Kondo model has a $2e^2/h$ zero

bias anomalous conductance peak. This conductance peak is thus considered as the Majorana signature, in contrast to the Andreev reflection induced conductance that varies between zero and $4e^2/h$[1]. First Majorana feature based on this model has been observed by L. Kouwenhoven's group at TU Delft. However, it is not until recently that they have observed the quantized conductance signature [194].

Another way to detect the Majorana fermion is to couple the Majorana-hosted nanowire to the quantum dot of a mesoscopic system [62; 123]. As introduced in Section 8.1, when coupled to a Majorana fermion, the feature of the quantum dot is greatly modified, leading to some peculiar tunneling features in both the Anderson and the Kondo models. However, to our knowledge, those Majorana non-trivial features in all these models are unstable against the coupling between two edge Majorana zero modes, thus leading to the experimental complexity in the observation of Majorana signatures. One of our goals of this chapter, is to demonstrate that quantum frustration can stabilize the non-trivial signature of a resonant level model whose quantum dot has coupled to an edge Majorana zero mode.

8.3 Stabilization of a MZM with a Dissipation-free Resonant Level Model

In this section we study the stabilization of a MZM when its partner couples to a dissipation-free resonant level model. Meanwhile, a large spin polarization is assumed through this paper so that the system is spinless.

8.3.1 the Model and Hamiltonian

The system we consider is shown in Fig. 8.1, where two MZMs at two ends of a topological superconductor proximatized nanowire couple to two resonant level models. The topological superconductor is represented by the rectangle in Fig. 8.1, with the

[1] Since Andreev reflection process is marginal from the RG point of view, its zero temperature conductance varies depending on the junction details.

red small dots representing two Majorana fermions γ_1 and γ_2. Meanwhile, the topological superconducting island is grounded to be free from the charging energy.

To probe the state of γ_1, we place a spinless resonant level model (that is marked as "L", the left resonant level model) and couple one of its impurity Majorana fermions $(d_L + d_L^\dagger)/\sqrt{2}$ to γ_1. The conductance of this MZM-coupled resonant level model has been studied already, where it is proved that the coupling between two MZMs is relevant and will drive the resonant level model away from the non-trivial fixed point (with conductance $e^2/2h$) to the trivial fixed point (with conductance e^2/h) [123]. To stabilize the MZM γ_1, in this section we couple another resonant level model (labeled as "R") to the partner Majorana fermion γ_2.

System Hamiltonian based on the construction of Fig. (8.1) becomes $H = H_{\text{Impurities}} + H_{\text{Leads}} + H_{\text{T}}$ where $H_{\text{Impurities}}$ involves two quantum dots, two MZMs and their interactions

$$\begin{aligned} H_{\text{Impurities}} = \epsilon_L d_L^\dagger d_L + \epsilon_R d_R^\dagger d_R + i\epsilon_M \gamma_1 \gamma_2 \\ + it_L(d_L^\dagger + d_L)\gamma_1 + it_R(d_R^\dagger + d_R)\gamma_2, \end{aligned} \tag{8.4}$$

where $\epsilon_{L,R}$ is the dot energy level, $t_{L,R}$ is the coupling strength between a quantum dot and its corresponding MZM, and ϵ_M is the coupling between two MZMs. For simplicity, we have assumed that both quantum dots are well-tuned such that $\epsilon_L = \epsilon_R = 0$. Notice that in Eq. (8.4) we have assumed that both γ_1 and γ_2 couple to the same type of impurity Majorana fermion $(d^\dagger + d)/\sqrt{2}$. In real experiments, γ_1 and γ_2 couple to random self-conjugate impurity Majorana fermions [2]. However, since these impurity Majorana forms are equivalent when the impurities are well-tuned, we are free to choose the MZM-impurity coupling form in Eq. (8.4) without loss of generality.

[2] In real experiments, the MZM could couple to the impurity Majorana fermion $\eta d + \eta^* d^\dagger$, with any η that satisfies $|\eta| = 1/2$. Based on my knowledge, this parameter η is not yet experimentally controllable.

Next we introduce the lead Hamiltonian and the lead-dot hybridizations

$$\begin{aligned} H_{\text{Leads}} &= \sum_{k,\alpha} \epsilon_k (c^\dagger_{kL\alpha} c_{kL\alpha} + c^\dagger_{kR\alpha} c_{kR\alpha}) \\ H_{\text{T}} &= V_L \sum_{k\alpha} c^\dagger_{kL\alpha} d_L + V_R \sum_{k\alpha} c^\dagger_{kR\alpha} d_R + h.c., \end{aligned} \tag{8.5}$$

where L, R labels the left and right resonant level models and $\alpha = t, b$ labels the top and bottom leads in each model. For simplicity here we have assumed that the quantum dot symmetrically couples to top and bottom leads so that actually the Hamiltonian of Eq. (8.5) describes two independent on-resonance resonant level models.

8.3.2 Equilibrium Conductance

With the model defined in section 8.3.1, we are ready to calculate the zero temperature conductance of the left resonant level model that probes the γ_1 MZM. With symmetric coupling, its equilibrium conductance relates to the impurity spectrum as

$$G_L = -\Gamma_L \frac{e^2}{h} \int \frac{d\omega}{2\pi} \text{Im}[G^R(d_L, d_L^\dagger)(\omega)], \tag{8.6}$$

where $G^R(d_L, d_L^\dagger)(\omega)$ is the Fourier transformed retarded Green's function $G^R(d_L, d_L^\dagger)(t) = -i\Theta(t)\langle \left\{ d_L(0), d_L^\dagger(t) \right\} \rangle$ of the left resonant model and $\Gamma_L = \pi \rho_0 V_L^2$ is its level broadening.

Since system Hamiltonian Eq. (8.5) is quadratic, we can easily calculate the retarded impurity Green's function of the left resonant level model through the equation of motion method [22]

$$G^R(d_L, d_L^\dagger)(\omega) = \frac{1}{\omega + i\Gamma_L - \epsilon_L - \Sigma(\omega)}, \tag{8.7}$$

with $\Sigma(\omega)$ the self energy

$$\Sigma(\omega)^{-1} = \frac{\omega}{t_L^2} - \frac{1}{\omega + \epsilon_L + i\Gamma_L} - \frac{\epsilon_M^2}{t_L^2}\Big(\omega - \frac{t_R^2}{\omega + \epsilon_R + i\Gamma_R} - \frac{t_R^2}{\omega - \epsilon_R + i\Gamma_R}\Big)^{-1}, \tag{8.8}$$

where the first two terms indicate the interaction between the impurity d_L and γ_1, and the last term represents higher order interactions between d_L, γ_2 and the right resonant level model.

With Eqs. (8.6), (8.7) and (8.8), the conductance of the left resonant level model becomes

$$G_L = \frac{e^2}{h}\frac{2t_L^2 t_R^2 + \epsilon_M^2\Gamma_L\Gamma_R}{4t_L^2 t_R^2 + \epsilon_M^2\Gamma_L\Gamma_R}. \tag{8.9}$$

Eq. (8.9) indicates a crossover between the trivial (with conductance e^2/h) and non-trivial (with conductance $e^2/2h$) fixed points. It shows that the presence of the right resonant level model partially stabilizes γ_1 against its coupling to γ_2.

8.3.3 Physical Interpretation of the Conductance

We interpret Eq. (8.9) at different fixed points . We begin with the fixed point where $\epsilon_M = 0$. We call it the non-trivial fixed point since at this point the MZM γ_1 fully captures the impurity Majorana fermion $(d_L + d_L^\dagger)/\sqrt{2}$, producing the non-trivial conductance $e^2/2h$. This conductance has been explained by considering the left resonant level model as two parallel Majorana chains [123]. As shown by Fig. (8.4), if we define lead Majorana fermions as $\alpha_j \equiv (c_j + c_j^\dagger)/\sqrt{2}$ and $\beta_j \equiv i(-c_j + c_j^\dagger)/\sqrt{2}$, the kinetic term of the lead $c_j^\dagger c_{j+1} + h.c.$ becomes $i(-\beta_j\alpha_{j+1} + \alpha_j\beta_{j+1})$, equivalent to the hopping along two independent Majorana chains. Consequently, if $\epsilon_M = 0$, Majorana fermion $(d_L + d_L^\dagger)/\sqrt{2}$ combines with γ_1 into a singlet, blocking the Majorana chain "2" in Fig. (8.4) and decreasing the on resonant conductance by half. Since this

non-trivial conductance origins from the coupling of the impurity to the MZM γ_1, it has been considered as the signal of the MZM.

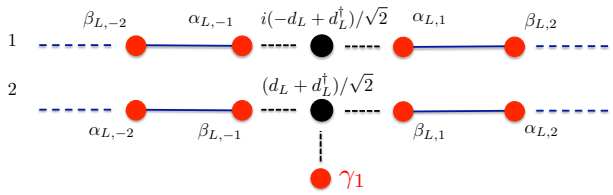

FIGURE 8.4: Two decoupled Majorana chains of the resonant level model. With a fine tuned quantum dot, the resonant level model can be considered as two impurity Majorana fermion chains. Without loss of generality, here we couple the MZM γ_1 to the Majorana channel "2".

The second fixed point resides where $\epsilon_M \neq 0$ and $t_R = 0$. This point has the quantized conductance e^2/h and we thus call it the trivial fixed point. This fixed point corresponds to the ground state of Fig. (8.1) when the left and right parts decouple. Earlier investigation [123] of this fixed point proves that at zero temperature γ_1 and γ_2 form into a singlet, thus breaking the coupling between $(d_L + d_L^\dagger)/\sqrt{2}$ and γ_1. Consequently, the MZM γ_1 fails to capture the Majorana impurity $(d_L + d_L^\dagger)/\sqrt{2}$, leading to a fixed point with trivial conductance e^2/h where the leads completely hybridize the quantum dot. It is also worth noticing that both the trivial and non-trivial fixed points are non-degenerate ground states.

Finally, with $t_R \neq 0$ and $\epsilon_M \neq 0$, the conductance is between $e^2/2h$ and e^2/h. In this regime, γ_1 partially combines with γ_2 and $(d_L + d_L^\dagger)/\sqrt{2}$. The MZM-decoupled impurity degrees of freedom hybridizes with the leads so that the final ground state is also non-degenerate. This non-degeneracy feature at every point indicates a crossover between the non-trivial and trivial fixed points. Meanwhile, the comparison between Eq. (8.9) and the conductance of the trivial fixed point ($t_R = 0$) shows that the coupling between γ_2 and the right resonant level model partially stabilizes the MZM γ_1 against the hybridization with its partner.

To understand the physics, notice that there are two competing processes. First

one is the ϵ_M term which tends to combine γ_1 and γ_2. This process is accompanied by the impurity-lead hybridization $\Gamma_{L,R}$ that tends to smooth out the quantum impurities so that ϵ_M is dressed by $\sqrt{\Gamma_L\Gamma_R}$. As its competitor, γ_1 and γ_2 choose to combine with $(d_L + d_L^\dagger)/\sqrt{2}$ and $(d_R + d_R^\dagger)/\sqrt{2}$, respectively, breaking half of the tunneling channels. The combination of those two processes forms a crossover between the trivial and non-trivial fixed points, leading to the conductance Eq. (8.9).

We can also understand Eq. (8.9) from the view point of renormalization group. We begin with the case with an unstable MZM where $t_R = 0$. When $\epsilon_M = 0$ and $t_L \neq 0$, γ_1 and $(d_L + d_L^\dagger)/\sqrt{2}$ form into a singlet at zero temperature. This singlet, however, will be weakly destabilized if we turn on a small ϵ_M and thus enabling the hopping between $\alpha_{L,\pm1}$ and $(d_L + d_L^\dagger)/\sqrt{2}$ in Fig. 8.4. This hopping process has scaling dimension 1/2 so that it increases and finally cuts the coupling between γ_1 and $(d_L + d_L^\dagger)/\sqrt{2}$. The relevance of ϵ_M indicates the RG flow from the non-trivial to the trivial fixed point without the presence of t_R.

The RG flow above changes when $t_R \neq 0$. To better understand it, we start with the situation where $\epsilon_M \ll t_L, t_R$. In this case, $\gamma_{1,2}$ combines with $(d_{L,R} + d_{L,R}^\dagger)/\sqrt{2}$ into a singlet. If we call this ground state as $|0\rangle_L \otimes |0\rangle_R$ [here $|0\rangle_{L,R}$ is the ground state formed by two Majorana fermions $(d_{L,R} + d_{L,R}^\dagger)/\sqrt{2}$ and $\gamma_{1,2}$, whose exact form depends on the sign of $t_{L,R}$], then a finite ϵ_M changes this ground state to be a linear combination of $|0\rangle_L \otimes |0\rangle_R$ and $|1\rangle_L \otimes |1\rangle_R$ [3], with $|1\rangle$ the excited state formed by two Majorana fermions. Consequently, only higher order hybridization operators are possible where tunnelings at both resonant level models happen simultaneously. This coherent tunneling formalism has twice the scaling dimension of that of the single tunneling process (1/2 as given before) so that the hybridization becomes marginal.

As a summary, with the presence of the right resonant level model, ϵ_M becomes

[3] The missing of states $|0\rangle_L \otimes |1\rangle_R$ and $|1\rangle_L \otimes |0\rangle_R$ originates from the fact that the operator $\gamma_1\gamma_2$ flips the fermion parity at each side simultaneously.

marginal, with the effective value $\epsilon_M\sqrt{\Gamma_L\Gamma_R}/t_R$. Due to this feature, experimentally we can decrease the effect of ϵ_M by decreasing the level broadening Γ_L and Γ_R, thus approaching the non-trivial $e^2/2h$ conductance. However, by doing so, one needs a lower temperature for the system to arrive at the resonant regime. An alternative option is to increase the competing process of ϵ_M by increasing t_L and t_R.

8.4 Stabilize the MZM with Quantum Frustration

In last section we have shown that the presence of the right resonant level model stabilizes γ_1 by coupling one of its impurity Majorana fermions to γ_2. However, since this impurity Majorana fermion also couples to a hybridization channel, its coupling to γ_2 is only marginal so that a crossover forms between two fixed points with conductance $e^2/2h$ and e^2/h, respectively.

To further stabilize γ_1, one natural idea is to couple γ_2 to an isolated Majorana fermion instead of a lead-hybridized quantum dot —- this can be seen by taking $\Gamma_R = 0$ in Eq. (8.9), where ϵ_M becomes irrelevant.

This isolated Majorana fermion, as has been introduced in the introduction, is known to exist in a 2CK model. More specifically, the frustration between two channels leaves an effective Majorana fermion $(d + d^\dagger)/\sqrt{2}$ untouched, where $d \equiv iS_x - S_y$ [165] is the effective fermionic operator and S_σ is the Pauli matrix of the impurity spin. However, due to its spin operator nature, this effective Majorana fermion will not naturally couple with γ_2 into a singlet. To solve this problem, here we generate the isolated Majorana fermion with a dissipative quantum dot model with $R = R_Q$. This model has been proved in Chapter 7 to be equivalent to the 2CK model and the Luttinger liquid resonant level model with Luttinger liquid interaction $g = 1/2$, and it thus hosts a real decoupled impurity Majorana fermion. Since this Majorana fermion is "real", its coupling to γ_2 can be naturally treated as the standard Majorana coupling. For clarification, by calling it "real", we are

emphasizing that this Majorana fermion is different from that in a spin 2CK model, whose Majorana fermion consists of spin operators (for details see Section 4.4). It is thus more complicated to couple the MZM to the effective Majorana fermion in the spin 2CK model.

Consequently, here we choose to further stabilize γ_1 by coupling γ_2 to a dissipative $R = R_Q$ resonant level model. For later convenience we define the frustration-induced Majorana fermion that decouples with the leads as $\chi_1 = (d_R + d_R^\dagger)/\sqrt{2}$ and the lead-hybridized one as $\chi_2 = i(-d_R + d_R^\dagger)/\sqrt{2}$. Notice that unlike that of the dissipation-free case, χ_1 and χ_2 are now inequivalent.

To proceed, it is known that at zero temperature, the on resonant $R = R_Q$ dissipative resonant level model flows to a point where only the charge flavor field couples to the quantum dot, leaving the charge field decoupled [171; 103; 195]. We thus introduce the refermionization of the charge flavor field

$$\psi_f^\dagger(x) \equiv \frac{F}{\sqrt{2\pi a_0}} e^{-i\phi_f(x)}, \tag{8.10}$$

with a_0 the lattice constant and $\phi_f(x) = [\phi_{R,t}(x) - \phi_{R,b}(x)]/\sqrt{2}$ is the charge flavor boson after the bosonization of the right resonant level model [195]. With the definition of the charge flavor operator, the effective Hamiltonian becomes

$$\begin{aligned}
H_{\text{Leads}} &= \sum_{k,\alpha} \epsilon_k c_{kL\alpha}^\dagger c_{kL\alpha} + \sum_k \epsilon_k \psi_{k,f}^\dagger \psi_{k,f} \\
H_{\text{T}} &= V_L \sum_{k,\alpha} (c_{kL\alpha}^\dagger d_L + h.c.) \\
&\quad + i\sqrt{2} V_R \sum_k (\psi_{k,f}^\dagger + \psi_{k,f}) \chi_2 \\
H_{\text{impurities}} &= \epsilon_L d_L^\dagger d_L + i\epsilon_R \chi_1 \chi_2 + i\epsilon_M \gamma_1 \gamma_2 \\
&\quad + i t_L (d_L^\dagger + d_L)\gamma_1 + i t_{R1} \chi_1 \gamma_2 + i t_{R2} \chi_2 \gamma_2.
\end{aligned} \tag{8.11}$$

Notice that in Eq. (8.11) the MZM γ_2 couples to both χ_1 and χ_2 with strengths t_{R1} and t_{R2}, respectively —- since χ_1 and χ_2 are inequivalent, we must use the most general form. In this model we only need particle-hole symmetry at the right resonant level model $\epsilon_R = 0$. We do not need a well-tuned ϵ_L since the left dot detuning is RG irrelevant with $\epsilon_M \neq 0$.

The Hamiltonian Eq. (8.11) is again quadratic and can be easily solved with equation of motion method [22]. The conductance through the left resonant level model becomes

$$G_L = e^2/2h, \tag{8.12}$$

which is independent of the value of t_{R2} or ϵ_M. Conductance of Eq. (8.12) is the main result of this chapter, which indicates that the introduction of the $R = R_Q$ resonant level model stabilizes γ_1. Meanwhile, the independence from t_{R2} of Eq. (8.12) shows that t_{R2} is less relevant compared with t_{R1} so that experimentally one does not need to fine tune the coupling between γ_2 and the right dot. Also notice that Eq. (8.12) is only valid with $\epsilon_M \ll \Delta, \Gamma_R$, where Δ is the superconducting gap in the proximitized nanowire and Γ_R is the level broadening of the right resonant level model — this is the prerequisite to arrive at the regime where Eq. (8.11) faithfully describes the system.

Now we try to understand this result by considering the RG flow in several limits. To begin with, we consider the regime $t_{R1} \gg t_{R2}$ where γ_2 and χ_1 forms into a singlet that is disturbed by t_{R2}. At this point, the low temperature conductance through the left resonant level model is $e^2/2h$ since ϵ_M is irrelevant with finite t_{R1}. To determine its stability, we notice that at this fixed point, the right part of the system (that consists of γ_2 and the right resonant level model) is effectively the same as the left part in Fig. (8.1) with $t_R = 0$ through the substitution $t_{R1} \to \epsilon_M$ and $t_{R2} \to t_L$. More specifically, t_{R1} now behaves effectively as the inter-MZM hybridization and

t_{R2} behaves as the dot-MZM hybridization. Consequently, with similar explanation as in Section 8.3, we know that t_{R2} is irrelevant so that this fixed point is stable.

As the opposite extreme limit, when $t_{R1} \ll t_{R2}$ we can approximately ignore the effect of t_{R1} in high-temperature RG flows so that χ_2 is partially screened by the lead and partially coupled to γ_2. Similar as the physics in Section 8.3, these two processes have the same scaling dimension so that their competition leads the system to some non-degenerate ground state with the conductance through the probing resonant level model between $e^2/2h$ and e^2/h. To study the stability of these fixed points against the coupling t_{R1}, we further assume $t_{R2} \gg \epsilon_M$. In this case, the coupling t_{R1} between γ_2 and χ_1 once again mimics the effect of ϵ_M in Fig. 8.1 with $t_R = 0$ so that it is relevant. At the opposite limit, if $t_{R2} \ll \epsilon_M$, we can basically drop γ_2 and the ψ_f chain that screens it. In this case, the model reduces to the system of Fig. 8.1 with $\Gamma_R = 0$ where t_{R1} is known to be relevant.

Consequently, t_{R1} is always more relevant than t_{R2} so that we can drop the $it_{R2}\gamma_2\chi_2$ term in Hamiltonian Eq. (8.11) if we are only interested in the low temperature physics. We can also understand the analysis above from the g-theorem [5]: only when γ_2 and χ_1 form into a singlet can the system arrive at a non-degenerate ground state.

The analysis above guarantees that experimentally we do not need to fine tune t_{R1} or t_{R2}.

8.5 Full Counting Statistics

To further support the analysis in previous sections, here we calculate the current and shot noise of the model at different fixed points with full counting statistics [121; 73; 101].

In this section, we drop t_{R2} from system Hamiltonian for simplicity since t_{R2} is irrelevant with finite t_{R1}. Strictly speaking, t_{R2} only appears in higher order terms

and will not change the physics of the fixed point so that it is reasonable to drop it unless the leading term vanishes. Meanwhile, since we are calculating Green's functions of the left resonant level model, we simplify the notation by taking $d_L \to d$, $\gamma_1 \to \gamma$ and $\Gamma_L \to \Gamma$.

8.5.1 Full Counting Statistic in the Majorana Fermion-Coupled Resonant Level Model

We begin with some preliminaries of the full counting statistics method. In full counting statistics, one calculates the current and noise through the generating function $\chi(\lambda) = \sum_q e^{iq\lambda} P_q$ where P_q is the probability that charge qe transfers during the measuring time τ and λ is the measuring field. Through this generating function, we can calculate current and shot noise with

$$I = \frac{e\langle \delta q \rangle}{\tau}, \quad \text{and} \quad S = \frac{2e^2\langle \delta^2 q \rangle}{\tau}, \tag{8.13}$$

where

$$\langle \delta^n q \rangle = (-i)^n \frac{\partial^n}{\partial \lambda^n} \ln \chi(\lambda) \mid_{\lambda=0} . \tag{8.14}$$

Here we calculate the generating function with the expression $\ln \chi(\lambda) = -i\tau U(\lambda, -\lambda)$, where $U(\lambda, -\lambda)$ is the adiabatic potential. In our case, the adiabatic potential of the left resonant level model becomes

$$\begin{aligned} \frac{\partial}{\partial_{\lambda_-}} U(\lambda_-, \lambda_+) = \frac{\gamma_L^2}{2} \int d\omega [& e^{-i(\lambda_- - \lambda_+)/2} G^{-+} g_L^{+-} \\ & - e^{i(\lambda_- - \lambda_+)/2} g_L^{-+} G^{+-}], \end{aligned} \tag{8.15}$$

where G^{+-} (G^{-+}) is the full greater (lesser) impurity Green's function and g_L is the bare lead Green's function with the expressions [73; 101]

$$\begin{aligned} g_\alpha^{--}(\omega) &= g_\alpha^{++}(\omega) = i2\pi\rho_0(n_\alpha - 1/2), \\ g_\alpha^{-+}(\omega) &= i2\pi\rho_0 n_\alpha, \\ g_\alpha^{+-}(\omega) &= -i2\pi\rho_0(1 - n_\alpha), \end{aligned} \tag{8.16}$$

where $n_{t,b} = n_F(\epsilon \pm V/2)$ is the distribution function of the leads and $V > 0$ is the bias between the top and bottom leads. Here we take ρ_0 as the constant density of states. At zero temperature, we take $n_t = \Theta(-\epsilon - V/2)$ and $n_b = \Theta(-\epsilon + V/2)$ for simplification. With the lead Green's function in Eq. (8.16), we only need to calculate the lesser and greater Green's functions.

To calculate the complete lesser Green's function, we first divide the system Hamiltonian into $H = H_0 + \delta H$, where H_0 is the spinless Anderson model Hamiltonian of the left resonant level model and δH is its coupling to the rest parts of the system. With this choice, the "interacting" Hamiltonian δH becomes purely equilibrium.

The system H_0 has been solved with its Green's functions already known [73]

$$G_0(\omega) = \frac{1}{\omega^2 + \Gamma^2 e^{i\lambda}} \begin{pmatrix} \omega - i\Gamma & ie^{i\lambda}\Gamma \\ -i\Gamma & -\omega - i\Gamma, \end{pmatrix}, \tag{8.17}$$

with the four entries referring to the retarded, lesser, greater and advanced Green's functions of the impurity of the left resonant level model.

With interaction δH, the complete lesser Green's function relates to other Green's functions through [168]

$$\begin{aligned} G^< &= G^R \Sigma^< G^A \\ &\quad + (1 + G^R \Sigma^R) G_0^< (1 + \Sigma^A G^A). \end{aligned} \tag{8.18}$$

In our case, $\Sigma^< = 0$ [101; 73] so that based on Eq. (8.18), our targeted Green's function becomes

$$\begin{aligned} G^<(d, d^\dagger)(\omega) = G_0^<(d, d^\dagger)(\omega) &+ G^R(d, \gamma)\Sigma_{\gamma,d} G_0^<(d, d^\dagger)\Sigma_{d^\dagger,\gamma} G^A(\gamma, d^\dagger)(\omega) \\ &+ G^R(d, \gamma)\Sigma_{\gamma,d^\dagger} G_0^<(d^\dagger, d)\Sigma_{d,\gamma} G^A(\gamma, d^\dagger)(\omega) \\ &+ G^R(d, \gamma)(\omega)\Sigma_{\gamma,d} G_0^<(d, d^\dagger) + G_0^<(d, d^\dagger)\Sigma_{d^\dagger,\gamma} G^A(\gamma, d^\dagger)(\omega) \end{aligned} \tag{8.19}$$

where we have dropped all zero terms. Now, with the interactions $\Sigma_{d^\dagger,\gamma} = \Sigma_{\gamma,d} = -\Sigma_{\gamma,d^\dagger} = -\Sigma_{d,\gamma} = t_L$ and impurity Green's function

$$G_0^<(d^\dagger, d)(\omega) = \frac{-i\Gamma e^{-i\lambda}}{\omega^2 + \Gamma^2 e^{-i\lambda}} \tag{8.20}$$

known, we can calculate the adiabatic potential from Eq. (8.19) after acquiring the expression of $G^R(d,\gamma)(\omega)$ and $G^A(\gamma, d^\dagger)(\omega)$.

These two Green's functions can be calculated with Dyson equation $G^R(\omega) = G_0^R(\omega) + G_0^R(\omega)\Sigma^R G^R(\omega)$ [101]

$$\begin{aligned}
G^R(d,\gamma)(\omega) &= 0 + G_0^R(d, d^\dagger)(\omega)\Sigma_{d^\dagger,\gamma} G^R(\gamma,\gamma)(\omega) \\
G^R(\gamma,\gamma)(\omega) &= G_0^R(\gamma,\gamma)(\omega) \\
&\quad + G_0^R(\gamma,\gamma)(\omega)\Sigma_{\gamma,d} G^R(d,\gamma)(\omega) \\
&\quad + G_0^R(\gamma,\gamma)(\omega)\Sigma_{\gamma,d^\dagger} G^R(d^\dagger,\gamma)(\omega) \\
G^R(d^\dagger,\gamma)(\omega) &= 0 + G_0^R(d^\dagger, d)(\omega)\Sigma_{d,\gamma} G^R(\gamma,\gamma)(\omega).
\end{aligned} \tag{8.21}$$

Now, we substitute the Green's functions solved from linear equations Eq. (8.21) into Eqs. (8.15) and (8.19), we get the adiabatic potential and from which we know the current and the shot noise.

In the rest part of this section, we expand the the expressions of current and shot noise to the third order of the bias since the complete expressions are quite complicated. To validate the expansion, here we also assume that the bias V is much less than any other relevant energy scales.

8.5.2 Non-interacting MZMs ($\epsilon_M = 0$)

We begin with the simple case $\epsilon_M = 0$. In this case, γ_1 is free from its partner γ_2 so that the left resonant level model has the non-trivial $e^2/2h$ equilibrium conductance at zero temperature.

The current calculated from the adiabatic potential in this case becomes

$$I(V) = \frac{e^2}{h}[\frac{V}{2} - (\frac{1}{\Gamma^2} - \frac{\Gamma^2}{4t_L^4})\frac{1}{24}V^3 + O(V^4)], \tag{8.22}$$

where $O(V^4)$ indicates ignored higher order terms with respect to bias.

We can see several features from Eq. (8.22). To begin with, the equilibrium conductance calculated from Eq. (8.22) is $e^2/2h$, which agrees with the result in Eq. (8.9) with $\epsilon_M = 0$. A more interesting feature happens at the $O(V^3)$ term, where we can see the competition between the backscattering in the healed chain and the trial of the broken chain to hybridize $(d_L + d_L^\dagger)/\sqrt{2}$. More specifically, when $\Gamma^2 > 2t_L^2$ the screening processes is stronger so that the $O(V^3)$ current increases with an increasing bias and vice versa. Meanwhile, the singularity of Eq. (8.22) at $t_L = 0$ indicates that t_L is relevant in the $\epsilon_M = 0$ situation.

And at this point, the shot noise becomes

$$S = 2\frac{e^3}{h}[\frac{V}{4} + (-\frac{1}{\Gamma^2} - \frac{\Gamma^2}{4t_L^4} + \frac{1}{t_L^2})\frac{V^3}{48} + O(V^4)], \tag{8.23}$$

with the leading term proportional to bias. This linear term indicates a non-perfect transmission process at zero temperature. We also see the competing feature as in the current —- when $\Gamma^2 > 2t_L^2$, the screening of the impurity is more important so that the $\propto V^3$ noise term decreases with increasing bias and vice versa. This result is consistent with the current calculated in Eq. (8.22).

We also notice that near equilibrium, the Fano factor is 1/2, implying the transmission with quasi-particle $e^* = e/2$ at zero temperature. Similar as the charge 2CK case [113], here the $e^* = e/2$ fractional charge feature origins from the fact that one lead Majorana chain (chain "1" in Fig. 8.4 in our case) decouples with the impurity. However, in contrast to their case, here the Fano factor is defined with respect to the tunneling current instead of the "backscattering current" [113].

8.5.3 *Interacting MZMs ($\epsilon_M \neq 0$) and Decoupled right resonant level model ($t_R = 0$)*

Now we add back the interaction between two MZMs.

The current calculated with the full counting statistics method now becomes

$$I(V) = \frac{e^2}{h}[V - \frac{1 + 2t_L^2/\epsilon_M^2 + 2t_L^4/\epsilon_M^4}{12\Gamma^2}V^3 + O(V^4)], \tag{8.24}$$

which has the equilibrium conductance e^2/h that is different from Eq. (8.22) and agrees with the expectation in previous sections.

Meanwhile, in contrast to Eq. (8.22), the term proportional to V^3 is always larger than the backscattering-induced current. This extra decreasing of current originates from the coupling between γ_1 and $i(d_L + d_L^\dagger)/\sqrt{2}$ with the presence of bias. Finally, the singularity with a vanishing ϵ_M indicates the RG relevance of the inter-MZM coupling, as has been predicted.

Next is the shot noise

$$S = 2\frac{e^3}{h}[(\frac{t_L^4}{\epsilon_M^4} + 1)\frac{V^3}{12\Gamma^2} + O(V^4)]. \tag{8.25}$$

Compared with Eq. (8.23), the most significant feature of Eq. (8.25) is the missing of the term proportional to V, which indicates a perfect equilibrium tunneling at zero temperature. Meanwhile, the shot noise in Eq. (8.25) contains both backscattering-induced noise and that generated by the coupling between γ_1 and $i(-d_L + d_L^\dagger)$. Those two features are consistent with the current expression Eq. (8.24).

Since the linear term in the shot noise vanishes, here the quasiparticle charge can be defined as the ratio between shot noise and twice the value of the "backscattering current" as in the charge 2CK model [113]. From Eqs. (8.24) and (8.25), we can see that the quasiparticle charge is a function that depends on the ration t_L/ϵ_M, varying between $e^* = e/2$ and $e^* = e$: in contrast to the resonant level model where electron backscattering is the leading irrelevant process, here the leading irrelevant

term consists of a combination of electron backscattering and the Majorana coupling between γ_1 and $i(-d_L + d_L^\dagger)$.

Notice that since the leading term (term $\propto V$) of the shot noise vanishes at this point, strictly speaking one needs to include the coupling t_{R2} and the term with scaling dimension 3/2 in the effective 2CK model into the calculation of the Fano factor. This correction, however, is irrelevant to the topic of this chapter and is thus ignored.

8.5.4 Interacting MZMs ($\epsilon_M \neq 0$) stabilized by frustration ($t_R \neq 0$)

Comparison between the results from sections 8.5.2 and 8.5.3 further verifies our analysis that the coupling between two pairing MZMs is relevant and will destroy the Majorana signature when one MZM is detected by a resonant level model. In this section we add the frustration-induced Majorana fermion χ_1 and show that it can stabilize the probed MZM.

In this case, current becomes

$$\begin{aligned} I(V) = \frac{e^2}{h}[\frac{V}{2} + (\frac{\epsilon_M^4\Gamma^2}{t_L^4 t_R^4} + \frac{2\epsilon_M^2\Gamma^2}{t_L^4 t_R^2} + \frac{\Gamma^2}{t_L^4} - \frac{4}{\Gamma^2})\frac{V^3}{96} \\ + O(V^4)]. \end{aligned} \tag{8.26}$$

As can be seen, Eq. (8.26) reduces to Eq. (8.22) simply by taking $\epsilon_M = 0$. This results verifies our analysis that the presence of χ_1 stabilizes the γ_1 MZM against the inter-MZM coupling so that the zero temperature conductance has the non-trivial Majorana feature.

Now shot noise becomes

$$\begin{aligned} S = 2\frac{e^2}{h}[\frac{V}{4} + (-\frac{1}{4\Gamma^2} - \frac{\Gamma^2}{16t_L^4} + \frac{1}{4t_L^2} \\ - \frac{\epsilon_M^4\Gamma^2}{16t_L^4 t_R^4} - \frac{\epsilon_M^2\Gamma^2}{8t_L^4 t_R^2} + \frac{\epsilon_M^2}{4t_L^2 t_R^2})\frac{V^3}{12} + O(V^4)], \end{aligned} \tag{8.27}$$

which also reduces to Eq. (8.23) by simply taking $\epsilon_M = 0$. And we have also reproduced the $e^* = e/2$ fractional charge feature as that in the $\epsilon_M = 0$ case.

Based on the results above, we have verified our argument in previous sections that the isolated Majorana fermion χ_1 stabilizes the MZM γ_1 against its coupling to γ_2 and experimentally one can use the left resonant level model to detect γ_1.

8.6 summary

We analyze a model where the quantum dot of a resonant level model couples to a MZM to probe the state of this MZM. It is known that the non-trivial signature of this MZM —- the $e^2/2h$ zero temperature conductance of the resonant level model is unstable against the hybridization between the MZM and its partner. We showed that this unstable signature becomes marginal by coupling the partner MZM to the impurity of another resonant level model. We further demonstrate that if this resonant level model is dissipative with $R = R_Q$, it can be effectively considered as the isolated Majorana fermion generated by the frustration between two screening channels. When coupled to the partner MZM, this frustration induced Majorana fermion will further stabilize the probed MZM, thus stabilizing the Majorana-featured $e^2/2h$ conductance.

To verify our demonstration, we calculate both the near equilibrium conductance and shot noise. We also use the RG method and g-theorem to interpret the physics of our result —- briefly, this stabilization origins from the effort of the system to arrive at a non-degenerate ground state by coupling the partner MZM and the isolated Majorana fermion into a singlet.

Based on those results, we have shown that the long-ignored frustration generated Majorana fermion in a dissipative resonant level model is detectable. This isolated Majorana fermion is also useful in the stabilization of a MZM against the coupling to its partner.

9

Conductance Behavior of a Dissipative Anderson Model

We study the on-resonance conductance of a dissipative Anderson model. Unlike that of the resonant level model, the on-resonance conductance peak of an Anderson model happens far away from the particle-hole symmetric point. The lack of the particle-hole symmetry protection thus leads to the shifting of the on-resonance peak position as a function of the applied bias. Meanwhile, the on-resonance peak conductance varies as a function of the dissipation strength, in strong contrast to the invariant e^2/h peak conductance of the resonant level model. We provide an understanding of the shifting of the on-resonance point of the dissipative Anderson model with RG equations. Meanwhile, we explain the dissipation-dependent peak value by mapping the model to a two-dimensional quantum Brownian motion (QBM) model, where a stable intermediate fixed point is predicted to exist. Our theoretical result qualitatively agrees with the experimental data provided by Professor Gleb Finkelstein's group[1].

[1] All experimental data comes from experiments by Chung-Ting Ke et al from Professor Gleb Finkelstein's group. This chapter only provides theoretical explanation.

9.1 Introduction

As has been introduced in Section 4.3.1, the Anderson model [16] is a simple mesoscopic model that consists of free leads, a quantum dot, and the lead-dot hybridization. Despite its simple appearance, the Anderson model involves two interesting physical phenomena, including the localizing influence from Coulomb interactions and the formation of an electronic resonance [42]. Originally, the Anderson model is introduced to study the interaction between electrons in a Fermi sea and an immersed ion [42].

More recently, the Anderson model has also been applied to describe the system where a quantum dot is embedded between two leads or reservoirs. The model has been introduced in Section 4.3.1, with system Hamiltonian Eqs. (4.6), (4.7) and (4.8). Instead of the magnetic impurity, a quantum dot contains more energy levels. However, with low enough temperature and high enough onsite interaction, a quantum dot can be considered as having only one relevant level with impurity operators d and $d^\dagger$. In the Anderson model, the dot-lead interaction t [of Eq. (4.8)] is normally considered as a momentum independent constant.

As introduced in Section 4.3.1, by tuning the quantum dot energy ϵ_d the system enters different regimes, including the famous Kondo regime where charge tunneling occurs through second-order Kondo exchange processes. This regime has been thoroughly studied with [63] or without dissipation present [19].

Another interesting point is the resonant tunneling point $\epsilon_d = 0$. Compared with the Kondo regime, this resonant tunneling regime, especially under the influence of dissipation, has not been well studied, either theoretically or experimentally. In this chapter, I thus provide an analytical study of the on-resonance regime of the dissipative Anderson model. The experimental data contained in this section is provided by Prof. Gleb Finkelstein's group.

9.1.1 *Introduction to the Quantum Brownian Motion Model and Its Connection to the Mesoscopic Models*

For later convenience, we postpone a little bit to introduce the QBM model that is relevant in the understanding of the dissipative resonant level model and dissipative Anderson model.

The Brownian motion was observed in 1827 and named after R. Brown who noticed the random motion of pollen suspended in water. Since its discovery, the Brownian motion has been widely studied with various methods, including the Boltzmann equation and the Langevin equation. For instance, the Langevin equation models the Brownian motion as [59]

$$M\ddot{q} + \eta\dot{q} + \frac{\partial V}{\partial q} = \xi(t), \tag{9.1}$$

where q is the position of the "pollen particle", $V(q)$ is the external potential and the "randomness" is incorporated by the fluctuating force that obeys $\langle\xi(t)\rangle = 0$ and $\langle\xi(t)\xi(t')\rangle = 2\eta T\delta(t-t')$. Unlike the classical Brownian motion model whose randomness disappears at zero temperature $T = 0$, the QBM model studies the behavior of a single particle under the influence of dissipative forces. The Hamiltonian of the most general QBM model consists of three parts: the single particle Hamiltonian under the potential $V(q)$, the reservoir Hamiltonian (dissipation) and the Hamiltonian that models their interactions. In principle, given the details of the particle potential, reservoir parameters and the interaction details, the QBM model can be solved through the Feynman-Vernon theory, which incorporates the influence of the reservoir modes onto the particle through a partial trace [25].

However, in reality the interactions are generally too complicated to be solved analytically. To overcome this complexity, one choice is to assume a weak particle-reservoir coupling. With this assumption, the reservoir can be considered as a collection of simple harmonic bosonic modes that are weakly coupled to the particle [25].

More specifically, the 1d QBM model that describes the motion of a particle that is weakly affected by the dissipative environment has the Hamiltonian

$$H_{\rm QBM} = \frac{P^2}{2M} + V(Q) + \sum_\alpha \frac{p_\alpha^2}{2m_\alpha} + \frac{1}{2}\sum_\alpha m_\alpha \omega_\alpha^2 \Big(x_\alpha + \frac{\lambda_\alpha}{m_\alpha \omega_\alpha^2} Q\Big)^2, \tag{9.2}$$

where $V(Q)$ is the potential of a free particle at position Q, and P is the particle momentum operator. As described above, the reservoir is modeled by a collection of bosonic modes with mass m_α and frequency ω_α. They couple to the particle position with strength λ_α as shown in the last term of Eq. (9.2). With the simplified Eq. (9.2), both the reservoir and the particle-reservoir interactions are quadratic so that the environment can be exactly integrated out. In this chapter we use the periodic potential $V(q) = \cos[2\pi q(\tau)/q_0]$, with q_0 the lattice constant. With those assumptions, at zero temperature, the effective action of the QBM model becomes [59]

$$S = \int_0^\infty d\tau \frac{M}{2}\dot{q}^2(\tau) - V\int_0^\infty d\tau \cos\Big(\frac{2\pi q(\tau)}{q_0}\Big) + \frac{\eta}{4\pi}\int_0^\infty d\tau \int_{-\infty}^\infty d\tau' \Big[\frac{q(\tau)-q(\tau')}{\tau-\tau'}\Big]^2, \tag{9.3}$$

where we have taken $\beta = 1/T \to \infty$ and $\hbar = 1$ for simplicity. In Eq. (9.3), the first and second terms are the free particle Hamiltonian, and the third term $\propto \eta$ is the interaction from the dissipative environment. To see the connection between the QBM model and the Luttinger liquid model, it is convenient to define the bosonic field factor $\phi(\tau) = 2\pi q(\tau)/q_0$ and the effective dissipation strength $\eta_e = e\eta q_0^2/2\pi$: after that, the effective QBM model in the bosonic form becomes

$$S = \frac{1}{2}\int \eta_e \frac{d\omega}{4\pi^2}|\omega||\phi(\omega)|^2 - V\int d\tau \cos[\phi(\tau)], \tag{9.4}$$

where the first part has been written with frequency instead of time variables. Eq. (9.4) has the basic form of a boundary Sine-Gordon model and the effective

0d action of a single barrier Luttinger liquid model [Eq. (3.16)]. Consequently, we have built up the connection between the QBM model and the mesoscopic systems. More specifically, with small V, Eq. (9.4) describes a particle that is approximately free in the k space and has a small chance $\propto V$ to change its momentum by $2\pi/q_0$. The RG relevance of this tunneling term is determined by the dissipation strength η_e. This is mathematically equivalent to the single barrier Luttinger liquid model with a small tunneling strength [186; 87]. The close connection between the QBM model and mesoscopic models thus enables us to better understand the I-V feature of the dissipative Anderson model.

9.1.2 Organization of this Chapter

This chapter is organized as follows. We begin with the introduction of the Hamiltonian of the dissipative Anderson model in Section 9.2. We will also briefly introduce the experimentally observed I-V curve of this model at the end of this section. This is followed by the RG study of the system in Section 9.3, which qualitatively explains the position shifting of the on-resonance peak. After that, in Section 9.4 we provide a physical picture to interpret the dissipation dependent on-resonance conductance. In this chapter we show that the dissipative Anderson model maps to a two dimensional QBM model, where a stable intermediate fixed point exists. With different dissipation, this stable intermediate fixed point changes and has a different mobility, thus leading to the change of the conductance in the dissipative Anderson model. Finally we conclude this chapter in Section 9.5.

9.2 System Hamiltonian

To begin with, the system Hamiltonian of the dissipative Anderson model simply consists of five parts $H = H_{\rm lead} + H_{\rm dot} + H_{\rm T} + H_{Kondo} + H_{\rm env}$. The last part is the dissipative environment. As has been introduced multiple times, $H_{\rm env}$ grants

dynamics to the dissipative phase and it is thus more convenient to work with its action form [the dynamics of the dissipative phase has been discussed in Section 2.3.3]

$$S_{env} = \frac{1}{2r}\frac{1}{\beta}\sum_{n}|\omega_n||\varphi(\omega_n)|^2. \tag{9.5}$$

The free lead is described by the Hamiltonian $H_{\rm lead}$

$$H_{\rm lead} = iv_F\int_{-\infty}^{\infty}dx\sum_{\alpha\sigma}\psi^{\dagger}_{\alpha\sigma}(x)\frac{d}{dx}\psi_{\alpha\sigma}(x), \tag{9.6}$$

where v_F represents the Fermi velocity. $\alpha = R/L$ and $\sigma = \uparrow / \downarrow$ label the (left/right) lead and the (up/down) spin of lead fermions, respectively. Notice that in writing the Hamiltonian Eq. 9.6 we have made the equilibrium assumption. Meanwhile, to validate the linear dispersion relation we have assumed that the chemical potential is in the middle of an energy band and the relevant energy cutoff is much less than the bandwidth.

Similar as that of the dissipative resonant level model, the effective interaction is represented by the dissipative phase φ in the tunneling Hamiltonian H_T

$$H_{\rm T} = \sum_{\alpha\sigma}t_{\alpha}e^{i\varphi_{\alpha}}d^{\dagger}_{\sigma}\psi_{\alpha\sigma}(0) + h.c., \tag{9.7}$$

where $\varphi_L = -\varphi_R = \varphi/2$. Meanwhile, we assume that the impurity symmetrically couples to both leads such that $t_L = t_R = t$.

The final ingredients are the dot Hamiltonian and the Kondo processes [2]

$$
\begin{aligned}
H_{\text{dot}} &= \sum_{\sigma} \epsilon_{\sigma} n_{\sigma} + U n_{\uparrow} n_{\downarrow} \\
H_{\text{Kondo}} &= J_{ZB} \sum_{\alpha} \sum_{\sigma\sigma'} \sigma\sigma' d^{\dagger}_{\sigma'} d_{\sigma'} \psi^{\dagger}_{\alpha\sigma}(0) \psi_{\alpha\sigma}(0) + J_{\perp B} \sum_{\alpha} \left[d^{\dagger}_{\uparrow} d_{\downarrow} \psi^{\dagger}_{\alpha\downarrow}(0) \psi_{\alpha\uparrow}(0) + h.c. \right] \\
&\quad + J_{ZF} \sum_{\alpha} \sum_{\sigma\sigma'} \sigma\sigma' d^{\dagger}_{\sigma'} d_{\sigma'} \psi^{\dagger}_{\alpha\sigma}(0) \psi_{-\alpha\sigma}(0) e^{i(\varphi_{-\alpha} - \varphi_{\alpha})} \\
&\quad + J_{\perp F} \sum_{\alpha} \left[d^{\dagger}_{\uparrow} d_{\downarrow} \psi^{\dagger}_{\alpha\downarrow}(0) \psi_{-\alpha\uparrow}(0) e^{i(\varphi_{-\alpha} - \varphi_{\alpha})} + h.c. \right],
\end{aligned}
\tag{9.8}
$$

where $\sigma = \uparrow, \downarrow$ labels particle spin, $\epsilon_{\sigma} = \epsilon_0$ is the $SU(2)$ symmetric impurity energy and U is the impurity onsite interaction. Impurity number operator is defined as $\sum_{\sigma} n_{\sigma} = \sum_{\sigma} d^{\dagger}_{\sigma} d_{\sigma}$. To simplify the calculation, once again we have assumed that U is much larger than any other relevant energy scale such that double occupancy is excluded from further considerations.

The Kondo Hamiltonian in Eq. (9.8) describes the second order lead-dot transport. Its z component and transverse component are labeled by the Z and $\perp$ subscripts, respectively. Meanwhile, the "back-scattering" (electron stays in the same lead) and "forward-scattering" (electron is transferred to the other lead) Kondo processes are labeled by the B and F subscripts. In writing Eq. (9.8), we have also taken the notation that $-L = R$ to simplify the expression.

The introduction of the on-site interaction changes the feature of the on-resonance peak. Without the on-site interaction $U = 0$, the on-resonance point is protected by both the particle-hole and left-right symmetries [103; 124; 134]. However, this is not true with $U \neq 0$ since it destroys the particle-hole symmetry at the on-resonance point (the p-h symmetric point now moves towards the Kondo valley).

[2] Notice that the "bare" values (before RG flows) of those Kondo parameters are related to the Anderson parameters through the Schrieffer-Wolff transformation, as has been introduced in Section 4.3.2.

Before the end of this section, here we briefly introduce the observed I-V curve of the dissipative Anderson model. To begin with, Fig. 9.1 shows the conductance of the model as a functions of the applied bias and the backgate voltage. Here we emphasize that peaks in Figs. 9.1(c), (d) and (e) all bend towards the Kondo valley under low bias. This is in strong contrast to the invariant peak position of the resonant level model. Another important feature of the dissipative Anderson model is shown in Fig. 9.2, which presents the temperature dependent zero-bias conductance as a function of temperature and backgate voltage. In consistence with the result in Fig. 9.1, here the conductance peak positions also shift into the Kondo valley with decreasing temperature. Finally, through the comparison between the peak values in those three plots of Fig. 9.2, we see another important feature that the on-resonance peak value decreases with an increasing dissipation. [3]

[3] In contrast to the $r = 0.3$ and 0.5 cases, it is possible that the on-resonance peak of the $r = 0.75$ sample has not reached the saturating temperature. This fact, however, does not violate the general argument in this chapter.

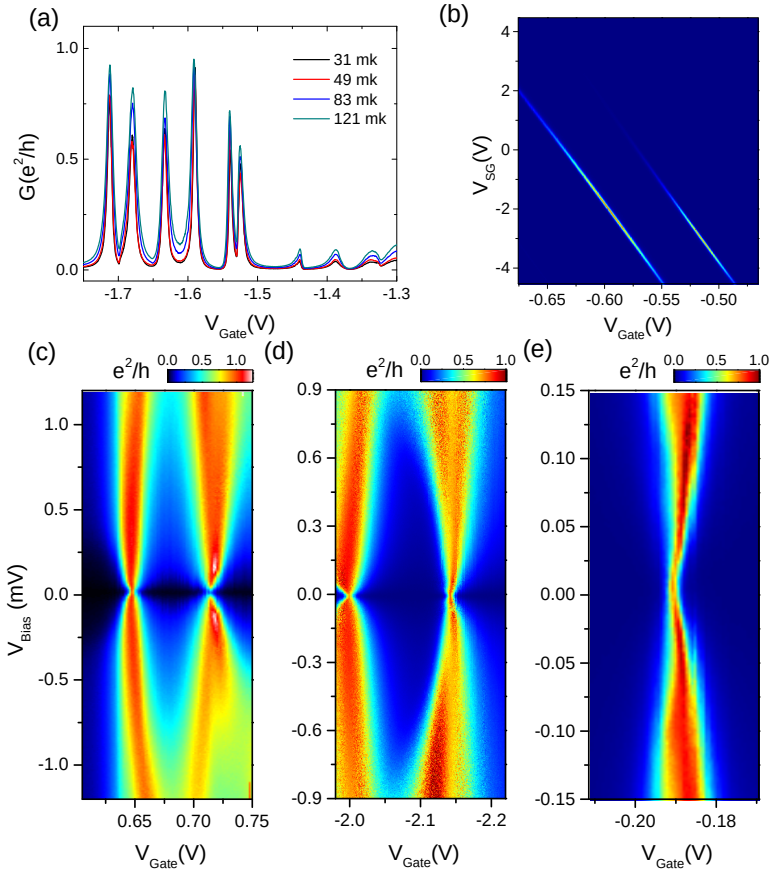

FIGURE 9.1: (a) The Coulomb blockade peaks measured at low temperatures from 31 mK to 120 mK for the $r = 0.5$ sample. The pairs of peaks can be observed. (b) Applying the side gate allows us to fine tune the barrier symmetry. At the maximum symmetric point, we can observed the conductance maximum for the Coulomb blockade peak. (c) and (d) are Coulomb blockade peaks with different dissipation strengths $r = 0.3$, 0.5 and 0.75, respectively. One common feature can be observed: symmetrically coupled peaks bend towards the single-electron valley under decreasing bias.

9.3 Renormalization Group Study of the Dissipative Anderson Model

To begin with, we introduce the study where we understand the shifting of the on-resonance peak position through the Coulomb gas renormalization group technique [18; 29; 103]. Similar as other RG methods, Coulomb gas RG calculates the flow equations of parameters by integrating out the ultraviolet modes. More specifically, in the Coulomb gas RG, we integrate out kink pairs with distance (in imaginary

time) larger than the cutoff and compare the partition function before and after the integral. The RG equations are then derived with the partition function invariant requirement.

Before the RG study, we need to first bosonize the Hamiltonian

$$\psi^{\dagger}_{\alpha\sigma} = \frac{F_{\alpha\sigma}}{\sqrt{2\pi a_0}} e^{-i\phi_{\alpha\sigma}}, \tag{9.9}$$

where $F_{\alpha\sigma}$ is the Klein factor and a_0 is the lattice constant and $\phi_{\alpha\sigma}$ is the chiral bosonic field for fermions in lead α with spin σ. For later convenience we once again rotate the bosonic operators

$$\begin{aligned} \phi_{c/s} &= (\phi_{L\uparrow} \pm \phi_{L\downarrow} + \phi_{R\uparrow} \pm \phi_{R\downarrow})/2 \\ \phi_{cf/sf} &= (\phi_{L\uparrow} \pm \phi_{L\downarrow} - \phi_{R\uparrow} \mp \phi_{R\downarrow})/2. \end{aligned} \tag{9.10}$$

Through straightforward comparison between Eqs. (9.7), (9.8) and (9.10), we see that the dissipative phase φ always has the same sign of ϕ_{cf}. One can thus combine those two fields

$$\begin{aligned} \phi'_{cf} &\equiv \sqrt{\frac{1}{1+r}}(\phi_{cf} + \frac{1}{\sqrt{2}}\varphi) \\ \varphi' &\equiv \sqrt{\frac{1}{1+r}}(\sqrt{r}\phi_{cf} - \frac{1}{\sqrt{2r}}\varphi), \end{aligned} \tag{9.11}$$

where φ' is totally decoupled and can thus be ignored in later paragraphs. Meanwhile, after ignoring φ', we can safely rewrite ϕ'_{cf} as ϕ_{cf} for simplicity. Through the rotation Eq. (9.11), the dynamics of the dissipative field φ has been absorbed by the ϕ_{cf} field, which now becomes effectively interacting.

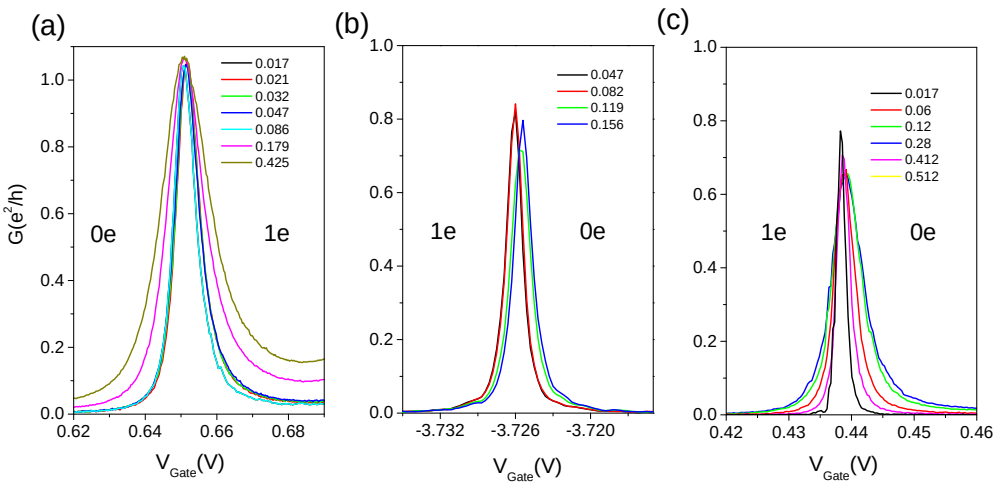

FIGURE 9.2: The temperature dependence of the Coulomb blockade peaks (with zero bias) for $r = 0.3$, 0.5 and 0.75. We can see that all three resonant peak positions shift towards the Kondo valley with a decreasing temperature. Meanwhile, the change of the on-resonance peak position is more subtle in the $r = 0.3$ case. This can be explained by its peak saturation at a higher temperature.

Basically, the Coulomb gas RG deals with the partition function of the system

$$\begin{aligned} Z &= T_r(e^{-\int_0^\beta d\tau H_0\tau + H_1\tau}) \\ &= \sum_{n=0}^{\infty}(-1)^n \int_0^{\tau_2} d\tau_1 \int_0^{\tau_3} d\tau_2 \cdots \int_0^{\beta} d\tau_n T_r e^{-\beta H_0} T_\tau[H_1(\tau_1)H_1(\tau_2)\cdots H_1(\tau_n)] \\ &= Z_0 \sum_{n=0}^{\infty}(-1)^n \int_0^{\tau_2} d\tau_1 \int_0^{\tau_3} d\tau_2 \cdots \int_0^{\beta} d\tau_n \langle T_\tau[H_1(\tau_1)H_1(\tau_2)\cdots H_1(\tau_n)\rangle_0 \end{aligned} \tag{9.12}$$

where $H_0 = H_{\text{leads}} + H_{\text{dot}}$ describes the isolated impurity and the free leads, while $H_1 = H_{\text{T}} + H_{\text{Kondo}}$ represents their interactions. The imaginary time τ runs from 0 to β (β is defined as the temperature inverse). Meanwhile, the expectation in the third line of Eq. 9.12 is calculated with respect to H_0. Physically, each term summed in Eq. 9.12 represents a circular historic chain with n "kinks" that change the system state at positions τ_1, τ_2... τ_n along the time axis. Three (out of four) bosonic fields

defined in Eq. 9.10 are non-interacting and share the same correlator

$$\langle\phi(\tau)\phi(0)\rangle = -\ln(i\omega_R t), \tag{9.13}$$

where ω_R is the frequency cutoff and ϕ can be ϕ_c, ϕ_s or ϕ_{sf} defined in Eq. (9.10). Since ϕ_{cf} is now interacting, it has a different correlator

$$\langle\phi_{cf}(\tau)\phi_{cf}(0)\rangle = -(1+2r)\ln(i\omega_R t). \tag{9.14}$$

At the beginning of the RG derivation, we assume an initial critical time τ_c with the assumption that any two kinks can not occur within the time interval τ_c. This critical time increases by $\delta\tau_c$ during each RG step, where $0 < \delta\tau_c \ll \tau_c$. With the new cutoff, we integrate out kink pairs with distance between τ_c and $\tau_c + \delta\tau_c$ and include their effect into the bare value of parameters (such as tunneling strengths and the impurity energy level). With an infinitesimal $\delta\tau_c$, parameter variations become continuous and can thus be modeled by differential equations (RG equations).

Based on the idea above, the RG study has already been carried in a Luttinger liquid Anderson model [167]. Similarly, we get the RG equations for the dissipative Anderson model

$$\begin{aligned} y_t'(l) = &\left[1 - \frac{K_1(l)}{8} - \frac{1}{8g_{cf}} - \frac{K_2(l)}{8} - \frac{1}{8}\right] y_t(l) + y_t(l) y_{pf}(l) e^{-\frac{1}{2}\epsilon(l)} \\ &+ y_t(l)\left[y_{zb}(l) + y_{pb}(l)\right] e^{-\frac{1}{2}\epsilon} \end{aligned} \tag{9.15a}$$

$$y_{pf}'(l) = \left[1 - \frac{K_2(l)}{2} - \frac{1}{2}\right] y_{pf}(l) + y_t^2(l) e^{\epsilon(l)} + 4 y_{pb}(l) y_{zb}(l) \tag{9.15b}$$

$$y_{pb}'(l) = \left[1 - \frac{1}{2g_{cf}} - \frac{K_2(l)}{2}\right] y_{pb}(l) + y_t^2(l) e^{\epsilon(l)} + 2 y_{pf}(l) y_{zb}(l) + 2 y_{pf}(l) y_{zb}(l) \tag{9.15c}$$

$$y_{zb}' = \left[1 - \frac{1}{2g_{cf}} - \frac{1}{2}\right] y_{zb}(l) + \frac{1}{2} y_t^2(l) e^{\epsilon(l)} + 2 y_{pf}(l) y_{pb}(l) \tag{9.15d}$$

$$K_1'(l) = -4\left[2e^{-\epsilon(l)} + e^{\epsilon(l)}\right] y_t^2(l) K_1(l) \tag{9.15e}$$

$$K_2'(l) = -4\left[2y_{pb}^2(l) + 2y_{pf}^2(l) + y_t^2 e^{\epsilon(l)}\right] K_2(l) \tag{9.15f}$$

$$\epsilon'(l) = \epsilon(l) - 4y_{zb}^2(l) - 2y_{pf}^2(l) - 2y_{pb}^2(l) + 2y_t^2(l)\left[-e^{\epsilon(l)} + 2e^{-\epsilon(l)}\right], \tag{9.15g}$$

where parameters above are defined as

$$\begin{aligned} y_t &\to \frac{t\tau_c}{\sqrt{2\pi a_0}} \qquad & y_{pf} &\to \frac{J_{\perp F}\tau_c}{2\pi a_0} \\ y_{pb} &\to \frac{J_{\perp B}\tau_c}{2\pi a_0} \qquad & y_{zb} &\to \frac{J_{ZB}\tau_c}{2\pi a_0} \\ y_{1v} &\to \frac{V_{1B}\tau_c}{2\pi a_0} \qquad & y_{0v} &\to \frac{V_{0B}\tau_c}{2\pi a_0} \\ \epsilon &\to \epsilon_0\tau_c \qquad & g_{cf} &= \frac{1}{1+2r}, \end{aligned} \tag{9.16}$$

and $K_1(0) = K_2(0) = 1$ are the initial 'interacting strengths' [4] of ϕ_c and ϕ_s fields. RG equations of Eq. (9.15) shows several similarities when compared with the Luttinger liquid resonant level model [103]. To begin with, the 'interacting strengths' of the fields that involve the dot (ϕ_c and ϕ_s) are decreasing to zero while that of the others (ϕ_{cf} and ϕ_{sf}) are invariant under the RG flow and are thus fixed to be one. Another similarity is the possible host of KT transition. Initially, $K_1(0) = K_2(0) = 1$ so that tunneling processes are relevant under the critical dissipation $r < r_c(0) = 2$. This critical dissipation, however, changes with an increasing l. More specifically, when $K_1(l) = K_2(l) = 0$, the critical dissipation changes to be $r_c(l) = 3$. Consequently, similar as the resonant level model [124], a KT transition is expected when $2 < r < 3$.

Despite these similarities, the spinful RG equations have several unique features. One of the most important features is the existence of higher-order tunneling processes such as the Kondo tunnelings. More importantly, in contrast to the resonant

[4] Here the 'interacting strength' models the coefficients of fields in the partition function Eq. (9.12) that change during the RG flow. It is thus effective and different from the real interactions such as the Luttinger liquid interaction.

level model RG equations where the on-resonance point is protected by the particle-hole symmetry, the $\epsilon = 0$ point is unstable in the dissipative Anderson model. This feature can be physically understood as the lack of particle-hole symmetry protection at the on-resonance peak of the dissipative Anderson model.

Fig. 9.3 shows the solution of the RG equations. Fig. 9.3(a) describes the energy flow of the impurity as a function of the RG "depth" l (as introduced in Section 3.2.1, it is proportional to the exponential of the temperature change) with dissipation strength $r = 0.5$. We choose such dissipation strength to exclude possible distraction from the Kondo effect [63]. When compared with the experiment, lower temperature corresponds to lower cutoff, or larger l. One can see that when the bare impurity energy is slightly below zero, it gradually increases. One can more directly see the effect of the RG flow from Fig. 9.3(b), where the on-resonance impurity energy of the dissipative Anderson model is plotted as a function of $\max(T, V_{\text{bias}})$. Apparently, with a decreasing temperature or bias, the on-resonance bare impurity energy flows into the Kondo valley, which agrees with the experimental data Fig. 9.1, where weak bias serves as the RG cutoff.

If we compare Fig. 9.3(b) with the experimental data Figs. 9.1 and 9.2, we see that RG equations successfully predict the shift of the on-resonance peak position of the dissipative Anderson model, which is significantly different from the invariant peak position of the resonant level model.

More strictly, the Coulomb gas RG equations are only reliable at the weak coupling regime. To compensate for this weakness, we provide an argument about the weak bias and low temperature features of the dissipative Anderson model. Basically, there are two possible energy flow patterns. To begin with, we expect the energy flows as shown in Fig. 9.4(a), where the energy RG flows do not change the relative sequence of energy levels [5]. Meanwhile, we expect the on-resonance energy becomes

[5] Alternatively, if $\epsilon_1(0) > \epsilon_2(0)$, then $\epsilon_1(l) > \epsilon_2(l)$ for any l.

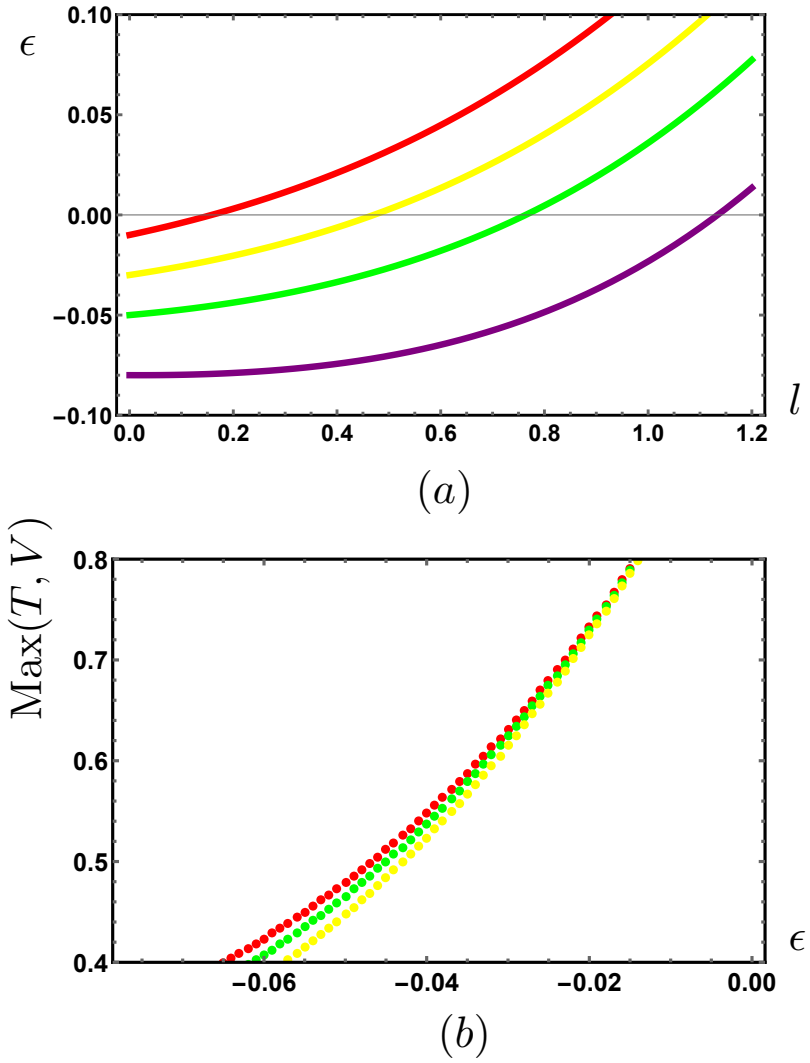

FIGURE 9.3: Main results from the RG equations Eq. (9.15). (a) The RG flow of the impurity energy with different initial energies. The dissipation strength is $r = 0.5$, smaller than the critical value $r_c = 2$. The bare level broadening is $\Gamma = 0.1$. The energy increases with increasing l or decreasing temperature/bias.(b) The on-resonance bare impurity energy as a function of the temperature. This plot contains RG flow result with dissipation strengths $r = 0.3$ (red), 0.5 (blue) and 0.75 (yellow). We can see that when the temperature decreases, the "on-resonance" bare energy flows towards the Kondo valley.

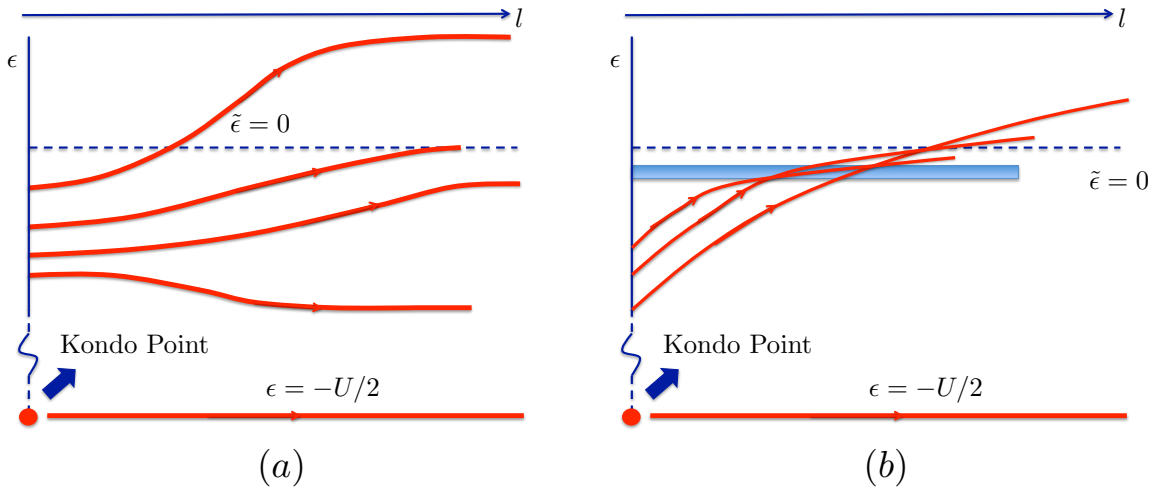

FIGURE 9.4: Two possible flows of the energy. (a) The expected flow of the quantum dot energy. In this case the quantum dot energy becomes invariant at low enough temperature/bias. This agrees with the experimental observation where the on-resonance peak postion becomes invariant after its saturation. (b) Another possibility that may not be physical. In this case, RG flows cross at multiple points.

invariant with low enough temperature/bias. As a comparison, another possibility is shown in Fig. 9.4(b). In this case, it is possible that the energy will flow back under some cutoff. However, if such case is true, then if one decreases the chemical potential to the regime highlighted by the blue box, then we would expect that the resonant energy moves back and forth, which is unlikely to be physical. Meanwhile, in the latter case, RG flow arrows intersect so that at some points the RG flow is ill-defined. Consequently, we would predict the energy flow like that given in Fig. 9.4(a). Notice that this RG flow diagram predicts a stable fixed point as the on-resonance peak. In Section 9.4 we will further discuss about the stability of this fixed point.

9.4 Understanding the Unquantized Saturated Conductance

In this section we convey the idea to understand the physics related to Fig. 9.2. As described in previous sections, for $r = 0.3$ and $r = 0.5$, we can see the saturation of the on-resonance peaks. Meanwhile, we believe the existence of the saturation peak

even for the $r = 0.75$ case. We understand the missing of its peak saturation as a lower saturation temperature under stronger dissipation.

Meanwhile, we have also noticed that the saturated peak height of the $r = 0.3$ case is larger than that of the $r = 0.5$ case.

9.4.1 Brief Introduction of the Quantum Brownian Motion Model

As introduced in Section 9.1.1, the QBM model describes the motion of a particle in a periodic lattice under the influence of dissipative modes. There we have also introduced the connection between the 1d QBM model and the single barrier Luttinger liquid model. A more systematic study about the connection between mesoscopic systems and the QBM models has been done by H. Yi and C. L. Kane [186]. In that paper, the connection is constructed by visiting the QBM model in two extreme regimes that are dual to each other. First one is the high-mobility regime. In this regime the QBM effective action can be written as

$$S = S_0[\vec{r}(\tau)] - \int \frac{d\tau}{\tau_c} \sum_{\vec{G}} v_{\vec{G}} \exp[i2\pi \vec{G} \cdot \vec{r}(\tau)], \tag{9.17}$$

where $\vec{r}(\tau)$ is the trajectory in the QBM lattice and $v_{\vec{G}}$ refers to the periodic potential with the reciprocal-lattice vector $\vec{G}$. Physically, the action Eq. (9.17) refers to the regime where the periodic potential is weak such that the motion is almost free (with the mobility $\mu \to 1$).

As its dual form, we also have the action for the weak-mobility regime

$$S = S_0[\vec{k}(\tau)] - \int \frac{d\tau}{\tau_c} \sum_{\vec{R}} t_{\vec{R}} \exp[i2\pi \vec{R} \cdot \vec{k}(\tau)]. \tag{9.18}$$

In this regime, the system has a strong potential so that particles are almost confined at the minimums of the periodic potential and t_R refers to the weak tunneling between

potential minimums connected by a lattice vector $\vec{R}$. With system actions given by Eq. 9.17 and 9.18, we can simply read off their scaling dimension as

$$\begin{aligned} \frac{dv_{\vec{G}}}{dl} &= (1-|\vec{G}|^2)v_{\vec{G}} \\ \frac{dt_{\vec{R}}}{dl} &= (1-|\vec{R}|^2)t_{\vec{R}}. \end{aligned} \tag{9.19}$$

For later convenience, we further define $\vec{G}_0$ and $\vec{R}_0$ as the vectors that connect the nearest neighbor sites in two dual lattices. In one-dimensional QBM models, the physics is simple since $|G_0||R_0| = 1$. Alternatively, if one of the fixed points is stable, the other one must be unstable and vice versa. However, in higher dimensional systems, $|G_0||R_0|$ may be different from unity so that there may exist another intermediate fixed point. More specifically, if $|G_0||R_0| > 1$, it can be possible that both $|G_0| > 1$ and $|R_0| > 1$ so that there will be an unstable intermediate fixed point that flows to either strong or weak mobility fixed point; on the contrary, if $|G_0||R_0| < 1$, there will be a stable intermediate fixed point if $|G_0| < 1$ and $|R_0| < 1$ are simultaneously satisfied. In this case, the stability of this intermediate fixed point can be understood to be protected by the subtle symmetry of the QBM lattice. For instance, the intermediate fixed point of the $r = 1$ 2d QBM model on a Kagome lattice has been believed to be protected by a $SU(3)$ symmetry [186].

9.4.2 Mapping our system to the Quantum Brownian Motion Model

For simplicity, we begin with the dissipation free case $r = 0$. We also only include the hybridization processes H_{T}. The action then becomes

$$\begin{aligned} S &= S_0 + S_T \\ &= S_0 + \int \frac{d\tau}{\tau_c} \frac{t}{\sqrt{2\pi a}} [d_\uparrow^\dagger e^{i\phi_{L\uparrow}} + d_\uparrow^\dagger e^{i\phi_{R\uparrow}} + h.c.], \end{aligned} \tag{9.20}$$

where the dot action has been included into S_0. The comparison between Eqs. (9.20) and the QBM action Eq. (9.17) shows several differences. One is the impurity energy. As discussed in previous sections, due to the lack of protection from the particle-hole symmetry, energy will keep flowing towards the Kondo valley so that the there will be some energy related terms $\epsilon(\tau_i - \tau_{i+1})$ in the action, where τ_i is the time of the ith kink. This problem is answered by Fig. 9.3(a). Based on the speculation, we expect that there will be a bare energy such that with $l > l_c$ the system approximately remains on resonance. So we can ignore the impurity energy and do the mapping after that cutoff.

Another difference is that the lead-impurity hybridization of the dissipative Anderson model contains impurity operators. Their presence forbids several operator configurations (for instance, $\exp(i\phi_{L\uparrow} + i\phi_{R\uparrow})$ is forbidden since the dot can not be doubly occupied). Our strategy is to forbid those non-physical processes manually by limiting the freedom of the lead fields. With those enforced restrictions, the number of freedom of the Anderson model do not simply equal that of the QBM model. Naively, the system with the action of Eq. (9.10) consists of four independent lead fields so we may want to map our model to a four dimensional QBM lattice. However, if we consider the restriction given by the impurity, the final lattice can only be two-dimensional. To better illustrate this point, we once again take the rotation as given by Eq. (9.10). Based on the Bosonization technique, we relate the common field ϕ_c with the electron number as

$$\phi_c(0) = -\int_0^\infty dx \partial_x \phi_c(x) = 2\pi \int_0^\infty dx \rho_c(x) \propto N, \tag{9.21}$$

where N is the total electron number in the leads which only has two possible values. Consequently, to remove impurity operators from the action Eq. (9.20), ϕ_c becomes bi-valued and can not be considered as free. The same argument also applies to the spin field ϕ_s. Consequently, the Anderson model maps to a 2d QBM lattice instead,

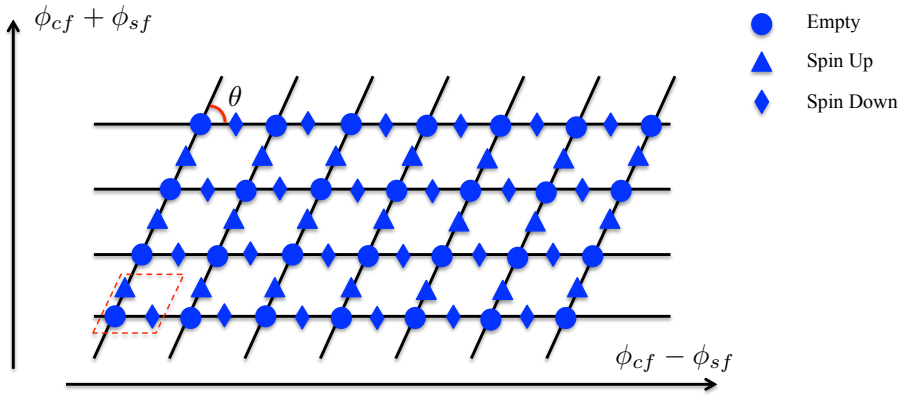

FIGURE 9.5: The lattice structure of the QBM model that is equivalent to the dissipative Anderson model. The dashed red parallelogram indicates the unit cell of the lattice. The angle between different axis θ is determined by the dissipation strength. Sublattices are defined based on the three different values of (ϕ_c, ϕ_s).

with ϕ_{cf} and ϕ_{sf} representing the lattice "axes". The different values of the vector (ϕ_c, ϕ_s) instead defines the sublattices. With those considerations, it is ready for us to map Eq. (9.20) to a two-dimensional QBM lattice as shown in Fig. 9.5.

We can see that the QBM lattice is in principle a Lieb lattice with three inequivalent sites labeling different impurity states. The angel θ is calculated by comparing the scaling dimension of the dot-lead tunneling and the Kondo tunneling processes. More specifically, with dissipation strength r, first order hybridization has scaling dimension $(1 + r)/4$, corresponding to a distance $\sqrt{1 + r}/2$ in the Lieb lattice (between the empty and filled sites). The leading Kondo process, on the other hand, has scaling dimension $1/2$, corresponding to the distance $1/\sqrt{2}$ between the nearest spin up and spin down sites in the lattice. Consequently, we can calculate the angle θ in Fig. 9.5. With this angle known, we can further calculate its reciprocal lattice constants. Through detailed calculation, we have the central result of this section that

$$|R_0| = \frac{\sqrt{1+r}}{2}, \quad |G_0| = \sqrt{\frac{1+r}{1+2r}} \quad \text{and} \quad |R_0||G_0| = \frac{1+r}{2\sqrt{1+2r}}. \tag{9.22}$$

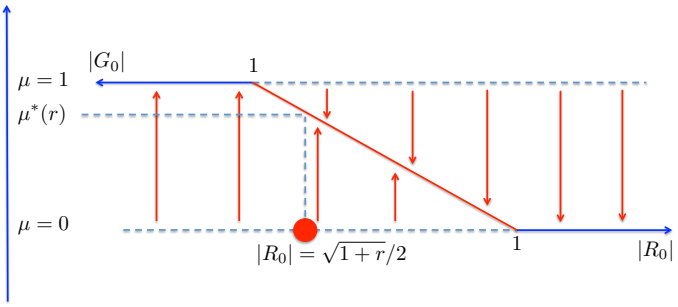

FIGURE 9.6: Flow of the QBM model and μ^* with dissipation strength r. When dissipation increases, the intermediate mobility $\mu^*(r)$ decreases monotonically, leading to a decreasing on-resonance conductance of the dissipative Anderson model.

One can first check that when $r > 3$, $|R_0| > 1$ such that the weak mobility regime is stable, which agrees with the RG calculation. Secondly, with any finite dissipation $0 < r < 3$, $|R_0| < 1$ and $|G_0| < 1$ such that there will be an intermediate fixed point with an intermediate mobility. If we call the mobility for the intermediate regime as μ^*, then μ^* decreases with an increasing r and reaches zero at $r = 3$, as shown by Fig. 9.6.

After knowing the mobility of the corresponding QBM lattice, we can calculate the conductance of the original carbon nanotube system. The basic idea is to include both the intermediate mobility as well as the effect of the barrier between the dissipative lead and the dissipation-free reservoir [87]. The result is

$$\begin{aligned} G &= \frac{2e^2}{h} \frac{\mu^*}{1 + 2r + 2r\mu^*} \frac{e^2}{h} \\ &= \frac{2e^2}{h} \frac{1}{(1 + 2r)/\mu^* + 2r}. \end{aligned} \tag{9.23}$$

As argued before, μ^* decreases with an increasing dissipation so that the conductance of the original dissipative Anderson model decreases under an increasing dissipation, which explains the decreasing of the saturated on-resonance peaks shown in Fig. 9.2. Finally, before the end of this section, we discuss a little bit about the protection of the intermediate fixed point. In dissipative resonant level model, the stability of its

on-resonance fixed point is protected by the particle-hole symmetry. In the QBM model, the intermediate fixed point is protected by the subtle symmetry between lattice QBM lattice constants. For instance, Y. Hu and C. L. Kane [87] proposed an analytical calculation for the $SU(3)$ symmetric Luttinger liquid Anderson model. In that model, the $SU(3)$ symmetry origins from the symmetry between the L-dot, R-dot hybridizations and the Kondo exchange. This Anderson model maps to a QBM model on a Kagome lattice with its intermediate fixed point protected by the $SU(3)$ symmetry. In the dissipative Anderson model, the intermediate fixed point can also be considered as protected by the subtle "geometric" symmetry of its equivalent QBM model.

9.5 Conclusion

We have analyzed the I-V feature of the dissipative Anderson model with dissipation $r = 0.3$, 0.5 and 0.75. Experimental observation of those models exhibits two main exotic features: (i) the shifting of the on-resonance peak position as a function of the applied temperature/bias and (ii) the decreasing of the saturated on-resonance conductance with an increasing dissipation strength. [6]

To explain the experimental results, we have studied the RG flows of the dissipative Anderson model. Based on those RG equations, impurity energy changes towards the Kondo valley, which qualitatively explains the experimental data. Physically, the energy shifting originates from the lack of protection from the particle-hole symmetry in the dissipative Anderson model. The understanding of the dissipation-dependent saturated peak conductance is provided through the mapping of the system to a 2d QBM model. More specifically, a dissipative Anderson model is equivalent to a QBM model in a Lieb lattice, where a stable intermediate fixed point with intermediate

[6] Actually, the fact that the saturated conductance value is not e^2/h is another significant result which worth further investigation.

mobility is protected by the subtle symmetry of the QBM lattice. By relating the mobility of the QBM model to the conductance of the dissipative Anderson model, we qualitatively explain the decreasing of the peak conductance as a function of the increasing dissipation.

10

Geometric Singularity and Geometric Phase in $R = R_Q$ dissipative resonant level model

The singularity at the QCP of a QPT-hosted system induces the possibility of a non-trivial geometric phase around the QCP. Been studied in detail around ten years ago, the prerequisite of a non-trivial geometric phase in bulk QPT-hosted systems has been worked out. This criteria, which claims that a non-trivial geometric phase requires a superextensive critical point, is however only proved in bulk QPTs. In this chapter we thus study the geometric phase-boundary QPT relation by analytically calculating the geometric phase in the $R = R_Q$ resonant level model. Here we show that although the dissipative resonant level model has an QCP that satisfies the superextensive criteria, its geometric phase remains zero since the geometric curvature vanishes everywhere. We further provide a general argument for the trivial geometric phase in systems without long range interactions.

10.1 Introduction

The Berry phase is a quantity defined within the adiabatic approximation, where time dependent Hamiltonian $H(t)$ is assumed to change slow enough such that the system stays at the ground state $|\psi_0(t)\rangle$ of the varying $H(t)$ [184]. Based on this assumption, if the Hamiltonian returns to the starting value after time T_0 such that $H(T_0) = H(0)$, the state also returns to the starting wave function, except for an extra phase factor

$$|\psi_0(T_0)\rangle = e^{i\gamma + i\theta_{\rm dyn}}|\psi_0(0)\rangle, \tag{10.1}$$

where

$$\theta_{\rm dyn} = -\frac{1}{\hbar}\int_0^{T_0} E_0(t)dt, \tag{10.2}$$

is defined as the dynamical phase and E_0 is the ground state energy. The phase in Eq. (10.2) represents the phase accumulated from the dynamical wave function evolution. The extra phase γ, which does not have any corresponding definition in time independent quantum mechanics, is called the Berry phase, named after the pioneering work by M. Berry in 1984 [1]. Due to its reflection of the geometry of system Hamiltonian in the parameter space, it is also called the geometric phase. To better understand the geometric phase, we assume a general expression of the time dependent Hamiltonian $H[\vec{R}(t)]$, where $\vec{R}(t)$ is the vector defined in the time dependent parameter space of the system. In such a system, it is easy to derive the Berry phase with the expression [184]

$$\gamma = \int_c d\vec{R}\cdot\vec{A}(\vec{R}), \tag{10.3}$$

where $\vec{A}(\vec{R}) = i\langle\psi_0(\vec{R})|\partial_{\vec{R}}|\psi_0(\vec{R})\rangle$ is the Berry connection that reflects the change of ground state wave function when the Hamiltonian evolves in the parameter space. The integral in Eq. (10.3) is along a closed loop c. As the loop integral of the Berry

connection, Berry phase thus indicates the collective change of the geometry in the parameter space after the system returns to its starting point.

As the feature of quantum mechanics, phases of imaginary wave functions preserve the possibility of interesting interference phenomena. However, the geometric phase has been long time considered as unimportant since the gauge transformation

$$|\psi_0(\vec{R})\rangle \rightarrow e^{i\chi(\vec{R})}|\psi_0(\vec{R})\rangle \tag{10.4}$$

changes the Berry connection in the way $\vec{A}(\vec{R}) \rightarrow \vec{A}(\vec{R}) - \partial_{\vec{R}}\chi(\vec{R})$, giving Berry phase an extra term $\chi[\vec{R}(0)] - \chi[\vec{R}(T)]$. The gauge dependence of the Berry connection once makes persons to believe that a proper gauge will cancel out the geometric phase. However, since the integral in Eq. (10.3) is taken around a closed loop, $\chi[\vec{R}(0)] - \chi[\vec{R}(T)]$ equals $2n\pi$ with n an integer to guarantee the equivalence of the starting and final wave functions. Consequently, the geometric phase defined in Eq. (10.3) is actually well defined (since an extra phase $2n\pi$ is irrelevant) and gauge independent.

Another way to calculate the geometric phase is through the geometric curvature

$$\vec{\Omega}(\vec{R}) = \vec{\bigtriangledown}_{\vec{R}} \times \vec{A}(\vec{R}), \tag{10.5}$$

which is the curl of the geometric connection. With the Stokes theorem, we can thus rewrite the geometric phase defined in Eq. (10.3) into a surface integral

$$\gamma = \int_s d\vec{S} \cdot \vec{\Omega}(\vec{R}), \tag{10.6}$$

in a closed surface s bounded by the loop c. From Eq. (10.6), we can better understand the efficiency of the geometric phase in the detecting of Hamiltonian singularities in the parameter space: normally, with infinitesimal area $s \rightarrow 0$, geometric phase from Eq. (10.6) vanishes. However, due to the singularity and the failure of the adiabatic theorem at the QCPs, it is natural to expect a possibly finite geometric phase when the infinitesimal closed surface contains a QCP.

Multiple researches have thus been carried out concerning the possible connection between bulk QPTs and a non-trivial geometric phase [31; 150; 197; 78; 28; 44; 145], including the 1d anisotropic spin XY and the 1d dissipative Ising models. Those papers involve more than studies of specific systems, but also include arguments about the general prerequisites of a non-trivial geometric phase in QPT-hosted systems [78; 28]: they argue that non-trivial geometric phase only occurs in QPT-hosted systems that have superextensive singularities at the critical point. Mathematically, if a QPT system has a superextensive QCP, it means that [28]

$$\Delta_{\mu\nu} \equiv \Delta_\mu + \Delta_\nu - 2Z - D < 0, \tag{10.7}$$

where μ and ν correspond to two independent operators in the parameter space that trigger the quantum phase transition and Δ_μ (Δ_ν) is the corresponding scaling dimension. Both μ and ν should be relevant so that $\Delta_\mu, \Delta_\nu < 2$ in bulk QPTs. Z is the scaling coefficient of the time variable and $Z = 1$ for linear dispersion relation. Finally D is the spacial dimension of the system. Consequently, bulk QPTs in higher dimensional models and with more relevant QPT-triggering operators have higher possibility to host a non-trivial geometric phase.

Naively, if Eq. (10.7) is applicable to boundary QPTs, the superextensive criteria in a relativistic system is always satisfied since $\Delta_\mu + \Delta_\nu < 2$ in boundary QPTs. However, despite the study about the bulk QPTs-geometric phase connection, to date no research has been carried out concerning the geometric phase in the boundary QPTs and the applicability of Eq. (10.7) in the boundary QPTs still remains unknown.

In this chapter, we thus provide the study of the connection between the boundary QPT and the geometric phase by calculating the geometric phase in the $R = R_Q$ dissipative resonant level model. Since the effective Hamiltonian of this model contains a decoupled impurity Majorana fermion (see Section 7.4 for details), it is also called

the Majorana resonant level model. As illustrated in Chapter 7, the dissipative resonant level model maps to the two channel Kondo model which has been thoroughly studied and can be analytically solved. Consequently, the dissipative resonant level model provides as the simplest model in the study of the boundary QPT-geometric phase connection. After multiple ways of calculation, we find that the dissipative resonant level model has a singular geometric connection at the critical point with the powerlaw as predicted by Eq. (10.7). However, since the geometric connection has zero curl, this singularity will not lead to a non-trivial geometric phase as predicted in bulk systems. Based on the study of the QCP of the dissipative resonant level model, we further provide a general argument to understand the missing of the geometric phase in boundary QPT-hosted systems [1].

This chapter is organized as follows. In Section 10.2 we briefly review the effective Hamiltonian of the Majorana resonant level model around the critical point. This is followed by the calculation of the geometric connection in Section 10.3. To understand this result, we calculate the geometric curvature with the geometric tensor using Green's function technique in Section 10.4. After that, we provide an understanding of the geometric phase in dissipative resonant level model and general boundary QPT hosted systems in Section 10.5. Finally we conclude this chapter in Section 10.6.

10.2 The System and the Effective Hamiltonian

As have been introduced in Chapter 7, the $r = 1$ dissipative resonant level model can be exactly mapped to the two channel Kondo model. More specifically, after bosonization and refermionization, the tunneling Hamiltonian effectively becomes

[1] In principle, this argument only applies to systems with local interactions.

(with $H_{\rm dot}$ included)

$$\begin{aligned}\tilde{H}_{\rm T} = (t_S - t_D)\frac{\psi_f^\dagger(0) - \psi_f(0)}{\sqrt{2}}a \\ + i(t_S + t_D)\frac{\psi_f^\dagger(0) + \psi_f(0)}{\sqrt{2}}b \\ + i[\epsilon_d - \pi v_F/\sqrt{2} : \psi_c^\dagger\psi_c(0) :]ab,\end{aligned} \tag{10.8}$$

where a and b are the two impurity Majorana fermions and ψ_f is the operator that comes from the refermionization of the phase difference between source and drain fermions. The corresponding lead part now contains free fermions ψ_f and ψ_c. Meanwhile, the environmental part $H_{\rm env}$ has been dropped since its effect has already been included into the definition of ψ_f. The second term of the last line is the effective density-density interaction between dot and the effective common fermion ψ_c. It has been proved that this term has scaling dimension 3/2 near the critical point [52; 2] and can thus be ignored if we are only interested in the zero temperature geometric phase. After dropping the last term, ψ_c becomes decoupled so that can be safely ignored in the lead Hamiltonian. For later convenience, we also ignore the f labeling of ψ_f and rewrite the Hamiltonian with operators ψ_k in the momentum space. With those simplification, the effective Hamiltonian becomes [2]

$$\tilde{H} = H_{\rm critical} + \delta H = \sum_k \epsilon_k \psi_k^\dagger \psi_k + i\epsilon_d ab + iV_1 \sum_k (\psi_k^\dagger + \psi_k)b + V_2 \sum_k (\psi_k^\dagger - \psi_k)a, \tag{10.9}$$

where $V_1 = (t_S + t_D)/2\sqrt{\pi a_0}$ and $V_2 = (t_S - t_D)/2\sqrt{\pi a_0}$ are the symmetric and asymmetric coupling strengths, defined for later convenience and the lattice constant is a_0. The critical Hamiltonian $H_{\rm critical}$ contains the first and third terms of Eq. (10.9).

[2] In deriving Eq. (10.9), the system is implicitly assumed to be infinite so that strictly speaking the momentum k should be considered as continuous here. However, since the effective Hamiltonian Eq. (10.9) has the same length of the original model, we can still use the discretized version of Eq. (10.9) to study the scaling behavior of the original model when the system size approaches infinity.

When $\delta H = 0$, $V_2 = \epsilon_d = 0$, zero temperature system is then described by the two channel Kondo quantum critical fixed point. At this point, the quantum frustration between the source and drain in the hybridization of the quantum dot leaves a Majorana fermion decoupled [74; 195]. However, with any asymmetry present, system flows to a Fermi liquid ground state. The phase diagram of the dissipative resonant level model is shown in Fig, 10.1. For later convenience, here we define $\vec{\lambda} = (V_2, \epsilon_d)$ as the vector in the parameter space that represents the deviation from the critical point.

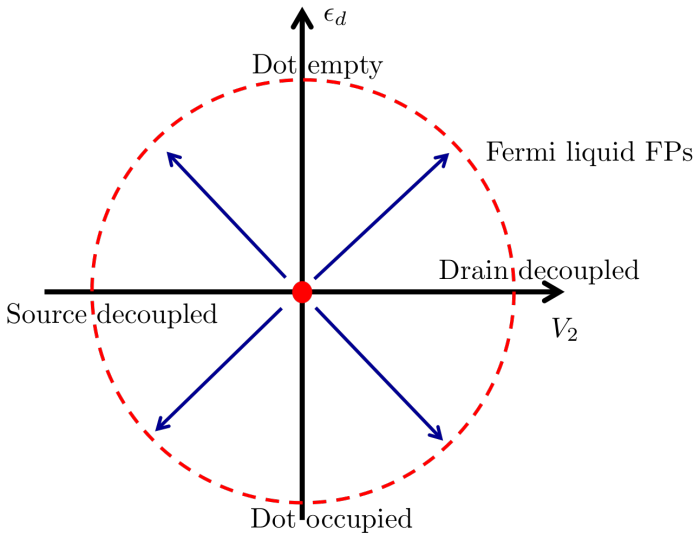

FIGURE 10.1: Phase diagram of the $r = 1$ resonant level model. The red dot is the two channel Kondo-like critical point and the red dashed line represents the Fermi liquid fixed points. The blue arrows represent the RG flow. Since all Fermi liquid fixed points have zero impurity entropy, they are related by marginal operators.

10.3 Geometric Connection of the Dissipative Resonant Level Model

There are multiple ways to calculate the geometric phase of the dissipative resonant level model. The most straightforward one is to calculate the geometric connection, which requires us to know about the ground state wave function of the effective Hamiltonian in Eq. (10.9).

Similar as that of the single barrier model, the eigenstates of Eq. (10.9) contain scattering states represented by operators that commute with the Hamiltonian. The derivation of the scattering state operators is finished in the 1990s with the "L operator" method [166], with the result

$$
\begin{aligned}
c_k^\dagger &= \psi_k^\dagger + V_2[G_{aa}(\epsilon_k + i\eta)\hat{\alpha}_k + G_{ba}(\epsilon_k + i\eta)\hat{\beta}_k] - iV_1[G_{ab}(\epsilon_k + i\eta)\hat{\alpha}_k + G_{bb}(\epsilon_k + i\eta)\hat{\beta}_k] \\
\hat{\alpha}_k &= a + V_2 \sum_{k'} \left(\frac{\psi_{k'}^\dagger}{\epsilon_k - \epsilon_{k'} + i\eta} - \frac{\psi_{k'}}{\epsilon_k + \epsilon_{k'} + i\eta}\right) \\
\hat{\beta}_k &= b + iV_1 \sum_{k'} \left(\frac{\psi_{k'}^\dagger}{\epsilon_k - \epsilon_{k'} + i\eta} + \frac{\psi_{k'}}{\epsilon_k + \epsilon_{k'} + i\eta}\right),
\end{aligned}
\tag{10.10}
$$

where $\eta \to 0^+$ is an infinitesimal positive number and

$$
\hat{G}(\omega) = \begin{pmatrix} G_{aa}(\omega) & G_{ab}(\omega) \\ G_{ba}(\omega) & G_{bb}(\omega) \end{pmatrix} \tag{10.11}
$$

is the Fourier transformed expression of the retarded Green's function. With the scattering state operators defined in Eq. (10.10), the Hamiltonian becomes simply $\tilde{H}' = \sum_k \epsilon_k c_k^\dagger c_k$. It is also straightforward to check that $[c_k^\dagger, \tilde{H}'] = -\epsilon_k c_k^\dagger + i\eta(\psi_k^\dagger - c_k^\dagger)$, which satisfies the requirement of the scattering state operators.

Before we calculate the geometric phase, we have to make several comments about the scattering state operators in Eq. (10.10) and the diagonalized Hamiltonian $\tilde{H}'$. To begin with, in deriving Eq. (10.10), we have made both the large band and continuous spectrum assumption. This means that these scattering wave operators are only valid for infinitely large systems with small enough lattice constant. Since QPTs only occur in infinite systems, this assumption is valid in the study of the criticality of the two channel Kondo fixed point. However, those scattering states are not valid if we want to study the powerlaw singularity of the critical point as a function of the system size. The second comment is that the spectrum of the scattering states

is the same as that of the free leads. This also requires an infinite system: at this limit, the impurity freedom will not alter the scattering states' spectrum. Finally, the effective Hamiltonian $\tilde{H}'$ only contains the scattering states and the decoupled impurity Majorana fermion (a) at the critical point ($\epsilon_d = V_2 = 0$) has been ignored.

With the scattering wave operators at hand, we thus write the ground state wave function as

$$|\Psi_0\rangle = C_N(\Pi_{k,\epsilon_k>0}c_k)(\Pi_{k',\epsilon_{k'}<0}c^\dagger_{k'})|0\rangle, \tag{10.12}$$

where $|0\rangle$ is the empty state in terms of original fermions where $\psi_k|0\rangle = 0$ for any k. The normalization factor is C_N. With this definition, it is straightforward to check that Eq. (10.12) satisfies the requirement of the ground state: $c^\dagger_k|\Psi_0\rangle = 0$ for $\epsilon_k < 0$ and $c_k|\Psi_0\rangle = 0$ for $\epsilon_k > 0$. Meanwhile, for simplicity here we assume $C_N \in \mathbf{R}$ is a real number. In general C_N may be complex. But as we have discussed in Section 10.1, we have the freedom to define the phase since it will not enter the geometric phase.

To calculate the geometric connection with the ground state wave function Eq. (10.12), we need to express the differentiation $\bigtriangledown_{\vec{\lambda}} c_k(\vec{\lambda})$ in terms of the scattering state operators. Instead of direct calculation, we use the fact that $\{c_k\}$ spans the entire Hilbert space such that [3]

$$\bigtriangledown_{\vec{\lambda}}\, c_k = \sum_{k'} \vec{\alpha}_{kk'} c_{k'} + \sum_{k'} \vec{\beta}_{kk'} c^\dagger_{k'}, \tag{10.13}$$

where $\vec{\alpha}_{kk'}$ and $\vec{\beta}_{kk'}$ are two momentum dependent constant vectors: two components of those vectors label the differentiation along two directions [$\vec{\lambda} = (V_2, \epsilon_d)$]. With coefficients defined in Eq. (10.13), when $\epsilon_k > 0$

$$C_N^2\langle 0|(\Pi_{k',\epsilon_{k'}<0}c_{k'})(\Pi_{k',\epsilon_{k'}>0}c^\dagger_{k'})(\Pi_{k',\epsilon_{k'}>\epsilon_k}c_{k'})\bigtriangledown_{\vec{\lambda}}c_k(\Pi_{k',0<\epsilon_{k'}<\epsilon_k}c_{k'})(\Pi_{k',\epsilon_{k'}<0}c^\dagger_{k'})|0\rangle = \vec{\alpha}_{kk}. \tag{10.14}$$

[3] Strictly speaking, this is not true at the QCP. However, this assumption is valid if we are calculating the geometric connection around the QCP.

Similarly, when $\epsilon_k < 0$, the expectation value produces $\vec{\alpha}^*_{kk}$ instead. For later convenience, if we define $\vec{\gamma}_{\epsilon_k} = \Theta(\epsilon_k)\vec{\alpha}_{kk} + \Theta(-\epsilon_k)\vec{\alpha}^*_{kk}$ with $\Theta(\epsilon)$ the step function, we get the expectation function

$$\langle\Psi_0|\bigtriangledown_{\vec{\lambda}}|\Psi_0\rangle = \sum_k \vec{\gamma}_{\epsilon_k} + (\bigtriangledown_{\vec{\lambda}} C_N)/C_N, \tag{10.15}$$

Notice that here the normalization factor C_N is $\vec{\lambda}$ dependent so that we are supposed to calculate its gradient in the $\vec{\lambda}$ parameter space. To avoid this complexity, we use the fact that $\bigtriangledown_{\vec{\lambda}}(\langle\Psi_0|\Psi_0\rangle) = 0 = (\bigtriangledown_{\vec{\lambda}}\langle\Psi_0|)|\Psi_0\rangle + \langle\Psi_0|\bigtriangledown_{\vec{\lambda}}|\Psi_0\rangle$, such that

$$\begin{aligned}\langle\Psi_0|\bigtriangledown_{\vec{\lambda}}|\Psi_0\rangle &= \frac{1}{2}(\langle\Psi_0|\bigtriangledown_{\vec{\lambda}}|\Psi_0\rangle - (\bigtriangledown_{\vec{\lambda}}\langle\Psi_0|)|\Psi_0\rangle) \\ &= i\sum_k \mathrm{Im}(\vec{\gamma}_{\epsilon_k}),\end{aligned} \tag{10.16}$$

where we have used the fact that C_N is a real number. Consequently, to calculate $\vec{\gamma}_{\epsilon_k}$, we just need to calculate $\langle\Psi_0|(\bigtriangledown_{\vec{\lambda}}c_k)c_k^\dagger|\Psi_0\rangle = \vec{\alpha}_{kk}$ for $\epsilon_k > 0$ and $\langle\Psi_0|(\bigtriangledown_{\vec{\lambda}}c_k^\dagger)c_k|\Psi_0\rangle = \vec{\alpha}^*_{kk}$ for $\epsilon_k < 0$. Both expectation values can be calculated through the Green's function method. More specifically, we start with the retarded Green's function $G_{(\bigtriangledown_{\vec{\lambda}}c_k)c_k^\dagger}(\omega)$ in the frequency regime. Then take the analytic continuation $\omega + i\eta \to i\omega_n$ to get the Matsubara Green's function. After that, we do the summation of the Matsubara Green's function and take the $\tau \to 0^+$ limit so that we get the expectation value of $\langle(\bigtriangledown_{\vec{\lambda}}c_k c_k^\dagger\rangle$, which is $\vec{\gamma}_{\epsilon_k}$. Finally, we integrate over $\vec{\gamma}_{\epsilon_k}$ in the continuous energy space and take the line integral of the Berry connection in the parameter space to get the geometric phase. The calculation is tedious but straightforward, with the Berry connection expressions

$$\begin{aligned}\langle\Psi_0|\partial_{\epsilon_d}|\Psi_0\rangle &= -\frac{i}{\pi}\frac{\epsilon_d}{\epsilon_d^2 + v_2^2} \\ \langle\Psi_0|\partial_{v_2}|\Psi_0\rangle &= -\frac{i}{\pi}\frac{v_2}{\epsilon_d^2 + v_2^2},\end{aligned} \tag{10.17}$$

where ρ is the density of states and $v_2 = 2\pi\rho V_1 V_2$ is the dressed source drain asymmetry. It is defined so that the two expressions in Eq. (10.17) are symmetric with respect to the differentiation along two directions.

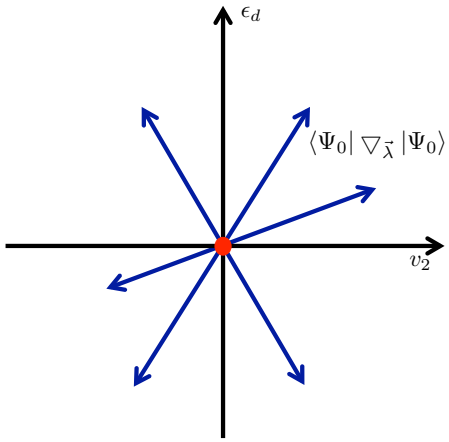

FIGURE 10.2: The plot of the geometric connection based on the expression Eq. (10.17). The red dot represents the critical point and the blue arrows are the geometric connection vectors. Since all vectors are pointing outward, the system has zero curvature everywhere.

The geometric connection given by Eq. (10.17) is plotted in Fig, 10.2. To begin with, the geometric connection is smooth everywhere except at the critical point: there geometric connection diverges as $1/|\vec{\lambda}|$ when $\vec{\lambda} \to 0$. This agrees with physical expectations where singularity occurs at the critical point. However, since all geometric connection vectors point outward, the corresponding geometric curvature will be zero everywhere. This can be easily realized when noticing $\partial_{v_2}\langle\Psi_0|\partial_{\epsilon_d}|\Psi_0\rangle = \partial_{\epsilon_d}\langle\Psi_0|\partial_{v_2}|\Psi_0\rangle$. Consequently, although singularity appears at the critical point, geometric phase will always be zero whatever loop c we choose. This radial form of the geometric connection is highly unusual and we are still trying to understand it.

10.4 Geometric Tensor and the Understanding of the Trivial Geometric Phase

As discussed before, the calculation of the geometric connection in Section 10.3 is only valid in infinite systems. This limits our understanding of the critical behavior of the system when the system size approaches infinity. The study of this critical behavior, however, leads to the superextensive criteria Eq. (10.7) in bulk QPT systems. Consequently, we should instead choose a method that is applicable to finite systems to better understand the vanishing of the geometric phase in the dissipative resonant level model.

To begin with, we introduce the geometric tensor [28]

$$Q_{\mu\nu} = \langle \partial_\mu \Psi_0 | \partial_\nu \Psi_0 \rangle - \langle \partial_\mu \Psi_0 | \Psi_0 \rangle \langle \Psi_0 | \partial_\nu \Psi_0 \rangle, \tag{10.18}$$

where $\mu, \nu = \epsilon_d$ or v_2 are the coefficient of the two QPT induced operators. It is straightforward to show that $\mathrm{Im}\, Q_{\mu\nu} = \partial_\mu A_\nu - \partial_\nu A_\mu$ such that the imaginary part of the geometric tensor coincides with the geometric curvature. To calculate the geometric tensor, we assume the wave function of the nth excited state as $|\Psi_n\rangle$, with its eigen-energy E_n. With those wavefunctions, we insert an identity $1 = \sum_{n \geqslant 0} |\Psi_n\rangle\langle\Psi_n|$ into Eq. (10.18)

$$Q_{\mu\nu}(\vec{\lambda}) = \sum_{n \geqslant 1} \frac{\langle \Psi_0(\vec{\lambda}) | \partial_\mu H(\vec{\lambda}) | \Psi_n(\vec{\lambda}) \rangle \langle \Psi_n(\vec{\lambda}) | \partial_\nu H(\vec{\lambda}) | \Psi_0(\vec{\lambda}) \rangle}{[E_n(\vec{\lambda}) - E_0(\vec{\lambda})]^2}. \tag{10.19}$$

With the expression in Eq. (10.19), it is straightforward to relate the geometric tensor to the Green's function

$$G_{\mu\nu}(\tau) = \Theta(\tau)[\langle \partial_\mu H(\tau) \partial_\nu H(0) \rangle - \langle \partial_\mu H(0) \rangle \langle \partial_\nu H(0) \rangle] \tag{10.20}$$

in the way

$$Q_{\mu\nu} = -i \frac{d}{d\omega} \tilde{G}_{\mu\nu} \Big|_{\omega=0} = \int_{-\infty}^{\infty} d\tau \tau G_{\mu\nu}(\tau). \tag{10.21}$$

Eq. (10.21) can be derived by noticing that

$$\tilde{G}_{\mu\nu}(\omega) = \int_{-\infty}^{\infty} d\tau e^{-i\omega\tau} G_{\mu\nu}(\tau) = \sum_{n\geqslant 1} \frac{\langle\Psi_0|\partial_\mu H|\Psi_n\rangle\langle\Psi_n|\partial_\nu H|\Psi_0\rangle}{i\omega + E_n}. \tag{10.22}$$

Notice that in the derivations above, we have assumed the uniqueness of the ground state wave function $|\Psi_0\rangle$. Strictly speaking, those equations are thus only valid in systems with smooth ground state variations in the parameter space. More specifically, near the QCP, when system size L becomes large, the energy difference $(E_0 - E_1) \propto L^{-\zeta} \to 0$, where $\zeta > 0$ is a dynamical constant. The vanishing of the energy difference, which signifies the QPT, makes the ground state $|\Psi_0\rangle$ ill-defined, thus invalidating the derivations between Eq. (10.18) and Eq. (10.22). However, although those equations are not applicable to the direct studies of the physics at the QCP of infinite systems, they are powerful in studying the critical behavior of finite systems. Alternatively, they can present how the geometric curvature at the QCP diverges with an increasing system size.

With the effective system Hamiltonian Eq. (10.9), in the dissipative resonant level model, $\partial_{V_2} H = \sum_k (\psi_k^\dagger - \psi_k) a$ and $\partial_{\epsilon_d} H = iab$. With those expressions and the Wick's theorem, the Green's function Eq. (10.20) simply becomes

$$\Theta(\tau)[\langle\sum_k(\psi_k^\dagger - \psi_k)(\tau)b(0)\rangle\langle a(\tau)a(0)\rangle - \langle\sum_k(\psi_k^\dagger - \psi_k)(\tau)a(0)\rangle\langle a(\tau)b(0)\rangle]. \tag{10.23}$$

Explicit calculation shows that Eq. (10.23) is identically zero in finite-size systems, leading to the vanishing of the geometric curvature everywhere. To understand the vanishing of this Green's function, we notice that one of the free lead Majorana fermion channels $\psi_k^\dagger - \psi_k$ couples only to the impurity Majorana fermion a in the effective Hamiltonian Eq. (10.9). The diagram is shown in Fig. (10.3). From those diagrams, we can see that the lead-impurity correlators in both terms of Eq. (10.23) produce the same free Majorana fermion propagator that couples to the same im-

purity Majorana a through the same vertex interaction V_2. They thus coincide with each other, which leads to the vanishing of the geometric curvature.

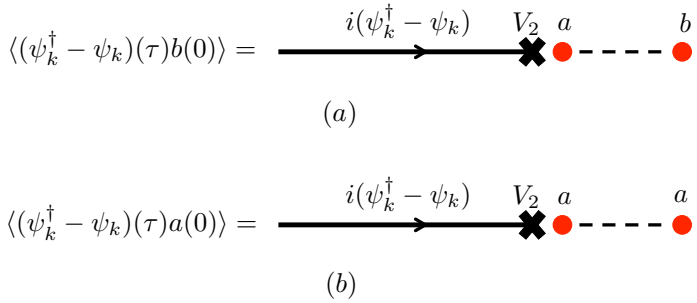

FIGURE 10.3: The diagram for the calculation of the Green's functions in Eq. (10.20). The straight arrow lines represent the free $i(\psi_k^\dagger - \psi_k)$ Majorana fermions. The cross labels the impurity-lead Majorana interaction and the dashed line represents the Green's function between two impurity Majorana fermions. Notice that since $i(\psi_k^\dagger - \psi_k)$ only interacts with a in Eq. (10.9), the interaction vertex only has one category.

Physically, the vanishing of the Berry curvature origins from the independence between two lead Majorana fermions $\sum_k i(\psi_k^\dagger - \psi_k)$ and $\sum_k(\psi_k^\dagger + \psi_k)$. This can be simply verified through the calculation of the correlator between these two lead Majorana fermions. To reach this independence, it is only required that the system has a spectrum that is particle-hole symmetric. This requirement is generally considered as satisfied in systems with linearized dispersion relation. Consequently, in the dissipative resonant level model, the geometric tensor Q_{v2,ϵ_d} is identically zero even in finite size systems. This is in great contrast to that in bulk QPTs: in those systems, the geometric curvature of finite size systems at the critical point is finite. And the divergence of the system size thus leads to the singularity of the geometric curvature.

10.5 Interactions and Possible Geometric Phase in Boundary QPTs?

Based on the previous section, we see that the vanishing of the geometric phase in the dissipative resonant level model comes from the fact that these two QPT inducing operators $i\epsilon_d ab$ and $V_2\sum_k(\psi_k^\dagger - \psi_k)a$ are always diagonal to each other and

create identically zero geometric curvature. To remedy this, one natural choice is to change the dissipation strength $R \neq R_Q$ such that the effective Hamiltonian becomes interacting. In this case, the effective deviation Hamiltonian becomes (see Chapter 7 for details)

$$\delta H = \tilde{\Delta} \cos[\sqrt{g}\tilde{\phi}_f]a + \tilde{V}_2 \sin[\sqrt{g}\tilde{\phi}_f]a, \tag{10.24}$$

where $g = \sqrt{2/(1+r)}$ is the effective interaction and $\tilde{\phi}_f$ is the bosonized phase describing the inter-lead charge tunneling. Notice that it is different from the original phase ϕ_f due to the the absorption of the Majorana b by the lead. With the interacting effective Hamiltonian Eq. (10.24), the calculation of the geometric tensor now involves the correlator $\langle \cos[\sqrt{g}\tilde{\phi}_f(\tau)] \sin[\sqrt{g}\tilde{\phi}_f(0)]\rangle$. Naively, in contrast to the two Majorana fermionic channels, those two operators $\cos[\sqrt{g}\tilde{\phi}_f(\tau)]$ and $\sin[\sqrt{g}\tilde{\phi}_f(0)]$ are not independent. However, straightforward calculation shows that

$$\begin{aligned}
&\langle \cos[\sqrt{g}\phi(t)] \sin[\sqrt{g}\phi(t')]\rangle \\
&= -\frac{1}{4i}[\langle e^{i\sqrt{g}\phi(t)} e^{-i\sqrt{g}\phi(t')}\rangle - \langle e^{-i\sqrt{g}\phi(t)} e^{i\sqrt{g}\phi(t')}\rangle] \\
&= -\frac{1}{4i}[\langle e^{i\sqrt{g}\phi(t)} e^{-i\sqrt{g}\phi(t')}\rangle - e^{ig\pi\Theta(t'-t)}\langle e^{i\sqrt{g}\phi(t')} e^{-i\sqrt{g}\phi(t)}\rangle] \\
&\propto -\frac{1}{|t-t'|^g} e^{ig\pi\Theta(t'-t)/2} + e^{ig\pi\Theta(t'-t)} \frac{1}{|t'-t|^g} e^{-ig\pi\Theta(t'-t)/2} \\
&= 0,
\end{aligned} \tag{10.25}$$

where we have used

$$\begin{aligned}
\langle e^{i\sqrt{g}\phi(t)} e^{-i\sqrt{g}\phi(t')}\rangle &= e^{-g\langle[\phi(t)-\phi(t')]\phi(t')\rangle} \propto e^{-g\ln[i\omega_R(t-t')]} \\
&= e^{-g\ln|\omega_R(t-t')| - ig\pi\Theta(t-t')/2}
\end{aligned} \tag{10.26}$$

and ω_R is the environment ultraviolet cutoff. As mentioned in Chapter 6, changing dissipation corresponds to changing Luttinger liquid interaction in the two chan-

nel Kondo model. In this point, adding local Luttinger liquid interactions will not remedy the vanishing of the geometric curvature.

At this point, one natural question is that whether or not there exists a boundary QPT-hosted system whose geometric phase is non-trivial. To date we can only claim that such system does not exist if long-range interaction does not exist. To better illustrate this, we assume a system with boundary quantum phase transition with the Hamiltonian

$$H = H_{\text{critical}} + \lambda_1 \hat{O}^1_{\text{lead}}(0)\hat{O}^1_{\text{impurity}} + \lambda_2 \hat{O}^2_{\text{lead}}(0)\hat{O}^2_{\text{impurity}}, \tag{10.27}$$

where H_{critical} is the critical Hamiltonian and the latter two terms in Eq. (10.27) are assumed to lead to some boundary quantum phase transitions with $\hat{O}^{1,2}_{\text{lead}}(0)$ a lead operator that couples to an impurity operator $\hat{O}^{1,2}_{\text{impurity}}$ [4]. Since those two operators can induce a boundary quantum phase transition, both $\hat{O}^1_{\text{impurity}}$ and $\hat{O}^2_{\text{impurity}}$ must be isolated from the lead freedoms at the point $\lambda_1 = \lambda_2 = 0$ [5]. Consequently, if we calculate the expectation value of $\langle \partial_{\lambda_1} H(\tau) \partial_{\lambda_2} H(0) \rangle$ at the QCP, it becomes

$$\begin{aligned} &\langle \hat{O}^1_{\text{lead}}(\tau)\hat{O}^1_{\text{impurity}}(\tau)\hat{O}^2_{\text{lead}}(0)\hat{O}^2_{\text{impurity}}(0)\rangle\Big|_{\lambda_1=\lambda_2=0} \\ &= \langle \hat{O}^1_{\text{lead}}(\tau)\hat{O}^2_{\text{lead}}(0)\rangle\langle \hat{O}^1_{\text{impurity}}(\tau)\hat{O}^1_{\text{impurity}}(0)\rangle\Big|_{\lambda_1=\lambda_2=0}. \end{aligned} \tag{10.28}$$

In Eq. (10.28), the later part is irrelevant of the system size so that will not diverge with an increasing system size. Our question then becomes that whether or not the first part (lead part) of Eq. (10.28) can be zero when $L \to \infty$ but finite otherwise? In the two channel Kondo and two impurity Kondo models, this seems impossible

[4] Here we have not assumed any limitation on those operators. They can be linear, quadratic, quartic or whatever...

[5] In boundary QPTs, the RG flowing from the unstable intermediate fixed point (for instance, the QCP) to the stable ground state must be accompanied by the decreasing of the impurity entropy as introduced in Chapter 4 (the g theorem). The decreasing of impurity entropy, on the other hand, indicates the hybridization of the decoupled impurity degrees of freedom (at the QCP) by the lead operators.

since we can integrate out the $x \neq 0$ parts in both models [103]. Consequently, the correlator of the lead part should also be independent of the system size. As a summary, in systems where long-range interaction is absent, the geometric curvature is supposed to vanish everywhere, leading to a trivial geometric phase.

10.6 Conclusion

In this chapter we have calculated the geometric phase of the $R = R_Q$ resonant level model. The calculation is carried out in two ways: either calculating the geometric connection with scattering state operators or calculating the geometric curvature with the geometric tensor. The first method is only valid in an infinite system where the QPT is hosted. In contrast to that, the geometric curvature calculation is more general and applies to finite-size systems so that can be used in the study of the scaling law of the criticality of the $R = R_Q$ resonant level model. Based on both calculations, although the quantum critical point of the model hosts a singularity of geometric connection at the quantum critical point, the geometric curvature vanishes everywhere in the parameter space, leading to a trivial geometric phase. Based on the geometric tensor calculation, it can be seen that this trivial geometric phase origins from the vanishing of the correlator between two QPT inducing operators even when the system is finite. This correlator remains zero when the system has local interactions (for instance, Luttinger liquid density interactions). We further argue that in a general boundary QPT-hosted system, the geometric curvature remains zero once its lead (or reservoir) can be legally integrated out: in this case the scaling law studied in the bulk QPT-hosted systems becomes invalid.

11

Conclusions

In the final chapter, I summarize the main results and findings contained in this thesis. Based on those results, I will further suggest future directions.

11.1 Conclusions

In this thesis, we have investigated the effect of dissipation or quantum noise in several systems where boundary QPTs are hosted. In those studies, we have shown that in contrast to the naive expectation that dissipation destroys QPTs by reducing system coherence, dissipation in boundary systems leads to non-trivial system behaviors and may even restore the boundary QPTs. Meanwhile, since the boundary systems are generally simpler and more experimental friendly, they provide great platforms in the study of general features of QPTs. This thesis begins with the introduction of the background information in the first four chapters —- including the introduction to the phenomenon and useful techniques in 1d systems, QPTs as well as boundary QPTs.

In Chapter 5, we begin with the two impurity Kondo model where a continuous QPT between the Kondo fixed point and the local singlet fixed point is sabotaged

by the charge tunneling process. It is shown that when the lead of the two impurity Kondo model becomes dissipative, the dissipative modes only couple to the charge tunneling process and will not touch the Kondo or exchange process. Consequently, in the two impurity Kondo model, dissipation plays a highly non-trivial role that restores the boundary QPT by reducing the relevance of charge tunneling. This result can also be experimentally verified by checking the conductance-temperature powerlaws at different fixed points.

In Chapter 6, we provide a study concerning the non-equilibrium I-V curve of a dissipative resonant level model at the QCP. In this model, the leading tunneling processes at weak coupling regime are relevant so that perturbative expansion with respect to the weak tunneling does not apply. To overcome this difficulty, we study the RG flow of the system and find out the leading irrelevant operator at the critical point in the strong coupling regime. With this operator, we calculate the non-equilibrium I-V curve of the system with the dynamical Coulomb blockade method, which strictly deals with the dissipation and bias. The comparison between our theoretical result and the experimental data shows significant agreement. After the study of the non-equilibrium I-V at the QCP, in Chapter 7 we study the non-equilibrium tunneling feature when the system crosses over from the QCP to a Fermi-liquid ground state. This crossover is induced by the asymmetry present in the system. In this chapter, we find out the effective system Hamiltonian near the QCP, and use the known Boltzmann equation results to analytically calculate the non-equilibrium I-V feature in the crossover regime. We further provide a direct connection between the $R = R_Q$ resonant level model and the famous two channel Kondo model. Our theoretical result shows a great agreement with the experimental data.

Studies on Majorana fermion in condensed matter physics have become popular for years due to its possible connection to quantum computation. One interesting

Majorana-related topic is the interaction between a Majorana zero mode and a quantum dot system. Although those systems have highly non-trivial features due to the presence of the MZM, it is known that most of the Majorana signatures are unstable against the inter-MZM coupling. In Chapter 8 we provide an option to overcome this problem by coupling one of the MZM to the Majorana fermion generated in a dissipative resonant level model. Through the calculation of the zero temperature conductance of a MZM-coupled resonant level model, we show that the Majorana fermion of a disspative resonant level model successfully restores the non-trivial MZM feature.

Although the main features of the Anderson model have been thoroughly studied for years, the combination between the Anderson model and dissipation remains vague. In recent years Professor Gleb Finkelstein's group has acquired plenty of data that describes the I-V feature of a dissipative Anderson model with different dissipation strengths. Several observed features are highly non-trivial compared with that of the dissipative resonant level model, including of the shifting of peak positions and the dissipation-dependent saturation value of the on-resonant peak. In this chapter we provide a theoretical understanding of the experimental result through both the RG calculations and the mapping of the model towards a QBM model. Our results qualitatively agree with the main feature of the experimental data.

Finally, in Chapter 10 we study an important difference between boundary QPTs and bulk QPTs. In a bulk QPT it has been proved that a non-trivial geometric phase appears if the QCP is superextensive. This criteria, however, remains vague in boundary QPTs. In this chapter we thus study the connection between geometric phase and boundary QPTs by investigating the $R = R_Q$ resonant level model. We showed that although the QCP of the dissipative resonant level model satisfies the superextensive criteria, its geometric phase is identically zero no matter how we choose the integral contour. We further argue that the missing of the geometric

phase is related to the fact that in boundary QPTs the leads (or higher dimensional baths) can normally be integrated out so that the scaling law in bulk systems does not apply.

11.2 Perspectives

The Majorana community is greatly encouraged by multiple experimental triumphs in the experimental searching of the MZM, including the most recently discovered $2e^2/h$ Majorana featured conductance across a nanowire-topological superconductor structure [194]. Further studies concerning the application of Majorana fermions or the discovery of other anyons are thus highly interesting to the condensed matter physical society. Particularly, considering the trend of the study on Majorana-related physics as well as my personal experience, I propose to study on the following topics.

Recently, there are multiple researches on the study of the multichannel topological Kondo problem [20; 12; 82] where multiple MZMs in the Majorana island couple to different independent electronic reservoirs. In this problem, the spin doublet degeneracy of the original Kondo model is replaced by a topologically protected doublet degeneracy formed by two isolated MZM in the Majorana island. Although has been widely researched recently, the multichannel topological Kondo model deserves further investigation. One of the options is to add dissipation into the reservoirs. In the resonant level model, lead dissipation normally behaves equivalently to the Luttinger liquid interaction. This is not the case in the Majorana island model: the modeling of the strucutre will decide the strength of dissipation that couples to different fields. In this sense, dissipative reservoir may result to exotic features that are different compared with that of Luttinger liquid interactions.

Another possible research topic is the Majorana-superconductor interaction. Based on a recent paper [112], the Josephson coupling between a bulk superconductor and the Majorana island will introduce asymmetry that breaks the higher $SO(M)_2$ sym-

metry in the topological Kondo model. Further investigation includes two possible directions: the effect of interaction in the Josephson coupling and the supercurrent through the superconductor-Majorana island-superconductor Josephson junction as a function of reservoir number and interactions.

Instead of the MZM created in the 1d nanowire system introduced in Chapter 8, one could also try to build MZMs, or even anyons along a superconducting proximitized quantum Hall edge state. The coexistence of quantum Hall edge state and superconducting pairing effect has been experimentally proved to coexist in a graphene Josephson junction [14]. An advantage of the quantum Hall edge state is the manipulation of a space dependent boundary condition. As proposed [140], the periodically varying boundary condition potentially supports the existence of Majorana fermions and other more complicated anyons. Most recently, another work [88] also points out the possible realization of Fibonacci anyon along the Hall edge state. Although this theoretical work seems far from any experimental realization in a short period of time, it is encouraging for us to search for interesting anyons along the quantum Hall-superconducting edge states.

Finally, multiple mesoscopic problems also deserve further investigation. For instance, to date we have not got a deep understanding of the stable intermediate fixed point of the dissipative Anderson model. In Chapter 9, we have claimed that this intermediate fixed point is protected by the subtle symmetry of the equivalent QBM lattice. However, to date we have not known the method to calculate the intermediate conductance, nor can we write down the leading irrelevant operator around this fixed point. It will be rather interesting to learn about the intermediate conductance value and the scaling laws around this point. Through further investigation into this intermediate fixed point, we can even acquire better understanding about the connection between symmetries and quantum noise. As another interesting topic, I may continue to study the connection between geometric phase and boundary QPTs.

In Chapter 10 we have argued that the geometric phase vanishes in the 2CK and some other more general systems. However, this argument only applies to effective 0+1d systems where the bath can be integrated out. It is thus interesting to study models where long-range interaction dominates and invalidates the 0+1d effective model. The physics behind the peculiar geometric connection pattern in Fig. 10.2 also deserves further investigation.

Bibliography

[1] (1984), "Quantal phase factors accompanying adiabatic changes," *Proceedings of the Royal Society of London A: Mathematical, Physical and Engineering Sciences*, 392, 45–57.

[2] Affleck, I. (1995), "Conformal Field Theory Approach to the Kondo Effect," .

[3] Affleck, I. (1998), "Edge magnetic field in the xxz spin-1/2 chain," *J. Phys. A: Math. Gen.*, 31, 2761–2766.

[4] Affleck, I. and Giuliano, D. (2013), "Topological superconductorLuttinger liquid junctions," *Journal of Statistical Mechanics: Theory and Experiment*, 2013, P06011.

[5] Affleck, I. and Ludwig, A. W. W. (1991), "Universal noninteger "ground-state degeneracy" in critical quantum systems," *Phys. Rev. Lett.*, 67, 161–164.

[6] Affleck, I., Ludwig, A. W. W., Pang, H.-B., and Cox, D. L. (1992), "Relevance of anisotropy in the multichannel Kondo effect: Comparison of conformal field theory and numerical renormalization-group results," *Phys. Rev. B*, 45, 7918–7935.

[7] Affleck, I., Ludwig, A. W. W., and Jones, B. A. (1995), "Conformal-field-theory approach to the two-impurity Kondo problem: Comparison with numerical renormalization-group results," *Phys. Rev. B*, 52, 9528–9546.

[8] Albrecht, S. M., Higginbotham, A. P., Madsen, M., Kuemmeth, F., Jespersen, T. S., Nygård, J., Krogstrup, P., and Marcus, C. M. (2016), "Exponential protection of zero modes in Majorana islands," *Nature*, 531, 206 EP –.

[9] Alicea, J. (2012), "New directions in the pursuit of Majorana fermions in solid state systems," *Reports on Progress in Physics*, 75, 076501.

[10] Alicea, J., Oreg, Y., Refael, G., von Oppen, F., and Fisher, M. P. A. (2011), "Non-Abelian statistics and topological quantum information processing in 1D wire networks," *Nature Physics*, 7, 412 EP –.

[11] Altimiras, C., Portier, F., and Joyez, P. (2016), "Interacting Electrodynamics of Short Coherent Conductors in Quantum Circuits," *Phys. Rev. X*, 6, 031002.

[12] Altland, A. and Egger, R. (2013), "Multiterminal Coulomb-Majorana Junction," *Phys. Rev. Lett.*, 110, 196401.

[13] Altland, A. and Simons, B. (2006), *Condensed Matter Field Theory*, Cambridge University Press, Cambridge.

[14] Amet, F., Ke, C. T., Borzenets, I. V., Wang, J., Watanabe, K., Taniguchi, T., Deacon, R. S., Yamamoto, M., Bomze, Y., Tarucha, S., and Finkelstein, G. (2016), "Supercurrent in the quantum Hall regime," *Science*, 352, 966–969.

[15] Amit, D. and Martin-Mayor, V. (2005), *Field Theory, the Renormalization Group, and Critical Phenomena: Graphs to Computers Third Edition*, World Scientific.

[16] Anderson, P. (1961), "Localized Magnetic States in Metals," *Physical Review*, 124, 41–53.

[17] Anderson, P. W. (1970), "A poor man's derivation of scaling laws for the Kondo problem," *Journal of Physics C: Solid State Physics*, 3, 2436.

[18] Anderson, P. W., Yuval, G., and Hamann, D. R. (1970), "Exact Results in the Kondo Problem. II. Scaling Theory, Qualitatively Correct Solution, and Some New Results on One-Dimensional Classical Statistical Models," *Phys. Rev. B*, 1, 4464–4473.

[19] Andrei, N., Furuya, K., and Lowenstein, J. H. (1983), "Solution of the Kondo problem," *Rev. Mod. Phys.*, 55, 331–402.

[20] Béri, B. and Cooper, N. R. (2012), "Topological Kondo Effect with Majorana Fermions," *Phys. Rev. Lett.*, 109, 156803.

[21] Bomze, Y., Mebrahtu, H., Borzenets, I., Makarovski, A., and Finkelstein, G. (2009), "Resonant tunneling in a dissipative environment," *Phys. Rev. B*, 79, 241402.

[22] Bruus, H. and Flensberg, K. (2004), *Many-Body Quantum Theory in Condensed Matter Physics*, Oxford University Press, New York.

[23] Cai, Z. and Barthel, T. (2013), "Algebraic versus Exponential Decoherence in Dissipative Many-Particle Systems," *Phys. Rev. Lett.*, 111, 150403.

[24] Cai, Z., Schollwöck, U., and Pollet, L. (2014), "Identifying a Bath-Induced Bose Liquid in Interacting Spin-Boson Models," *Phys. Rev. Lett.*, 113, 260403.

[25] Caldeira, A. and Leggett, A. (1983a), "Path integral approach to quantum Brownian motion," *Physica A: Statistical Mechanics and its Applications*, 121, 587 – 616.

[26] Caldeira, A. and Leggett, A. (1983b), "Quantum tunnelling in a dissipative system," *Annals of Physics*, 149, 374 – 456.

[27] Callan, C. G., Klebanov, I. R., Ludwig, A. W. W., and Maldacena, J. M. (1994), "Exact solution of a boundary conformal field theory," *Nucl. Phys. B*, 422, 417–448.

[28] Campos Venuti, L. and Zanardi, P. (2007), "Quantum Critical Scaling of the Geometric Tensors," *Phys. Rev. Lett.*, 99, 095701.

[29] Cardy, J. L. (1981), "One-dimensional models with 1/r 2 interactions," *Journal of Physics A: Mathematical and General*, 14, 1407.

[30] Cardy, J. L. (1989), "Boundary conditions, fusion rules and the Verlinde formula," *Nuclear Physics B*, 324, 581 – 596.

[31] Carollo, A. C. M. and Pachos, J. K. (2005), "Geometric Phases and Criticality in Spin-Chain Systems," *Phys. Rev. Lett.*, 95, 157203.

[32] Castro Neto, A. H., Novais, E., Borda, L., Zaránd, G., and Affleck, I. (2003), "Quantum Magnetic Impurities in Magnetically Ordered Systems," *Phys. Rev. Lett.*, 91, 096401.

[33] Cazalilla, M. A., Sols, F., and Guinea, F. (2006), "Dissipation-Driven Quantum Phase Transitions in a Tomonaga-Luttinger Liquid Electrostatically Coupled to a Metallic Gate," *Phys. Rev. Lett.*, 97, 076401.

[34] Chang, A. M. (2003), "Chiral Luttinger liquids at the fractional quantum Hall edge," *Rev. Mod. Phys.*, 75, 1449–1505.

[35] Chang, A. M. and Chen, J. C. (2009), "The Kondo effect in coupled-quantum dots," *Rep. Prog. Phys.*, 72, 096501.

[36] Cheng, M., Becker, M., Bauer, B., and Lutchyn, R. M. (2014), "Interplay between Kondo and Majorana Interactions in Quantum Dots," *Phys. Rev. X*, 4, 031051.

[37] Chung, C.-H., Glossop, M. T., Fritz, L., Kirćan, M., Ingersent, K., and Vojta, M. (2007), "Quantum phase transitions in a resonant-level model with dissipation: Renormalization-group studies," *Phys. Rev. B*, 76, 235103.

[38] Chung, C.-H., Le Hur, K., Vojta, M., and Wolfle, P. (2009), "Nonequilibrium Transport at a Dissipative Quantum Phase Transition," *Phys. Rev. Lett.*, 102, 216803.

[39] Chung, C.-H., Le Hur, K., Finkelstein, G., Vojta, M., and Wölfle, P. (2013), "Nonequilibrium quantum transport through a dissipative resonant level," *Phys. Rev. B*, 87, 245310.

[40] Churchill, H. O. H., Fatemi, V., Grove-Rasmussen, K., Deng, M. T., Caroff, P., Xu, H. Q., and Marcus, C. M. (2013), "Superconductor-nanowire devices from tunneling to the multichannel regime: Zero-bias oscillations and magnetoconductance crossover," *Phys. Rev. B*, 87, 241401.

[41] Cohen, G., Gull, E., Reichman, D. R., and Millis, A. J. (2014), "Green's Functions from Real-Time Bold-Line Monte Carlo Calculations: Spectral Properties of the Nonequilibrium Anderson Impurity Model," *Phys. Rev. Lett.*, 112, 146802.

[42] Coleman, P. (2015), *Introduction to Many-Body Physics*, Cambridge University Press.

[43] Cox, D. L. and Zawadowski, A. (1998), "Exotic Kondo effects in metals: Magnetic ions in a crystalline electric field and tunnelling centres," *Advances in Physics*, 47, 599–942.

[44] Cui, H. T. and Yi, J. (2008), "Geometric phase and quantum phase transition: Two-band model," *Phys. Rev. A*, 78, 022101.

[45] Dalla Torre, E. G., Demler, E., Giamarchi, T., and Altman, E. (2010), "Quantum critical states and phase transitions in the presence of non-equilibrium noise," *Nat. Phys.*, 6, 806–810.

[46] Dalla Torre, E. G., Demler, E., Giamarchi, T., and Altman, E. (2012), "Dynamics and universality in noise-driven dissipative systems," *Phys. Rev. B*, 85, 184302.

[47] Das, A., Ronen, Y., Most, Y., Oreg, Y., Heiblum, M., and Shtrikman, H. (2012), "Zero-bias peaks and splitting in an Al–InAs nanowire topological superconductor as a signature of Majorana fermions," *Nature Physics*, 8, 887 EP –.

[48] Deng, M. T., Yu, C. L., Huang, G. Y., Larsson, M., Caroff, P., and Xu, H. Q. (2012), "Anomalous Zero-Bias Conductance Peak in a NbInSb NanowireNb Hybrid Device," *Nano Letters*, 12, 6414–6419, PMID: 23181691.

[49] Deng, M. T., Yu, C. L., Huang, G. Y., Larsson, M., Caroff, P., and Xu, H. Q. (2014), "Parity independence of the zero-bias conductance peak in a nanowire based topological superconductor-quantum dot hybrid device," *Scientific Reports*, 4, 7261 EP –.

[50] Devoret, M. H., Esteve, D., and Urbina, C. (1995), "Single Electron Phenomena in Metallic Nanostructures," in *Mesoscopic Quantum Physics: Les Houches Session LXI*, eds. E. Akkermans, G. Montambaux, P. J.-L., and J. Zinn-Justin, pp. 605–658, Elsevier, Amsterdam.

[51] Dorda, A., Ganahl, M., Evertz, H. G., von der Linden, W., and Arrigoni, E. (2015), "Auxiliary master equation approach within matrix product states: Spectral properties of the nonequilibrium Anderson impurity model," *Phys. Rev. B*, 92, 125145.

[52] Eggert, S. and Affleck, I. (1992), "Magnetic impurities in half-integer-spin Heisenberg antiferromagnetic chains," *Phys. Rev. B*, 46, 10866–10883.

[53] Emery, V. J. and Kivelson, S. (1992), "Mapping of the two-channel Kondo problem to a resonant-level model," *Phys. Rev. B*, 46, 10812–10817.

[54] Fendley, P., Ludwig, A. W. W., and Saleur, H. (1995a), "Exact Conductance through Point Contacts in the $\nu = 1/3$ Fractional Quantum Hall Effect," *Phys. Rev. Lett.*, 74, 3005–3008.

[55] Fendley, P., Ludwig, A. W. W., and Saleur, H. (1995b), "Exact nonequilibrium transport through point contacts in quantum wires and fractional quantum Hall devices," *Phys. Rev. B*, 52, 8934–8950.

[56] Ferrier, M., Arakawa, T., Hata, T., Fujiwara, R., Delagrange, R., Weil, R., Deblock, R., Sakano, R., Oguri, A., and Kobayashi, K. (2016), "Universality of non-equilibrium fluctuations in strongly correlated quantum liquids," *Nat. Phys.*, 12, 230–235.

[57] Finck, A. D. K., Van Harlingen, D. J., Mohseni, P. K., Jung, K., and Li, X. (2013), "Anomalous Modulation of a Zero-Bias Peak in a Hybrid Nanowire-Superconductor Device," *Phys. Rev. Lett.*, 110, 126406.

[58] Fisher, M. P. A. and Glazman, L. I. (1996), "Transport in a one-dimensional Luttinger liquid," .

[59] Fisher, M. P. A. and Zwerger, W. (1985), "Quantum Brownian motion in a periodic potential," *Phys. Rev. B*, 32, 6190–6206.

[60] Flensberg, K. (1993), "Capacitance and conductance of mesoscopic systems connected by quantum point contacts," *Phys. Rev. B*, 48, 11156–11166.

[61] Flensberg, K. (2010), "Tunneling characteristics of a chain of Majorana bound states," *Phys. Rev. B*, 82, 180516.

[62] Flensberg, K. (2011), "Non-Abelian Operations on Majorana Fermions via Single-Charge Control," *Phys. Rev. Lett.*, 106, 090503.

[63] Florens, S., Simon, P., Andergassen, S., and Feinberg, D. (2007), "Interplay of electromagnetic noise and Kondo effect in quantum dots," *Phys. Rev. B*, 75, 155321.

[64] Foss-Feig, M., Hazzard, K. R. A., Bollinger, J. J., Rey, A. M., and Clark, C. W. (2013), "Dynamical quantum correlations of Ising models on an arbitrary lattice and their resilience to decoherence," *New J. Phys.*, 15, 113008.

[65] Fröjdh, P. and Johannesson, H. (1996), "Magnetic impurity in a Luttinger liquid: A conformal field theory approach," *Phys. Rev. B*, 53, 3211–3236.

[66] Furusaki, A. (1998), "Resonant tunneling through a quantum dot weakly coupled to quantum wires or quantum Hall edge states," *Phys. Rev. B*, 57, 7141–7148.

[67] Furusaki, A. and Matveev, K. A. (1995), "Theory of strong inelastic cotunneling," *Phys. Rev. B*, 52, 16676–16695.

[68] Furusaki, A. and Nagaosa, N. (1993), "Resonant tunneling in a Luttinger liquid," *Phys. Rev. B*, 47, 3827–3831.

[69] Gan, J. (1995), "Solution of the two-impurity Kondo model: Critical point, Fermi-liquid phase, and crossover," *Phys. Rev. B*, 51, 8287–8309.

[70] Georges, A. and Meir, Y. (1999), "Electronic Correlations in Transport through Coupled Quantum Dots," *Phys. Rev. Lett.*, 82, 3508–3511.

[71] Giamarchi, T. (2004), *Quantum Physics in One Dimension*, Oxford University Press, Oxford UK.

[72] Ginsparg, P. (1988), "Applied Conformal Field Theory," .

[73] Gogolin, A. O. and Komnik, A. (2006), "Towards full counting statistics for the Anderson impurity model," *Phys. Rev. B*, 73, 195301.

[74] Gogolin, A. O., Nersesyan, A. A., and Tsvelik, A. M. (1998), *Bosonization and Strongly Correlated Systems*, Cambridge University Press, Cambridge UK.

[75] Goldstein, M. and Berkovits, R. (2010), "Duality between Different Geometries of a Resonant Level in a Luttinger Liquid," *Phys. Rev. Lett.*, 104, 106403.

[76] Grobis, M., Rau, I. G., Potok, R. M., and Goldhaber-Gordon, D. (2006), "Kondo Effect in Mesoscopic Quantum Dots," .

[77] Guinea, F., Hakim, V., and Muramatsu, A. (1985), "Bosonization of a two-level system with dissipation," *Phys. Rev. B*, 32, 4410–4418.

[78] Hamma, A. (2006), "Berry Phases and Quantum Phase Transitions," .

[79] Härtle, R. and Millis, A. J. (2014), "Formation of nonequilibrium steady states in interacting double quantum dots: When coherences dominate the charge distribution," *Phys. Rev. B*, 90, 245426.

[80] Haug, H. and Jauho, A.-P. (2008), *Quantum Kinetics in Transport and Optics of Semiconductors*, Springer-Verlag, Berlin, second edn.

[81] Heidrich-Meisner, F., Feiguin, A. E., and Dagotto, E. (2009), "Real-time simulations of nonequilibrium transport in the single-impurity Anderson model," *Phys. Rev. B*, 79, 235336.

[82] Herviou, L., Le Hur, K., and Mora, C. (2016), "Many-terminal Majorana island: From topological to multichannel Kondo model," *Phys. Rev. B*, 94, 235102.

[83] Hewson, A. C. (1993), *The Kondo Problem to Heavy Fermions*, Cambridge University Press, New York.

[84] Higginbotham, A. P., Albrecht, S. M., Kiršanskas, G., Chang, W., Kuemmeth, F., Krogstrup, P., Jespersen, T. S., Nygård, J., Flensberg, K., and Marcus, C. M. (2015), "Parity lifetime of bound states in a proximitized semiconductor nanowire," *Nature Physics*, 11, 1017 EP –.

[85] Honer, J. and Weiss, U. (2010), "Nonlinear conductance and noise in boundary sine-Gordon and related models," *Chemical Physics*, 375, 265 – 275, in Stochastic processes in Physics and Chemistry (in honor of Peter Hänggi).

[86] Hoyos, J. A. and Vojta, T. (2008), "Theory of Smeared Quantum Phase Transitions," *Phys. Rev. Lett.*, 100, 240601.

[87] Hu, Y. and Kane, C. L. (2016), "Universal Symmetry-Protected Resonances in a Spinful Luttinger Liquid," *arXiv*, arXiv: 1604.08280.

[88] Hu, Y. and Kane, C. L. (2018), "Fibonacci Topological Superconductor," *Phys. Rev. Lett.*, 120, 066801.

[89] Iftikhar, Z., Jezouin, S., Anthore, A., Gennser, U., Parmentier, F. D., Cavanna, A., and Pierre, F. (2015), "Two-channel Kondo effect and renormalization flow with macroscopic quantum charge states," *Nature*, 526, 233–236.

[90] Iftikhar, Z., Anthore, A., Mitchell, A. K., Parmentier, F. D., Gennser, U., Ouerghi, A., Cavanna, A., Mora, C., Simon, P., and Pierre, F. (2017), "Tunable Quantum Criticality and Super-ballistic Transport in a 'Charge' Kondo Circuit," *arXiv*, arXiv: 1708.02542.

[91] Ihn, T. (2010), *Semiconductor Nanostructures*, Oxford University Press, Oxford.

[92] Ingold, G.-L. and Nazarov, Y. (1992), "Charge Tunneling Rates in Ultrasmall Junctions," in *Single Charge Tunneling: Coulomb Blockade Phenomena in Nanostructures*, eds. H. Grabert and M. H. Devoret, pp. 21–107, Plenum, New York, and arXiv:cond-mat/0508728.

[93] Ivanov, D. A. (2001), "Non-Abelian Statistics of Half-Quantum Vortices in p-Wave Superconductors," *Phys. Rev. Lett.*, 86, 268–271.

[94] Ivanov, T. I. (2017), "Coherent tunneling through a double quantum dot coupled to Majorana bound states," *Phys. Rev. B*, 96, 035417.

[95] Jayaprakash, C., Krishna-murthy, H. R., and Wilkins, J. W. (1981), "Two-Impurity Kondo Problem," *Phys. Rev. Lett.*, 47, 737–740.

[96] Jayatilaka, F. W., Galpin, M. R., and Logan, D. E. (2011), "Two-channel Kondo physics in tunnel-coupled double quantum dots," *Phys. Rev. B*, 84, 115111.

[97] Jeong, H., Chang, A. M., and Melloch, M. R. (2001), "The Kondo Effect in an Artificial Quantum Dot Molecule," *Science*, 293, 2221–2223.

[98] Jezouin, S., Albert, M., Parmentier, F. D., Anthore, A., Gennser, U., Cavanna, A., Safi, I., and Pierre, F. (2013), "Tomonaga–Luttinger physics in electronic quantum circuits," *Nat Commun*, 4, 1802.

[99] Jones, B. A., Kotliar, B. G., and Millis, A. J. (1989), "Mean-field analysis of two antiferromagnetically coupled Anderson impurities," *Phys. Rev. B*, 39, 3415–3418.

[100] Joshi, C., Nissen, F., and Keeling, J. (2013), "Quantum correlations in the one-dimensional driven dissipative XY model," *Phys. Rev. A*, 88, 063835.

[101] Kamenev, A. (2011), *Field Theory of Non-Equilibrium Systems*, Cambridge University Press.

[102] Kane, C. L. and Fisher, M. P. A. (1992a), "Resonant Tunneling in an Interacting One-Dimensional Electron Gas," *Phys. Rev. B*, 46, 7268–7271(R).

[103] Kane, C. L. and Fisher, M. P. A. (1992b), "Transmission through barriers and resonant tunneling in an interacting one-dimensional electron gas," *Phys. Rev. B*, 46, 15233–15262.

[104] Kane, C. L. and Fisher, M. P. A. (1992c), "Transport in a one-channel Luttinger liquid," *Phys. Rev. Lett.*, 68, 1220–1223.

[105] Kapitulnik, A., Mason, N., Kivelson, S. A., and Chakravarty, S. (2001), "Effects of dissipation on quantum phase transitions," *Phys. Rev. B*, 63, 125322.

[106] Keller, A. J., Peeters, L., Moca, C. P., Weymann, I., Mahalu, D., Umansky, V., Zarand, G., and Goldhaber-Gordon, D. (2015), "Universal Fermi liquid crossover and quantum criticality in a mesoscopic system," *Nature*, 526, 237–240.

[107] Kitaev, A. Y. (2001), "Unpaired Majorana fermions in quantum wires," *Physics-Uspekhi*, 44, 131.

[108] Koerting, V., Andersen, B. M., Flensberg, K., and Paaske, J. (2010), "Nonequilibrium transport via spin-induced subgap states in superconductor/quantum dot/normal metal cotunnel junctions," *Phys. Rev. B*, 82, 245108.

[109] Komnik, A. and Gogolin, A. O. (2003), "Resonant Tunneling between Luttinger Liquids: A Solvable Case," *Phys. Rev. Lett.*, 90, 246403.

[110] Kondo, J. (1964), "Resistance Minimum in Dilute Magnetic Alloys," *Progress of Theoretical Physics*, 32, 37–49.

[111] Kretinin, A. V., Shtrikman, H., Goldhaber-Gordon, D., Hanl, M., Weichselbaum, A., von Delft, J., Costi, T., and Mahalu, D. (2011), "Spin-$\frac{1}{2}$ Kondo effect in an InAs nanowire quantum dot: Unitary limit, conductance scaling, and Zeeman splitting," *Phys. Rev. B*, 84, 245316.

[112] Landau, L. A. and Sela, E. (2017), "Two-channel Kondo physics in a Majorana island coupled to a Josephson junction," *Phys. Rev. B*, 95, 035135.

[113] Landau, L. A., Cornfeld, E., and Sela, E. (2018), "Charge Fractionalization in the Two-Channel Kondo Effect," *Phys. Rev. Lett.*, 120, 186801.

[114] Langreth, D. C. (1966), "Friedel Sum Rule for Anderson's Model of Localized Impurity States," *Phys. Rev.*, 150, 516–518.

[115] Law, K. T., Lee, P. A., and Ng, T. K. (2009), "Majorana Fermion Induced Resonant Andreev Reflection," *Phys. Rev. Lett.*, 103, 237001.

[116] Le Hur, K. (2004), "Coulomb blockade of a noisy metallic box: A realization of Bose-Fermi Kondo models," *Phys. Rev. Lett.*, 92, 196804.

[117] Le Hur, K. and Li, M.-R. (2005), "Unification of electromagnetic noise and Luttinger liquid via a quantum dot," *Phys. Rev. B*, 72, 073305.

[118] Lee, M., Lim, J. S., and López, R. (2013), "Kondo effect in a quantum dot side-coupled to a topological superconductor," *Phys. Rev. B*, 87, 241402.

[119] Leggett, A. J., Chakravarty, S., Dorsey, A. T., Fisher, M. P. A., Garg, A., and Zwerger, W. (1987), "Dynamics of the dissipative two-state system," *Rev. Mod. Phys.*, 59, 1–85.

[120] Leturcq, R., Schmid, L., Ensslin, K., Meir, Y., Driscoll, D. C., and Gossard, A. C. (2005), "Probing the Kondo Density of States in a Three-Terminal Quantum Ring," *Phys. Rev. Lett.*, 95, 126603.

[121] Levitov, L. S. and Reznikov, M. (2004), "Counting statistics of tunneling current," *Phys. Rev. B*, 70, 115305.

[122] Levy Yeyati, A., Martin-Rodero, A., Estève, D., and Urbina, C. (2001), "Direct Link between Coulomb Blockade and Shot Noise in a Quantum-Coherent Structure," *Phys. Rev. Lett.*, 87, 046802.

[123] Liu, D. E. and Baranger, H. U. (2011), "Detecting a Majorana-fermion zero mode using a quantum dot," *Phys. Rev. B*, 84, 201308.

[124] Liu, D. E., Zheng, H., Finkelstein, G., and Baranger, H. U. (2014), "Tunable quantum phase transitions in a resonant level coupled to two dissipative baths," *Phys. Rev. B*, 89, 085116.

[125] Majumdar, K., Schiller, A., and Hershfield, S. (1998), "Nonequilibrium Kondo impurity: Perturbation about an exactly solvable point," *Phys. Rev. B*, 57, 2991–2999.

[126] Makarovski, A., Zhukov, A., Liu, J., and Finkelstein, G. (2007), "SU(2) and SU(4) Kondo effects in carbon nanotube quantum dots," *Phys. Rev. B*, 75, 241407.

[127] Maldacena, J. M. and Ludwig, A. W. W. (1997), "Majorana fermions, exact mapping between quantum impurity fixed points with four bulk fermion species, and solution of the "Unitarity Puzzle"," *Nucl. Phys. B*, 506, 565–588.

[128] Malecki, J., Sela, E., and Affleck, I. (2010), "Prospect for observing the quantum critical point in double quantum dot systems," *Phys. Rev. B*, 82, 205327.

[129] Malecki, J., Sela, E., and Affleck, I. (2011), "Erratum: Prospect for observing the quantum critical point in double quantum dot systems [Phys. Rev. B **82**, 205327 (2010)]," *Phys. Rev. B*, 84, 159907(E).

[130] Marino, J. and Diehl, S. (2016), "Driven Markovian Quantum Criticality," *Phys. Rev. Lett.*, 116, 070407.

[131] Martín-Rodero, A. and Levy-Yeyati, A. (2011), "Josephson and Andreev transport through quantum dots," *Adv. Phys*, 60, 899–958.

[132] Matveev, K. A. and Glazman, L. I. (1993), "Coulomb blockade of tunneling into a quasi-one-dimensional wire," *Phys. Rev. Lett.*, 70, 990–993.

[133] Maurand, R., Meng, T., Bonet, E., Florens, S., Marty, L., and Wernsdorfer, W. (2012), "First-Order 0-π Quantum Phase Transition in the Kondo Regime of a Superconducting Carbon-Nanotube Quantum Dot," *Phys. Rev. X*, 2, 011009.

[134] Mebrahtu, H. T., Borzenets, I. V., Liu, D. E., Zheng, H., Bomze, Y. V., Smirnov, A. I., Baranger, H. U., and Finkelstein, G. (2012), "Quantum phase transition in a resonant level coupled to interacting leads," *Nature*, 488, 61–64.

[135] Mebrahtu, H. T., Borzenets, I. V., Zheng, H., Bomze, Y. V., Smirnov, A. I., Florens, S., Baranger, H. U., and Finkelstein, G. (2013), "Observation of Majorana Quantum Critical Behavior in a Resonant Level Coupled to a Dissipative Environment," *Nat. Phys.*, 9, 732–737, arXiv:1212.3857.

[136] Meden, V., Enss, T., Andergassen, S., Metzner, W., and Schönhammer, K. (2005), "Correlation effects on resonant tunneling in one-dimensional quantum wires," *Phys. Rev. B*, 71, 041302.

[137] Meir, Y. and Wingreen, N. S. (1992), "Landauer formula for the current through an interacting electron region," *Phys. Rev. Lett.*, 68, 2512–2515.

[138] Micolich, A. P. (2011), "What lurks below the last plateau: Experimental studies of the 0.7 conductance anomaly in one-dimensional systems," *J. Phys. Cond. Matt.*, 23, 443201.

[139] Mitchell, A. K., Landau, L. A., Fritz, L., and Sela, E. (2016), "Universality and Scaling in a Charge Two-Channel Kondo Device," *Phys. Rev. Lett.*, 116, 157202.

[140] Mong, R. S. K., Clarke, D. J., Alicea, J., Lindner, N. H., Fendley, P., Nayak, C., Oreg, Y., Stern, A., Berg, E., Shtengel, K., and Fisher, M. P. A. (2014), "Universal Topological Quantum Computation from a Superconductor-Abelian Quantum Hall Heterostructure," *Phys. Rev. X*, 4, 011036.

[141] Mott, N. F. (1990), *Metal-Insulator Transitions*, Taylor & Francis, London.

[142] Mourik, V., Zuo, K., Frolov, S. M., Plissard, S. R., Bakkers, E. P. A. M., and Kouwenhoven, L. P. (2012), "Signatures of Majorana Fermions in Hybrid Superconductor-Semiconductor Nanowire Devices," *Science*, 336, 1003–1007.

[143] Nagy, D. and Domokos, P. (2015), "Nonequilibrium Quantum Criticality and Non-Markovian Environment: Critical Exponent of a Quantum Phase Transition," *Phys. Rev. Lett.*, 115, 043601.

[144] Nayak, C., Simon, S. H., Stern, A., Freedman, M., and Das Sarma, S. (2008), "Non-Abelian anyons and topological quantum computation," *Rev. Mod. Phys.*, 80, 1083–1159.

[145] Nesterov, A. I. and Ovchinnikov, S. G. (2008), "Geometric phases and quantum phase transitions in open systems," *Phys. Rev. E*, 78, 015202.

[146] Novais, E., Castro Neto, A. H., Borda, L., Affleck, I., and Zárand, G. (2005), "Frustration of decoherence in open quantum systems," *Phys. Rev. B*, 72, 014417.

[147] Nozires, P. (1974), "A fermi-liquid description of the Kondo problem at low temperatures," *J Low Temp Phys*, 17, 31–42.

[148] Nozires, Ph. and Blandin, A. (1980), "Kondo effect in real metals," *J. Phys. France*, 41, 193–211.

[149] Oshikawa, M. and Affleck, I. (1997), "Boundary conformal field theory approach to the critical two-dimensional Ising model with a defect line," *Nucl. Phys. B*, 495, 533–582.

[150] Pachos, J. K. and Carollo, A. C. (2006), "Geometric phases and criticality in spin systems," *Philosophical Transactions of the Royal Society of London A: Mathematical, Physical and Engineering Sciences*, 364, 3463–3476.

[151] Pletyukhov, M. and Schoeller, H. (2012), "Nonequilibrium Kondo model: Crossover from weak to strong coupling," *Phys. Rev. Lett.*, 108, 260601.

[152] Poletti, D., Bernier, J.-S., Georges, A., and Kollath, C. (2012), "Interaction-Induced Impeding of Decoherence and Anomalous Diffusion," *Phys. Rev. Lett.*, 109, 045302.

[153] Polyakov, D. G. and Gornyi, I. V. (2003), "Transport of interacting electrons through a double barrier in quantum wires," *Phys. Rev. B*, 68, 035421.

[154] Potok, R. M., Rau, I. G., Shtrikman, H., Oreg, Y., and Goldhaber-Gordon, D. (2007), "Observation of the two-channel Kondo effect," *Nature*, 446, 167–171.

[155] Pustilnik, M. and Glazman, L. (2004), "Kondo effect in quantum dots," *Journal of Physics: Condensed Matter*, 16, R513.

[156] Pustilnik, M., Borda, L., Glazman, L. I., and von Delft, J. (2004), "Quantum phase transition in a two-channel-Kondo quantum dot device," *Phys. Rev. B*, 69, 115316.

[157] Rau, I. G., Amasha, S., Oreg, Y., and Goldhaber-Gordon, D. (2011), "Quantum Phase Transitions in Quantum Dots," in *Understanding Quantum Phase Transitions*, ed. L. D. Carr, pp. 341–367, CRC Press, Boca Raton.

[158] Read, N. and Green, D. (2000), "Paired states of fermions in two dimensions with breaking of parity and time-reversal symmetries and the fractional quantum Hall effect," *Phys. Rev. B*, 61, 10267–10297.

[159] Reimann, S. M. and Manninen, M. (2002), "Electronic structure of quantum dots," *Rev. Mod. Phys.*, 74, 1283–1342.

[160] Rosch, A., Paaske, J., Kroha, J., and Wölfle, P. (2003), "Nonequilibrium Transport through a Kondo Dot in a Magnetic Field: Perturbation Theory and Poor Man's Scaling," *Phys. Rev. Lett.*, 90, 076804.

[161] Sachdev, S. (2011), *Quantum Phase Transitions*, Cambridge University Press, Cambridge UK, 2 edn.

[162] Safi, I. and Joyez, P. (2011), "Time-dependent theory of nonlinear response and current fluctuations," *Phys. Rev. B*, 84, 205129.

[163] Safi, I. and Saleur, H. (2004), "One-Channel Conductor in an Ohmic Environment: Mapping to a Tomonaga-Luttinger Liquid and Full Counting Statistics," *Phys. Rev. Lett.*, 93, 126602.

[164] Sassetti, M. and Weiss, U. (1994), "Transport of 1D Interacting Electrons Through Barriers and Effective Tunnelling Density of States," *EPL (Europhysics Letters)*, 27, 311.

[165] Schiller, A. and Hershfield, S. (1995), "Exactly solvable nonequilibrium Kondo problem," *Phys. Rev. B*, 51, 12896–12899.

[166] Schiller, A. and Hershfield, S. (1998), "Toulouse limit for the nonequilibrium Kondo impurity: Currents, noise spectra, and magnetic properties," *Phys. Rev. B*, 58, 14978.

[167] Schiller, A. and Ingersent, K. (1997), "Renormalization-group study of a magnetic impurity in a Luttinger liquid," *EPL*, 39, 645.

[168] Sela, E. and Affleck, I. (2009a), "Nonequilibrium critical behavior for electron tunneling through quantum dots in an Aharonov-Bohm circuit," *Phys. Rev. B*, 79, 125110.

[169] Sela, E. and Affleck, I. (2009b), "Nonequilibrium Transport through Double Quantum Dots: Exact Results near a Quantum Critical Point," *Phys. Rev. Lett.*, 102, 047201.

[170] Sela, E. and Affleck, I. (2009c), "Resonant Pair Tunneling in Double Quantum Dots," *Phys. Rev. Lett.*, 103, 087204.

[171] Sengupta, A. M. and Georges, A. (1994), "Emery-Kivelson solution of the two-channel Kondo problem," *Phys. Rev. B*, 49, 10020–10022.

[172] Sengupta, K., Žutić, I., Kwon, H.-J., Yakovenko, V. M., and Das Sarma, S. (2001), "Midgap edge states and pairing symmetry of quasi-one-dimensional organic superconductors," *Phys. Rev. B*, 63, 144531.

[173] Sieberer, L. M., Huber, S. D., Altman, E., and Diehl, S. (2013), "Dynamical Critical Phenomena in Driven-Dissipative Systems," *Phys. Rev. Lett.*, 110, 195301.

[174] Tinkham, M. (1996), *Introduction to Superconductivity*, McGraw-Hill, New York, second edn.

[175] Voit, J. (1995), "One-dimensional Fermi liquids," *Reports on Progress in Physics*, 58, 977.

[176] Vojta, M. (2003), "Quantum phase transitions," *Reports on Progress in Physics*, 66, 2069.

[177] Vojta, M. (2006), "Impurity quantum phase transitions," *Philos. Mag.*, 86, 1807–1846.

[178] von Delft, J. and Schoeller, H. (1998), "Bosonization for Beginners — Refermionization for Experts," .

[179] Wang, P., Cao, Y., Gong, M., Li, S.-S., and Li, X.-Q. (2014), "Demonstrating nonlocality-induced teleportation through Majorana bound states in a semiconductor nanowire," *Physics Letters A*, 378, 937 – 940.

[180] Weiss, U. (2008), *Quantum Dissipative Systems*, World Scientific, Singapore, third edn.

[181] Werner, P., Völker, K., Troyer, M., and Chakravarty, S. (2005), "Phase Diagram and Critical Exponents of a Dissipative Ising Spin Chain in a Transverse Magnetic Field," *Phys. Rev. Lett.*, 94, 047201.

[182] Wilson, K. G. and Kogut, J. (1974), "The renormalization group and the ϵ expansion," *Physics Reports*, 12, 75 – 199.

[183] Wong, E. and Affleck, I. (1994), "Tunneling in quantum wires: A boundary conformal field theory approach," *Nucl. Phys. B*, 417, 403–438.

[184] Xiao, D., Chang, M.-C., and Niu, Q. (2010), "Berry phase effects on electronic properties," *Rev. Mod. Phys.*, 82, 1959–2007.

[185] Yennie, D. R. (1987), "Integral quantum Hall effect for nonspecialists," *Rev. Mod. Phys.*, 59, 781–824.

[186] Yi, H. and Kane, C. L. (1998), "Quantum Brownian motion in a periodic potential and the multichannel Kondo problem," *Phys. Rev. B*, 57, R5579–R5582.

[187] Yu. V. Nazarov and Blanter, Y. M. (2009), *Quantum Transport: Introduction to Nanoscience*, Cambridge University Press, Cambridge.

[188] Yu. V. Nazarov and Glazman, L. I. (2003), "Resonant Tunneling of Interacting Electrons in a One-Dimensional Wire," *Phys. Rev. Lett.*, 91, 126804.

[189] Zamolodchikov, A. B. (1986), "Irreversibility of the Flux of the Renormalization Group in a 2D Field Theory," *JETP Lett.*, 43, 730–732, [Pisma Zh. Eksp. Teor. Fiz.43,565(1986)].

[190] Zamolodchikov, A. B. and Zamolodchikov, A. B. (1979), "Factorized S-matrices in two dimensions as the exact solutions of certain relativistic quantum field theory models," *Annals of Physics*, 120, 253 – 291.

[191] Zaránd, G., Chung, C.-H., Simon, P., and Vojta, M. (2006), "Quantum Criticality in a Double-Quantum-Dot System," *Phys. Rev. Lett.*, 97, 166802.

[192] Zawadowski, A. (1980), "Kondo-like State in a Simple Model for Metallic Glasses," *Phys. Rev. Lett.*, 45, 211–214.

[193] Zhang, H., Gül, Ö., Conesa-Boj, S., Nowak, M., Wimmer, M., Zuo, K., Mourik, V., de Vries, F. K., van Veen, J., de Moor, M. W. A., Bommer, J. D. S., van Woerkom, D. J., Car, D., Plissard, S. R., Bakkers, E. P. A. M., Quintero-Pérez, M., Cassidy, M. C., Koelling, S., Goswami, S., Watanabe, K., Taniguchi, T., and Kouwenhoven, L. P. (2017), "Ballistic superconductivity in semiconductor nanowires," *Nature Communications*, 8, 16025 EP –.

[194] Zhang, H., Liu, C.-X., Gazibegovic, S., Xu, D., Logan, J. A., Wang, G., van Loo, N., Bommer, J. D. S., de Moor, M. W. A., Car, D., Op het Veld, R. L. M., van Veldhoven, P. J., Koelling, S., Verheijen, M. A., Pendharkar, M., Pennachio, D. J., Shojaei, B., Lee, J. S., Palmstrøm, C. J., Bakkers, E. P. A. M., Sarma, S. D., and Kouwenhoven, L. P. (2018), "Quantized Majorana conductance," *Nature*, 556, 74 EP –.

[195] Zheng, H., Florens, S., and Baranger, H. U. (2014), "Transport signatures of Majorana quantum criticality realized by dissipative resonant tunneling," *Phys. Rev. B*, 89, 235135.

[196] Zheng, W., Friedman, J. R., Averin, D. V., Han, S. Y., and Lukens, J. E. (1998), "Observation of strong Coulomb blockade in resistively isolated tunnel junctions," *Solid State Communications*, 108, 839–843.

[197] Zhu, S.-L. (2006), "Scaling of Geometric Phases Close to the Quantum Phase Transition in the XY Spin Chain," *Phys. Rev. Lett.*, 96, 077206.

Biography

Education

1. Gu Zhang was born February 1st, 1989 in Hechuan, Sichuan, China.

2. He received his B.S. degree from Nanjing University, China 2012. His B.S. thesis focuses on Andreev and non-local Andreev reflection in multiple P-N junction structures under the instruction of Prof. Rui Shen.

3. He was enrolled into the physics PhD program at Duke University, the USA since August, 2012. After joining Prof. Harold U. Baranger's group that year, he focused on the study of the effect of dissipation in mesoscopic systems, especially those with boundary quantum phase transitions. After 2016, he also started the research of the supercurrent through a graphene Josephson junction where the graphene layer is in the quantum Hall regime.

Finished Papers:

1. Gu Zhang, Eduardo Novais and Harold U. Baranger, "Rescuing a Quantum Phase Transition with Quantum Noise", *Physical Review Letters*, **118**, 050402 (2017)

2. Gu Zhang, Chung-Hou Chung, Chung-Ting Ke, Chao-Yun Lin, Henok Mebrahtu, Alex I. Smirnov, Gleb Finkelstein and Harold U. Baranger, "Universal Nonequilibrium I-V Curve at an Interacting Impurity Quantum Critical Point", arXiv: 1609.04765v2 (2018)

List of Awards since 2012

1. Fritz London Graduate Fellowship (2017)

2. Duke Graduate School Conference Travel Award (2017)

3. Nano Fellowship (2013)